

High Performance Non-Noble-Metal Based Catalysts for Water and Seawater Electrolysis

by
Libo Wu

A dissertation submitted to the Materials Science and Engineering Program,
Cullen College of Engineering
in partial fulfillment of the requirements for the degree of

DOCTOR OF PHILOSOPHY

in Materials Science and Engineering

Chair of Committee: Zhifeng Ren

Committee Member: Alamgir Karim

Committee Member: Jiming Bao

Committee Member: Paul Ruchhoeft

Committee Member: Shuo Chen

University of Houston
May 2022

Copyright 2022, Libo Wu

ACKNOWLEDGEMENTS

First and foremost, I would like to express my sincere thanks to Prof. Zhifeng Ren for his firm support and valuable guidance throughout my Ph.D. research career. I have always been grateful to Prof. Ren for giving me the precious opportunity to study in his group. Without his kind help, I would not be able to continue my Ph.D. study. Prof. Ren gives me a lot of freedom in experimental subjects and always encourages me to investigate something new and useful. His suggestion and guidance have helped me become the researcher I am today. I am also very grateful to Prof. Ren for generously sharing his experience and giving me constructive advice in my daily life. It is my pleasure to study under supervision of such a great advisor.

I appreciate the kind help and patient guidance from Prof. Shuo Chen, Dr. Luo Yu, and Dr. Shaowei Song during my Ph.D. career. They are serious and responsible and have helped me a lot in both my research work and daily life. At the same time, I would like to express my sincere thanks to other lab mates of the catalytic group: Mr. Fanghao Zhang, Mr. Minghui Ning, Dr. Sean Roubion, and Mr. Will Harrison for their encouragement and suggestion. We discuss research papers and experimental data together, which gives me a comprehensive understanding of this area and inspires me in my research work.

I would like to thank my current group mates Mr. Congcong Xu, Mr. Zhongxin Liang, Ms. Fengjiao Pan, Mr. Yu Wang, and former group mates Dr. Brian McElhenny, Dr. Dan Luo, Dr. Qing Zhu, Dr. Wuyang Ren, Dr. Jun Mao, Dr. Haoran Sun, Dr. Fei Tian, Dr. Jingying Sun, Dr. Qiancheng Zhu, Dr. Xin Xiao, Dr. Weiwu Chen, and Dr. Shan Li. I feel so lucky to meet and work with these wonderful colleagues in the past few years.

My sincere thanks to Prof. Jiming Bao, Prof. Alamgir Karim, Prof. Yan Yao, Prof. Boris Makarenko, Prof. Xiaonan Shan, Mr. Chuqing Yuan, Dr. Chunzheng Wu, Dr. Xinxin Xing, Mr. Tian Tong, Ms. Zhaoyang Chen, Mr. Chaojie Yang, and Dr. Xu Yang for their academic help. They are very generous in letting me use experimental equipment or patiently teaching me to do experiments. I would like to thank my roommate of four years, Mr. Shaoshuai Zhang, for his help in daily life.

Thanks to staffs at the Texas Center for Superconductivity at the University of Houston (TcSUH) and the Material Science and Engineering Program for their continuous support. I would like to thank Dr. Dezhi Wang, Ms. Suqing Li, Mr. Troy Christensen, Ms. Susan Butler, and Dr. Chrisdolyn Dawson.

I would like to thank the committee members: Prof. Zhifeng Ren, Prof. Alamgir Karim, Prof. Jiming Bao, Prof. Paul Ruchhoeft, and Prof. Shuo Chen for their help and guidance during the entire period toward my graduation.

Finally, I am deeply grateful to my parents, Shouying Wu and Xia Li, for their never-ending love and unconditional support in my life. They have raised me to be the person I am today. Thank you. I would like to thank my girlfriend Qian Hua for her love. Good luck with your Ph.D. study.

ABSTRACT

Water and seawater electrolysis to produce high caloric hydrogen gas is a sustainable and environmentally friendly energy-conversion technology that can be used to decrease the excessive consumption of fossil fuels. In general, water electrolysis is composed of two half reactions: oxygen evolution reaction (OER) on the anode and hydrogen evolution reaction (HER) on the cathode. To make electrolysis process energy-efficient and cost-effective, catalysts, which can promote the sluggish kinetics of OER or HER by lowering their activation energy, are extensively studied. However, conventional noble-metal based catalysts such as Pt-/Ir-/Ru- composites suffer from high cost and scarce availability despite their high catalytic activity. Developing alternative non-noble-metal based catalysts with high catalytic activity and long-term durability is desirable but remains a challenge. At the same time, seawater electrolysis is attracting growing research attention due to its obvious advantages such as inexhaustible resource reserves, easy combination with ocean-related renewable-energy technologies and by-production of freshwater. However, the complicated composition of natural seawater can result in additional challenges for direct seawater electrolysis including competing chlorine evolution reaction, chloride corrosion, and catalyst poisoning. Addressing these challenges requires rational design of catalysts dedicated to seawater electrolysis.

Here we apply various synthetic approaches to synthesize efficient non-noble-metal based catalysts for large-current-density water and seawater electrolysis, including tungsten-doped nickel iron layered double hydroxides (Ni-Fe-W LDH), boron-modified cobalt iron layered double hydroxides (B-Co₂Fe LDH), and core-

shell-structured $\text{CoP}_x@FeOOH$ for OER, heterogeneous metallic nickel and molybdenum nitride (Ni-MoN) for HER, and bimetallic phosphide ($\text{Ni}_2\text{P-Fe}_2\text{P}$) for both OER and HER. Rational design enables these novel catalysts to exhibit high catalytic activity, long-term durability, and enhanced chemical/structural stability to work well in both alkaline freshwater and seawater electrolytes. In these specific works, the effects of elemental doping, structural tuning, crystallinity adjustment, phase combination, electronic structure optimization, surface properties, corrosion resistance, and many other conditions on catalytic performance are investigated. Theoretical calculations are attempted to investigate the active sites and physical and chemical characterizations before and after catalytic reactions are conducted to reveal the transformation of these catalysts during electrolysis process.

TABLE OF CONTENTS

ACKNOWLEDGEMENTS	iii
ABSTRACT	v
TABLE OF CONTENTS	vii
LIST OF FIGURES	xi
CHAPTER 1 INTRODUCTION	1
1.1 Introduction to Water and Seawater Electrolysis.....	1
1.2 Fundamentals of Alkaline Water Electrolysis	4
1.2.1 Principles of Alkaline OER and HER.....	4
1.2.2 Important Parameters to Evaluate Catalytic Activity.....	5
1.3 Typical Self-supported Catalysts	8
1.3.1 Layered Double Hydroxides (LDHs).....	9
1.3.2 Transition Metal Phosphides (TMPs)	10
1.3.3 Transition Metal Nitrides (TMNs).....	11
1.4 Typical Synthesis Methods	12
1.4.1 Hydrothermal Reaction.....	12
1.4.2 Water Bath Reaction	13
1.4.3 Electrodeposition.....	14
1.4.4 Ion Exchange.....	14
1.4.5 Annealing	15
CHAPTER 2 TUNGSTEN-DOPED NICKEL IRON LAYERED DOUBLE HYDROXIDE NANOSHEETS FOR WATER OXIDATION	16
2.1 Introduction.....	16
2.2 Experimental Section	18
2.2.1 Synthesis of Catalysts	18
2.2.2 Physical and Chemical Characterization.....	19
2.2.3 Electrochemical Characterization	19
2.3 Results and Discussion.....	21
2.3.1 Structural and Compositional Analysis Results.....	21
2.3.2 Catalytic Performance of Synthesized Catalysts.....	27
2.3.3 Discussion	31

2.4 Conclusion	32
CHAPTER 3 BORON-MODIFIED COBALT IRON LAYERED DOUBLE HYDROXIDES FOR HIGH EFFICIENCY SEAWATER OXIDATION	33
3.1 Introduction	33
3.2 Experimental Section	35
3.2.1 Synthesis of Catalysts	35
3.2.2 Physical and Chemical Characterization.....	36
3.2.3 Electrochemical Characterization	37
3.2.4 Calculation of TOF	38
3.2.5 Gas Chromatography Testing	39
3.3 Results and Discussion.....	39
3.3.1 Structural and Compositional Analysis Results.....	39
3.3.2 OER Performance in Alkaline Freshwater.....	45
3.3.3 OER Performance in Alkaline Seawater.....	48
3.3.4 Discussion	55
3.4 Conclusion	56
CHAPTER 4 RATIONAL DESIGN OF CORE-SHELL-STRUCTURED CoP_x@FeOOH FOR SEAWATER ELECTROLYSIS.....	58
4.1 Introduction	58
4.2 Experimental Section	59
4.2.1 Synthesis of Catalysts	59
4.2.2 Physical and Chemical Characterization.....	61
4.2.3 Electrochemical Characterization	62
4.2.4 Calculation of TOF	63
4.2.5 Calculation of Faradaic Efficiency.....	63
4.3 Results and Discussion.....	63
4.3.1 Structural and Compositional Analysis Results.....	63
4.3.2 Catalytic Performance of Synthesized Catalysts.....	70
4.3.3 Chloride Corrosion Resistance Analysis.....	70
4.3.4 Discussion and Expansion.....	70
4.4 Conclusion	83

CHAPTER 5 EFFICIENT ALKALINE WATER/SEAWATER HYDROGEN EVOLUTION BY Ni-MoN CATALYST WITH FAST WATER-DISSOCIATION KINETICS.....	84
5.1 Introduction	84
5.2 Experimental Section	87
5.2.1 Synthesis of Catalysts	87
5.2.2 Physical and Chemical Characterization.....	89
5.2.3 Electrochemical Characterization	90
5.2.4 Calculation of TOF	91
5.2.5 Overall Water Electrolysis Driven by a Thermoelectric Module	92
5.2.6 Theoretical Calculations.....	93
5.3 Results and Discussion.....	94
5.3.1 Structural and Compositional Analysis Results.....	94
5.3.2 HER Performance in Alkaline Freshwater.....	103
5.3.3 HER Performance in Alkaline Seawater.....	110
5.3.4 DFT Calculation Results	114
5.3.5 Overall Water/Seawater Electrolysis Performance.....	118
5.4 Conclusion	122
CHAPTER 6 BIMETALLIC PHOSPHIDE Ni₂P-Fe₂P AS A BIFUNCTIONAL CATALYST FOR WATER AND SEAWATER ELECTROLYSIS.....	123
6.1 Introduction	123
6.2 Experimental Section	125
6.2.1 Synthesis of Catalysts	125
6.2.2 Physical and Chemical Characterization.....	126
6.2.3 Electrochemical Characterization	127
6.2.4 Calculation of TOF	128
6.2.5 Calculation of Faradaic Efficiency.....	129
6.3 Results and Discussion.....	130
6.3.1 Structural and Compositional Analysis Results.....	130
6.3.2 Catalytic Performance of Synthesized Catalysts.....	137
6.3.3 Discussion	150
6.4 Conclusion.....	152

CHAPTER 7 SUMMARY AND PERSPECTIVE	153
REFERENCES.....	155
LIST OF PUBLICATIONS.....	185

LIST OF FIGURES

Figure 1.1. (a) Schematic diagram of the alkaline electrolysis cell. ¹⁴ (b) Polarization curves for HER (red) and OER (navy). ¹⁵	2
Figure 1.2. (a) The Pourbaix diagram of an aqueous saline electrolyte. ²³ (b) Precipitate and corrosion challenges for seawater electrolysis. ¹⁰	3
Figure 2.1. (a) Schematic illustration of the synthesis of Ni-Fe-W LDH catalysts. (b) XRD patterns of Ni ₃ Fe and Ni ₃ FeW LDH catalysts. SEM images of (c-d) Ni ₃ Fe LDH and (e-h) Ni ₃ FeW LDH.	22
Figure 2.2. SEM images of (a-b) Ni ₃ FeW _{0.5} LDH, (c-d) Ni ₃ FeW ₂ LDH, and (e-f) Ni ₃ FeW ₃ LDH.	22
Figure 2.3. AFM images and corresponding height profiles of (a, b) Ni ₃ Fe LDH and (c, d) Ni ₃ FeW LDH nanosheets.	23
Figure 2.4. (a, b) TEM and (c, d) HRTEM images and (e) SAED pattern of Ni ₃ FeW LDH nanosheets. (f) TEM image of a Ni ₃ FeW LDH nanosheet and the corresponding (g-k) EDX elements mapping images.	25
Figure 2.5. (a, b) TEM and (c, d) HRTEM images of Ni ₃ FeW LDH nanosheets. (e) TEM image of two layers of Ni ₃ FeW LDH nanosheets and (f) the corresponding nanoparticle diameter distribution measured from (e).	26
Figure 2.6. (a) XPS spectra of Ni ₃ Fe LDH and Ni ₃ FeW LDH. High-resolution XPS spectra of (b) Ni and (c) Fe in Ni ₃ Fe LDH and Ni ₃ FeW LDH and of (d) W in Ni ₃ FeW LDH.	27
Figure 2.7. (a) OER LSV curves of Ni ₃ FeW _x LDH samples in 1.0 M KOH. (b) Tafel plots derived from the polarization curves in (a). (c) Double-layer capacitance (<i>C_{dl}</i>) plots and (d) Nyquist plots of these samples.	29
Figure 2.8. CV curves of (a) Ni ₃ Fe LDH, (b) Ni ₃ FeW _{0.5} LDH, (c) Ni ₃ FeW LDH, (d) Ni ₃ FeW ₂ LDH, and (e) Ni ₃ FeW ₃ LDH at different scan rates in a non-faradaic region.....	30
Figure 2.9. (a) CV cycling performance of Ni ₃ FeW LDH. (b) SEM images of Ni ₃ FeW LDH after 5000 CV scans. (c) Chronopotentiometric curve of Ni ₃ FeW LDH. (d) OER LSV curves of Ni ₃ FeM (M = W, Mo, Co, and Ru) LDH. .	31
Figure 3.1. Schematic illustration of the formation of B-Co ₂ Fe LDH <i>via</i> a two-step water bath reaction-chemical reduction procedure.	39
Figure 3.2. (a-c) SEM, (f) TEM, (e) HRTEM images, and (f) SAED pattern of the Co ₂ Fe LDH precursor.	40
Figure 3.3. SEM images of (a-c) Co(OH) ₂ and (d-f) Fe CH precursors.	41
Figure 3.4. (a-c) SEM, (f) TEM, (e) HRTEM images, and (f) SAED pattern of the B-Co ₂ Fe LDH (g) TEM image of the B-Co ₂ Fe LDH and the EDX element mapping images.	42

Figure 3.5. (a-b) SEM images of B-Co(OH) ₂ . (c) XRD patterns of the Fe CH precursor and B-Fe CH. (d-e) SEM images of B-Fe CH. (f) XRD patterns of the Co(OH) ₂ precursor and B-Co(OH) ₂	43
Figure 3.6. (a) XRD patterns of the Co ₂ Fe LDH and B-Co ₂ Fe LDH. High-resolution XPS spectra of (b) Co, (c) Fe, (d) B, and (e) O for these catalysts. (f) EPR spectra of Co ₂ Fe LDH and B-Co ₂ Fe LDH.....	45
Figure 3.7. (a) OER polarization curves and (b) Tafel plots of as-prepared catalysts in 1 M KOH. (c) Nyquist plots, (d) ECSA, and (e) ECSA-normalized OER activity, and (f) TOF curves of these catalysts.....	47
Figure 3.8. CV curves of (a) B-Co(OH) ₂ , (b) B-Fe CH, (c) Co ₂ Fe LDH, (d) B-Co ₂ Fe LDH, and (e) IrO ₂ in a non-faradaic region. (f) C _{dl} values of these catalysts calculated from (a-e).....	48
Figure 3.9. (a-c) SEM images of B-Co ₂ Fe LDH after immersion in natural seawater. Corrosion polarization curves of (d) Co ₂ Fe LDH and (e) B-Co ₂ Fe LDH. (f) Corrosion potentials and corrosion current densities of these catalysts.....	50
Figure 3.10. OER polarization curves of these catalysts in (a) 1 M KOH + 0.5 M NaCl and (b) 1 M KOH seawater. (c) OER CV curves of B-Co ₂ Fe LDH catalyst. (d) and (e) Tafel plots. (f) Comparison of the Tafel slope values. 50	
Figure 3.11. (a) Gaseous products from B-Co ₂ Fe LDH in 1 M KOH seawater. (b) <i>in situ</i> and (c) <i>ex situ</i> Raman spectra of B-Co ₂ Fe LDH. XPS spectra of (d) Co, (e) Fe, (f) B, and (g) O in B-Co ₂ Fe LDH before and after CV scans.	52
Figure 3.12. (a) OER polarization curves of B-Co ₂ Fe LDH before and after CV scans in 1 M KOH. Insert to (a): digital image of 1 M KOH. (b-d) SEM images and (e) EDS spectrum of B-Co ₂ Fe LDH after CV scans in 1 M KOH.....	53
Figure 3.13. (a) OER polarization curves of B-Co ₂ Fe LDH before and after CV scans in 1 M KOH seawater. (b-d) SEM images, (e) EDS spectrum, and (f-h) TEM images of B-Co ₂ Fe LDH after CV scans in 1 M KOH seawater.	54
Figure 3.14. Chronopotentiometric curves of B-Co ₂ Fe LDH in (a) 1 M KOH and (b) 1 M KOH seawater. (c) Colorimetric reagent testing result for hypochlorite production in the 1 M KOH seawater electrolyte.	55
Figure 4.1. Schematic illustration of the synthesis of core-shell-structured CoP _x @FeOOH <i>via</i> a three-step hydrothermal-phosphidation-electrodeposition procedure.	63
Figure 4.2. (a-d) SEM images of the CoP _x nanowire mesh. (e) Co and (f) P EDS mapping images corresponding to (d). (g-h) TEM, and (i-j) HRTEM images of CoP _x	65
Figure 4.3. (a-e) SEM and (f) TEM images, (g) SAED pattern, and (h) HRTEM image of CoP _x @FeOOH. (i) TEM image of a CoP _x @FeOOH mesh and the EDX element mapping for (j) Co, (k) P, (l) Fe, and (m) O.....	66

Figure 4.4. (a-e) SEM images of pristine FeOOH on NF. (f) Fe and (g) O EDS mapping images corresponding to (e).....	67
Figure 4.5. Digital images of a droplet of seawater placed on the surface of (a-c) CoP _x , (d-f) CoP _x @FeOOH, and (g-i) Ni foam to investigate their wettability.....	67
Figure 4.6. XRD patterns of (a) Co(OH) ₂ , (b) FeOOH, and (c) CoP _x and CoP _x @FeOOH.....	68
Figure 4.7. (a) Raman spectra of pristine FeOOH and CoP _x @FeOOH. High-resolution XPS spectra of (c) Co and (d) P in CoP _x and CoP _x @FeOOH and of (e) Fe in FeOOH and CoP _x @FeOOH.....	70
Figure 4.8. (a) OER polarization curves of Co(OH) ₂ , CoP _x , FeOOH, CoP _x @FeOOH, and IrO ₂ catalysts in 1 M KOH. (b) Tafel plots derived from (a). (c) Nyquist plots and (d) TOF slopes of these catalysts.....	72
Figure 4.9. (a) OER polarization curves of these catalysts in 1 M KOH seawater. (b) Tafel plots derived from (a). (c) OER polarization curves of CoP _x @FeOOH before and after CV scans.....	74
Figure 4.10. (a) SEM images of CoP _x @FeOOH after 5,000 CV cycles in 1 M KOH seawater. (b) XRD patterns and (c) Raman spectra of CoP _x @FeOOH before and after 5,000 CV cycles in 1 M KOH seawater.....	74
Figure 4.11. Chronopotentiometric curves of CoP _x @FeOOH catalysts at constant current densities of 100 and 500 mA cm ⁻² in (a) 1 M KOH and (b) 1 M KOH seawater.....	75
Figure 4.12. (a) OER polarization curves of these catalysts in 1 M KOH + 0.5 M NaCl. (b) Tafel plots derived from (a). (c) Comparison of the Tafel slope values of these catalysts in different electrolytes.....	76
Figure 4.13. HER polarization curves of these catalysts in (a) 1 M KOH and (c) 1 M KOH seawater. (b) and (d) Tafel plots. (e) HER polarization curves of CoP _x in 1 M KOH seawater. Stability performance of Co(OH) ₂ and CoP _x	77
Figure 4.14. (a) Overall freshwater/seawater electrolysis of the CoP _x CoP _x @FeOOH pair. (b) Gaseous products, (c) CV cycling performance, and (d) stability performance of this pair in 1 M KOH seawater.....	78
Figure 4.15. SEM images of (a) CoP _x @FeOOH and (b) CoP _x after immersion in seawater. Corrosion polarization curves of the (c) CoP _x , (d) FeOOH, and (e) CoP _x @FeOOH in seawater. (f) Corrosion performance of these catalysts.....	80
Figure 4.16. SEM images of (a) CoP _x @CoOOH and (b) CoP _x @NiOOH. (c) OER polarization curves of FeOOH, CoP _x @FeOOH, CoOOH, CoP _x @CoOOH, NiOOH, and CoP _x @NiOOH catalysts in 1 M KOH seawater.....	82
Figure 5.1. (a) Schematic illustrations of the synthesis of Ni-MoN and corresponding SEM images at different synthesis stages. Photographs of (b) CF, (c) NiMoO ₄ ·xH ₂ O, (d) Ni-MoN, and (e) SSM.....	95

- Figure 5.2.** (a-c) SEM and (d-e) TEM images, (f) EDS line scan, and (k) XRD pattern of the $\text{NiMoO}_4 \cdot x\text{H}_2\text{O}$ precursor. (g) TEM image and corresponding (h) Ni, (i) Mo, and (j) O EDS mapping images of the $\text{NiMoO}_4 \cdot x\text{H}_2\text{O}$ precursor. .96
- Figure 5.3.** (a-c) SEM and (e-f) TEM images, (d) EDS spectrum, and (g) SAED pattern of Ni-MoN. (h) EDS line scan of a single Ni-MoN nanorod. (i) HAADF image and corresponding (j-n) EDS mapping images of Ni-MoN.99
- Figure 5.4.** (a) TEM images of the Ni-MoN catalyst. (b) Diameter distribution of the nanoparticles. (c-d) Detailed HRTEM images of the Ni-MoN catalyst. ..100
- Figure 5.5.** (a-c) SEM images and (f) XRD pattern of the Ni-Ni₄N. (d) Ni and (e) N EDS mapping images. (g-i) SEM images and (l) XRD pattern of the Mo-N. (j) Mo and (k) N EDS mapping images.100
- Figure 5.6.** (a) XRD pattern of Ni-MoN. (b) EPR spectra and (c) nitrogen adsorption-desorption isotherms of $\text{NiMoO}_4 \cdot x\text{H}_2\text{O}$ and Ni-MoN. High-resolution XPS spectra of (d) Ni, (e) Mo, and (f) N and Mo for these catalysts.....103
- Figure 5.7.** (a) HER LSV curves and (b) Tafel plots of these catalysts in 1 M KOH. (c) Comparison of HER activity. (d) Nyquist plots and (e) ECSA-normalized HER LSV curves. (f) TOF curves. (g) Stability performance of Ni-MoN.106
- Figure 5.8.** CV curves of (a) $\text{NiMoO}_4 \cdot x\text{H}_2\text{O}$, (b) Ni-Ni₄N, (c) Mo-N, and (d) Ni-MoN catalysts. (e) Corresponding C_{dl} values of these catalysts calculated from (a-d). (f) ECSA values of $\text{NiMoO}_4 \cdot x\text{H}_2\text{O}$, Ni-Ni₄N, Mo-N, and Ni-MoN.106
- Figure 5.9.** Digital images of hydrogen gas bubbles on the surfaces of (a) Ni-MoN and (b) CF at a current density of 100 mA cm^{-2} in 1 M KOH electrolyte.107
- Figure 5.10.** SEM images of Ni-MoN catalysts with different Ni:Mo ratios of (a) 2:7, (b) 4:7, and (c) 12:7. (d) HER LSV curves these catalysts in 1 M KOH..109
- Figure 5.11.** SEM images of Ni-MoN catalysts annealed at (a) 300 °C and (b) 500 °C in a mixed ammonia-argon flow. (c) XRD patterns and (d) HER LSV curves of these catalysts in 1 M KOH.....109
- Figure 5.12.** (a) HER LSV curves and (b) Tafel plots of these catalysts in 1 M KOH seawater. (c) CV cycling performance, (e) HER LSV curves, and (d) and (f) stability performance of the Ni-MoN in different electrolytes.112
- Figure 5.13.** (a-d) SEM images, (e) TEM image, (f) SAED pattern, and (g) HRTEM image of the Ni-MoN after stability testing. (h) XPS and (i) Raman spectra of the Ni-MoN before and after 19,000 CV cycles in 1 M KOH.113
- Figure 5.14.** (a-e) SEM images and (f) EDS spectrum of the Ni-MoN catalyst after 115-h stability testing at a constant current density of 100 mA cm^{-2} in alkaline saline electrolytes.114
- Figure 5.15.** Side and top views, respectively, of the (a-b) Ni-MoN, (c-d) metallic Ni (111), and (e-f) MoN (202) models for DFT calculations.115

- Figure 5.16.** Charge density distributions of (a) MoN and (b) Ni-MoN. (c) Side and (d) top views of charge density differences in Ni-MoN. (e) DOS calculated for Mo, N, and Ni in Ni-MoN. The black dotted line indicates the Fermi level.115
- Figure 5.17.** Structure models for water adsorption, transition state, water dissociation, and hydrogen adsorption over (a) Ni (111), (b) Mo (202), (c) Ni sites and (d) Mo sites in Ni-MoN. Red: O; green: H.118
- Figure 5.18.** (a) Adsorption energy of H₂O, (b) energy diagram for H₂O dissociation, and (c) free energy diagram for H adsorption for metallic Ni, Mo sites in MoN, and Ni and Mo sites in Ni-MoN.118
- Figure 5.19.** (a-b) Overall water/seawater electrolysis performance of Ni-MoN||SSM and Pt/C||Ni-Fe LDH pairs. (c) Comparison of the catalytic performance. (d-e) Stability performance of Ni-MoN||SSM pair in different electrolytes.119
- Figure 5.20.** (a) Schematic illustration of a TE device. (b) Overall water electrolysis testing at the temperature difference of 61 °C. (c). Real-time dynamics of current density driven by a TE device at different temperature.....120
- Figure 5.21.** HER LSV curves of the Ni-MoN under industrial condition. (b) Overall water/seawater electrolysis curves and (c) stability performance of the Ni-MoN||SSM pair under industrial condition.121
- Figure 6.1.** Schematic illustration of the formation of Ni₂P-Fe₂P/NF *via* a three-step *in situ* growth-ion exchange-phosphidation procedure.130
- Figure 6.2.** SEM images of (a, b) pristine Ni foam and (c, d) Ni(OH)₂/NF. (e) XRD patterns of pristine Ni foam and Ni(OH)₂/NF samples. (f) Raman spectrum of Ni(OH)₂/NF sample.131
- Figure 6.3.** (a) Photograph of pristine NF undergoing ion exchange in 0.1 M iron nitrate solution. Photographs of Ni(OH)₂/NF undergoing ion exchange in (b) 0.025 M, (c) 0.05 M, (d) 0.1 M, and (e) 0.15 M iron nitrate solutions.132
- Figure 6.4.** (a, b) SEM images and (c) Ni and (d) P EDS mapping images corresponding to (b) of nickel phosphide. (f) XRD pattern of a nickel phosphide sample obtained from the phosphidation of a Ni(OH)₂/NF.....133
- Figure 6.5.** (a-c) SEM, (d) TEM, and (e) HRTEM images, and (f) SAED pattern of Ni₂P-Fe₂P. (g) TEM image and (h-i) corresponding EDX mapping images of a Ni₂P-Fe₂P microsheet. (k) XRD pattern of nickel iron phosphide. ...135
- Figure 6.6.** (a) AFM image and (b) corresponding height profile of a Ni₂P-Fe₂P microsheet.135
- Figure 6.7.** SEM images of (a-b) Ni₂P-Fe₂P/NF-0.025, (c-d) Ni₂P-Fe₂P/NF-0.05, and (e-f) Ni₂P-Fe₂P/NF-0.15.....135
- Figure 6.8.** (a) Overall XPS spectra of Ni₂P-Ni₅P₄ and Ni₂P-Fe₂P. High-resolution XPS spectra of (b) Ni and (c) P in Ni₂P-Ni₅P₄ and Ni₂P-Fe₂P and of (d) Fe in Ni₂P-Fe₂P.137

- Figure 6.9.** (a) OER CV and (d-e) HER LSV curves of these catalysts in 1 M KOH. (b) LSV curves collected from high to low potentials from (a). Comparison of the overpotentials of these catalysts for (c) OER and (f) HER.139
- Figure 6.10.** (a) OER LSV curves, (b) Tafel plots, and (c) Nyquist plots of these catalysts in 1 M KOH. (d) OER LSV curves of Ni₂P-Fe₂P/NF before and after CV cycles. (e) Stability performance of Ni₂P-Fe₂P/NF for OER.140
- Figure 6.11.** TOF curves of the corresponding of Ni₂P-Fe₂P and Ni₂P-Ni₅P₄ electrodes for (a) OER and (b) HER. Unit cells of (c) Ni₂P, (d) Ni₅P₄, and (e) Fe₂P.140
- Figure 6.12.** (a) HER LSV curves, (b) Tafel plots, and (c) Nyquist plots of these catalysts in 1 M KOH. (d) HER LSV curves of Ni₂P-Fe₂P/NF before and after CV cycles. (e) Stability performance of Ni₂P-Fe₂P/NF for OER.142
- Figure 6.13.** (a) OER and (b) HER LSV curves of these catalysts in 1 M KOH seawater. (c) Overpotentials required for the Ni₂P-Fe₂P/NF for OER and HER. Stability performance of Ni₂P-Fe₂P/NF for (d) OER and (e) HER.143
- Figure 6.14.** SEM images of Ni₂P-Fe₂P electrodes after 36 h continuous testing for (a-b) OER and (c-d) HER catalysis. EDS spectra of (e) post-OER, (f) original, and (g) post-HER Ni₂P-Fe₂P. XPS spectra of (h) Ni, (i) Fe, and (j) P.....145
- Figure 6.15.** OER CV curves of Ni₂P-Fe₂P/NF in different electrolytes (a) with and (b) without *iR* compensation. HER LSV curves of the Ni₂P-Fe₂P/NF sample in different electrolytes (c) with and (d) without *iR* compensation.145
- Figure 6.16.** (a) Overall water/seawater electrolysis of Ni₂P-Fe₂P/NF and Pt/C||IrO₂ pairs. (b) Comparison of the catalytic performance. Stability performance of Ni₂P-Fe₂P/NF pair in (c) 1 M KOH and (d) 1 M KOH seawater.147
- Figure 6.17.** (a) GC signals of H₂ and O₂ gas during 90 min GC testing. (b) Measured (dots) and theoretical (solid line) gaseous products by the two-electrode electrolyzer at a current of 100 mA in 1 M KOH seawater.148
- Figure 6.18.** (a-b) Photographs of different electrolyzers. (c) Overall water/seawater electrolysis performance and (d) comparison of the overpotentials of Ni₂P-Fe₂P using the electrolyzers in (a) and (b), respectively.....149
- Figure 6.19.** (a) Overall seawater electrolysis and (b) Voltages of Ni₂P-Fe₂P using different electrolyzers with and without *iR* compensation. (c) Stability testing of Ni₂P-Fe₂P and (d) corresponding ClO⁻ formation testing result.150

CHAPTER 1 INTRODUCTION

1.1 Introduction to Water and Seawater Electrolysis

The emission of greenhouse gases and other environmental pollution issues related to the excessive consumption of fossil fuels such as coal, petroleum, and natural gas have aroused intensive research interest in renewable energy technologies. As one of these candidates, hydrogen has been reported to be an ideal energy carrier for sustainable energy systems due to its zero-carbon emissions and high energy density (142 kJ g^{-1}).¹⁻³ Hydrogen production through water electrolysis is a more efficient and “greener” technology compared with the traditional steam-reforming method and coal gasification method, which are based on the consumption of natural gas and coal, respectively. In particular, water electrolysis can be driven by the electricity generated by clean and sustainable energy sources, making it economically affordable and environmental friendly. In general, the water electrolysis process is composed of two half reactions: oxygen evolution reaction (OER) on the anode and hydrogen evolution reaction (HER) on the cathode (**Figure 1.1a**).⁴⁻⁵ It is widely acknowledged that the OER process, which is kinetically slower than HER and controls the overall efficiency, limits the practical utilization of overall water electrolysis (**Figure 1.1b**).^{6,7} To make water electrolysis more energy-efficient and cost-effective, catalysts, which can promote the sluggish kinetics of OER or HER by lowering their activation energy, are widely employed in hydrogen production. In addition, compared with acid water electrolysis, alkaline water electrolysis is currently more appealing due to its inexpensive equipment requirements and effective avoidance of acid fog and corrosion.⁸⁻¹⁰ Conventional noble-metal based catalysts like Ir/Ru- and Pt-based

composites have been identified as state-of-the-art catalysts for OER and HER, respectively.¹¹ However, their high cost, scarce availability, and instability in alkaline media at large current density significantly impede the large-scale industrial applications of these noble-metal based catalysts.¹² Thus, it is highly desirable to search for and develop non-noble-metal catalysts to replace these expensive ones. In the past few decades, significant progress has been made in fabricating novel alternative non-noble-metal based catalysts.^{4, 13}

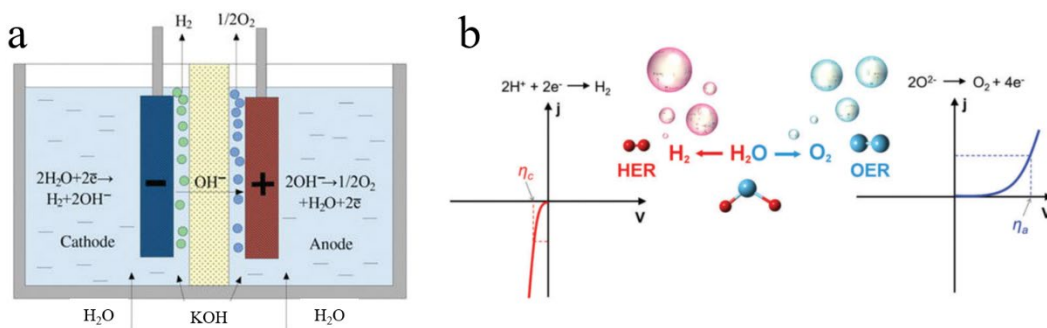


Figure 1.1. (a) Schematic diagram of the alkaline electrolysis cell.¹⁴ (b) Polarization curves for HER (red) and OER (navy).¹⁵

Another issue is that freshwater, which is widely used for research on water electrolysis in the laboratory, is a scarce resource in many parts of the world and could be a bottleneck if water electrolysis technology is employed on a large scale.¹⁶ Seawater, representing around 96.5% of the world's total water supply, can be regarded as an unlimited resource.¹⁷ Some renewable power-generation technologies are related to the ocean such as wave, solar, and wind making it easy to combine seawater electrolysis with these clean and sustainable energy technologies.¹⁸⁻¹⁹ Moreover, the consumption of H₂ gas produced by seawater electrolysis can produce safe freshwater, which is very meaningful for the coastal arid areas. However, the complicated composition of natural seawater can result in additional challenges for

direct seawater electrolysis. The most critical challenge in seawater electrolysis is the possible chloride evolution reaction (CIER) or the formation of hypochlorite (ClO^-), which originates from the existence of chloride anions (Cl^- , $\sim 0.5 \text{ M}$) in seawater and may compete with OER on the anode side.^{17, 20-22} Compared with acid or neutral electrolytes, an alkaline electrolyte can provide a larger overpotential window for selective OER. Under an alkaline condition ($\text{pH} > 7.5$), the theoretical voltage for hypochlorite formation in seawater ($\text{Cl}^- + 2\text{OH}^- = \text{ClO}^- + \text{H}_2\text{O} + 2\text{e}^-$) is around 480 mV higher than that of OER.^{16, 23} In other words, without considering the extra overpotential needed to trigger the CIER, the maximum overpotential applied on an OER catalyst should be lower than 480 mV in order to achieve 100% seawater oxidation. Besides enabling the competing CIER, chloride ions in natural seawater can corrode the catalyst, which is another critical challenge that needs to be considered for long-term seawater electrolysis.¹⁸ In addition, insoluble precipitates, either in the seawater itself (dust, colloids, and bacteria) or formed by the alkali metallic cations in the seawater reacting with the conductive reagent OH^- in the alkaline electrolyte [$\text{Ca}(\text{OH})_2$ and $\text{Mg}(\text{OH})_2$], will poison the catalyst and degrade its catalytic activity and durability.

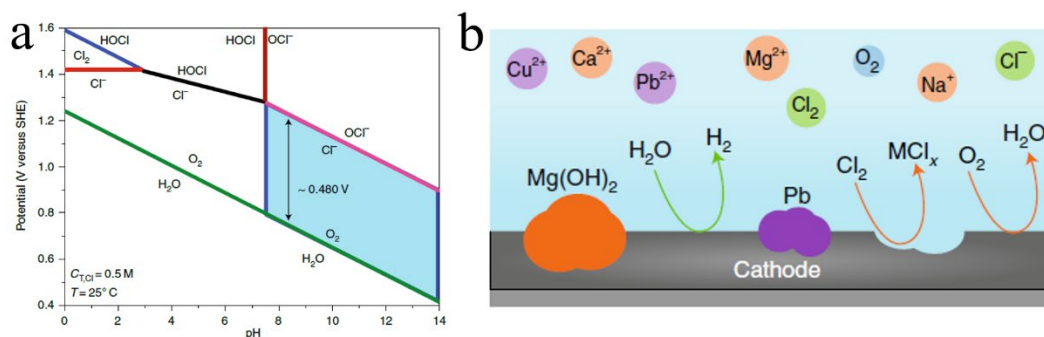


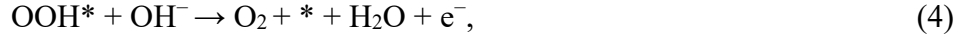
Figure 1.2. (a) The Pourbaix diagram of an aqueous saline electrolyte.²³ (b) Precipitate and corrosion challenges for seawater electrolysis.¹⁰

Addressing the challenges mentioned above requires rational design of novel catalysts specifically for seawater electrolysis. For example, to meet the current density requirement for industrial hydrogen production while at the same time avoiding hypochlorite formation, the OER catalyst should have excellent catalytic activity to reach a high current density at an overpotential below 480 mV. Additionally, both the OER and HER catalysts should have high chloride-corrosion resistance and good structural stability to avoid electrode corrosion or collapse and thus maintain their catalytic activity in long-term seawater electrolysis. A hierarchical structured catalyst with a large surface area and abundant active sites is more favorable since insoluble precipitates in seawater might cover and deactivate some active sites. Some recent works also point out that corrosion-resistant electrolyzers and affordable membranes play important roles in direct seawater electrolysis, which can affect the device lifetime and efficiency of the system.^{10, 24-25} All these challenges have impeded the development of seawater-electrolysis technology.

1.2 Fundamentals of Alkaline Water Electrolysis

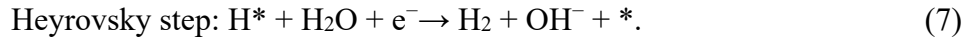
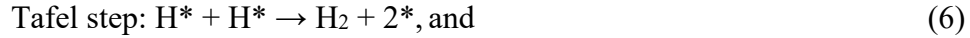
1.2.1 Principles of Alkaline OER and HER

In broad terms, the alkaline OER process can be divided into three sequential steps. First, adsorption of hydroxide (OH^-) onto the catalyst surface to form OH^* . Then, the OH^* further adsorb OH^- to generate H_2O macular and O^* intermediate, which will form the subsequent OOH^* by reacting with another OH^- . Finally, the OOH^* intermediates would combine with OH^- to generate H_2O macular and oxygen molecular.²⁶ The general reaction process of OER in alkaline media (such aqueous KOH solution) can be expressed as follows:²⁷



here * represents the adsorption site on the catalyst and O*, OH*, and OOH* denote adsorbed intermediates. Each equation above generates one electron, so the whole OER process in alkaline media includes a four-electron transfer.

Alkaline HER process can be divided into two sequential steps. First, adsorption of H₂O molecules onto the catalyst surface and split of the water into OH⁻ (Volmer step). Then, desorption of hydrogen molecules *via* either a chemical (Tafel step) or an electrochemical (Heyrovsky step) route:²⁸



1.2.2 Important Parameters to Evaluate Catalytic Activity

The catalytic activity of a specific OER or HER process can be preliminarily evaluated by cyclic voltammetry (CV) and linear sweep voltammetry (LSV) testing. However, to fairly judge the OER performance of a given catalyst, some other crucial parameters, including overpotential (η), Tafel plot (b), exchange current density (j_0), and turnover frequency (TOF), are necessary.¹⁵ In the following, we will explain each of these parameters in more detail.

1.2.2.1 Overpotential (η)

Among the parameters mentioned above, overpotential (η) is the most important one. In theory, the catalytic reaction of water electrolysis can be driven by applying a voltage equal to the equilibrium hydrolysis potential (1.23 V vs. RHE). In reality, however, extra electrical energy (overpotential, η) is needed to surpass the kinetic barrier. According to the Nernst equation, for an catalytic redox reaction, the applied potential can be expressed as Equation (8):²⁷

$$E = E^0 + RT/nF \cdot \ln(C_O/C_R), \quad (8)$$

$$\eta = E - E_{eq}, \quad (9)$$

where E and E^0 are applied potential and standard potential, respectively; R is the gas constant; T is the absolute temperature; n is the number of electrons transferred; F is the Faraday constant; and C_O and C_R represent the concentrations of oxidized and reduced reagents, respectively.²⁹ Overpotential is defined as the difference between applied potential (E) and equilibrium potential (E_{eq}) as illustrated in Equation (9). In many cases, the overpotential required to achieve a current density of 10 mA cm^{-2} , which matches a photoelectrochemical water-splitting efficiency of 12.3%, is employed as an important reference to assess electrocatalysts.³⁰

1.2.2.2 Tafel Slope (b) and Exchange Current Density (j_0)

The Tafel slope (b) is another important parameter to analyze the kinetics and the reaction mechanism of the OER process. The relationship between overpotential (η) and current density (j) can be illustrated through the Tafel equation [Equation (10)], in which b is the Tafel slope. The linearly fitted Tafel slope can be described as “how fast the current increases against overpotential”.¹⁵ Additionally, exchange current

density (j_0), which shows the catalyst's catalytic activity at equilibrium status, can be calculated through the Tafel equation by assuming an overpotential of 0. An ideal catalyst should have a small Tafel slope (b) and a high exchange current density (j_0):

$$\eta = a + b \log(j). \quad (10)$$

1.2.2.3 Turnover Frequency (TOF)

Evaluating the overpotential or the Tafel slope values of a given catalyst is not a perfect method to judge its overall catalytic performance due to differences in loading mass.⁸ Turnover frequency (TOF), which is defined as the number of reactant molecules transformed per catalytic site over a unit of time, has been proposed to address this problem. TOF can be calculated through equation (11):

$$\text{TOF} = jA/zFn, \quad (11)$$

here j is the current density, A is the working area, z is the number of transferred electrons, F is the Faraday constant, and n is the mole amount. However, it should be noted that a precise TOF value is very difficult to obtain because not all active atoms are involved in a real catalytic reaction, so the mole amount n in this equation cannot be precisely calculated.³⁰

Apart from the important parameters mentioned above, the faradaic efficiency (FE), which is calculated as the ratio between the quantity of produced gas obtained in the experiments to the theoretical quantity, electrochemically active surface area (ECSA), and mass activity (MA) and specific activity (SA), which are calculated as the measured current normalized on the mass or the ECSA of the catalyst, are also used to assess the catalytic properties.²⁸

1.3 Typical Self-supported Catalysts

Although non-noble-metal based catalysts have been developed for many years due to their various advantages, such as low cost, abundance, and tunable composition, the poor durability and low conductivity of the powdery catalysts greatly hinder their catalytic performance and practical application. More importantly, a non-conductive polymer binder is usually needed to attach the catalyst powder onto a conductive substrate for electrode preparation. On one hand, using a non-conductive binder significantly increases the charge-transfer resistance of the electrode. On the other hand, the formation of strong bubbles during the water electrolysis process would damage the connection between the powdery catalyst and the substrate, leading to catalyst collapse. A self-supported catalyst architecture with enhanced kinetics and stability is more attractive than the conventional coated powdery form. In addition to their excellent charge-transfer ability, conventional supports like nickel foam (NF), copper foam (CF), and carbon cloth (CC) can provide a large surface area for active catalysts to grow. Generally speaking, the in-situ growth of self-supported catalysts on substrates can accelerate the catalysis process based on the following aspects: (1) direct growth of catalyst on conductive bones not only immobilizes the catalyst's structure on the electrode surface, but also promotes electron transport from the catalyst to the substrate due to the intimate interfacial connection; (2) the large surface area of this open structure is beneficial to the contact between the electrode and the electrolyte media, which guarantees that the active sites effectively take part in the catalytic reaction and avoid potential aggregation; (3) the self-supported catalyst with an ordered structure and open space are helpful for the gas-bubble release by

providing smooth diffusion paths for gaseous products; and (4) compared with powdery catalysts, a self-supported catalyst on a substrate can be directly utilized as an electrode for the electrochemical tests, while the former often requires the addition of an insulating polymeric binder and a multi-step operation to assemble the electrode.

Here we select three types of typical catalysts: layered double hydroxides (LDHs), transition metal phosphides (TMPs), and transition metal nitrides (TMNs) for introduction. Their catalytic performance toward water and seawater electrolysis and details for some synthetic methods are discussed.

1.3.1 Layered Double Hydroxides (LDHs)

In general, layered double hydroxide (LDH) materials are brucite-like lamellar crystals composed of positive host layers and charge-balancing interlayers. All of the LDH materials can be classified by a formula as $M^{2+}_{1-x}M^{3+}_x(OH)_2(A^{n-})_{x/n} \cdot yH_2O$, in which M^{2+} and M^{3+} represent divalent and trivalent cations such as Ni^{2+} , Co^{2+} , Fe^{2+} , Zn^{2+} and Fe^{3+} , Al^{3+} , Cr^{3+} , Mn^{3+} *etc.*, respectively, and A^{n-} is the charge-compensating interlayer anion such as CO_3^{2-} , NO_3^- , SO_4^{2-} , Cl^- *etc.*^{12, 29, 31-32} Most LDH materials exhibit two-dimensional (2D) layered nanosheet structures, on which metal cations can be located.²⁹ Such a 2D nanosheet structures make the cations and anions in the host layers and interlayers flexibly tunable, which offers more opportunities for fabricating novel LDH catalysts.²⁷

Among all of the self-supported LDH catalysts reported thus far, nickel (Ni)-based LDHs have been studied the most. The fabrication of NiFe LDH was achieved in early studies, but its application for alkaline OER was barely studied until Gong *et al.* used the solvothermal method to synthesize crystalline NiFe LDH nanoplates on carbon

nanotubes as OER catalysis in 2013.³³ Following this achievement, quite a few studies have focused on this kind of highly efficient catalyst for water oxidation. In particular, to conquer the drawback of low conductivity associated with powdery LDH, constructing three-dimensional (3D) LDH on a substrate is highly desirable. Self-supported bi-/tri-metallic LDH as well as their complex have been synthesized and studied.³⁴

1.3.2 Transition Metal Phosphides (TMPs)

Over the past few years, transition-metal phosphides (TMPs) have attracted intense attention due to their high intrinsic catalytic activity, tunable structure, and composition.³⁵ It has been reported that P atoms in TMPs possess more electronegativity and can draw electrons from metal atoms.³⁶ The negatively charged P can act as base to trap positively charged proton during electrochemical HER. Therefore, TMPs first emerging as efficient HER catalysts in earlier research.³⁶ Binary Ni_2P ,³⁷ Ni_5P_4 ,³⁸ FeP ,³⁹ and CoP ⁴⁰ and ternary NiCo_2P_x ⁴¹ and $\text{Ni}_{2(1-x)}\text{Mo}_{2x}\text{P}$,⁹ as well as $\text{CoP}/\text{Ni}_5\text{P}_4/\text{CoP}$,⁴² have been successfully synthesized and demonstrated to be high-performance HER catalysts. Very recently, there has been a focus on heterogeneous bimetallic phosphides, including $(\text{Ni}_{0.33}\text{Fe}_{0.67})_2\text{P}$,⁴³ $\text{FeP}/\text{Ni}_2\text{P}$,⁴⁴ $\text{Ni}_2\text{P}-\text{Cu}_3\text{P}$,⁴⁵ $\text{Fe}-\text{Co}-\text{P}$,⁴⁶ and NiCoP ,⁴⁷⁻⁴⁸ as OER or bifunctional catalysts due to their various structural and chemical advantages.⁴⁹⁻⁵⁰ First, compared with the other transition-metal-based bifunctional catalysts such as transition-metal sulfides, nitrides, carbides, and layered double hydroxides,⁵¹⁻⁵³ the electronegative P atoms in the bimetallic phosphides can not only act as a base to trap positively charged protons, but also provide high activity for the dissociation of H_2 to boost HER activity.³⁶ Second, with an appropriate atomic

ratio of metal and P, bimetallic phosphides are able to exhibit excellent conductivity. Finally, with P alloying, metal dissolution will be thermodynamically less favored, leading to enhancement of both corrosion resistance and chemical stability.³⁵⁻³⁶

1.3.3 Transition Metal Nitrides (TMNs)

Transition metal nitrides (TMNs) are a class of interstitial compounds in which the nitrogen atoms are integrated into the interstitial sites of the parent metals, possessing the properties of covalent compounds, ionic crystals, and transition metals.⁵⁴ In general, the M-N bonding in TMNs leads to expansion of the parent metal lattice and constriction of the metal d-band.⁵⁵⁻⁵⁶ Such a deficiency in the d-band and higher density of states (DOS) of the metal near the Fermi level allow noble metal-like behavior in catalysis and ensure good adsorption between the surface of TMNs and reactants. Bimetallic and high-entropy metal nitrides usually show superior catalytic activities to monometallic nitrides due to the coordination between metal atoms. Thus, proper design toward the structural engineering and electronic modulation of TMNs is crucially needed for electrochemical energy applications.⁵⁴

Over the past decades, TMNs have attracted considerable attention due to their good electrical conductivity and outstanding mechanical robustness. Recent experimental and theoretical results suggest that TMNs have moderate binding capabilities toward reactants (water molecules, atomic hydrogen, or protons), allowing them outstanding HER catalytic activity.^{54, 56-58} To further boost the alkaline HER performance of TMNs, effective sites for water dissociation should be introduced to enhance its sluggish kinetics. However, studies of these heterogeneous TMN-based catalysts have mainly focused on freshwater electrolysis at small current densities

usually lower than 500 mA cm^{-2} . For large-current-density water electrolysis, the catalytic performance might be limited by insufficient active sites and structural instability.⁵⁹

1.4 Typical Synthesis Methods

To synthesize self-supported LDHs, TMPs, and TMNs with excellent catalytic activity, both the substrates and synthesis methods should be taken into consideration. Typically, a substrate can not only serve as a current collector for catalyst growth, but can also provide a tremendous number of diffusion pathways for the release of oxygen or hydrogen bubbles. Conductive substrates like nickel foam (NF), copper foam (CF), carbon cloth (CC), and carbon paper (CP) are usually chosen to grow catalysts because of their low cost, good conductivity, and outstanding stability in alkaline electrolyte. A variety of fabrication techniques has been explored to synthesize self-supported catalysts with specific structures and morphologies. Here, some most-used methods are introduced to provide a comparative overview of catalyst fabrication.

1.4.1 Hydrothermal Reaction

Synthesizing self-supported LDHs through a hydrothermal reaction is thought to be an advantageous method due to its easy operation process and simple chemical reaction.⁶⁰ A hydrothermal reaction is carried out by mixing metal salts and precipitating agents together into a solvent and subjecting the solution to thermal treatment under a specified temperature higher than boiling point of water. The precipitator like urea or ammonia plays a significant role in this method because the OH^- anions provided by the precipitator can attract metal ions to form metal hydroxides in the initial nucleation step and help to form layered structures during the

subsequent hydrothermal treatment. Typically, the self-supported LDH-based catalysts obtained through hydrothermal reaction are homogeneously ordered nanoplates or nanorods with high crystallinity and relatively large surface areas.⁶¹ The morphology and structure of self-supported LDHs obtained *via* hydrothermal reaction can be easily controlled by adjusting the reaction parameters, such as temperature, pressure, and reaction time. Moreover, dopants and composites could be introduced into the as-obtained self-supported LDHs through a second hydrothermal reaction. However, it should be noted that the chemical composition and growth rate of LDHs fabricated *via* hydrothermal reaction cannot be precisely controlled because of the sealed reaction environment employed and the long thermal-treatment time required.

1.4.2 Water Bath Reaction

Different from the widely employed hydrothermal reaction operated in a sealed container, water bath reaction is a facile and scalable method which can be performed under mild conditions. As mentioned, hydrothermal reaction commonly requires strict reaction conditions (maintenance at temperatures above the boiling point of water in a sealed container) that are not suitable for scaling up and always lead to a nanosheet or nanorod structure for LDH catalyst. In contrary, water bath reaction can be conducted in an open beaker with at temperatures lower the boiling point of water. The chemicals used in water bath reaction can be the same as or similar to that in hydrothermal reaction since both use water as the solvent. The synthetic route used to prepare a catalyst determines its structure, and structure determines activity. Thus, a totally different synthesis method can lead to different structured catalyst with different catalytic performance even though the chemicals used are the same.

1.4.3 Electrodeposition

The electrodeposition method is often applied to fabricate self-supported LDH or oxyhydroxide films on conductive substrates in a two- or three-electrode configuration. The substrate is employed as the working electrode while an aqueous solution containing metal salts acts as the electrolyte in this system. The reduction reactions between the metal ions and OH^- leads to the formation of a self-supported LDH or oxyhydroxide nanoarray on the substrate. This simple and time-saving process can be finished within a quite short amount of time ranging from several seconds to several minutes. The thickness and crystallinity of the LDH/oxyhydroxide can be adjusted by changing the deposition parameters, such as the current density and working time, while its chemical composition can be controlled by changing the metal salts in the electrolyte.

1.4.4 Ion Exchange

Ion exchange is generally conducted to fabricate self-supported LDHs or hydroxides *via* replacing the ions of the host material with other high-mobility ions in the solvent. When employed to synthesize a self-supported LDHs/ hydroxides, the ion-exchange method can introduce new cations into the precursor while inheriting its morphology and microstructure. For example, Wang *et al.* dipped an as-prepared NiCo LDH precursor into an iron nitrate aqueous solution to substitute Fe^{3+} for Ni^{2+} and Co^{2+} . Various types of NiCoFe LDHs with different amounts of iron could thus be obtained by changing the iron nitrate content in the solvent.⁶²

1.4.5 Annealing

To synthesize TMP and TMN catalysts, metallic composite precursors are usually required, followed by the phosphidation or nitridation process at high annealing temperatures. For example, to synthesize TMPs, red phosphorous or sodium hypophosphite monohydrate powder can be placed upstream in a tube to serve as the phosphorous source and a precursor can be put at the center of the tube for phosphidation. Subsequently, when annealed above the decomposition temperature of phosphorous source, the P atoms can react with precursor through the Ar steam to form TMPs. Similarly, to synthesize TMNs, reductive ammonia gas, serving as both the reducing agent and the nitrogen source, can react with the precursor to form TMNs at a high annealing temperature.

CHAPTER 2 TUNGSTEN-DOPED NICKEL IRON LAYERED DOUBLE HYDROXIDE NANOSHEETS FOR WATER OXIDATION

Note: The material in this chapter has been published. The introduction, experimental section, and figure captions were adjusted for dissertation consistency. Reproduced with permission from Royal Society of Chemistry.⁵³

2.1 Introduction

Electrochemical water splitting to produce high-purity hydrogen is an efficient and CO₂-free alternative to traditional steam-reforming technology, which is based on the consumption of methane or coal.^{5, 63-64} However, the overall water-electrolysis process is significantly limited by the high energy barrier and sluggish kinetics of the oxygen evolution reaction (OER) on the anode.¹⁵ Thus, OER catalysts, which can promote the OER kinetics by lowering the activation energy, are widely employed in hydrogen production.⁶⁵⁻⁶⁶ Noble-metal-based catalysts like IrO₂ and RuO₂ have been identified as state-of-the-art OER catalysts in alkaline electrolyte. However, their high price and scarcity severely impede their large-scale industrial application.⁶⁷ It is thus desirable to develop alternative cost-efficient and catalytically active non-noble-metal based OER catalysts to replace these expensive ones.

Layered double hydroxide (LDH) materials have emerged as appealing OER electrocatalysts due to their unique layered structures and high catalytic activity.^{12, 60, 68} Bimetallic LDH materials like NiFe LDH, NiCo LDH, CoFe LDH, *etc.* have been synthesized and utilized as efficient OER catalysts. Moreover, these LDH materials

can be *in situ* grown on conductive bones (*e.g.*, nickel foam, copper foam, and carbon cloth) to fabricate self-supported LDH catalysts, which are considered to have a large active surface area, good conductivity, and a high density of active sites, resulting in excellent catalytic activity.⁶⁹⁻⁷⁰ Additionally, pristine bimetallic LDH can be easily transformed into trimetallic LDH *via* a third type of metal cation doping due to the flexibility of cations in LDH layers. For example, Co, Al, Zn, and Ir have been chosen as dopants to synthesize self-supported NiFeCo LDH,⁷¹ Ni₃FeAl_x LDH,⁷² NiFeZn LDH,⁹ and NiFeIr LDH⁷³ on conductive bones. More recently, high valence state dopants like Cr, V, and Ru have attracted intense interest because they are not only able to create more active sites but can also tune the electronic structure of bimetallic LDH, producing strong synergetic effects between the doping cations and the host cations. For example, Yang *et al.* demonstrated that Cr cations can readily adopt high valence oxidation states during the OER process and have a positive effect on the active species for water oxidation.⁷⁴ Li *et al.* explained that the incorporation of V into NiFe LDH layers can optimize the electronic structure and promote the intrinsic catalytic activity.⁷⁵ Chen *et al.* accelerated the oxygen evolution kinetics of NiFe LDH by Ru doping.⁷⁶ Zhang *et al.* employed both theoretical calculations and practical experiments to reveal that FeCoW oxyhydroxides could exhibit better OER activity than CoFe LDH, indicating that W could be an efficient dopant.⁷⁷ On the other hand, it has been reported recently that the crystalline-amorphous phase boundaries could enhance OER activity by providing highly defective interfaces.⁷⁸⁻⁸⁰

Inspired by the analysis above, here we have selected high valence state tungsten (W) as a dopant to synthesize self-supported ultrathin Ni-Fe-W LDH nanosheets on

commercial nickel foam (NF) *via* a water bath reaction. These Ni-Fe-W LDH nanosheets are further composed of mesoporous nanoparticles and have abundant crystalline-amorphous phase boundaries. We obtained a series of Ni₃FeW_x (x = 0.5, 1, 2, and 3) LDH samples by tuning the W ratio in the initial reactants. The optimized one, Ni₃FeW LDH, was found to retain a low overpotential and fast current increase toward OER due to its unique open porous architecture and the intrinsically high catalytic activity of the Ni-Fe-W LDH. The synthesis method employed here is also versatile and can be applied to produce various self-supported Ni-Fe-M (M = Co, Ru, and Mo) LDH/NF catalysts with good OER activity.

2.2 Experimental Section

2.2.1 Synthesis of Catalysts

Ni₃FeW LDH nanosheets were grown on NF *via* a one-step water bath reaction. Briefly, a piece of NF (5 cm × 3 cm) was cleaned by HCl solution (2 M) and deionized water with the assistance of sonication for 15 min each. To synthesize Ni₃FeW LDH, 0.75 mmol nickel nitrate hexahydrate [Ni(NO₃)₂·6H₂O, Sigma Aldrich], 0.25 mmol iron nitrate nonahydrate [Fe(NO₃)₃·9H₂O, Alfa Aesar], 0.0208 mmol ammonium tungsten oxide hydrate [(NH₄)₆W₁₂O₃₉·xH₂O, Alfa Aesar] (the atomic ratio of Ni:Fe:W is 3:1:1), 3 mmol ammonium fluoride (NH₄F, Alfa Aesar), and 15 mmol urea [CO(NH₂)₂, Promega Corporation] were dissolved in 60 mL deionized water in a beaker with continuous stirring. After 30 min intensive stirring, the previously washed NF was put into this beaker, which was then transferred to a water bath oven maintained at 90 °C for 7 h. The sample was then naturally cooled

down to room temperature, removed from the beaker, and rinsed several times with deionized water.

Other Ni_3FeW_x LDH ($x = 0.5, 2, \text{ and } 3$) samples were synthesized *via* a similar procedure with different amounts of $(\text{NH}_4)_6\text{W}_{12}\text{O}_{39}\cdot x\text{H}_2\text{O}$ (0.0104 mmol, 0.0417 mmol, and 0.0625 mmol, respectively) in the initial reactants. For comparison, pristine Ni_3Fe LDH was synthesized without the addition of $(\text{NH}_4)_6\text{W}_{12}\text{O}_{39}\cdot x\text{H}_2\text{O}$. Ni_3FeCo LDH, Ni_3FeMo LDH, and Ni_3FeRu LDH were synthesized using the same procedure except for replacing the tungsten source with a cobalt source (0.25 mmol $\text{Co}(\text{NO}_3)_2\cdot 6\text{H}_2\text{O}$), a molybdenum source (0.25 mmol $\text{Na}_2\text{MoO}_4\cdot 2\text{H}_2\text{O}$), and a ruthenium source (0.25 mmol $\text{RuCl}_3\cdot x\text{H}_2\text{O}$), respectively.

2.2.2 Physical and Chemical Characterization

The phase and crystal structure data for the as-obtained samples were obtained by X-ray diffraction (XRD, PANalytical X'pert PRO, Cu $K\alpha$ radiation). The microstructure and X-ray energy-dispersive spectroscopy (EDS) mapping were characterized by scanning electron microscopy (SEM, LEO 1525) and transmission electron microscopy (TEM, JEOL 2010F). The X-ray photoelectron spectroscopy (XPS) was acquired using a PHI Quantera XPS scanning microprobe with an Al monochromatic $K\alpha$ source. Atomic force microscopy (AFM) characterization was performed with a Bruker 8 Atomic Force Microscope system to measure the thickness of the nanosheets.

2.2.3 Electrochemical Characterization

Electrochemical characterizations were evaluated on a Gamry Reference 600 electrochemical station with a three-electrode configuration in 1 M KOH electrolyte.

Pt wire was used as the counter electrode, Hg/HgO electrode was used as the reference electrode, and Ni-Fe-W LDH was used as the working electrode. All potentials applied were calibrated to a reversible hydrogen electrode (RHE) using the equation: $E_{\text{RHE}} = E_{\text{Hg/HgO}} + 0.098 + 0.059 \times \text{pH}$. Linear sweep voltammetry (LSV) curves were recorded at a scan rate of 5 mV s^{-1} with iR compensation. The overpotential (η) for OER was calculated by $\eta = E_{\text{RHE}} - 1.23 \text{ V}$ and the Tafel slope (b) was calculated by $\eta = a + b \log(j)$, where b is the Tafel slope and j is the current density. The electrochemically active surface area (ECSA) was evaluated by measuring the double-layer capacitance (C_{dl}) in a non-Faradaic region. Briefly, cyclic voltammetry (CV) measurements were carried out with scan rates ranging from 10 to 100 mV s^{-1} in the potential range from around 1.13 to 1.23 V vs. RHE . By plotting the capacitive current against the scan rate, the C_{dl} was obtained as half of the slope and the ECSA can be derived from the equation $\text{ECSA} = C_{\text{dl}}/C_s$, where C_s is the specific capacitance.⁸¹ Electrochemical impedance spectroscopy (EIS) was performed at an overpotential of 300 mV from 0.01 Hz to 100 kHz at an alternating current voltage amplitude of 10 mV . For durability testing, 5000 CV cycles were performed between 1.125 and 1.525 V vs. RHE with a scan rate of 100 mV s^{-1} , and the LSV curves were recorded before and after the CV cycles were performed. Chronopotentiometric measurements were measured at a current density of 100 mA cm^{-2} for 50 h . The current densities were all normalized by the geometric area of the Ni foam immersed in the electrolyte.

2.3 Results and Discussion

2.3.1 Structural and Compositional Analysis Results

As illustrated in **Figure 2.1a**, nanoparticle-stacked Ni-Fe-W LDH nanosheets were synthesized *via* a one-step water bath reaction using urea and NH_4F as precipitants. We first investigated the crystal structure and composition of the as-prepared Ni_3FeW and Ni_3Fe LDH catalysts by X-ray diffraction (XRD). The blue curve of Ni_3Fe LDH in **Figure 2.1b** corresponds to iron nickel carbonate hydroxide (JCPDS#40-0215), confirming that LDH material can be successfully synthesized through this water bath reaction. After introducing W, Ni_3FeW LDH sample retain the same crystal structure and phases as pristine Ni_3Fe LDH. Scanning electron microscopy (SEM) was performed on these Ni_3FeW_x LDH samples to verify their structures. As shown in **Figure 2.1c-d**, dense Ni_3Fe LDH nanosheets up to 15 μm in length were vertically grown on the NF substrate. For the $\text{Ni}_3\text{FeW}_{0.5}$ (**Figure 2.2a-b**) and Ni_3FeW LDH (**Figure 2.1e-h**) samples, the surfaces of the NF substrates are uniformly covered by Ni-Fe-W LDH nanosheets of smaller size (around 500 nm in length). These nanosheets interconnect with each other to form an open porous structure that is beneficial for the connection between the active material and the electrolyte. Higher amounts of W lead to fewer nanosheets (Ni_3FeW_2 LDH in **Figure 2.2c-d**) and finally result in forming a dense film on the NF (Ni_3FeW_3 LDH in **Figure 2.2e-f**). It can be concluded that the morphology and structure of these Ni_3FeW_x LDH samples can be tuned by adjusting the molar ratio of W in the initial reactants.

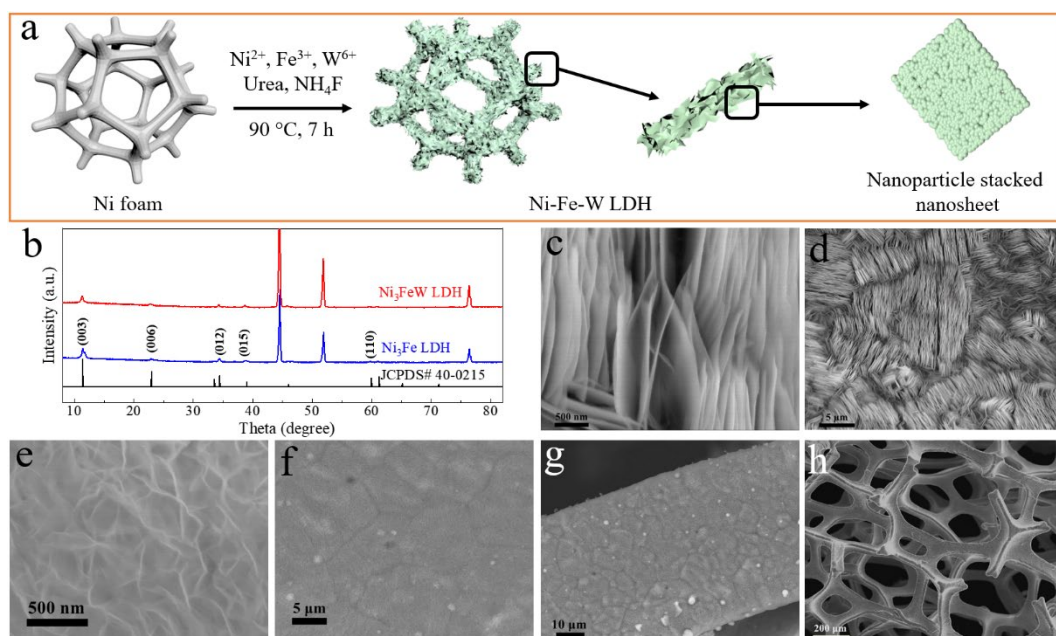


Figure 2.1. (a) Schematic illustration of the synthesis of Ni-Fe-W LDH catalysts. (b) XRD patterns of Ni₃Fe and Ni₃FeW LDH catalysts. SEM images of (c-d) Ni₃Fe LDH and (e-h) Ni₃FeW LDH.

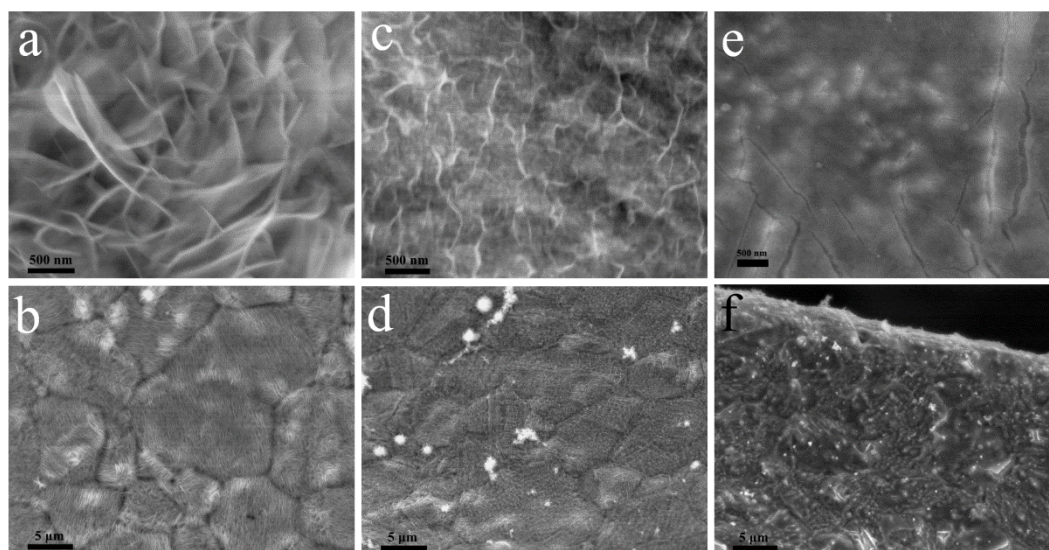


Figure 2.2. SEM images of (a-b) Ni₃FeW_{0.5} LDH, (c-d) Ni₃FeW₂ LDH, and (e-f) Ni₃FeW₃ LDH.

The thicknesses of the Ni₃Fe LDH and Ni₃FeW LDH nanosheets were measured by atomic force microscopy (AFM). As shown in **Figure 2.3**, the thickness of the Ni₃FeW LDH nanosheets is only 5.2 nm, which is around 1/3 that of the pristine Ni₃Fe

LDH nanosheets (16.8 nm), indicating that W doping decreases the thickness of the LDH nanosheets. An open porous architecture with such ultrathin Ni_3FeW LDH nanosheets is indeed beneficial for providing a large surface area and exposing abundant active for catalytic reaction.

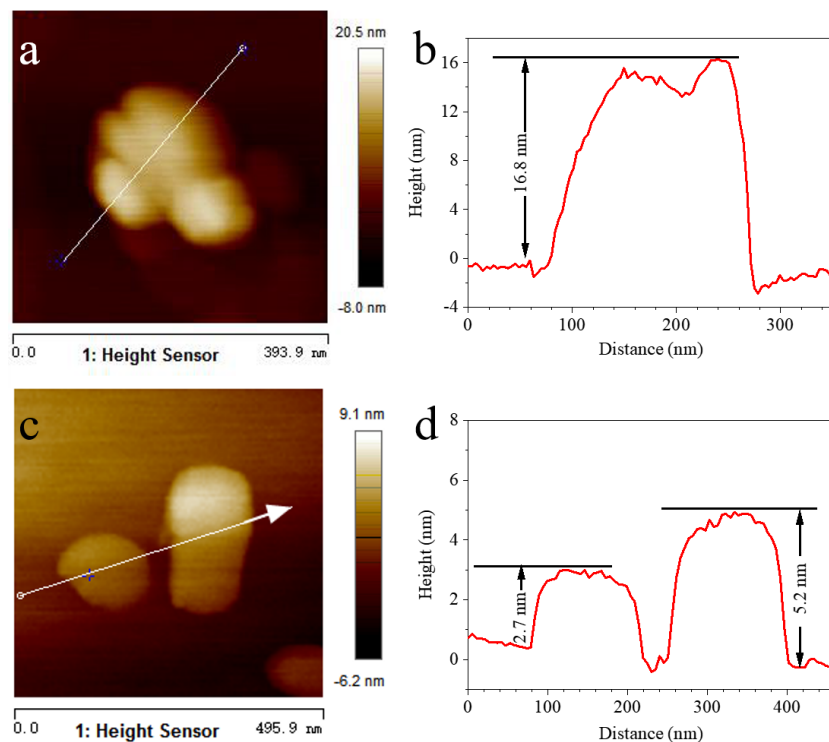


Figure 2.3. AFM images and corresponding height profiles of (a, b) Ni_3Fe LDH and (c, d) Ni_3FeW LDH nanosheets.

We selected the Ni_3FeW LDH nanosheets for transmission electron microscopy (TEM) and energy-dispersive X-ray spectrometry (EDX) measurements. A single slice of nearly transparent nanosheet is observed in **Figure 2.4a** due to its ultrathin nature. The higher magnification TEM image in **Figure 2.4b** indicates that these ultrathin Ni_3FeW LDH nanosheets are further composed of nanoparticles. The high-resolution TEM (HRTEM) image in **Figure 2.4c** reveals that lattice fringes can only be observed in a small portion of the nanoparticles due to the amorphous structure of LDH

materials.⁸² The randomly oriented crystal nanoparticles mixed with the amorphous phase are clearly observed in an enlarged HRTEM image (**Figure 2.4d**). Some recent studies have proved that the amorphous phase can offer a high density of adsorption sites for hydroxide while the crystalline phase can enhance charge transfer between adsorbates and metal-metalloid compounds.⁷⁸⁻⁷⁹ The broad-ring pattern with discrete dots in the selected area electron diffraction (SAED) pattern in **Figure 2.4e** reveals the characteristic (006), (101), and (015) facets of Ni₃FeW LDH, which are consistent with the diffraction peaks at 22.8, 33.5, and 39.0 degrees in its XRD pattern (**Figure 2.1b**). The distributions of Ni, Fe, W, and O were measured by EDX elemental mapping. The uniform distribution of these elements shown in **Figure 2.4f-k** not only confirms the existence of Ni₃FeW LDH but might also be highly beneficial for the synergistic effects among these elements. The TEM images (**Figure 2.5a-d**) of another Ni₃FeW LDH nanosheet with different magnification show that it has the same structure as that shown in **Figure 2.4**. The diameter distribution of these nanoparticles ranges from 2 to 6 nm (**Figure 2.5e-f**), which is close to the thickness data measured by AFM.

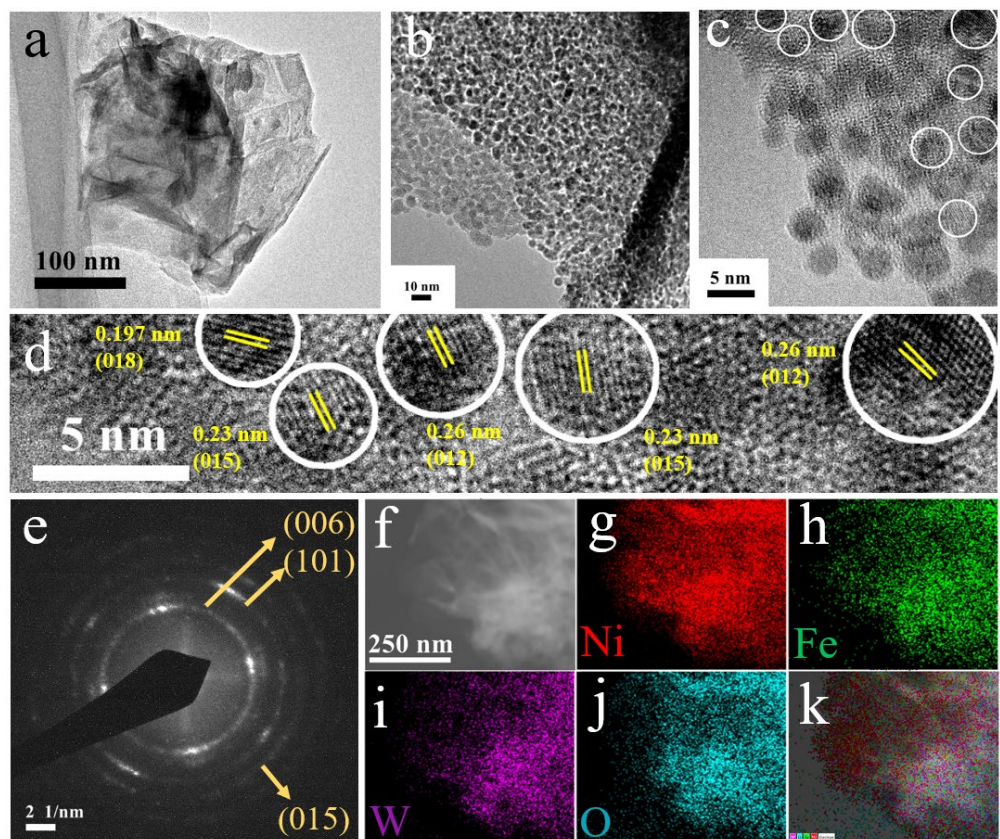


Figure 2.4. (a, b) TEM and (c, d) HRTEM images and (e) SAED pattern of Ni_3FeW LDH nanosheets. (f) TEM image of a Ni_3FeW LDH nanosheet and the corresponding (g-k) EDX elements mapping images.

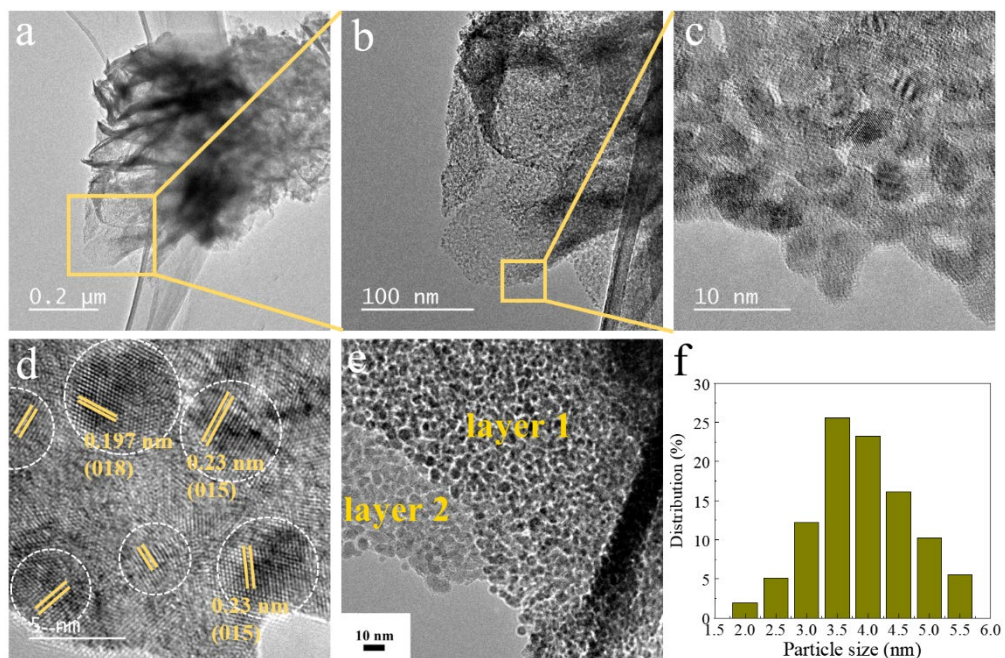


Figure 2.5. (a, b) TEM and (c, d) HRTEM images of Ni₃FeW LDH nanosheets. (e) TEM image of two layers of Ni₃FeW LDH nanosheets and (f) the corresponding nanoparticle diameter distribution measured from (e).

To gain insight into the chemical composition and valence states of the Ni₃FeW LDH, X-ray photoelectron spectroscopy (XPS) was performed. The signals of elemental Ni, Fe, W, and O were clearly detected in the overall XPS spectra of Ni₃FeW LDH (red line in **Figure 2.6a**), which matches well with the EDX mapping results. In addition to two shakeup satellites, the Ni 2p spectra of pristine Ni₃Fe LDH shown in **Figure 2.6b** is composed of a pair of peaks with binding energies at 855.6 and 873.7 eV, corresponding to the Ni²⁺ 2p_{3/2} and Ni²⁺ 2p_{1/2}, respectively⁷¹. Compared with that of Ni₃Fe LDH, the main peak for Ni²⁺ 2p_{3/2} in Ni₃FeW LDH is negatively shifted 1.1 eV. The Fe 2p_{3/2} peak for Ni₃FeW LDH in **Figure 2.6c** corresponds to Fe³⁺, which shows a positive shift to 713.3 eV from 712 eV for that in Ni₃Fe LDH. The lower oxidation valence state of the Ni sites⁸³⁻⁸⁴ and the higher oxidation state of the Fe sites⁷⁴ have been reported to be more favorable for OER activity. The XPS spectra of W in Ni₃FeW LDH displayed in **Figure 2.6d** show that the binding energies of W 4f_{7/2} and W 4f_{5/2} are located at 35.1 and 37.7 eV, respectively, and are assigned to W⁶⁺. The above analysis demonstrates that high-valence W was successfully doped into the Ni₃Fe LDH and modified the electronic structure of both the Ni and Fe sites.

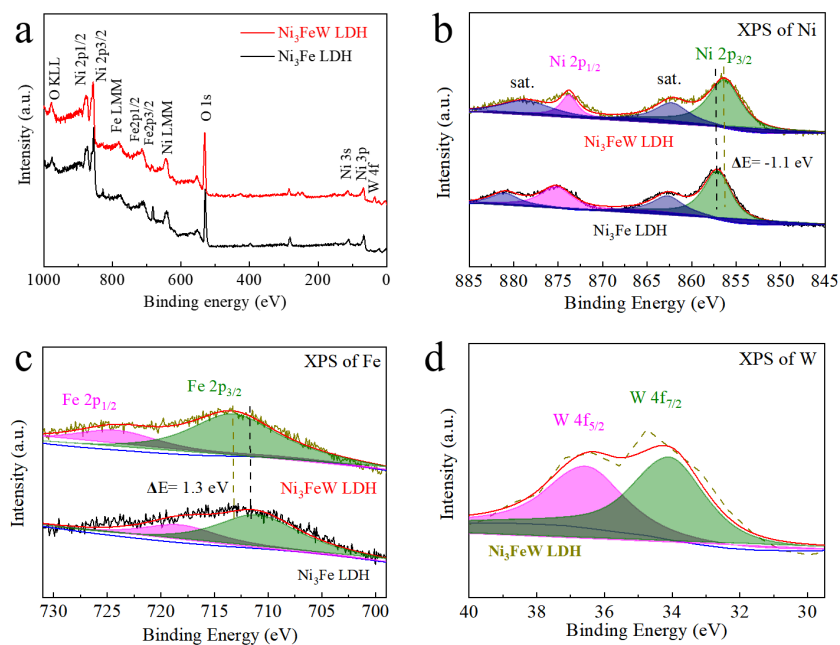


Figure 2.6. (a) XPS spectra of Ni₃Fe LDH and Ni₃FeW LDH. High-resolution XPS spectra of (b) Ni and (c) Fe in Ni₃Fe LDH and Ni₃FeW LDH and of (d) W in Ni₃FeW LDH.

2.3.2 Catalytic Performance of Synthesized Catalysts

The OER performance of the as-synthesized Ni₃FeW_x ($x = 0, 0.5, 1, 2,$ and 3) LDH catalysts was measured using a three-electrode configuration in 1 M KOH electrolyte. The linear sweep voltammetry (LSV) curves shown in **Figure 2.7a** indicate that Ni₃FeW LDH requires a low overpotential of 230 mV to drive a current density of 50 mA cm⁻², which is clearly smaller than that of Ni₃Fe LDH (255 mV), Ni₃FeW_{0.5} LDH (256 mV), Ni₃FeW₂ LDH (272 mV), and Ni₃FeW₃ LDH (342 mV). To drive higher current densities of 100, 500, and 1,000 mA cm⁻², the Ni₃FeW LDH sample requires overpotentials of 247, 294, and 320 mV, respectively, which are also superior to those for both pristine Ni₃Fe LDH and other trimetallic Ni₃FeW_x LDH samples. Compared with pristine Ni₃Fe LDH, both the trimetallic Ni₃FeW_{0.5} LDH and Ni₃FeW LDH samples require lower overpotentials to drive large current densities like

500 and 1,000 mA cm⁻², indicating an enhancement of OER activity by W doping. In particular, many bubbles are produced under such large current densities during the water-splitting process, and the open porous nanosheets structure of Ni₃FeW_{0.5} LDH/NF and Ni₃FeW LDH/NF guarantees the rapid release of the bubbles and maintains good contact between the catalyst and the electrolyte. High-ratio W doping (Ni₃FeW₂ LDH and Ni₃FeW₃ LDH) results in increased overpotential, which might be attributed to structure change (from porous nanosheets to dense films). To further assess the intrinsic catalytic activity, the OER kinetics of the as-synthesized Ni₃FeW_x (x = 0, 0.5, 1, 2, and 3) LDH catalysts were measured using the corresponding Tafel plots calculated from **Figure 2.7a**. As shown in **Figure 2.7b**, the Tafel slope value of Ni₃FeW LDH is as low as 55 mV dec⁻¹, which is lower than that of Ni₃Fe LDH (66 mV dec⁻¹), Ni₃FeW_{0.5} LDH (64 mV dec⁻¹), Ni₃FeW₂ LDH (67 mV dec⁻¹), and Ni₃FeW₃ LDH (85 mV dec⁻¹), indicating its higher transfer coefficient and enhanced electrocatalytic kinetics.¹⁵ To elucidate the improved OER activity of the Ni₃FeW LDH catalyst, we then determined its electrochemically active surface area (ECSA), which is proportional to the double-layer capacitance (*C_{dl}*, **Figure 2.7c**) calculated from the cyclic voltammetry (CV) scans in **Figure 2.8**. Ni₃FeW LDH has the largest *C_{dl}* of 18.1 mF cm⁻² among the samples studied, higher than that of pristine Ni₃Fe LDH (13.7 mF cm⁻²), suggesting that more electrochemically active sites are created by the introduction of W.⁷⁵ An electrochemical impedance spectroscopy (EIS) analysis was performed to study the conductivity properties of these self-supported electrocatalysts and is shown in **Figure 2.7d**. The charge-transfer resistance of Ni₃FeW LDH is clearly much smaller than that of pristine Ni₃Fe LDH, which further

confirms the enhanced electrocatalytic kinetics by W doping. On the other hand, too much W doping (Ni_3FeW_3 LDH) results in increased charge-transfer resistance, which might be another reason for the degraded performance as shown by the LSV curves.

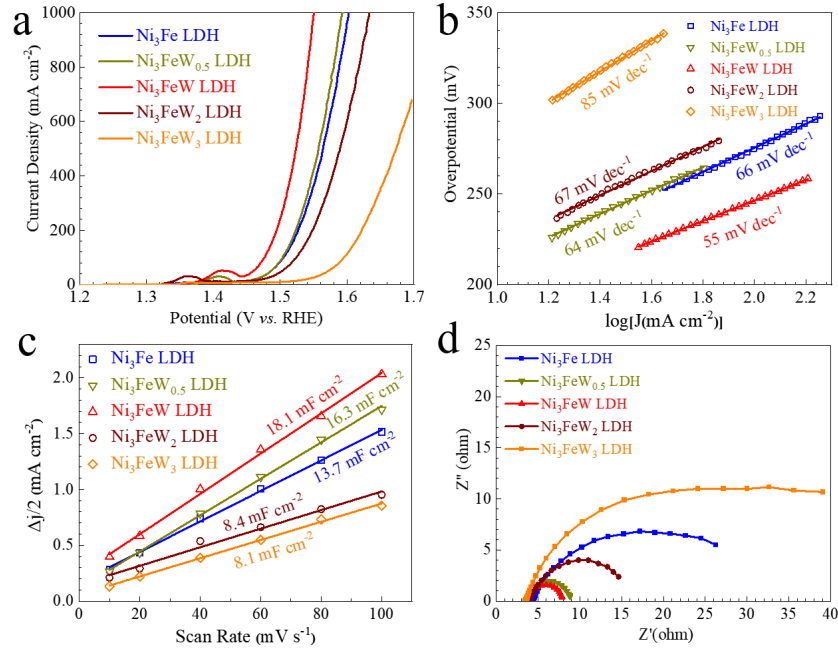


Figure 2.7. (a) OER LSV curves of Ni_3FeW_x LDH samples in 1.0 M KOH. (b) Tafel plots derived from the polarization curves in (a). (c) Double-layer capacitance (C_{dl}) plots and (d) Nyquist plots of these samples.

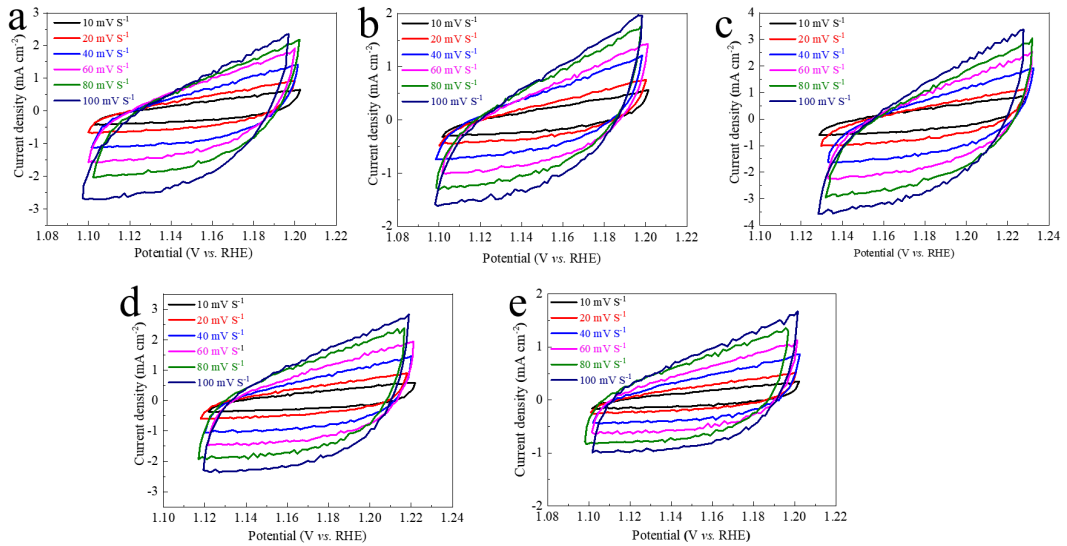


Figure 2.8. CV curves of (a) Ni₃Fe LDH, (b) Ni₃FeW_{0.5} LDH, (c) Ni₃FeW LDH, (d) Ni₃FeW₂ LDH, and (e) Ni₃FeW₃ LDH at different scan rates in a non-faradaic region.

The OER LSV curves of the Ni₃FeW LDH sample before and after 5000 CV cycles are shown in **Figure 2.9a**. The polarization curve shows negligible change after 5000 CV scans and the SEM images of the catalyst after CV testing shown in **Figure 2.9b** confirm that the open porous nanosheets structure is well maintained, indicating good stability during CV cycling. The catalyst's stability was also confirmed by a long-term electrochemical durability test performed at a current density of 100 mA cm⁻² for 50 h (**Figure 2.9c**). The facile water bath reaction method used here has also been demonstrated to be versatile and was applied to synthesize Ni₃FeMo LDH/NF, Ni₃FeRu LDH/NF, and Ni₃FeCo LDH/NF with good OER activity by changing the dopants. The OER performance of these catalysts in 1.0 M KOH is indicated by the LSV curves shown in **Figure 2.9d**.

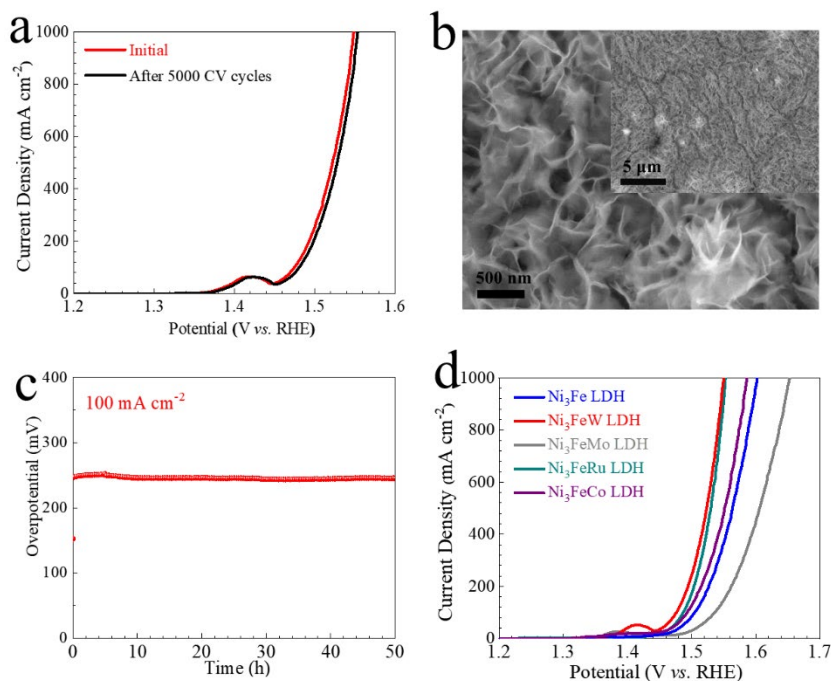
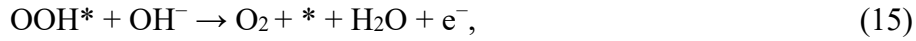
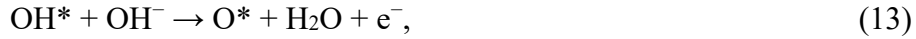


Figure 2.9. (a) CV cycling performance of Ni₃FeW LDH. (b) SEM images of Ni₃FeW LDH after 5000 CV scans. (c) Chronopotentiometric curve of Ni₃FeW LDH. (d) OER LSV curves of Ni₃FeM (M = W, Mo, Co, and Ru) LDH.

2.3.3 Discussion

The widely accepted alkaline OER mechanism can be described as follows:



where * is the adsorption site on the catalyst surface and O*, OH*, and OOH* denote adsorbed intermediates.^{29, 34} After incorporating W into Ni-Fe LDH, its XPS patterns show that the Ni sites change to a lower oxidation valence state while the Fe sites change to a higher oxidation state. The multiple oxidation states of Fe (2+ or 3+) and W (from 4+ to 6+) make them versatile coordination hosts, and both can absorb the intermediate species to form Fe-OOH or W-OOH. The adsorption energy of OH* is too strong on the FeOOH (010) surface, but too weak on the WO₃ (001) surface.⁷⁷ It is reasonable that the Ni-Fe-W LDH complex might have optimal adsorption energies for intermediates, allowing it to exhibit excellent OER performance due to this synergistic effect. In addition to the electronic structure adjustment and synergistic effects originating from high-valence W, the excellent OER activity of the self-supported Ni₃FeW LDH catalyst can further be attributed to the following aspects. First, the direct growth of open porous Ni₃FeW LDH nanosheets on conductive nickel foam not only stabilizes the unique layered structure of LDH, but also provides a large surface area to guarantee the intimate contact between the active material and the

electrolyte media. Ensuring that the active sites always take part in the OER process is very important, especially at high current densities when large numbers of oxygen bubbles are produced and can separate the electrode from the electrolyte. Second, the crystalline nanoparticles and the highly abundant crystalline-amorphous phase boundaries in ultrathin Ni₃FeW LDH nanosheets lead to a high transfer coefficient and good catalytic kinetics. Third, with the introduction of a moderate amount of W, the same phase as pristine Ni₃Fe LDH is maintained, but the electrochemically active surface area is increased and the charge-transfer resistance between the LDH nanosheets and the electrolyte is reduced.

2.4 Conclusion

We have introduced a scalable water bath reaction to synthesize self-supported Ni₃FeW LDH nanosheets as produce efficient OER catalysts. Such open porous nanosheets with a high density of crystalline-amorphous phase boundaries can provide a large active surface area and guarantee continued good contact between the electrode and the electrolyte. Additionally, W doping leads to enhanced conductivity, favorable kinetics, and modification of the electronic structure of both the Ni and Fe sites, producing favorable synergistic effects for OER. With an optimized W ratio, Ni₃FeW LDH exhibits much better catalytic activity than that of pristine Ni₃Fe LDH. This study shows that Ni-Fe-W LDH can be used as highly efficient catalysts and provides a general way to fabricate trimetallic LDH-based OER catalysts.

CHAPTER 3 BORON-MODIFIED COBALT IRON LAYERED DOUBLE HYDROXIDES FOR HIGH EFFICIENCY SEAWATER OXIDATION

Note: The material in this chapter has been published. The introduction, experimental section, and figure captions were adjusted for dissertation consistency. Reproduced with permission from Elsevier.⁸⁵

3.1 Introduction

Among all of the catalysts studied for alkaline freshwater oxidation, layered double hydroxides (LDHs) are the most promising ones due to their high intrinsic OER activity and tunable chemical composition feature.^{34, 86} Ni-Fe LDH was reported as an advanced OER catalyst by Gong *et al.* in 2013 and tremendous bi- and trimetallic LDHs, as well as their compositions, have been explored and demonstrated to be efficient OER catalysts.^{12, 33, 51-52, 71, 75, 87-92} However, LDH-based catalysts still suffer from deficiencies like poor electronic conductivity and limited active sites, which need further enhancement for their application in industrial hydrogen production.^{12, 27} Constructing self-supported LDH-based catalysts on conductive substrates like nickel foam,^{52, 75, 87} copper foam,^{51, 90} and carbon cloth⁷¹ is an effective way to enhance their conductivity and stability but is still not adequate. Another issue is that hydrothermal reaction, the most used synthesis method for LDH-based catalysts, commonly requires strict reaction conditions (maintenance at temperatures above the boiling point of water for 6-12 h in a sealed container) that are not suitable for scaling up and always lead to a nanosheet structure.³⁴ An easily scalable synthesis method, as well as a novel structure that can rivet and expose more active sites to enhance the

catalytic activity should be explored to promote the potential practical application of the LDH catalysts. Recently, amorphous catalysts have been greeted with great enthusiasm due to their structural and chemical advantages.⁹³⁻⁹⁶ Amorphous catalysts normally possess strong corrosion resistance, a large number of percolation pathways, and a fast ion-diffusion feature due to their structure disorder and relatively loose packing of atoms.^{93, 97-101} Among various amorphous catalysts, boron-based ones such as Co₂B,⁹⁴ Fe-Ni-P-B-O,⁹⁵ Gd-CoB@Au,¹⁰² and Cr_{1-x}Mo_xB₂¹⁰³ have recently been synthesized and shown to exhibit high catalytic activity.

Considering the features of LDH- and amorphous boron-based catalysts, amorphous boron-modified LDH materials might be promising catalysts for seawater electrolysis, although relevant studies remain quite limited. Here, for the first time, we synthesized partially amorphous boron-modified cobalt iron layered double hydroxides (denoted as B-Co₂Fe LDH) using a two-step water bath reaction-chemical reduction approach in an open beaker at low temperature. A unique hierarchical nanosheet-nanoflake structure was obtained by optimizing the Co/Fe ratio in the reactants and the partial amorphousness feature was then achieved by the boron modification. The catalyst's open and hierarchical architecture, along with the partial amorphousness feature, allows for abundant active sites, enhanced electronic kinetics, and high corrosion resistance. Typically, it requires overpotentials of only 205 and 246 mV to drive current densities of 10 and 100 mA cm⁻², respectively, in 1 M KOH and it exhibits a small Tafel slope of 39.2 mV dec⁻¹, which place it among the best self-supported OER catalysts reported thus far. As for seawater oxidation, it requires overpotentials of 310 and 376 mV to drive current densities of 100 and 500 mA cm⁻²,

respectively, in 1 M KOH seawater and can work continuously for 100 h without producing any hypochlorite. *in situ* and *ex situ* Raman tests and post-OER analysis were applied to reveal its transformation during OER. Long-term immersion and corrosion testing, as well as chronopotentiometric measurements, were applied to prove its corrosion resistance and catalytic durability.

3.2 Experimental Section

3.2.1 Synthesis of Catalysts

3.2.1.1 Synthesis of Co₂Fe LDH

Co₂Fe layered double hydroxide (Co₂Fe LDH) was *in situ* grown on the surface of Nickel foam (NF, areal density: 350 g m⁻²) *via* a one-step water bath reaction. Briefly, a piece of commercial NF (4 cm × 3 cm) was first cleaned by HCl solution and ethanol with the assistance of sonication. Afterward, 1 mmol cobalt nitrate hexahydrate [Co(NO₃)₂·6H₂O, Sigma Aldrich], 0.5 mmol iron nitrate nonahydrate [Fe(NO₃)₃·9H₂O, Alfa Aesar], 3.75 mmol ammonium fluoride (NH₄F, Alfa Aesar), and 15 mmol urea [CO(NH₂)₂, Promega Corporation] were dissolved in 50 mL deionized (DI) water in a beaker with continuous stirring. After 30 min intensive stirring, the previously washed NF was put into this beaker, which was then transferred to a water bath oven maintained at 90 °C for 7 h. The sample was then naturally cooled down to room temperature, removed from the beaker, and rinsed several times with DI water. After drying in air naturally, Co₂Fe LDH was successfully obtained, and the loading mass was measured to be 1.14 mg cm⁻². Co(OH)₂ and Fe CH precursors were prepared *via* a similar procedure using 0.5 mmol Co(NO₃)₂·6H₂O and 4 mmol urea in the reactants and 0.5 mmol Fe(NO₃)₃·9H₂O, 3.75

mmol NH_4F , and 15 mmol urea in the reactants, respectively.

3.2.1.2 Synthesis of Partially Amorphous B- Co_2Fe LDH

To synthesize partially amorphous boron-modified Co_2Fe LDH (B- Co_2Fe LDH), the as-prepared Co_2Fe LDH precursor was soaked in a 0.5 M aqueous sodium borohydride solution (NaBH_4 , Sigma Aldrich), which contains 0.25 M NaOH to slow the hydrolysis of NaBH_4 , at room temperature for 1 h to ensure the complete reaction. After this boron-modification procedure, the partially amorphous B- Co_2Fe LDH sample was removed from the solution and then dried in vacuum. The loading mass of B- Co_2Fe LDH was measured to be 1.08 mg cm^{-2} . Here, NaBH_4 serves as both the reducing agent and the boron source in this reaction. Similarly, boron-modified $\text{Co}(\text{OH})_2$ [B- $\text{Co}(\text{OH})_2$] and boron-modified Fe CH (B-Fe CH) were prepared by soaking each of their precursors in a 0.5 M aqueous NaBH_4 solution, and the loading masses were measured to be 0.51 and 0.44 mg cm^{-2} , respectively.

3.2.1.3 Preparation of IrO_2 Electrode

A noble-metal-based IrO_2 electrode was prepared for comparison in this experiment. First, 40 mg iridium oxide (IrO_2 , 99%, Alfa Aesar) was dissolved in a mixture solution containing 810 μL ethanol, 90 μL Nafion 117 solution (5%, Sigma Aldrich), and 600 μL DI water with the assistance of ultrasonication. The NF was then soaked in the solution for 1 h to let the active material load onto the surface, followed by drying at $50 \text{ }^\circ\text{C}$ for 12 h in an oven.

3.2.2 Physical and Chemical Characterization

X-ray diffraction (XRD, PANalytical X'pert PRO, $\text{Cu K}\alpha$ radiation) tests were conducted to identify the crystal structures and compositions of these as-prepared

samples. Morphology characterizations and energy-dispersive spectroscopy (EDS) were performed using scanning electron microscopy (SEM, LEO 1525) and transmission electron microscopy (TEM, JEOL 2010F). X-ray photoelectron spectroscopy (XPS, PHI Quantera) was conducted to identify the valence states. The wettability of pure NF and B-Co₂Fe LDH was tested by dropping droplets (DI water or seawater) onto each catalyst's surface. *in situ* and *ex situ* Raman tests were conducted on a Horiba iHR320 Raman spectrometer using a He-Ne laser (excitation wavelength: 532 nm). Electron paramagnetic resonance (EPR) spectroscopy was analyzed using a Bruker A300 spectrometer.

3.2.3 Electrochemical Characterization

Electrochemical characterizations of these as-prepared catalysts were conducted on a Gamry Reference 600 electrochemical station using a three-electrode configuration. A Pt plate was used as the counter electrode, an Hg/HgO electrode was used as the reference electrode, and the as-prepared catalyst was used as the working electrode. The stable polarization curve of each catalyst was recorded at a scan rate of 2 mV s⁻¹ with *iR* compensation after running at least 100 cyclic voltammetry (CV) cycles for activation and stabilization. The potential ($E_{\text{Hg/HgO}}$) was calibrated to the reversible hydrogen electrode (RHE) using the equation: $E_{\text{RHE}} = E_{\text{Hg/HgO}} + 0.098 + 0.0591 \times \text{pH}$ and the overpotential (η) was calculated by: $\eta = E_{\text{RHE}} - 1.23 \text{ V}$. The Tafel slope (b) was calculated by $\eta = a + b \log(j)$, in which j is the current density. Electrochemical impedance spectroscopy (EIS) was performed at the overpotential of 300 mV from 100 kHz to 0.01 Hz in 1 M KOH electrolyte. To evaluate the electrochemically active surface area (ECSA) of each catalyst, CV cycling was

performed in the potential range from 0.9 to 1.0 V *vs.* RHE with scan rates ranging from 20 to 100 mV s⁻¹. By plotting the capacitive current at 0.95 V *vs.* RHE against the scan rates, the double-layer capacitance (C_{dl}) was obtained as half of the corresponding slope, and then the ECSA was derived from the equation: $ECSA = C_{dl}/C_s$, in which C_s is the specific capacitance for a flat surface (40 $\mu\text{F cm}^{-2}$). For the durability testing, 2,000 CV cycles were performed between 1.125 and 1.525 V *vs.* RHE with a scan rate of 50 mV s⁻¹, and the corresponding polarization curves were recorded before and after CV cycling. Chronopotentiometric measurements were recorded at the current densities of 100 and 500 mA cm⁻² in both 1 M KOH and 1 M KOH seawater electrolytes. Natural seawater was collected from Galveston Bay, Galveston, Texas, USA (29.303° N, 94.772° W). There was no pre-treatment of the natural seawater and the electrochemical testing in 1 M KOH seawater electrolyte was performed after most of the particles visible to the naked eye had settled. Corrosion testing was conducted on a SP-200 Biologic electrochemical station in natural seawater using a saturated calomel electrode (SCE) as the reference electrode.

3.2.4 Calculation of TOF

The plots of current density can be converted into turnover frequency (TOF) plots using the equation: $TOF = j \times A / 4 \times F \times n$, where j is the current density (A cm^{-2}), A is the surface area of the electrode, 4 represents a four-electron oxygen evolution reaction, F is the Faraday constant (96485.3 C mol⁻¹), and n represents the moles of active material on the substrate, which can be calculated by the loading mass and the molecular weight of the catalyst.^{48, 75} Since the nature of the active sites is not yet understood, we estimated the number of active sites using the total loading mass (1.14

mg cm⁻² for Co₂Fe LDH and 1.08 mg cm⁻² for B-Co₂Fe LDH, respectively) and each metal cation (either Co or Fe) represents one active site, which may underestimate the real TOF.

3.2.5 Gas Chromatography Testing

Gas chronopotentiometry (GC, GOW-MAC 350 TCD) testing was conducted with a constant current density of 500 mA cm⁻² in 1 M KOH seawater electrolyte. The theoretical amount of generated O₂ gases was calculated using the equation: $n = i \times t / (n \times F)$, where n is the theoretical amount (mol) of gaseous products, i is the current (A), t is the time (s), n is the number of electrons transferred (4), and F is the Faraday constant.

3.3 Results and Discussion

3.3.1 Structural and Compositional Analysis Results

As illustrated in **Figure 3.1**, a two-step water bath reaction-chemical reduction procedure was applied to synthesize partially amorphous B-Co₂Fe LDH. Here, commercial nickel foam (NF) was employed as the substrate due to its three-dimensional structure, high conductivity, and low cost.

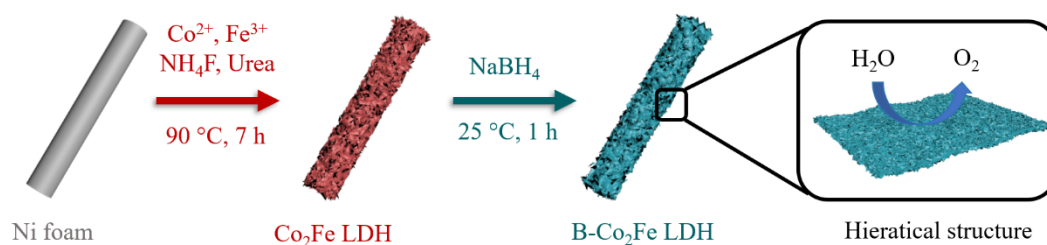


Figure 3.1. Schematic illustration of the formation of B-Co₂Fe LDH *via* a two-step water bath reaction-chemical reduction procedure.

Scanning electron microscopy (SEM) images in **Figure 3.2a-c** show that the structure of the Co₂Fe LDH precursor has a hierarchical structure composed of

nanosheets with numerous nanoflakes attached on the surface. Transmission electron microscopy (TEM) analysis was then performed to characterize the structures in detail. As shown in **Figure 3.2d**, a slice of almost transparent Co_2Fe LDH precursor nanosheet with numerous nanoflakes on its edges can be clearly observed. The interplanar spacings in the high-resolution TEM (HRTEM) image in **Figure 3.2e** were measured to be 0.38 and 0.23 nm, corresponding to the (006) and (015) planes of Co_2Fe LDH, respectively. Additionally, the discrete dots in the selected area electron diffraction (SAED) pattern shown in the inset to **Figure 3.2f** reveal the characteristic (015) and (110) facets of Co_2Fe LDH. The clear space fringes along with the sharp discrete dots indicate that the Co_2Fe LDH precursor has a crystalline structure. Meanwhile, $\text{Co}(\text{OH})_2$ (**Figure 3.3a-c**) and $\text{Fe}_6(\text{OH})_{12}\text{CO}_3 \cdot 2\text{H}_2\text{O}$ (Fe CH) (**Figure 3.3d-f**) precursors exhibit nanoflake and nanosheet structures, respectively.

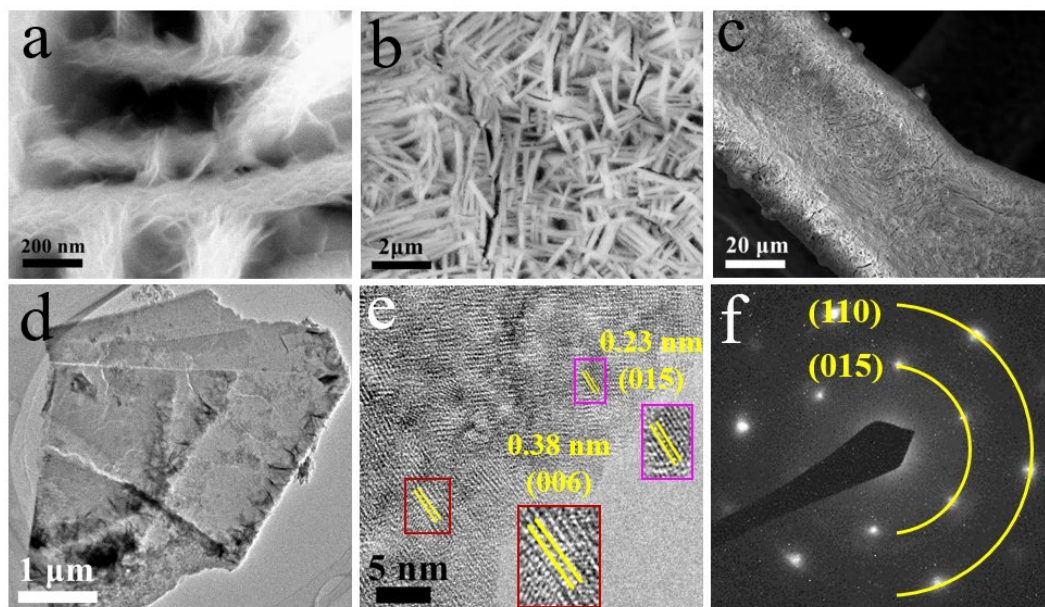


Figure 3.2. (a-c) SEM, (f) TEM, (e) HRTEM images, and (f) SAED pattern of the Co_2Fe LDH precursor.

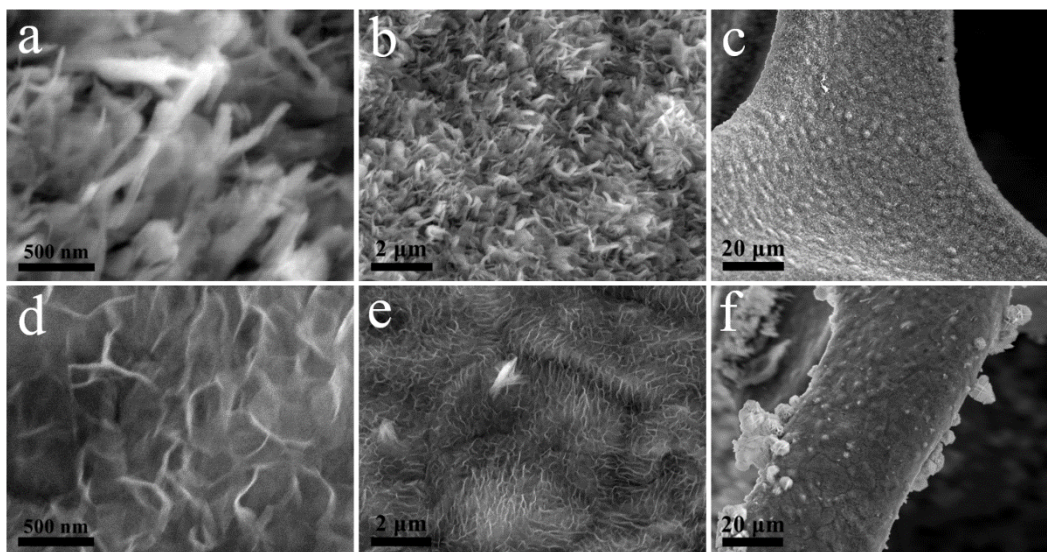


Figure 3.3. SEM images of (a-c) $\text{Co}(\text{OH})_2$ and (d-f) Fe CH precursors.

In the subsequent chemical reduction step, B- Co_2Fe LDH sample was obtained by soaking Co_2Fe LDH precursors in 0.5 M NaBH_4 solution at room temperature for 1 h. The H^- , which originates from NaBH_4 and exhibits strong reducing ability, can act as an oxygen scavenger to create oxygen defects and modify the crystallinity of the precursor.^{97, 104} As shown in **Figure 3.4a-c**, B- Co_2Fe LDH samples share a thinner nanosheet and more porous nanoflake structure compared with the Co_2Fe LDH precursor. Such hierarchical structure can dramatically enhance the surface area to disperse and expose more active sites for water electrolysis compared with the pure nanosheet structure.^{12, 34} On the other hand, the TEM image of B- Co_2Fe LDH in **Figure 3.4d** shows a more porous structure and the detailed HRTEM image in **Figure 3.4e** indicates that parts of the sample are amorphous (marked by yellow ellipses), which is further confirmed by the broad rings, normally recognized as the intrinsic characteristic of an amorphous material,^{95, 105} in the SAED pattern shown in **Figure 3.4f**. The uniform modification of boron inside a single B- Co_2Fe LDH nanosheet

(Figure 3.4g) is illustrated by the energy-dispersive X-ray spectrometry (EDX) mapping images in Figure 3.4h-k. The SEM images of B-Co(OH)₂ and B-Fe CH shown in Figure 3.5a-b and 3.5d-e, respectively, also confirm that their structures could be slightly tuned through modification by the NaBH₄ solution.

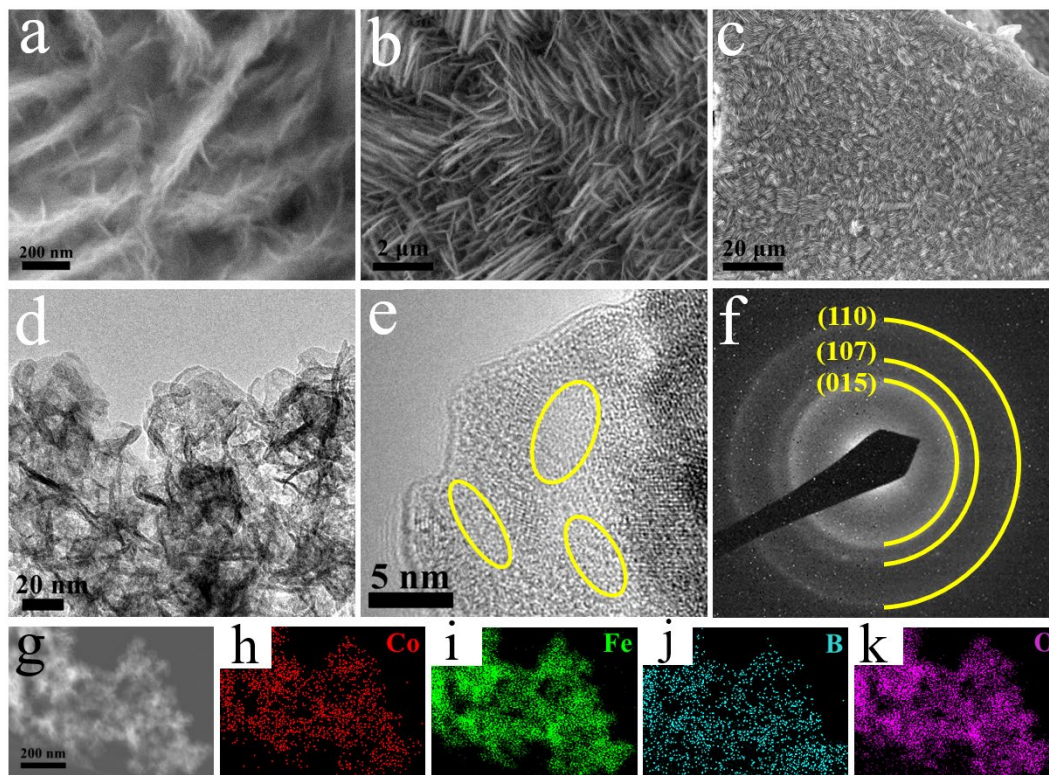


Figure 3.4. (a-c) SEM, (f) TEM, (e) HRTEM images, and (f) SAED pattern of the B-Co₂Fe LDH (g) TEM image of the B-Co₂Fe LDH and the EDX element mapping images.

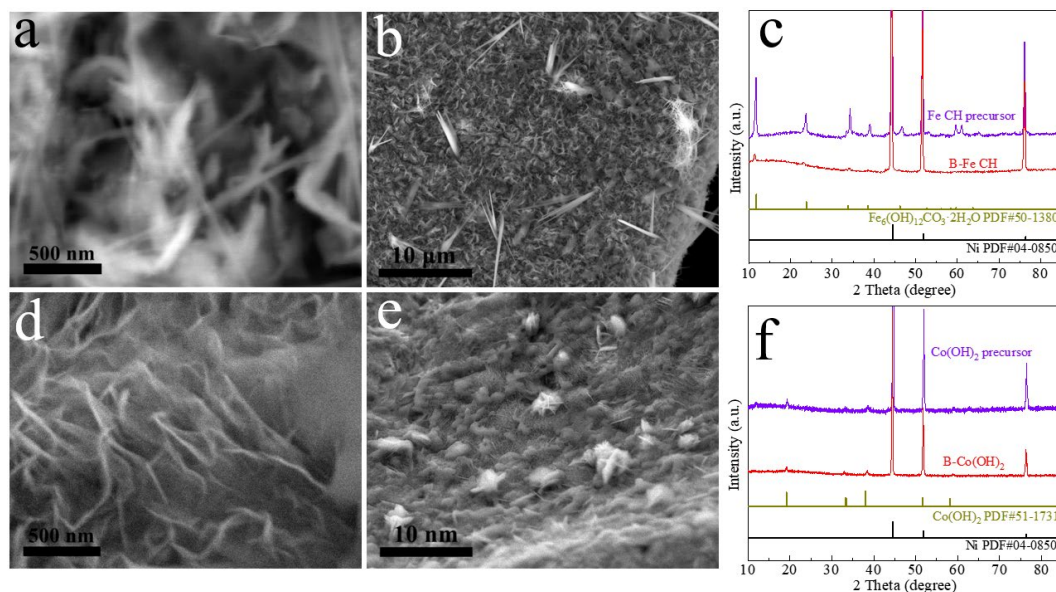


Figure 3.5. (a-b) SEM images of B-Co(OH)₂. (c) XRD patterns of the Fe CH precursor and B-Fe CH. (d-e) SEM images of B-Fe CH. (f) XRD patterns of the Co(OH)₂ precursor and B-Co(OH)₂.

The exact phase compositions and crystal structures of these samples were detected by X-ray diffraction (XRD). The resulting curve for the Co₂Fe LDH precursor in **Figure 3.6a** corresponds well to cobalt iron carbonate hydroxide (JCPDS#50-0235). Compared with that of the Co₂Fe LDH precursor, the lower intensity and broader half-width of the main diffraction peaks in the B-Co₂Fe LDH curve indicates that the modification by boron can decrease the crystallinity.^{96, 102, 106} This phenomenon can also be observed in the XRD patterns of B-Co(OH)₂ and B-Fe CH samples (**Figure 3.5c** and **3.5f**, respectively), in which the intensity of the main peaks for the boron-modified samples is lower than that for the initial precursors. A similar phenomenon, that the NaBH₄ solution can lower the crystallinity of the material being modified or even transform it to completely amorphous, has been previously reported.^{79, 96-97, 102, 106} To investigate the change of the valence states before and after the boron-modification, X-ray photoelectron spectroscopy (XPS) was

conducted. As shown in **Figure 3.6b**, in addition to a pair of satellite peaks, the high-resolution XPS spectra of Co 2p for the Co₂Fe LDH precursor can be deconvoluted to a Co²⁺ 2p_{3/2} peak at 781.3 eV and a Co²⁺ 2p_{1/2} peak at 796.7 eV.⁹² An additional peak for Co-B at 778.0 eV can be observed in both B-Co₂Fe LDH and B-Co(OH)₂, suggesting that the modification by boron could lead to the formation of a Co-B bond.⁹⁴ Similarly, a peak for Fe-B at 707.4 eV can be observed in the high-resolution XPS spectra of Fe for both the B-Co₂Fe LDH and B-Fe CH samples, in addition to the regular Fe³⁺ 2p_{3/2} and 2p_{1/2} peaks (**Figure 3.6c**). Both Co and Fe were positively shifted to higher oxidation states by the boron modification. As for the XPS spectra of B (**Figure 3.6d**), in addition to the huge oxidation peak for B-O at 192.0 eV, peaks for B-Co at 188.1 eV and B-Fe at 187.9 eV can be found in B-Co₂Fe LDH. These XPS results prove that the NaBH₄ solution can not only tune the structure and phase of Co₂Fe LDH, but can also react with it to form metallic boride.⁹⁵ As for the XPS spectra of O in **Figure 3.6e**, the peaks located at 529.3, 531.1, and 532.8 eV are assigned to oxygen-metal (O-M), hydroxide (O-H), and chemisorbed water on the surface (H₂O), respectively.^{71, 98} Additionally, an extra peak for O-B located at 533 eV can be found for each of the boron-modified catalysts. The asymmetric nature of the high energy hydroxide bond (O-H) in the XPS spectrum indicates the presence of oxygen vacancies, so the relative peak area ratio of O-H/O-M can be used to roughly assess the amount of oxygen defects.^{98, 107-108} **Figure 3.6e** clearly shows that the ratio of O-H/O-M in the B-Co₂Fe LDH is higher than that of the pristine Co₂Fe LDH precursor, confirming relatively more oxygen defects. Additionally, the stronger magnetic signal at around 3514 G for the B-Co₂Fe LDH catalyst, determined by

electron paramagnetic resonance (EPR) spectroscopy (**Figure 3.6f**) indicates a higher concentration of unpaired electrons, which generally results from oxygen defects.^{97, 109} Thus, both XPS and EPR data prove that more oxygen defects were created by boron modification.

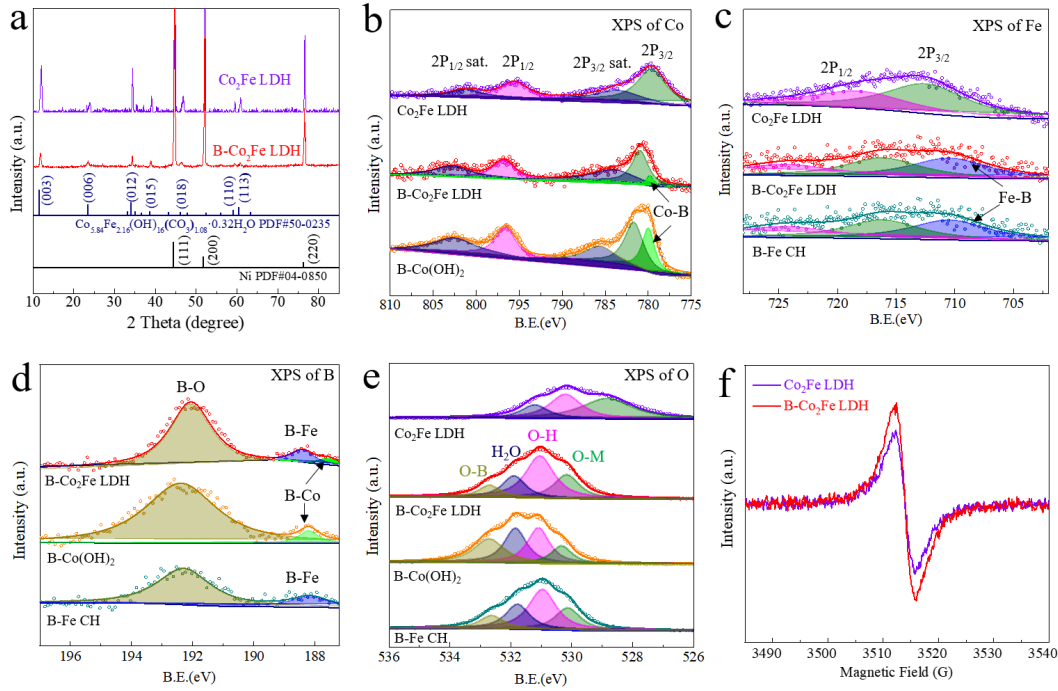


Figure 3.6. (a) XRD patterns of the Co_2Fe LDH and $\text{B-Co}_2\text{Fe}$ LDH. High-resolution XPS spectra of (b) Co, (c) Fe, (d) B, and (e) O for these catalysts. (f) EPR spectra of Co_2Fe LDH and $\text{B-Co}_2\text{Fe}$ LDH.

3.3.2 OER Performance in Alkaline Freshwater

The OER activity of these catalysts was evaluated in three types of electrolytes (1 M KOH, 1 M KOH + 0.5 M NaCl, and 1 M KOH seawater), respectively. To avoid the oxidation peak and precisely measure the overpotential at small current density, all polarization curves for these catalysts were collected from high to low potential with a scan rate of 2 mV s^{-1} . As shown in **Figure 3.7a**, the optimal partially amorphous $\text{B-Co}_2\text{Fe}$ LDH catalyst requires overpotentials of only 205, 246, 289, and 309 mV to attain current densities of 10, 100, 500, and $1,000 \text{ mA cm}^{-2}$, respectively, in 1 M KOH,

superior to that of boron-modified single-metallic hydroxide catalysts [B-Co(OH)₂ and B-Fe CH], the pristine bimetallic LDH catalyst (Co₂Fe LDH), and the benchmark noble-metal-based catalyst (IrO₂). There is no peeled-off catalyst can be observed even with vigorous O₂ bubbles released from the surface of the catalyst, demonstrating excellent structure stability at high current densities. The Tafel slope value of partially amorphous B-Co₂Fe LDH is only 39.2 mV dec⁻¹ (**Figure 3.7b**), which is the lowest among all of these catalysts and indicates a higher transfer coefficient and enhanced electrocatalytic kinetics. Such low overpotentials ($\eta_{10} = 205$ mV and $\eta_{100} = 246$ mV, where η_{10} and η_{100} are the overpotentials required to achieve current densities of 10 and 100 mA cm⁻², respectively) together with a small Tafel slope (39.2 mV dec⁻¹) place the B-Co₂Fe LDH catalyst among the best documented self-supported catalysts reported thus far. The modification by boron can significantly enhance the conductivity of these catalysts as revealed by the electrochemical impedance spectroscopy (EIS) analysis in **Figure 3.7c**. Based on the equivalent circuit (inset, **Figure 3.7c**), the charge-transfer resistance (R_{ct}) values of partially amorphous B-Co₂Fe LDH, B-Co(OH)₂, and B-Fe CH were measured to be ~1.3, ~3.0, and ~1.9 Ω , respectively, much smaller than those of the Co₂Fe LDH precursor (~11.7 Ω) and IrO₂ (~16.4 Ω). The electrochemically active surface area (ECSA) of each catalyst, which is proportional to its double-layer capacitance (C_{dl}) shown in **Figure 3.8** can be used to evaluate the catalyst's intrinsic surface-area activity. As shown in **Figure 3.7d**, the ECSA of B-Co₂Fe LDH (202.5 cm⁻²_{ECSA}) is larger than that of the Co₂Fe LDH precursor (140 cm⁻²_{ECSA}), which is due to the greater number of oxygen defects and the partial amorphousness feature created through the modification by boron. We

further normalized current density by the ECSA (**Figure 3.7e**) and the B-Co₂Fe LDH catalyst still exhibited the best OER activity, indicating its highest intrinsic catalytic activity among these catalysts. Furthermore, the turnover frequency (TOF) value of the B-Co₂Fe LDH catalyst at the potential of 1.50 V vs. RHE ($\eta = 270$ mV) is calculated to be 0.065 s⁻¹ (**Figure 3.7f**), which is much higher than that of B-Co(OH)₂ (0.0089 s⁻¹), B-Fe CH (0.026 s⁻¹), and the pristine Co₂Fe LDH precursor (0.023 s⁻¹), indicating its highest instantaneous efficiency for OER.

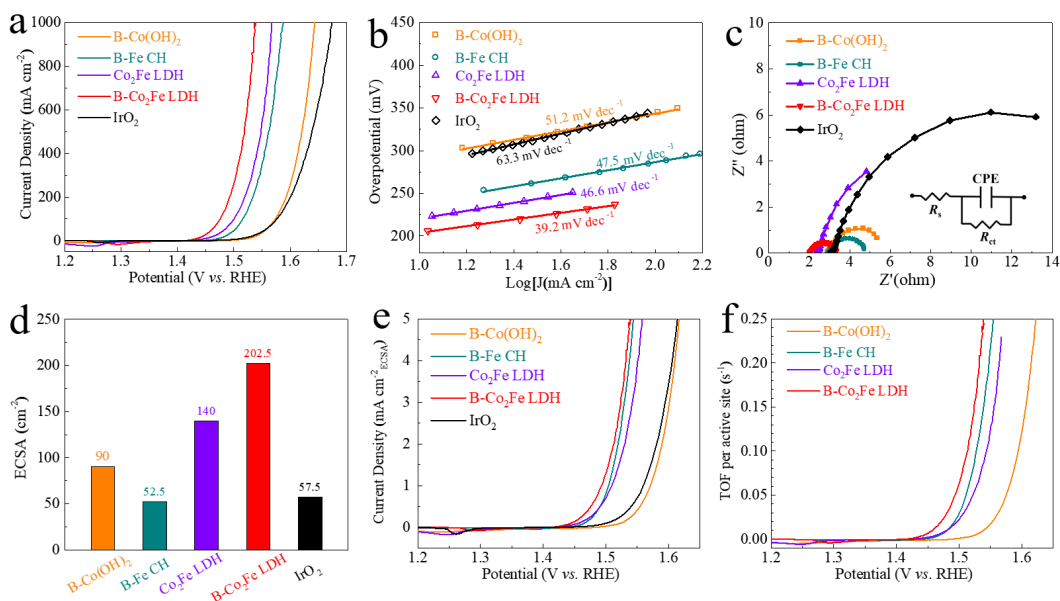


Figure 3.7. (a) OER polarization curves and (b) Tafel plots of as-prepared catalysts in 1 M KOH. (c) Nyquist plots, (d) ECSA, and (e) ECSA-normalized OER activity, and (f) TOF curves of these catalysts.

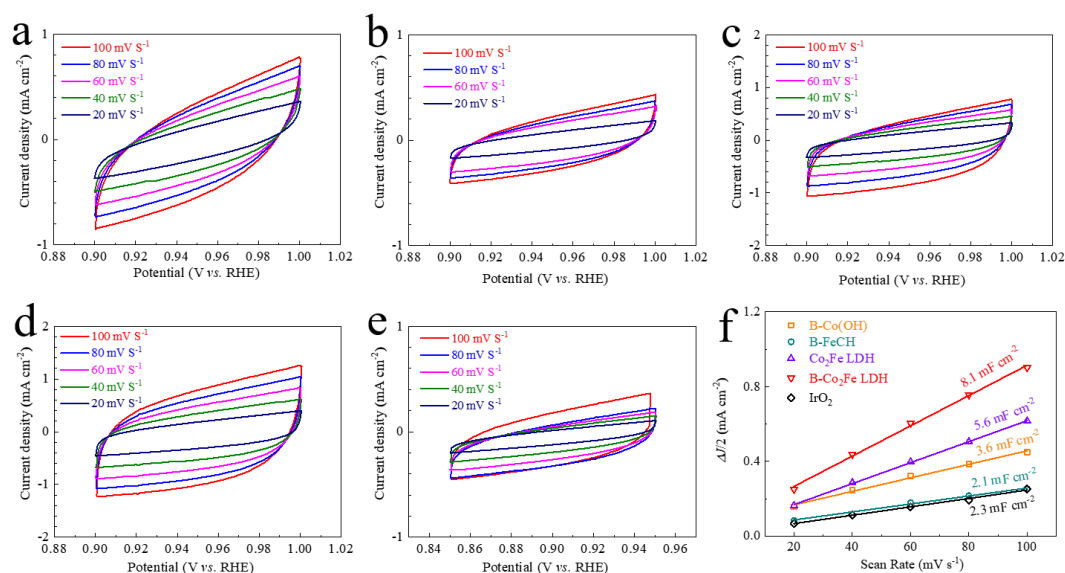


Figure 3.8. CV curves of (a) B-Co(OH)₂, (b) B-Fe CH, (c) Co₂Fe LDH, (d) B-Co₂Fe LDH, and (e) IrO₂ in a non-faradaic region. (f) C_{dl} values of these catalysts calculated from (a-e).

3.3.3 OER Performance in Alkaline Seawater

The corrosion resistance performance of B-Co₂Fe LDH catalyst in natural seawater was first roughly evaluated using long-term immersion testing. As shown in **Figure 3.9a-c** no obvious corrosion pitting or structural collapse can be found at different magnification levels after immersion in natural seawater for 28 days, indicating excellent structure stability. We then conducted corrosion testing of Co₂Fe LDH and B-Co₂Fe LDH catalysts in natural seawater, and the corresponding data are displayed in **Figure 3.9d-f**. The corrosion current density of B-Co₂Fe LDH is merely 1.38 μA cm⁻², which is around half of that of Co₂Fe LDH (2.4 μA cm⁻²), showing its higher corrosion resistance after boron modification. The excellent structure stability and the high corrosion resistance indicate that this partially amorphous B-Co₂Fe LDH has a high probability to be a stable catalyst for seawater oxidation. As mentioned above, the most critical challenge for alkaline seawater electrolysis is the formation of

hypochlorite, which will compete with OER and severely lower the efficiency of seawater oxidation. This B-Co₂Fe LDH catalyst requires an overpotential of 309 mV to drive a large current density of 1,000 mA cm⁻² in 1 M KOH, much lower than the maximum theoretical value of ~480 mV for avoiding the formation of hypochlorite. We then measured the OER activity of all these as-prepared catalysts in both alkaline saline (1 M KOH in 0.5 M NaCl water, simulated seawater electrolyte) and alkaline seawater (1 M KOH seawater). As shown in **Figure 3.10a** and **3.10c**, all five catalysts show a slight decline in OER activity when tested in alkaline saline water than in pure water due to the blockage of active sites by the Cl⁻. This decline greatly increased when the catalysts were tested under the actual seawater condition (**Figure 3.10b-c**), which has a much more complicated composition, such as including alkaline metal cations (Ca²⁺, Mg²⁺, Na⁺, K⁺) chloride ions (Cl⁻), sulfate ions (SO₄²⁻), and insoluble precipitates. Specifically, the B-Co₂Fe LDH catalyst requires overpotentials of 245, 310, 376, and 415 mV to drive current densities of 10, 100, 500, and 1,000 mA cm⁻², respectively, in 1 M KOH seawater. The Tafel slope values of these catalysts in different electrolytes shown in **Figure 3.10d-f** also indicate that their catalytic kinetics and transfer coefficient values are slightly and severely lowered in saline and natural seawater, respectively. Even though the Co₂Fe LDH precursor shows the second-best OER activity among these catalysts in 1 M KOH, its performance declined more heavily than that of the boron-modified ones when tested in alkaline seawater. This proves that the modification by boron, which can enhance a catalyst's conductivity and enlarge its ECSA, contributes significantly to maintaining catalytic activity in the critical seawater electrolyte.

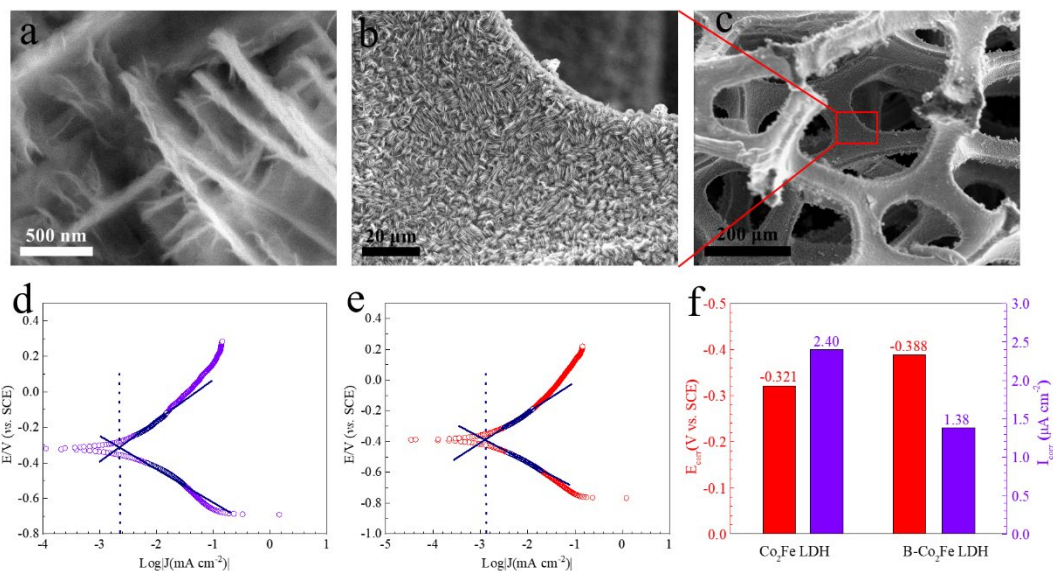


Figure 3.9. (a-c) SEM images of B- Co_2Fe LDH after immersion in natural seawater. Corrosion polarization curves of (d) Co_2Fe LDH and (e) B- Co_2Fe LDH. (f) Corrosion potentials and corrosion current densities of these catalysts.

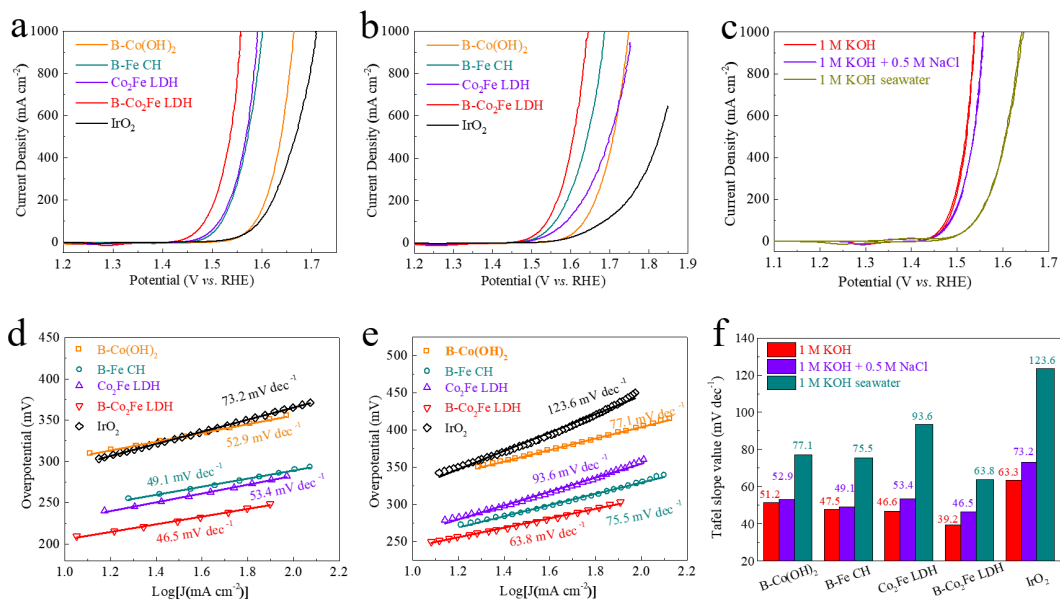


Figure 3.10. OER polarization curves of these catalysts in (a) 1 M KOH + 0.5 M NaCl and (b) 1 M KOH seawater. (c) OER CV curves of B- Co_2Fe LDH catalyst. (d) and (e) Tafel plots. (f) Comparison of the Tafel slope values.

The faradaic efficiency of B- Co_2Fe LDH was measured by a gas chromatography (GC) test performed at a current density of 500 mA cm^{-2} in 1 M KOH seawater to identify whether this catalyst can work efficiently for seawater oxidation. As shown in

Figure 3.11a, the amount of measured O₂ gas matches well with the theoretical values, showing a nearly 100% faradaic efficiency. *in situ* Raman testing was then performed to reveal the transformation of this catalyst during OER. As shown in **Figure 3.11b**, the peaks corresponding to the -LDH system (at around 431 and 508 cm⁻¹) gradually changed to the -OOH system (at around 459 and 531 cm⁻¹) while the peaks corresponding to the B-O bond (at around 263 and 708 cm⁻¹) gradually disappeared with the application of higher oxidation potential.¹¹⁰⁻¹¹² *ex situ* Raman spectra of the catalyst displayed in **Figure 3.11c** show more obvious -OOH peaks without the interference of the electrolyte liquid and the O₂ bubbles. These results indicate that the gradually formed Co-/Fe- (oxy)hydroxide, which have the optimized adsorption/desorption ability of intermediates (O*, OH*, and OOH*),¹¹³ are the active sites of B-Co₂Fe LDH for OER. The corresponding XPS spectra of B-Co₂Fe LDH after 2,000 CV scans in 1 M KOH seawater (**Figure 3.11d-g**) show that the specific peak for B almost disappeared, indicating that boron in this case serves more as a modifier to the crystallinity of Co₂Fe LDH than to form a metallic boride catalyst (either Fe-B or Co-B). Both Co and Fe were oxidized to higher oxidation states corresponding to Co-/Fe-OOH, as shown by the slight shifts in their XPS spectra in **Figure 3.11d-e**, respectively. The increased intensity of the specific peak for O in **Figure 3.11g** proves the formation of -OOH during CV cycling, matching the Raman result (**Figure 3.11c**).

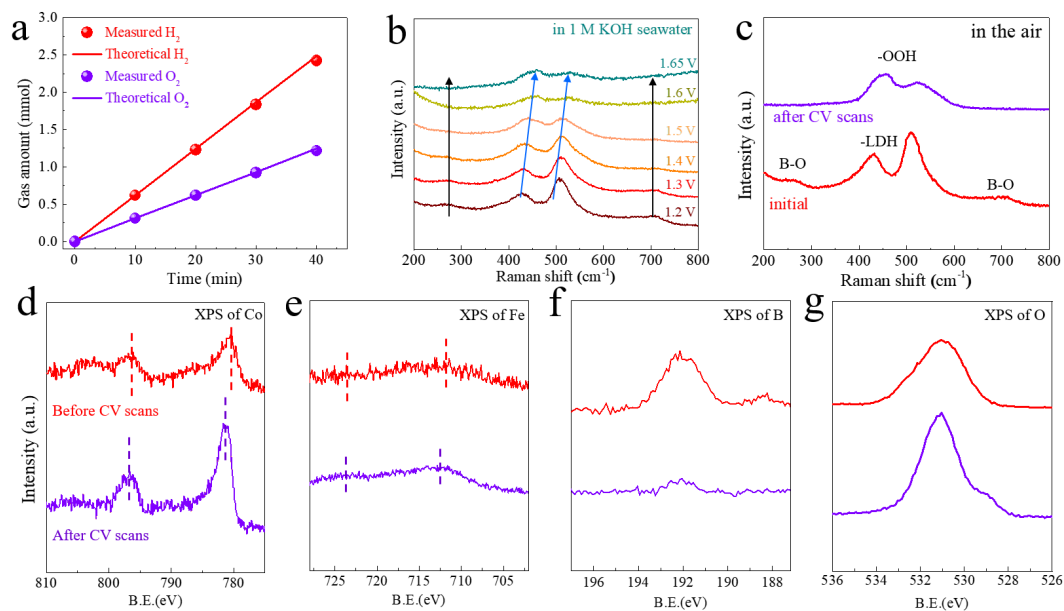


Figure 3.11. (a) Gaseous products from B-Co₂Fe LDH in 1 M KOH seawater. (b) *in situ* and (c) *ex situ* Raman spectra of B-Co₂Fe LDH. XPS spectra of (d) Co, (e) Fe, (f) B, and (g) O in B-Co₂Fe LDH before and after CV scans.

Catalytic durability is another important criterion for the practical application of a catalyst. The almost overlapping polarization curves before and after 2,000 cyclic voltammetry CV scans in 1 M KOH (**Figure 3.12a**) and the well-maintained hierarchical structure after CV scanning (**Figure 3.12b-d**) prove that this B-Co₂Fe LDH catalyst has excellent catalytic durability and structural stability in alkaline freshwater. When cycled in 1 M KOH seawater, the resultant polarization curve shows some decline compared with the initial curve (**Figure 3.13a**). SEM images of the post-cycling catalyst (**Figure 3.13b-d**) show that even though some cracks and insoluble precipitates can be observed on the macro scale, the overall hierarchical nanosheet-nanoflake structure is maintained on the micro scale, confirming the good chlorine corrosion resistance of the partially amorphous B-Co₂Fe LDH catalyst. Some common metal elements such as Mg and Ca in the natural seawater can be clearly observed in the corresponding EDS spectrum in **Figure 3.13e**. The well-maintained hierarchical

structure and the partially amorphous phase feature were also confirmed by TEM and HRTEM images obtained after CV scanning and shown in **Figure 3.13f-g** and **3.13h**, respectively. This result reveals that even though some portions of the surface of this catalyst become covered by the precipitates, the underlying or side parts of the catalyst can remain in contact with, and react with, the electrolyte to allow the seawater electrolysis to continue. Such a hierarchical nanosheet-nanoflake structure feature, which provides large surface area to expose active sites, is more important in seawater electrolysis due to the existence of insoluble precipitates.

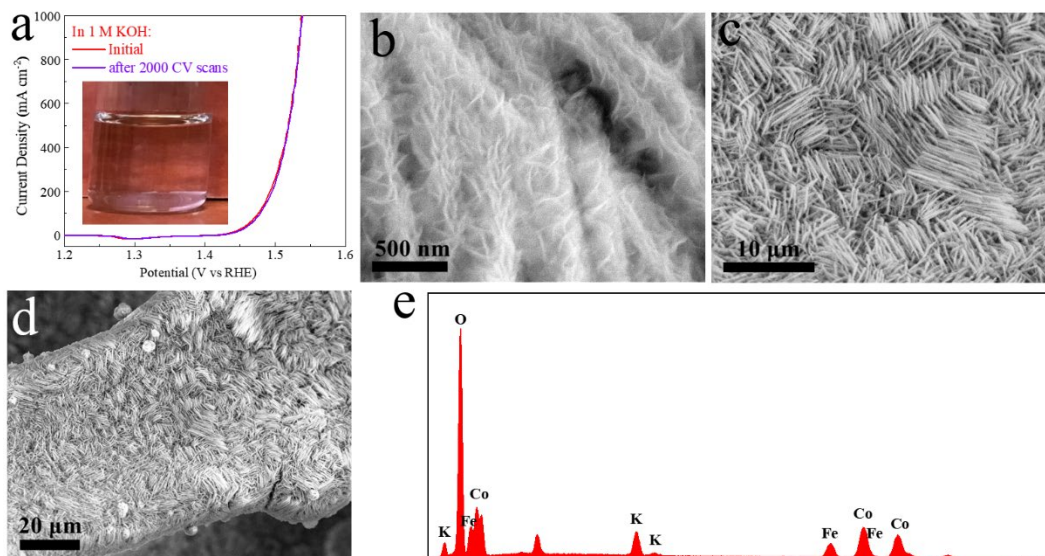


Figure 3.12. (a) OER polarization curves of B-Co₂Fe LDH before and after CV scans in 1 M KOH. Insert to (a): digital image of 1 M KOH. (b-d) SEM images and (e) EDS spectrum of B-Co₂Fe LDH after CV scans in 1 M KOH.

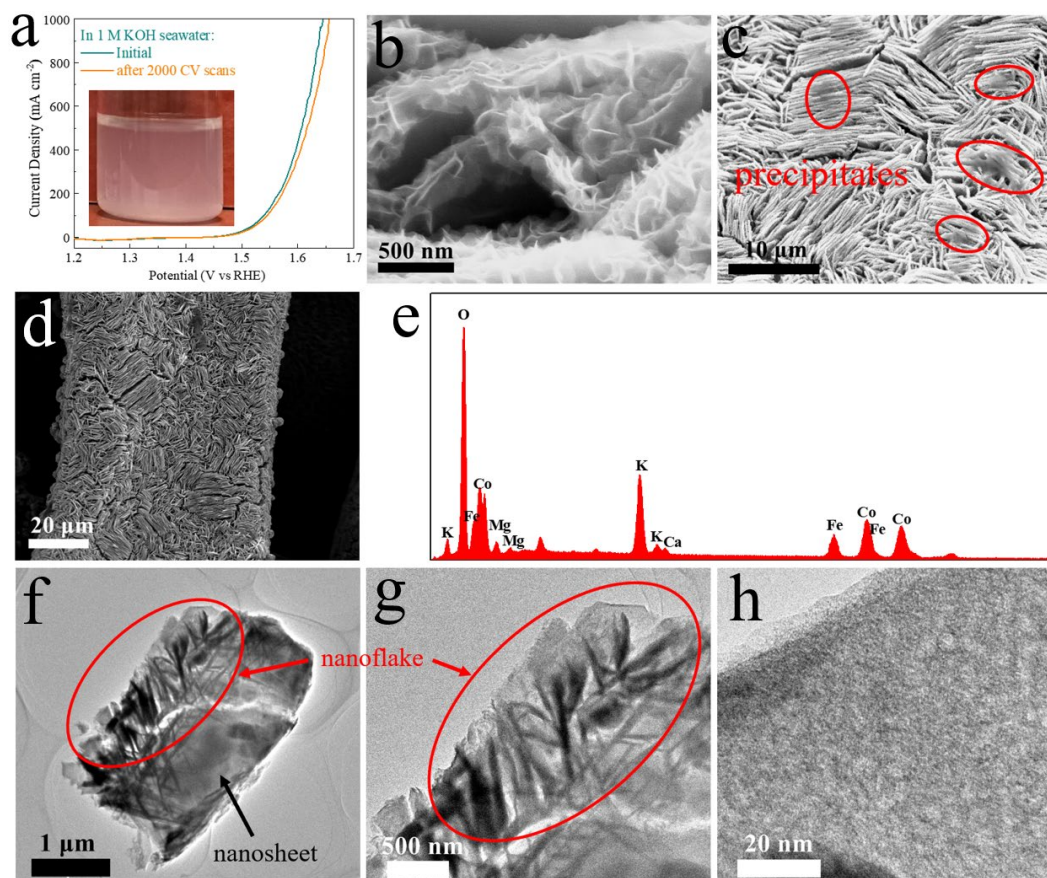


Figure 3.13. (a) OER polarization curves of B-Co₂Fe LDH before and after CV scans in 1 M KOH seawater. (b-d) SEM images, (e) EDS spectrum, and (f-h) TEM images of B-Co₂Fe LDH after CV scans in 1 M KOH seawater.

The durability of the B-Co₂Fe LDH catalyst was then determined by chronopotentiometric measurements performed at industrial-scale densities of 100 and 500 mA cm⁻² in both 1 M KOH and 1 M KOH seawater electrolytes. As shown in **Figure 3.14a**, the potential fluctuations at current densities of 100 and 500 mA cm⁻² over 100 h continuous testing in 1 M KOH are only 22 and 37 mV, respectively. In 1 M KOH seawater (**Figure 3.12b**), this catalyst can still work over such long-term testing with only slight increases in the potential fluctuations (46 and 65 mV for 100 and 500 mA cm⁻², respectively), showing great potential for practical fuel gas production from natural seawater at industrial-scale current densities. The poorer

catalytic activity in seawater is mainly due to obstruction of active sites by chlorine ions and surface poisoning by insoluble precipitates, which has also been discussed in previous studies.^{10, 17-18, 23, 114} Additionally, the possible existence of hypochlorite products in the 1 M KOH seawater electrolyte after long-term stability testing was determined using a colorimetric reagent. As shown in **Figure 3.14c**, there is no color change in the reagent after OER stability testing of B-Co₂Fe LDH at 500 mA cm⁻² for 100 h, indicating that no hypochlorite was formed during OER stability testing, which matches well with the GC test result shown in **Figure 3.11a** (nearly 100% seawater oxidation efficiency).

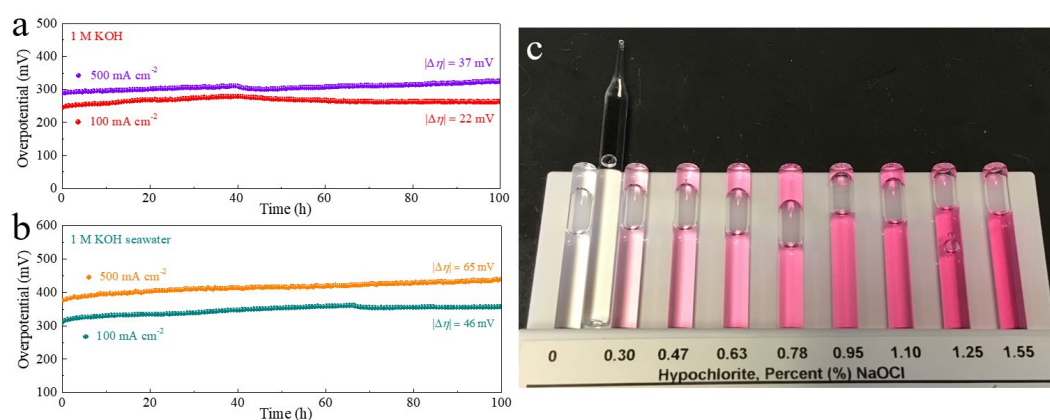


Figure 3.14. Chronopotentiometric curves of B-Co₂Fe LDH in (a) 1 M KOH and (b) 1 M KOH seawater. (c) Colorimetric reagent testing result for hypochlorite production in the 1 M KOH seawater electrolyte.

3.3.4 Discussion

A tremendous amount of research on LDH-based catalysts has been reported in the last few years, most of which has focused on doping or coupling with other compounds to enhance the catalytic performance, while structure modeling and crystallinity tuning have been less studied. Here, to overcome the drawbacks of LDH catalysts, such as poor conductivity and limited active sites, a novel and scalable

strategy was developed to synthesize partially amorphous B-Co₂Fe LDH with a hierarchical nanosheet-nanoflake structure. First, the direct growth of the B-Co₂Fe LDH catalyst on conductive NF can enhance the transportation of electrons and stabilize the structure, while the hierarchical structure can provide a large surface area to rivet and disperse the active sites. The self-supported and hydrophilic characteristics of the B-Co₂Fe LDH catalyst can provide adequate space for the diffusion of the electrolyte and accelerate the release of the bubbles, ensuring superior OER catalytic activity and long-term stability at high current density. Second, in the modification step, NaBH₄ serves as both the boron source and the reduction reactant, which can not only react with the metallic cations to form metallic boride but also creates a great number of oxygen defects by extracting the oxygen and tuning the Co₂Fe LDH precursor into a partially amorphous phase.^{97, 104, 106} Additionally, the defective interfaces located in the crystalline-amorphous phase boundaries can act as active sites while the amorphous phase can enhance the amount of adsorption sites for hydroxide. The modification by boron can also enhance the intrinsic catalytic kinetics and enlarge the ECSA of partially amorphous B-Co₂Fe LDH, which together lead to superior OER catalytic activity in both fresh water and seawater. Finally, the enhanced stability and corrosion resistance of B-Co₂Fe LDH, which result from its partial amorphousness feature, help it maintain both the hierarchical nanosheet-nanoflake structure and catalytic durability well in the critical seawater condition.^{93, 95}

3.4 Conclusion

We have successfully synthesized a partially amorphous B-Co₂Fe LDH catalyst using a two-step water bath reaction-chemical reduction approach. Its hierarchical

nanosheet-nanoflake structure, along with its hydrophilic feature, help it possess abundant active sites and accelerated bubble-release ability, producing favorable synergistic effects for seawater electrolysis. It also has higher intrinsic catalytic kinetics, a larger ECSA, and an improved TOF, as compared with the Co₂Fe LDH precursor, resulting from the modification by boron. *in situ* Raman testing and post-OER analysis were applied to reveal its chemical and physical transformation during OER. Therefore, our work not only introduces and analyzes an OER catalyst for highly selective and stable seawater oxidation, but also provides a novel approach toward the fabrication of partially amorphous boron-modified LDH-based catalysts.

CHAPTER 4 RATIONAL DESIGN OF CORE-SHELL- STRUCTURED $\text{CoP}_x@FeOOH$ FOR SEAWATER ELECTROLYSIS

Note: The material in this chapter has been published. The introduction, experimental section, and figure captions were adjusted for dissertation consistency. Reproduced with permission from Elsevier.¹¹⁵

4.1 Introduction

Iron oxyhydroxide ($FeOOH$), in which the oxyhydroxide species are considered to be the active species for OER,¹¹⁶⁻¹¹⁷ is a type of alkaline water oxidation catalyst. $FeOOH$ -based catalysts such as amorphous $FeOOH$,¹¹⁸ $(Ni,Fe)OOH$,⁹ $FeOOH(Se)$,¹¹⁹ $Ni_3S_2@MoS_2/FeOOH$,¹²⁰ $S-(Ni,Fe)OOH$,¹²¹ and $Ni-FeOOH@NiFe$ alloy¹²² have been demonstrated to be efficient OER or bifunctional catalysts. However, pure-phase $FeOOH$ still suffers from deficiencies like low conductivity, limited active sites, and excessively strong absorption energy to OER intermediates, all of which hinder their application in practical hydrogen production.^{52, 119, 123} On the other hand, the self-supported cobalt-phosphide catalyst has features like tunable structure, excellent conductivity, and high thermal stability, making it a suitable HER catalyst for seawater electrolysis.^{4, 40, 124-125}

Here, we employ heterogeneous cobalt phosphide (CoP_x , $CoP-CoP_2$) as the core to construct core-shell-structured $CoP_x@FeOOH$ as an efficient OER catalyst for seawater oxidation. Beyond their simple physical mixture, the combination of the highly conductive CoP_x core and the OER-active $FeOOH$ shell generates excellent synergistic effects such as high conductivity, large surface area, and improved

turnover frequency. Insight analysis reveals that the negatively charged CoP_x core can moderate the absorption energy between the oxyhydroxide active species and the OER intermediates to achieve very good intrinsic catalytic activity. Additionally, its micron-scale mesh structure and hydrophilic surface equip this $\text{CoP}_x@FeOOH$ catalyst with sufficient mechanical strength and high mass transfer efficiency at high current density. The catalyst's enhanced chloride corrosion resistance and chemical stability, which originate from the thermodynamically stable CoP_x core, help it work well in seawater. Specifically, it requires overpotentials of only 235, 283, and 337 mV to attain current densities of 10, 100, and 500 mA cm^{-2} , respectively, in 1 M KOH seawater electrolyte. It can sustain 80 h of continuous testing at current densities of 100 and 500 mA cm^{-2} in alkaline seawater without forming any hypochlorite. When coupled with the HER-active CoP_x core, the $\text{CoP}_x||\text{CoP}_x@FeOOH$ pair requires low voltages of 1.710 and 1.867 V to attain current densities of 100 and 500 mA cm^{-2} , respectively, with a high Faradaic efficiency and long-term catalytic durability. In general, this work demonstrates a novel strategy for the design and preparation of promising catalysts for efficient seawater electrolysis.

4.2 Experimental Section

4.2.1 Synthesis of Catalysts

4.2.1.1 Synthesis of Co(OH)_2 Nanowire Mesh

Co(OH)_2 nanowire mesh was *in situ* grown on commercial nickel foam (NF) using a modified hydrothermal reaction based on previous reports.^{40, 126} Briefly, 2 mmol cobalt nitrate hexahydrate [$\text{Co(NO}_3)_2 \cdot 6\text{H}_2\text{O}$, Sigma Aldrich], 10 mmol urea [$\text{CO(NH}_2)_2$, Promega Corporation], and 5 mmol ammonium fluoride (NH_4F , Alfa

Aesar) were dissolved homogeneously in 60 mL deionized (DI) water. After stirring for 15 min, the mixed solution and a clean piece of NF (3 cm × 3.5 cm) were put into a 100 mL Teflon-lined stainless steel autoclave, which was then transferred to an oven maintained at 120 °C for 6 h. After cooling down to room temperature, the sample was removed from the autoclave and rinsed several times with DI water. The loading mass of the active material was measured to be 2.21 mg cm⁻².

4.2.1.2 Synthesis of CoP_x Nanowire Mesh

To synthesize CoP_x nanowire mesh, 500 mg sodium hypophosphite monohydrate (NaH₂PO₂·H₂O, Alfa Aesar) was placed upstream in a tube as the phosphorous source. The as-prepared Co(OH)₂ precursor was placed at the center of the tube, followed by phosphidation at 400 °C for 2 h under flowing argon. The product was denoted CoP_x and the loading mass was measured to be 2.28 mg cm⁻².

4.2.1.3 Synthesis of Core-shell-structured CoP_x@FeOOH

To construct the core-shell-structured CoP_x@FeOOH, FeOOH was electrodeposited on CoP_x in a three-electrode configuration, in which the CoP_x, a platinum plate, and a saturated calomel electrode (SCE) were used as the working, counter, and reference electrodes, respectively. The electrodeposition electrolyte was prepared by dissolving 15 mmol iron sulfate heptahydrate (FeSO₄·7H₂O, Sigma Aldrich) in 50 mL DI water under a continuous argon flow to prevent the oxidation of Fe²⁺. The electrodeposition parameter was set as -1.0 V vs. SCE for 2 min to synthesize the optimal CoP_x@FeOOH sample. The loading mass of active material (FeOOH shell) was measured to be 1.82 mg cm⁻².

Pristine FeOOH was electrodeposited directly on NF (donated FeOOH) using the same electrodeposition procedure, and its loading mass was measured to be 1.33 mg cm⁻². CoP_x@CoOOH (CoOOH) and CoP_x@NiOOH (NiOOH) were synthesized using the same procedure except for replacing the iron sulfate heptahydrate with cobalt nitrate hexahydrate [Co(NO₃)₂·6H₂O, Sigma Aldrich] and nickel nitrate hexahydrate [Ni(NO₃)₂·6H₂O, Sigma Aldrich], respectively, in the electrodeposition step.

4.2.1.4 Preparation of IrO₂ and Pt/C Electrodes

To prepare the IrO₂ and Pt/C electrodes, 40 mg active material (either iridium oxide or platinum on carbon) was uniformly dispersed in a mixture solution containing 90 μL Nafion solution, 810 μL ethanol, and 600 μL DI water with the assistance of intense ultrasonication. A clean piece of NF was then soaked in the solution for 1 h to let the active material coat the surface, followed by drying in air.

4.2.2 Physical and Chemical Characterization

X-ray diffraction (XRD, PANalytical X'pert PRO, Cu K α radiation) was employed to identify the crystal structure and chemical composition of these as-prepared samples. X-ray photoelectron spectroscopy (XPS, PHI Quantera) was conducted to identify the valence states of the elements. Raman tests were conducted on a Horiba iHR320 Raman spectrometer using a He-Ne laser (excitation wavelength: 532 nm). Morphology characterization and energy-dispersive spectroscopy (EDS) analysis were performed using scanning electron microscopy (SEM, LEO 1525) and transmission electron microscopy (TEM, JEOL 2010F). The wettability of pure NF, CoP_x, and CoP_x@FeOOH was tested by depositing seawater droplets onto the surface of each catalyst.

4.2.3 Electrochemical Characterization

The catalytic performance of these catalysts was evaluated on a Gamry Reference 600 electrochemical station using a three-electrode configuration in which a Pt plate and a carbon rod were used as the counter electrodes for OER and HER testing, respectively; a Hg/HgO electrode was used as the reference electrode; and each catalyst (the size of each active part in the electrolyte is 0.5-0.8 cm²) was used as the working electrode. After at least 100 cyclic voltammetry (CV) cycles were performed, the stable polarization curve was recorded with *iR* compensation in three types of electrolyte (1 M KOH, 1 M KOH + 0.5 M NaCl, and 1 M KOH seawater) at a scan rate of 2 mV s⁻¹. The recorded potential ($E_{\text{Hg/HgO}}$) was calibrated to the reversible hydrogen electrode (RHE) using the equation: $E_{\text{RHE}} = E_{\text{Hg/HgO}} + 0.098 + 0.0591 \times \text{pH}$. Electrochemical impedance spectroscopy (EIS) was performed at the overpotential of 300 mV for OER from 100 kHz to 0.01 Hz in 1 M KOH. For the OER durability test, 2,000 and 5,000 CV scans were performed between 1.075 and 1.525 V vs. RHE at a scan rate of 100 mV s⁻¹ and the corresponding polarization curves were recorded before and after the CV cycling. The chronopotentiometric measurements were recorded at the current densities of 100 and 500 mA cm⁻² in 1 M KOH and 1 M KOH seawater, respectively. Overall seawater/freshwater electrolysis were carried out in an H-type electrolyzer cell with CoP_x@FeOOH as the anodic electrode (0.5 cm²), CoP_x as the cathodic electrode (0.5 cm²), and an anion-exchange membrane (Fumasep, FAA-3-PK-130) as the separator. Natural seawater was collected from Galveston Bay, Texas, USA (29.364° N, 94.810° W), from which Mg and Ca salts were first mostly removed by adding 0.68 g Na₂CO₃ into 100 mL natural seawater before application.

Corrosion polarization curves were obtained on a SP-200 Biologic electrochemical station in untreated natural seawater using SCE as the reference electrode.

4.2.4 Calculation of TOF

The plots of current density for OER can be converted into turnover frequency (TOF) plots using the equation: $\text{TOF} = j \times A / (4 \times F \times n)$, in which j is the current density (A cm^{-2}), A is the active surface area of each electrode (cm^2), 4 represents a four-electron transfer process, F is the Faraday constant ($96485.3 \text{ C mol}^{-1}$), and n is the amount of active sites (mol), which can be roughly evaluated by the loading mass and the molecular weight of the active material.^{74, 126}

4.2.5 Calculation of Faradaic Efficiency

Faradaic efficiency (FE) testing was conducted using the drainage method at a constant current density of 500 mA cm^{-2} in 1 M KOH seawater. FE was calculated by the equation: $\text{FE} = V / [V_m \times i \times t / (n \times F)] \times 100\%$, in which V is the volume of the gas products (L), V_m is the standard molar volume at room temperature (24.4 L mol^{-1}), i is the current (A), t is the time (s), n is the number of electrons needed to form a molecule of gas products (4 for O_2 and 2 for H_2), and F is the Faraday constant.

4.3 Results and Discussion

4.3.1 Structural and Compositional Analysis Results

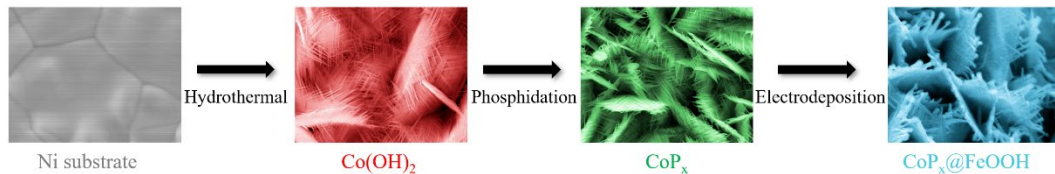


Figure 4.1. Schematic illustration of the synthesis of core-shell-structured $\text{CoP}_x@FeOOH$ via a three-step hydrothermal-phosphidation-electrodeposition procedure.

As schematically illustrated in **Figure 4.1**, the core-shell-structured $\text{CoP}_x@FeOOH$ catalyst was synthesized *via* a three-step hydrothermal-phosphidation-electrodeposition procedure. A self-supported Co(OH)_2 precursor was first *in situ* grown on conductive nickel foam (NF),^{40, 126} which was then phosphated into CoP_x to enhance its conductivity, chloride corrosion resistance, and HER activity. The scanning electron microscopy (SEM) images in **Figure 4.2a-d** show numerous micron-scale CoP_x nanowire meshes, which are composed of cross-linked nanowires that are tens of nanometers in diameter, vertically stand on the entire surface of the NF substrate. Corresponding energy-dispersive spectroscopy (EDS) mapping images in **Figure 4.2e-f** reveal that elemental Co and P are uniformly dispersed over the entire NF substrate, indicating a homogeneous and complete phosphidation. To characterize the structure of CoP_x in detail, transmission electron microscopy (TEM) analysis was performed. As shown in **Figure 4.2g-h**, the CoP_x nanowire meshes are consisted of linear smooth nanowires with diameters ranging from 70 to 100 nm. The interplanar spacings in the high-resolution TEM (HRTEM) images in **Figure 4.2i-j**, which are precisely measured to be 0.228 and 0.231 nm, respectively, correspond to the respective (210) plane of CoP_2 and the (201) plane of CoP , indicating that CoP_x is a mixture of heterogeneous cobalt phosphide (CoP-CoP_2).

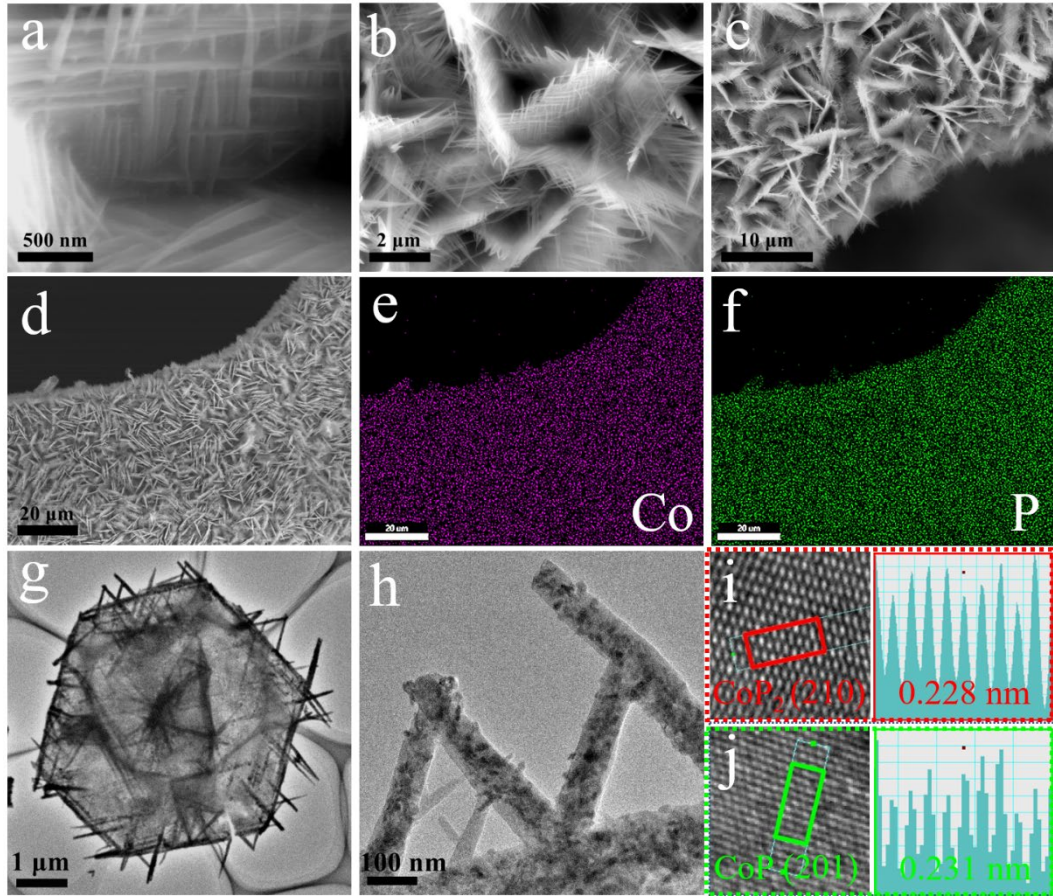


Figure 4.2. (a-d) SEM images of the CoP_x nanowire mesh. (e) Co and (f) P EDS mapping images corresponding to (d). (g-h) TEM, and (i-j) HRTEM images of CoP_x .

In the final step, an OER-active FeOOH shell was electrodeposited on the surface of the CoP_x core to construct the core-shell-structured $\text{CoP}_x@/\text{FeOOH}$. SEM images in **Figure 4.3a-e** and TEM image in **Figure 4.3f** clearly show that the CoP_x nanowire mesh core was completely covered by the porous FeOOH shell. An open-structured CoP_x core with a FeOOH shell of suitable thickness will be beneficial for reducing the charge-transfer resistance. The ring patterns from selected area electron diffraction (SAED) in **Figure 4.3g** reveal the characteristic (112) facet of CoP and the (104) and (315) facets of FeOOH . Distinctive lattice fringes with interplanar spacings of 0.241 nm, which is assigned to the (104) plane of FeOOH , can be measured in the shell part

in the HRTEM image shown in **Figure 4.3h**. The core-shell structure feature of the $\text{CoP}_x@FeOOH$ catalyst can also be confirmed by the energy-dispersive X-ray spectrometry (EDX) mapping images in **Figure 4.3i-m**, in which elemental Co and P (**Figure 4.3j-k**, respectively) can only be observed in the core, while elemental Fe and O (**Figure 4.3l-m**, respectively) can be observed over the entire selected area.

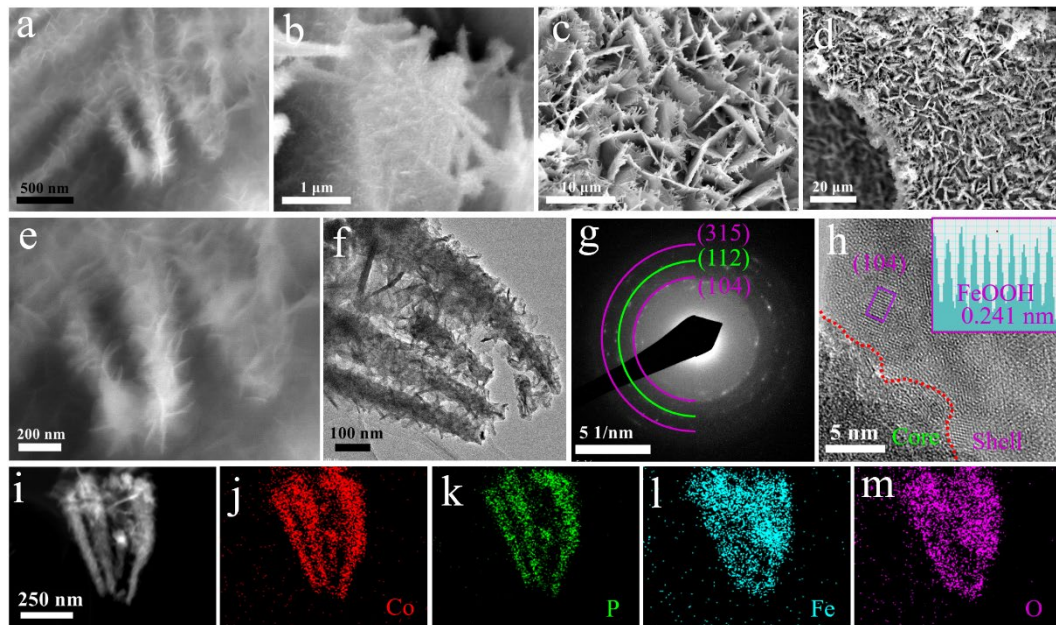


Figure 4.3. (a-e) SEM and (f) TEM images, (g) SAED pattern, and (h) HRTEM image of $\text{CoP}_x@FeOOH$. (i) TEM image of a $\text{CoP}_x@FeOOH$ mesh and the EDX element mapping for (j) Co, (k) P, (l) Fe, and (m) O.

Compared with the irregular film structure of pristine FeOOH (**Figure 4.4**), the hierarchical structure of $\text{CoP}_x@FeOOH$ can dramatically enlarge the surface area to expose more active sites during electrolysis, which is very important for achieving a high current density at a low overpotential. In addition, both CoP_x and $\text{CoP}_x@FeOOH$ catalysts exhibit a hydrophilic feature for seawater as demonstrated in **Figure 4.5a-c** and **Figure 4.5d-f**, respectively, in sharp contrast with the pure Ni foam, which exhibits a hydrophobic feature as demonstrated in **Figure 4.5g-i**. Some studies have

illustrated that a hydrophilic surface is helpful for fast electrolyte diffusion and easy gas bubble release, which will be of great benefit in maintaining catalytic durability at high current density.^{20, 127-128}

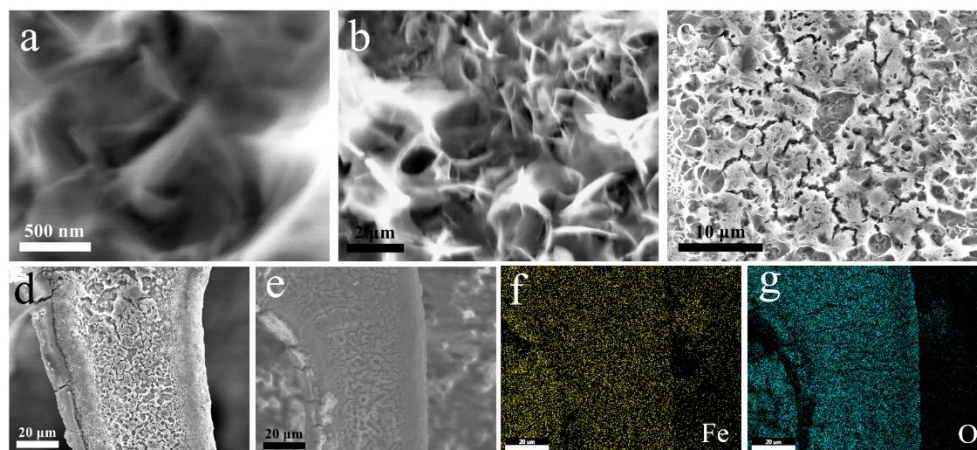


Figure 4.4. (a-e) SEM images of pristine FeOOH on NF. (f) Fe and (g) O EDS mapping images corresponding to (e).

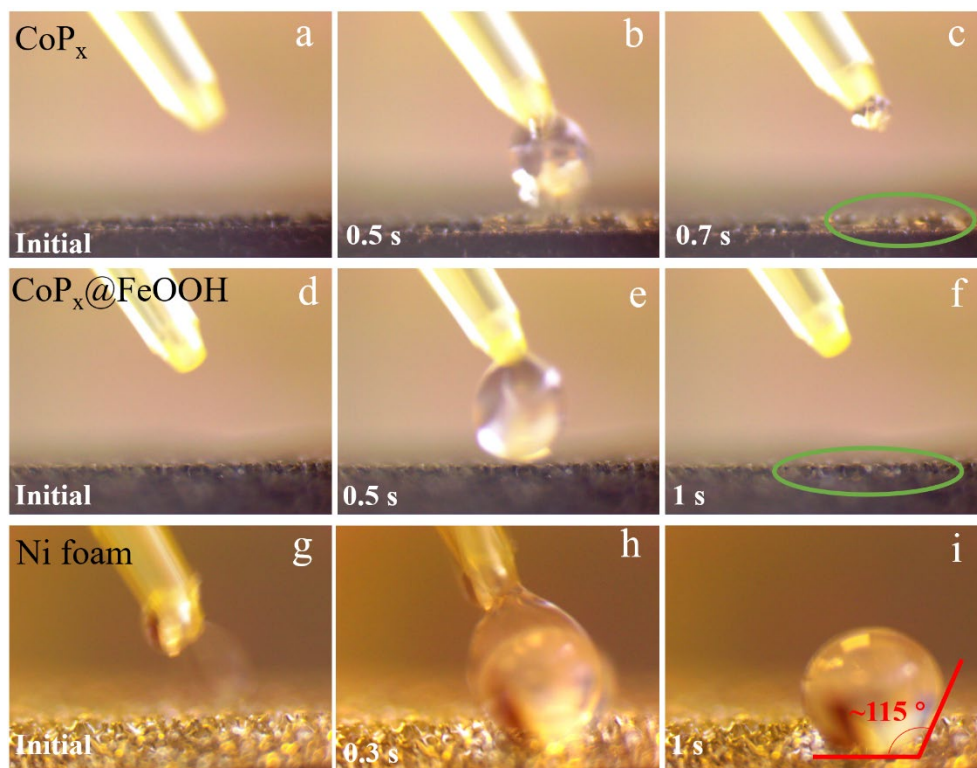


Figure 4.5. Digital images of a droplet of seawater placed on the surface of (a-c) CoP_x , (d-f) $\text{CoP}_x@FeOOH$, and (g-i) Ni foam to investigate their wettability.

The exact chemical compositions of these as-prepared catalysts were detected by X-ray diffraction (XRD) testing. As respectively shown in **Figure 4.6a** and **4.6b**, the XRD curves of the $\text{Co}(\text{OH})_2$ precursor and pristine FeOOH correspond to the standard PDF cards for cobalt hydroxide [$\text{Co}(\text{OH})_2$, JCPDS#50-0235] and iron oxyhydroxide (FeOOH , JCPDS#22-0353), respectively. The XRD pattern of CoP_x displayed in **Figure 4.6c** shows that it is a mixture of two kinds of cobalt phosphide (CoP , JCPDS#29-0497 and CoP_2 , JCPDS#22-0481), in good agreement with the HRTEM result. Besides the peaks for CoP and CoP_2 , some extra peaks corresponding to iron oxyhydroxide (FeOOH , JCPDS#22-0353) can be found in the XRD pattern of $\text{CoP}_x@FeOOH$ shown in **Figure 4.6c**.

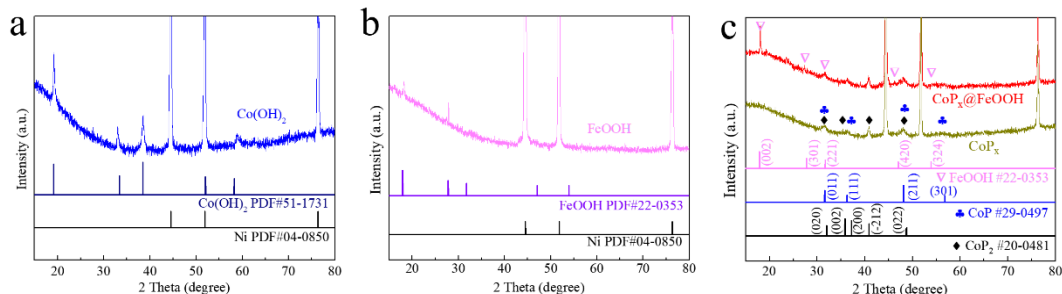


Figure 4.6. XRD patterns of (a) $\text{Co}(\text{OH})_2$, (b) FeOOH , and (c) CoP_x and $\text{CoP}_x@FeOOH$.

To verify the compositions of FeOOH and $\text{CoP}_x@FeOOH$ more accurately, Raman testing was then conducted and the corresponding results are shown in **Figure 4.7a**. Compared with the sharp peaks in the Raman spectrum of pristine FeOOH , the peaks corresponding to iron oxyhydroxide in that of $\text{CoP}_x@FeOOH$ are relatively lower in intensity due to the limited amount of iron oxyhydroxide on the shell.^{118, 122, 129-130} X-ray photoelectron spectroscopy (XPS) was further performed in order to investigate the valence states of the elements in these catalysts. As shown in **Figure**

4.7b, the high-resolution XPS spectra of Co 2p for CoP_x and CoP_x@FeOOH can be deconvoluted to a Co²⁺ 2p_{3/2} peak at 782.1 eV and a Co²⁺ 2p_{1/2} peak at 798.0 eV accompanied by a pair of satellite peaks.^{125, 131-132} A tiny metallic peak for Co at 777.8 eV can be observed in the XPS spectrum for CoP_x. As for the XPS spectra of P 2p (**Figure 4.7c**), in addition to a huge oxidation peak for P-O at 134.5 eV, which is mainly caused by the oxidation of the metallic phosphide when being exposed to the air, the peaks for P 2p_{3/2} at 128.3 eV and for P 2p_{1/2} at 129.8 eV can only be identified in the CoP_x sample. Due to the coverage by the FeOOH shell, the intensity of the Co and P peaks for CoP_x@FeOOH is relatively lower than that for CoP_x. The XPS spectra of Fe for CoP_x@FeOOH in **Figure 4.7d** exhibit peaks for Fe³⁺ 2p_{3/2} at 711.5 eV and Fe³⁺ 2p_{1/2} at 724.3 eV along with a satellite peak at 718.6 eV.¹²² Compared with those for pristine FeOOH, the Fe peaks for CoP_x@FeOOH are positively shifted to a higher oxidation state by ~0.3 eV.

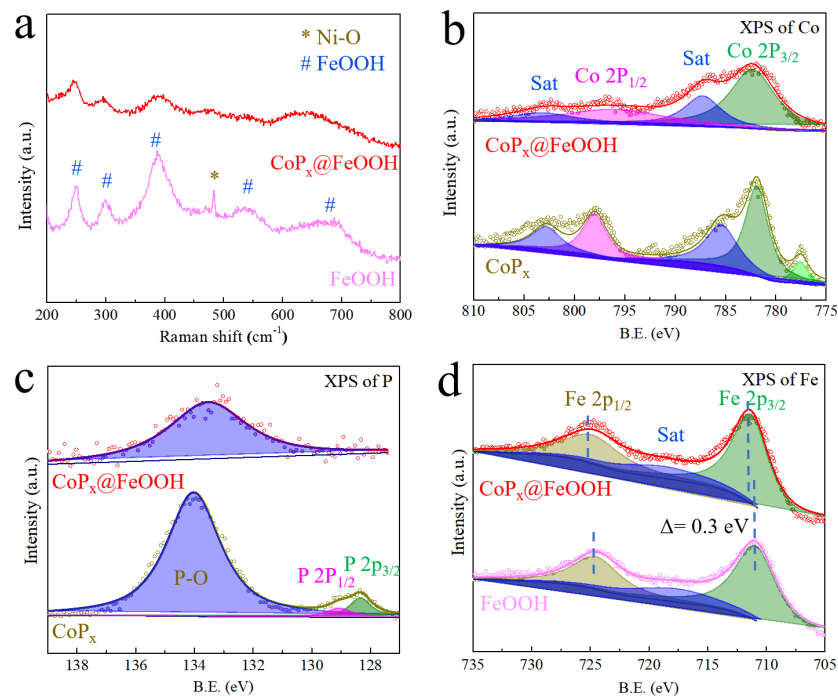


Figure 4.7. (a) Raman spectra of pristine FeOOH and CoP_x@FeOOH. High-resolution XPS spectra of (c) Co and (d) P in CoP_x and CoP_x@FeOOH and of (e) Fe in FeOOH and CoP_x@FeOOH.

4.3.2 Catalytic Performance of Synthesized Catalysts

4.3.2.1 OER Performance in Alkaline Freshwater and Seawater

These self-supported catalysts as well as the benchmark IrO₂ catalyst were then directly used as working electrodes in a standard three-electrode configuration to evaluate their catalytic performance. For OER testing, all polarization curves were collected from high to low potential at a scan rate of 2 mV s⁻¹ to avoid the oxidation-peak effect and to determine the overpotentials at small current densities precisely. As shown in **Figure 4.8a**, the CoP_x@FeOOH catalyst displays catalytic activity for freshwater oxidation superior to that of Co(OH)₂, CoP_x, FeOOH, and IrO₂, requiring overpotentials of 222, 254, 292, and 303 mV to attain current densities of 10, 100, 500, and 800 mA cm⁻², respectively, in 1 M KOH. Impressively, its Tafel slope value is calculated to be only 37.6 mV dec⁻¹ (**Figure 4.8b**), indicating a high transfer coefficient and rapid electrocatalytic kinetics. Notably, to attain current densities of 10 and 100 mA cm⁻², the second-best catalyst studied here, pristine FeOOH, requires overpotentials of 244 and 287 mV, respectively, lower than those for Co(OH)₂ (299 and 370 mV, respectively) and CoP_x (297 and 346 mV, respectively), demonstrating higher intrinsic OER catalytic activity among oxyhydroxide-based catalysts in comparison with hydroxide- and phosphide-based ones. To reveal the origin of the excellent catalytic activity of CoP_x@FeOOH, electrochemical impedance spectroscopy (EIS) and turnover frequency (TOF) analyses were conducted. Based on the equivalent circuit in the EIS analysis (**Figure 4.8c**),¹³³ the charge-transfer

resistance (R_{ct}) value of CoP_x is calculated to be $\sim 1.58 \Omega$, much smaller than that of the Co(OH)_2 precursor ($\sim 12.87 \Omega$), implying that phosphidation can dramatically enhance the charge transfer kinetics. Even coated by poorly conductive FeOOH , the R_{ct} value of $\text{CoP}_x@FeOOH$ only increases to $\sim 2.51 \Omega$, still lower than that of pristine FeOOH (5.13Ω), suggesting a remarkable enhancement in conductivity through the combination with the CoP_x core. In addition, the TOF value for $\text{CoP}_x@FeOOH$ at the potential of 1.52 V vs. RHE is calculated to be 0.059 s^{-1} (**Figure 4.8d**), which is around three times as high as that for pristine FeOOH (0.021 s^{-1}), showing a much higher instantaneous efficiency for OER catalysis. According to the theoretical calculations in previous reports, pure-phase FeOOH has excessively strong absorption ability toward the negatively charged OER intermediates (O^* , OH^* , and OOH^*), which hinders the dislocation of products.^{77, 134-135} It is reasonable that the negatively charged P atoms can repel these OER intermediates to reach an optimal absorption energy for the $\text{CoP}_x@FeOOH$ catalyst. This may explain why the core-shell-structured $\text{CoP}_x@FeOOH$ exhibits intrinsic catalytic activity that is much better than that of both pristine FeOOH and CoP_x , as revealed by the TOF analysis.

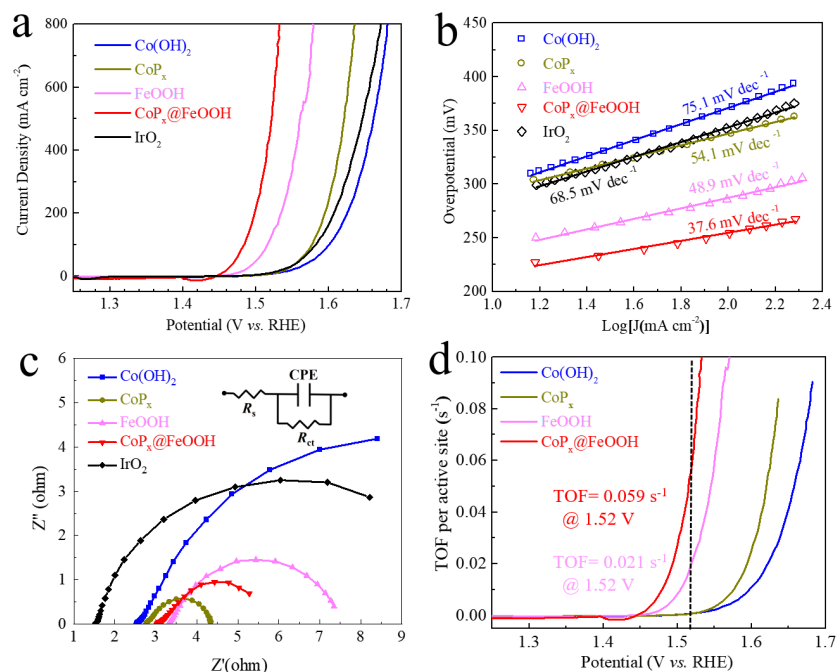


Figure 4.8. (a) OER polarization curves of $\text{Co}(\text{OH})_2$, CoP_x , FeOOH , $\text{CoP}_x@FeOOH$, and IrO_2 catalysts in 1 M KOH. (b) Tafel plots derived from (a). (c) Nyquist plots and (d) TOF slopes of these catalysts.

Considering the excellent OER catalytic activity of the $\text{CoP}_x@FeOOH$ catalyst in alkaline freshwater, we then evaluated its performance for seawater oxidation in both alkaline saline (1 M KOH in 0.5 M NaCl water, simulated seawater) and alkaline natural seawater (1 M KOH seawater). When measured in 1 M KOH seawater, the polarization curves in **Figure 4.9a** reveal that the $\text{CoP}_x@FeOOH$ catalyst requires overpotentials of 235, 283, 337, and 354 mV to attain current densities of 10, 100, 500, and 800 mA cm^{-2} , respectively, much lower than the maximum potential (~ 480 mV) for avoiding the formation of hypochlorite. Compared with the FeOOH catalyst, which experiences a severe drop in its catalytic activity, the $\text{CoP}_x@FeOOH$ catalyst maintains its catalytic activity well in natural seawater, showing the great benefit from its high conductivity and hierarchical core-shell structure. The Tafel slope value of $\text{CoP}_x@FeOOH$ catalyst in 1 M KOH seawater is calculated to be only 50.3 mV dec^{-1}

(**Figure 4.9b**), indicating the rapid electrocatalytic kinetics was maintained in natural seawater condition. The catalytic durability of the $\text{CoP}_x@FeOOH$ catalyst were verified by both CV cycling and chronopotentiometric measurement in 1 M KOH and 1 M KOH seawater electrolytes. As shown in **Figure 4.9c**, the CV cycling durability of this catalyst in 1 M KOH is confirmed by the nearly overlapping polarization curves obtained before and after 5,000 CV cycles. A slight decline in the resultant polarization curves can be observed after cycling in 1 M KOH seawater due to the obstruction of active sites by Cl^- and the poisoning of the catalyst by insoluble precipitates. SEM images of the $\text{CoP}_x@FeOOH$ catalyst after CV cycling in 1 M KOH seawater indicate that the core-shell structure on the micro scale (**Figure 4.10a**) and the nanowire mesh structure on the macro scale (Insert **Figure 4.10a**) are both maintained, confirming good structural stability and high corrosion resistance. The peaks refer to FeOOH phase disappeared in the XRD pattern of post-OER sample (**Figure 4.10c**), indicating an amorphous phase was reconstructed on the surface.^{114, 118} This can be confirmed by the Raman spectra shown in **Figure 4.10c**, in which a pair of huge peaks refer to -OOH species appeared in the post-OER sample. Based on the XRD and Raman analysis, we can conclude that the OER active sites are Fe-OOH species in the reconstructed amorphous shell in the $\text{CoP}_x@FeOOH$ catalyst.

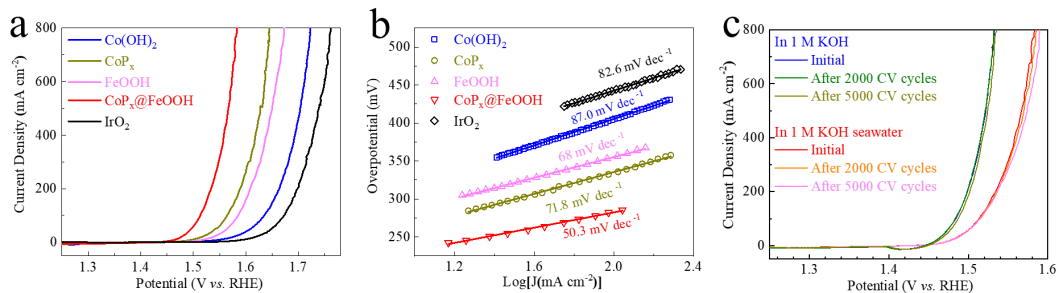


Figure 4.9. (a) OER polarization curves of these catalysts in 1 M KOH seawater. (b) Tafel plots derived from (a). (c) OER polarization curves of $\text{CoP}_x@FeOOH$ before and after CV scans.

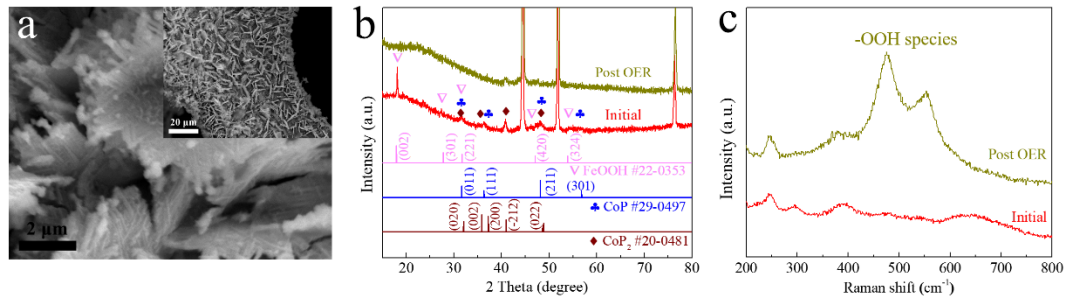


Figure 4.10. (a) SEM images of $\text{CoP}_x@FeOOH$ after 5,000 CV cycles in 1 M KOH seawater. (b) XRD patterns and (c) Raman spectra of $\text{CoP}_x@FeOOH$ before and after 5,000 CV cycles in 1 M KOH seawater.

The chronopotentiometric measurement curves in **Figure 4.11a-b** show that the potential fluctuation of the $\text{CoP}_x@FeOOH$ catalyst over 80 h continuous testing at a current density of 100 mA cm^{-2} in 1 M KOH seawater is merely 29 mV, slight worse than its performance in 1 M KOH (15 mV over 50 h testing). When tested at the industrial-scale current density of 500 mA cm^{-2} , this $\text{CoP}_x@FeOOH$ catalyst can still work steadily despite some increase in the potential fluctuations (70 mV over 80 h testing and 51 mV over 50 h testing in 1 M KOH seawater and 1 M KOH electrolytes, respectively). These low potential fluctuations at such a high current density for such long testing durations place the $\text{CoP}_x@FeOOH$ catalyst among the best self-supported catalysts reported thus far.

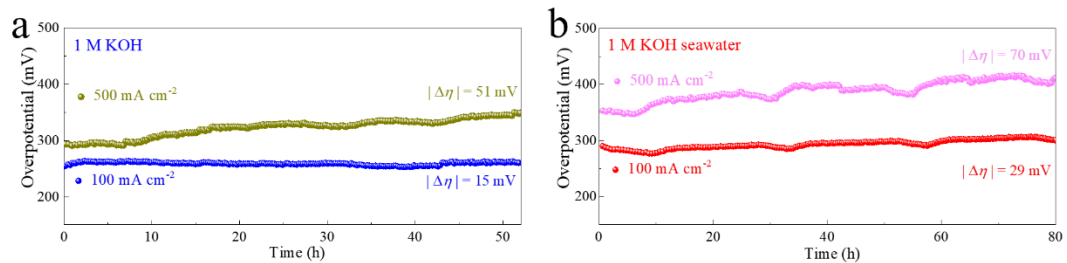


Figure 4.11. Chronopotentiometric curves of $\text{CoP}_x@FeOOH$ catalysts at constant current densities of 100 and 500 mA cm^{-2} in (a) 1 M KOH and (b) 1 M KOH seawater.

When measure in alkaline saline, the OER catalytic activity of the five studied catalysts (**Figure 4.12a-b**) is well maintained in 1 M KOH + 0.5 M NaCl despite a slight decline caused by the blocking of some active sites by the Cl^- . To assess the catalytic kinetics of these catalysts in each electrolyte, corresponding Tafel slope values are calculated and summarized in **Figure 4.12c**. Notably, all of these catalysts have increasing Tafel slope values in the same order of 1 M KOH, 1 M KOH + 0.5 M NaCl, and 1 M KOH seawater electrolytes, indicating that their catalytic kinetics and transfer coefficient values are slightly and severely lowered in saline and natural seawater, respectively. Additionally, both the catalytic activity and the Tafel slope values of these catalysts obtained in freshwater are very close to those obtained in simulated seawater but are much better than those obtained in natural seawater. Compared with simulated seawater (0.5 M NaCl in freshwater), natural seawater has a low conductivity and a more complicated composition, containing alkaline metal cations (Ca^{2+} , Mg^{2+} , Na^+ , K^+), chloride ions (Cl^-), sulfate ions (SO_4^{2-}), insoluble precipitates (dust, colloids, and bacteria), *etc.*^{17, 85, 136} Thus, for study of seawater electrolysis, it is more reasonable to use the data obtained in natural seawater, although it is worse than that obtained in simplified simulated seawater.

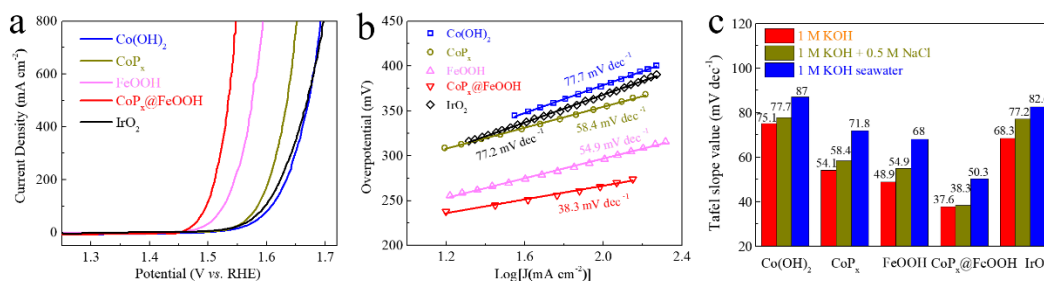


Figure 4.12. (a) OER polarization curves of these catalysts in 1 M KOH + 0.5 M NaCl. (b) Tafel plots derived from (a). (c) Comparison of the Tafel slope values of these catalysts in different electrolytes.

4.3.2.2 HER Performance in Alkaline Freshwater and Seawater

It is widely accepted that phosphide-based catalysts normally have high HER catalytic activity because the P atoms can trap H* intermediates and easily dissociate H₂ molecules.^{35-36, 40, 137} In particular, the CoP_x catalyst in this work, due to its heterogeneous phase composition (CoP-CoP₂) with a higher ratio of P atoms compared to pure-phase CoP, has relatively more active sites (either defective phase interfaces or P atoms) for HER catalysis.^{36, 125, 131, 138} Additionally, the nanowire mesh structure not only can expose each nanowire for contact and reaction with the electrolyte, but also provides sufficient mechanical strength when these nanowires cross one another to form a micron-scale mesh. As shown in **Figure 4.13a-b**, the CoP_x catalyst exhibits much higher HER catalytic activity than the other three self-supported catalysts when working as a cathodic electrode in 1 M KOH electrolyte. When measured in 1 M KOH seawater, it requires low overpotentials of 117, 190, 248, and 269 mV to attain current densities of 10, 100, 500, and 800 mA cm⁻², respectively, with an acceptable Tafel slope value of 71.1 mV dec⁻¹ (**Figure 4.13c-d**). The catalyst's vertically standing nanowire mesh structure and its hydrophilic surface can promote electrolyte diffusion and H₂ bubble release, leading to excellent catalytic durability and structural stability in 1 M KOH seawater electrolyte,¹²⁷⁻¹²⁸ which is proved by the negligible decline in the resultant polarization curve after CV cycling (**Figure 4.13e**) and the stable chronopotentiometric measurement at constant current density of 500 mA cm⁻² in 1 M KOH seawater electrolyte (**Figure 4.13f**).

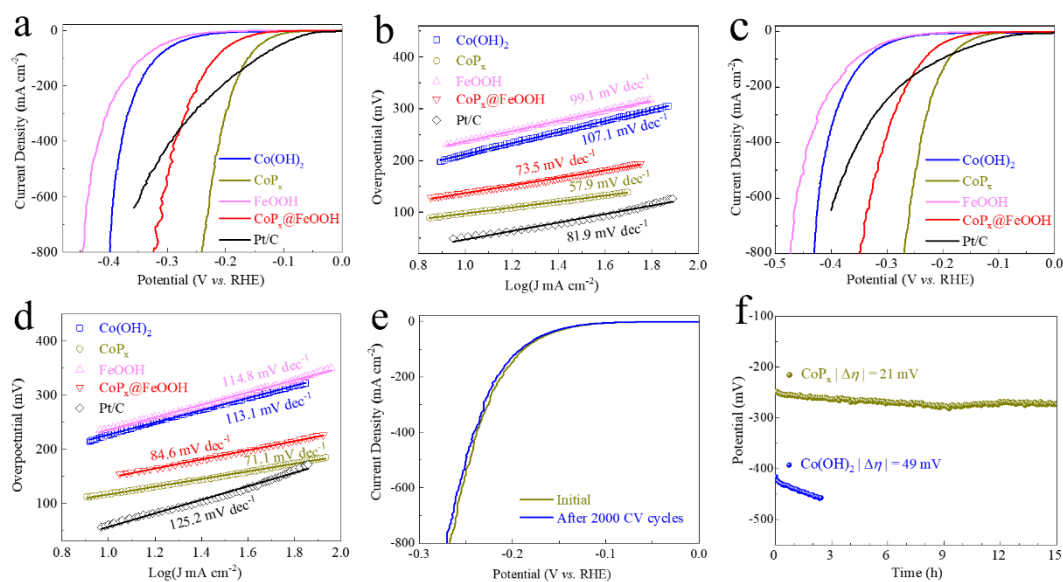


Figure 4.13. HER polarization curves of these catalysts in (a) 1 M KOH and (c) 1 M KOH seawater. (b) and (d) Tafel plots. (e) HER polarization curves of CoP_x in 1 M KOH seawater. Stability performance of Co(OH)₂ and CoP_x.

4.3.2.3 Overall Water and Seawater Electrolysis Performance of CoP_x||CoP_x@FeOOH Pair

Inspired by these exciting results, we then coupled the OER-active CoP_x@FeOOH as the anode electrode and the HER-active CoP_x as the cathode electrode for overall seawater electrolysis. As shown in **Figure 4.14a**, this CoP_x||CoP_x@FeOOH pair requires voltages of 1.549, 1.710, 1.867, and 1.922 V to attain current densities of 10, 100, 500, and 800 mA cm⁻², respectively, in 1 M KOH seawater. When measured in the 1 M KOH electrolyte, which is widely used in freshwater electrolysis studies, this pair requires voltages of only 1.478, 1.688, 1.833, and 1.881 V to attain the same respective current densities. The Faradaic efficiency (FE) of this pair for overall seawater electrolysis was measured at a constant current density of 500 mA cm⁻² using the drainage method. The resultant data was collected and is displayed in **Figure 4.14b**, which shows that the produced O₂ and H₂ gas amounts nearly match the

theoretical values, indicating the high FE ($> 98\%$) of this pair. Additionally, its catalytic durability was evaluated through CV cycling and chronopotentiometric measurement. As shown in **Figure 4.14c**, this $\text{CoP}_x\|\text{CoP}_x@\text{FeOOH}$ pair has incredible cycling stability in 1 M KOH electrolyte, which is proved by the slight difference in the polarization curves before and after 5,000 CV scans. Although there is some decline when cycled in 1 M KOH seawater electrolyte, this pair still maintains excellent overall seawater electrolysis activity, especially at large current densities. The catalytic durability of this pair is also proved by the results from a long-term chronopotentiometric measurement at an industrial-scale current density of 500 mA cm^{-2} , which show that it suffers a 53-mV potential fluctuation over 80 h continuous testing (**Figure 4.14d**). Their high FE and excellent catalytic durability at such a high current density make CoP_x and $\text{CoP}_x@\text{FeOOH}$ promising catalysts for realistic H_2 production from natural seawater.

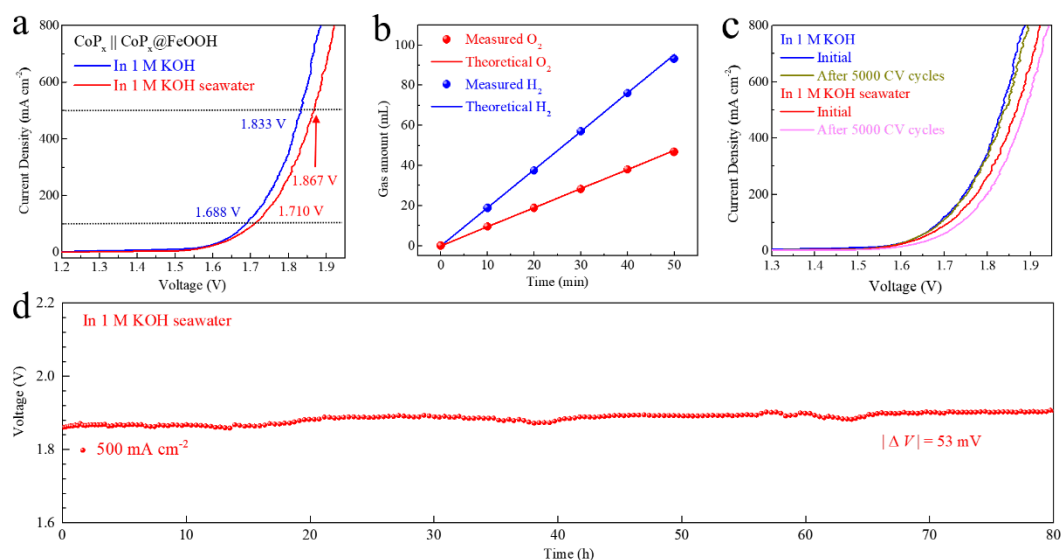


Figure 4.14. (a) Overall freshwater/seawater electrolysis of the $\text{CoP}_x\|\text{CoP}_x@\text{FeOOH}$ pair. (b) Gaseous products, (c) CV cycling performance, and (d) stability performance of this pair in 1 M KOH seawater.

4.3.3 Chloride Corrosion Resistance Analysis

Chloride corrosion is another severe challenge whose effect is difficult to determine during catalytic activity tests but will gradually take the center stage and limit the service life of a catalyst for seawater electrolysis. Here, the corrosion resistance performance of the $\text{CoP}_x@FeOOH$ and CoP_x catalysts was first determined by a 25-day immersion test in natural seawater. As shown in **Figure 4.15a-b**, the structures of these two catalysts are well maintained after long-term immersion. For the CoP_x in particular, no obvious corrosion pits or structural collapse can be found, indicating its outstanding corrosion resistance and structural stability. To analyze the corrosion resistance of these catalysts in depth, corresponding corrosion polarization curves (**Figure 4.15c-e**) were collected in pure natural seawater without adding the conductive reagent KOH and the resultant data is summarized in **Figure 4.15f**. CoP_x exhibits the highest corrosion potential (-0.071 V vs. SCE) and the lowest corrosion current density (0.0037 mA cm⁻²) among all of the catalysts measured, indicating its highest chloride corrosion resistance ability. When incorporated into core-shell-structured $\text{CoP}_x@FeOOH$, the corresponding corrosion potential declines to -0.377 V vs. SCE and the corrosion current density increases to 0.0439 mA cm⁻², which are still much better than those of pristine FeOOH (-0.758 V vs. SCE and 0.0818 mA cm⁻², respectively). The corrosion polarization curve analysis shows that the $\text{CoP}_x@FeOOH$ catalyst has remarkably enhanced chloride corrosion resistance compared with the pristine FeOOH catalyst. The alloying between the metallic Co and Fe cations and the P atoms can result in high thermodynamic stability and less metal dissolution, leading to enhancement in both chemical stability and corrosion resistance. The CoP_x core in

particular can act as a protection layer in the $\text{CoP}_x@FeOOH$ catalyst to repel the chloride ions and reduce electrode corrosion. Thus, beyond a simple physical mixture, such a core-shell-structured $\text{CoP}_x@FeOOH$ catalyst can effectively “hits two birds with one stone”, in which both the catalytic activity and chloride corrosion resistance are enhanced.

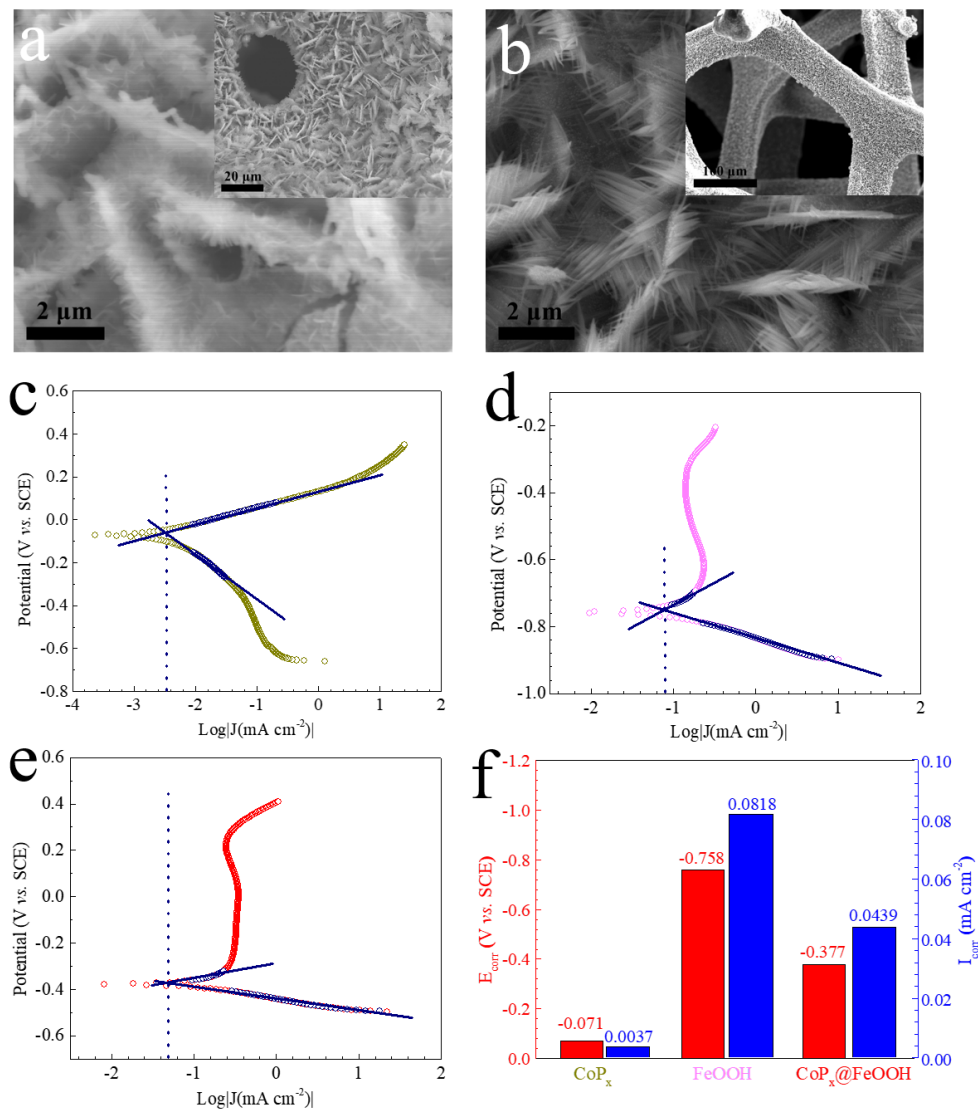


Figure 4.15. SEM images of (a) $\text{CoP}_x@FeOOH$ and (b) CoP_x after immersion in seawater. Corrosion polarization curves of the (c) CoP_x , (d) FeOOH , and (e) $\text{CoP}_x@FeOOH$ in seawater. (f) Corrosion performance of these catalysts.

4.3.4 Discussion and Expansion

With the limited supply of freshwater, seawater electrolysis is more appealing and has attracted tremendous research interest recently. However, due to critical challenges such as chlorine chemistry and catalyst poisoning, selective and stable catalysts are highly required for seawater electrolysis. Here, for the first time, we designed core-shell-structured $\text{CoP}_x@FeOOH$ as an OER catalyst and a CoP_x nanowire mesh core as a HER catalyst for overall seawater electrolysis. Such a combination generates remarkable benefits to conquer the deficiencies of pure-phase $FeOOH$ and thus can meet the requirement for selective seawater oxidation. First, besides enhancing the electron transport in the $FeOOH$ shell, the micron-scale CoP_x core can provide sufficient mechanical strength and enlarge the surface area to rivet and expose more oxyhydroxide active sites for OER catalysis, which can address the low conductivity of, and insoluble precipitates in, natural seawater. Second, negatively charged P atoms in the CoP_x core can moderate the absorption energy of the $FeOOH$ active sites to OER intermediates, leading to high intrinsic catalytic activity, which can effectively avoid the CIER and reach a high FE at industrial-scale current densities. Third, the employment of a binder-free NF substrate modified to exhibit a hydrophilic surface feature provides adequate space for electrolyte diffusion and accelerates bubble release, together ensuring the catalytic durability of $\text{CoP}_x@FeOOH$ and CoP_x catalysts at high current densities. Fourth, when alloying with P atoms, both the chloride corrosion resistance and the structural stability of the $\text{CoP}_x@FeOOH$ and CoP_x catalysts are enhanced due to their higher chlorine-repelling ability and less metal dissolution. The three-step hydrothermal-phosphidation-electrodeposition

procedure described here can also be exploited to synthesize core-shell-structured $\text{CoP}_x@ \text{CoOOH}$ (**Figure 4.16a**) and $\text{CoP}_x@ \text{NiOOH}$ catalysts (**Figure 4.16b**) by simply changing the electrodeposition electrolyte to $\text{Co}(\text{NO}_3)_2$ and $\text{Ni}(\text{NO}_3)_2$ aqueous solutions, respectively. As shown in **Figure 4.16c**, all of the core-shell-structured catalysts exhibit higher OER catalytic activity in alkaline seawater electrolyte than their counterparts directly electrodeposited on NF substrates, indicating that this may be an effective and universal method for synthesizing promising catalysts for seawater electrolysis.

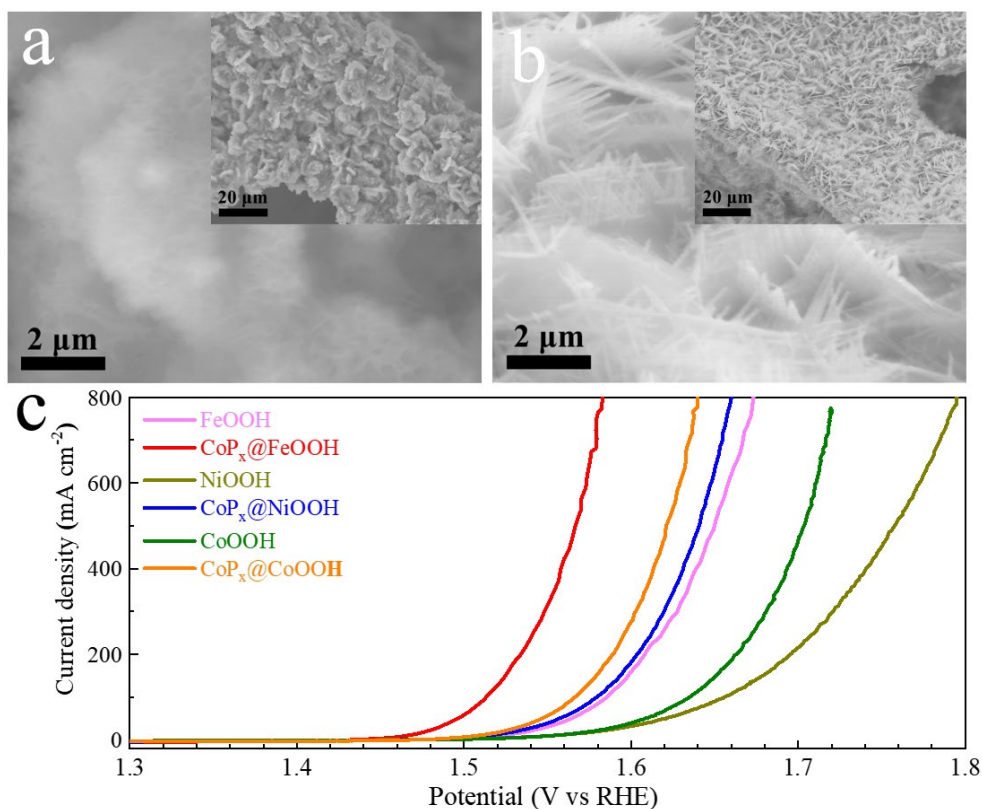


Figure 4.16. SEM images of (a) $\text{CoP}_x@ \text{CoOOH}$ and (b) $\text{CoP}_x@ \text{NiOOH}$. (c) OER polarization curves of FeOOH , $\text{CoP}_x@ \text{FeOOH}$, CoOOH , $\text{CoP}_x@ \text{CoOOH}$, NiOOH , and $\text{CoP}_x@ \text{NiOOH}$ catalysts in 1 M KOH seawater.

4.4 Conclusion

We have successfully constructed core-shell-structured $\text{CoP}_x@FeOOH$ as an efficient OER catalyst for seawater oxidation. Benefiting from the highly conductive and vertically standing CoP_x core as well as a hydrophilic surface, this hierarchical $\text{CoP}_x@FeOOH$ catalyst exhibits enhanced conductivity, enriched active sites, sufficient mechanical strength, and accelerated bubble-release ability, all of which lead to superior OER catalytic activity at high current densities. In addition, the high chloride corrosion resistance and enhanced chemical stability help it work well in alkaline seawater electrolyte. When coupled with the HER-active CoP_x core, the $\text{CoP}_x||\text{CoP}_x@FeOOH$ pair requires voltages of 1.710 and 1.867 V to attain current densities of 100 and 500 mA cm^{-2} , respectively, in 1 M KOH seawater electrolyte with high Faradaic efficiency and long-term stability. This work not only introduces and analyzes catalysts for selective seawater electrolysis, but also provides opportunities in engineering the structure and corrosion chemistry to design more innovative catalysts for seawater electrolysis.

CHAPTER 5 EFFICIENT ALKALINE WATER/SEAWATER HYDROGEN EVOLUTION BY Ni-MoN CATALYST WITH FAST WATER-DISSOCIATION KINETICS

Note: The material in this chapter has been published. The introduction, experimental section, and figure captions were adjusted for dissertation consistency. Reproduced with permission from Weily.

5.1 Introduction

Alkaline water electrolysis is currently more appealing than acid water electrolysis due to its inexpensive equipment requirements and effective avoidance of acid fog and corrosion.⁸⁻¹⁰ To accelerate the sluggish kinetics resulting from the extra water-dissociation step in alkaline electrolyte and to minimize the dynamic overpotential of the hydrogen evolution reaction (HER), efficient, highly stable catalysts, especially those that can sustain large current densities ($> 500 \text{ mA cm}^{-2}$), are desirable.^{127, 139-140} To date, platinum (Pt)-based catalysts remain the benchmark HER catalysts in both acid and alkaline electrolytes. Unfortunately, the high costs and scarce sources for their constituent elements seriously limit the widespread utilization of these catalysts.¹⁴¹⁻¹⁴² On the other hand, seawater electrolysis has recently attracted growing research interest due to the inexhaustible resource reserves and the great promise of massive hydrogen production without exacerbating freshwater shortages. However, the complicated composition of natural seawater can result in additional challenges for direct seawater electrolysis.^{23, 136, 143} For example, the chlorine evolution reaction (CLER) from chloride ions (Cl^- , $\sim 0.5 \text{ M}$) in the seawater might compete with the

oxygen evolution reaction (OER) on the anode and thus lower the overall seawater-electrolysis efficiency.^{17-18, 144} Catalyst corrosion by chloride ions and poisoning by insoluble precipitates (dust, colloids, and bacteria) will degrade catalytic activity and durability. Some recent works point out that corrosion-resistant electrolyzers and affordable membranes play important roles in direct seawater electrolysis, which can affect the device lifetime and efficiency of the system.^{10, 24-25} All these challenges have greatly impeded the development of seawater-electrolysis technology.

Over the past decades, tremendous effort has been devoted to exploring efficient non-noble-metal based catalysts intended to replace the Pt-based ones. Among these, transition metal nitrides (TMNs) have attracted considerable attention due to their good electrical conductivity and outstanding mechanical robustness. Recent experimental and theoretical results suggest that TMNs have moderate binding capabilities toward reactants (water molecules, atomic hydrogen, or protons), allowing them outstanding HER catalytic activity.^{54, 56-58} To further boost the alkaline HER performance of TMNs, effective sites for water dissociation should be introduced to enhance its sluggish kinetics. Thus, heterogeneous TMN-based catalysts, including Ni₃N/Ni, Co-Ni₃N, V-Co₄N, Cr-Co₄N, Co/MoN, Co-Mo₅N₆, and Ni_{0.2}Mo_{0.8}N/Ni, in which either the introduced metallic atoms or the original metals in the TMNs serve as effective water-dissociation sites, have been synthesized and have shown comparable or even better HER performance than the benchmark Pt/C.^{58, 65, 145-149} However, studies of these heterogeneous TMN-based catalysts have mainly focused on freshwater electrolysis at small current densities usually lower than 500 mA cm⁻². For large-current-density water electrolysis, the catalytic performance might be limited by

insufficient active sites and structural instability.⁵⁹ Additionally, scaling up alkaline water electrolysis technology and bringing it to market requires practical catalytic performance under industrial conditions (normally in 6 M KOH at 60-65 °C), long-term stability of the catalysts, and affordable catalysts and cells. Designing TMN-based catalysts with tailored structures, efficient catalytic activity, and long-term durability for large-current-density alkaline seawater electrolysis is very meaningful, although studies remain quite limited.

Here we demonstrate that a novel Ni-MoN catalyst consisting of dense crystalline Ni and MoN nanoparticles on an amorphous MoN nanorod matrix can be an efficient HER catalyst for both alkaline freshwater and seawater electrolysis. A nanorod-structured $\text{NiMoO}_4 \cdot x\text{H}_2\text{O}$ precursor was first obtained through a scalable water bath reaction and was subsequently converted to a hierarchical nanorod-nanoparticle-structured Ni-MoN catalyst with high surface roughness upon a second step of ammonia reduction. Its large surface area and multidimensional boundaries/defects can expose abundant active sites while its mesoporous structure (pore size of ~6.5 nm) and hydrophilic surface are beneficial for fast electrolyte diffusion and quick release of gas bubbles. Theoretical calculations show that charge exchange and electron redistribution occur at the interfaces between Ni and MoN, so Ni-MoN is in a metallic state with high conductivity. As a result, the Mo sites in Ni-MoN have high capability toward water adsorption and dissociation, which greatly enhances the sluggish alkaline HER kinetics. Consequently, the optimized Ni-MoN catalyst achieves remarkable HER catalytic activity with ultralow overpotentials of 61 and 136 mV to drive large current densities of 100 and 1,000 mA cm^{-2} , respectively, in 1 M KOH and exhibits a

small Tafel slope of 35.5 mV dec^{-1} , placing it among the best self-supported HER catalysts reported thus far. It also has outstanding catalytic durability at constant current densities up to 100 and 500 mA cm^{-2} during 200 h of continuous testing. The Ni-MoN catalyst can well maintain its catalytic activity and durability in alkaline natural seawater and high-chlorine-concentration alkaline saline electrolytes. When coupled with a commercial stainless-steel mat (SSM), the Ni-MoN||SSM pair exhibits remarkable overall water/seawater electrolysis performance that is superior to the benchmark Pt/C||Ni-Fe layered double hydroxide (LDH) pair and many other catalysts, showing great potential for sustainable, efficient, and stable hydrogen production from seawater electrolysis.

5.2 Experimental Section

5.2.1 Synthesis of Catalysts

5.2.1.1 Synthesis of $\text{NiMoO}_4 \cdot x\text{H}_2\text{O}$ Precursor

A self-supported $\text{NiMoO}_4 \cdot x\text{H}_2\text{O}$ precursor was grown on a Copper foam (CF) substrate *via* a scalable water bath reaction. Briefly, a piece of CF ($1.5 \text{ cm} \times 2.5 \text{ cm}$) was first cleaned by HCl solution, ethanol, and deionized (DI) water in sequence. Separately, 2 mmol nickel nitrate hexahydrate [$\text{Ni}(\text{NO}_3)_2 \cdot 6\text{H}_2\text{O}$, Sigma Aldrich], 0.25 mmol ammonium molybdate [$(\text{NH}_4)_6\text{Mo}_7\text{O}_{24} \cdot 4\text{H}_2\text{O}$, Sigma Aldrich], and 3 mmol urea [$\text{CO}(\text{NH}_2)_2$, Promega Corporation] were dissolved homogeneously in 20 mL DI water in a glass bottle. The washed CF was then immersed into the solution, and the glass bottle was transferred to a water bath oven maintained at $90 \text{ }^\circ\text{C}$ for 8 h. After rinsing several times with DI water and drying in air, the light green $\text{NiMoO}_4 \cdot x\text{H}_2\text{O}$ precursor was obtained.

5.2.1.2 Synthesis of Ni-MoN Catalyst

An ammonia reduction procedure was employed to convert the as-obtained $\text{NiMoO}_4 \cdot x\text{H}_2\text{O}$ precursor to a Ni-MoN catalyst. Typically, the $\text{NiMoO}_4 \cdot x\text{H}_2\text{O}$ precursor was annealed in the center of a glass tube under a mixed ammonia (120 sccm) and argon (60 sccm) flow at 400 °C for 2 h with a heating rate of 10 °C/min. Here, ammonia gas served as both the reducing agent and the nitrogen source. After naturally cooling down, the black product was denoted Ni-MoN.

To determine the optimal Ni:Mo ratio, other Ni-MoN catalysts were then prepared *via* a similar procedure except for varying the Ni:Mo ratio (2:7, 4:7, and 12:7) in the reactants. The annealing temperature was also tuned from 300 to 500 °C to reach the optimal ammonia reduction temperature. For a comprehensive comparison, nickel nitride (Ni-Ni₄N) and molybdenum nitride (Mo-N) catalysts were prepared *via* a similar procedure without adding a Mo or Ni source in the reactants for the respective catalysts.

5.2.1.3 Preparation of Pt/C Electrode

A noble-metal-based Pt/C catalyst was loaded on CF to serve as the benchmark HER catalyst for comparison. Briefly, 60 mg commercial platinum carbon powder (Pt/C, nominally 20% on carbon black, Alfa Aesar) was homogeneously dissolved in a mixture solution containing 810 μL ethanol, 90 μL Nafion solution, and 600 μL DI water with the assistance of ultrasonication. A piece of CF ($\sim 1.5 \text{ cm}^2$) was then soaked in the solution for 1.5 h, followed by drying in air.

5.2.1.2 Synthesis of Ni-Fe LDH

A Ni-Fe layered double hydroxide (LDH) catalyst was grown on CF *via* a water

bath reaction to serve as the benchmark oxygen evolution reaction (OER) catalyst. Briefly, 0.6 mmol nickel nitrate hexahydrate, 0.2 mmol iron nitrate nonahydrate [$\text{Fe}(\text{NO}_3)_3 \cdot 9\text{H}_2\text{O}$, Alfa Aesar], 2 mmol ammonium fluoride (NH_4F , Alfa Aesar), and 10 mmol urea were dissolved homogeneously in 40 mL DI water in a beaker. A piece of CF was placed inside the beaker and then underwent a water bath reaction at 90 °C for 8 h. The product was denoted Ni-Fe LDH.

5.2.2 Physical and Chemical Characterization

The morphology, structure, and elemental distribution of the as-prepared catalysts were comprehensively investigated using scanning electron microscopy (SEM, LEO 1525), transmission electron microscopy (TEM, JEOL 2010F), and aberration-corrected transmission electron microscopy (ACTEM, FEI Titan Themis) with energy-dispersive spectroscopy (EDS). X-ray diffraction (XRD, PANalytical X'pert PRO, $\text{Cu K}\alpha$ radiation) measurements were taken to identify the compositions of the as-prepared catalysts and X-ray photoelectron spectroscopy (XPS, PHI Quantera) was conducted to identify the valence states of their constituent elements. pH values of the electrolytes were measured using a pH meter (AR10, Fisher Scientific) at room temperature. The Brunauer-Emmett-Teller (BET) surface area and pore size distribution were measured using a TriStar II Plus (Micromeritics). Electron paramagnetic resonance (EPR) spectroscopy was performed using a Bruker A300 spectrometer. Raman tests were conducted on a Horiba iHR320 Raman spectrometer using a DPSS laser (excitation wavelength: 532 nm).

5.2.3 Electrochemical Characterization

Electrochemical characterizations of the as-prepared catalysts were performed on a Gamry Reference 600 or a Gamry Reference 3000 Potentiostat. In a typical three-electrode configuration, an as-prepared catalyst (the geometric surface area of each catalyst in the electrolyte is 0.5-1 cm²), a carbon rod, and a Hg/HgO electrode were used as the working, counter, and reference electrodes, respectively. The scan rate was set to be 1 mV s⁻¹ to achieve reliable catalytic performance and *iR* compensation was used for all electrochemical measurements. Linear sweep voltammetry (LSV) curves were recorded for HER and backward polarization curves were collected for OER. At least 100 cyclic voltammetry (CV) cycles were performed for activation and stabilization before the collection of each HER or OER polarization curve. At room temperature (298.15 K), the potential ($E_{\text{Hg/HgO}}$) was calibrated to the reversible hydrogen electrode (RHE) using the equation: $E_{\text{RHE}} = E_{\text{Hg/HgO}} + 0.098 + 0.0591 \times \text{pH}$, where the pH values of 1 M KOH and 1 M KOH seawater electrolytes were measured to be 13.91 and 13.83, respectively. The Tafel slope (*b*) was calculated using the equation $\eta = a + b \log(j)$, where η is the overpotential and *j* is the current density. Electrochemical impedance spectroscopy (EIS) was measured at a constant potential of -0.12 V vs. RHE (overpotential of 120 mV for HER) in 1 M KOH with varied frequency from 100 kHz to 0.01 Hz. The electrochemically active surface area (ECSA) was calculated through the double-layer capacitance (C_{dl}) method. Briefly, CV cycling was performed in a non-Faradaic region with different scan rates. The C_{dl} was then obtained as half of the slope in the plot of capacitive current as a function of scan rate. ECSA was calculated from the equation: $\text{ECSA} = C_{\text{dl}}/C_s$, where C_s is the

specific capacitance for a flat surface ($40 \mu\text{F cm}^{-2}$ was used here). For HER durability testing, CV cycling was performed between 0 and -0.17 V vs. RHE with a scan rate of 100 mV s^{-1} . Chronopotentiometric measurements were conducted at current densities of 100 and 500 mA cm^{-2} in both 1 M KOH and 1 M KOH seawater electrolytes. Overall water/seawater electrolysis was performed in an H-type electrolyzer with Ni-MoN as the cathodic electrode (0.5 cm^2), SSM as the anodic electrode (0.5 cm^2), and an anion-exchange membrane (AEM, Fumasep, FAA-3-PK-130) as the separator. For overall water/seawater electrolysis durability testing and to reach ultrahigh current density (3 A cm^{-2}), the AEM separator was not used because of its low stability and the limited mass transfer issue.

5.2.4 Calculation of TOF

The turnover frequency (TOF) value of HER was estimated using the following equation:

$$\text{TOF} = \frac{\text{Number of total hydrogen turn overs / geometrical area (cm}^2\text{)}}{\text{Number of surface active sites / geometrical area (cm}^2\text{)}}.$$

The total numbers of hydrogen turn overs:

$$\begin{aligned} \text{Number of H}_2 &= \left(j \frac{\text{A}}{\text{cm}^2} \right) \left(\frac{1 \text{ C s}^{-1}}{1000 \text{ mA}} \right) \left(\frac{6.02 \times 10^{23} \text{ H}_2 \text{ molecules}}{1 \text{ mol H}_2} \right) \left(\frac{1 \text{ mol e}^-}{96485.3 \text{ C}} \right) \left(\frac{1 \text{ mol H}_2}{2 \text{ mol e}^-} \right) \\ &= 3.12 \times 10^{15} \frac{\text{H}_2 \text{ s}^{-1}}{\text{cm}^2} \text{ per } \frac{\text{mA}}{\text{cm}^2}. \end{aligned}$$

We estimated the number of the active sites as the total number of the surface sites from the roughness factor together with the unit cell of the catalysts, which will underestimate the actual TOF. Taking Ni-MoN as an example, the upper limit of the

surface active sites (all Ni, Mo, and N atoms were included as active sites) per unit of actual surface area can be calculated using the following equations:

$$\text{Number of active sites} = \left(\frac{\text{Number of atoms/unit cell}}{\text{Volume/unit cell}} \right)^{2/3},$$

$$\text{Number of active sites (MoN)} = \left(\frac{16 \text{ atoms/unit cell}}{159.2 \text{ \AA}^3 / \text{unit cell}} \right)^{2/3} = 2.16 \times 10^{15} \text{ atoms cm}^{-2},$$

$$\text{Number of active sites (Ni)} = \left(\frac{4 \text{ atoms/unit cell}}{43.8 \text{ \AA}^3 / \text{unit cell}} \right)^{2/3} = 2.03 \times 10^{15} \text{ atoms cm}^{-2}, \text{ and}$$

Number of active sites

$$(\text{NiMoO}_4 \cdot x\text{H}_2\text{O}) = \left(\frac{24 \text{ atoms/unit cell}}{404.1 \text{ \AA}^3 / \text{unit cell}} \right)^{2/3} = 1.52 \times 10^{15} \text{ atoms cm}^{-2}.$$

Thus, the number of the active sites for Ni-MoN is around $2.1 \times 10^{15} \text{ atoms cm}^{-2}$ and that for $\text{NiMoO}_4 \cdot x\text{H}_2\text{O}$ is $1.52 \times 10^{15} \text{ atoms cm}^{-2}$. The plots of current density can be converted into TOF plots using the following formula:

$$\text{TOF}_{\text{HER}} = \frac{3.12 \times 10^{15} \frac{\text{H}_2 \text{ s}^{-1}}{\text{cm}^2} \text{ per } \frac{\text{mA}}{\text{cm}^2} \times j}{\text{Number of active sites} \times A_{\text{ECSA}}}.$$

5.2.5 Overall Water Electrolysis Driven by a Thermoelectric Module

A thermoelectric (TE) module, which can convert thermal energy to electricity, was used to drive the homemade electrolyzer according to our previous work.^{7, 20} In detail, a heater and a cooler were placed in contact with the TE module on its top and bottom, respectively, with two copper plates working as the thermal conductor in the middle. A constant hot-side temperature was maintained by tuning the DC power supply, while the cold-side temperature was controlled by a water-cooling system on the homemade testing platform. A relatively stable open circuit voltage could be

generated by the TE module when the temperature difference between the two sides was kept constant. A voltmeter and an ammeter were applied for real-time monitoring of the voltage and the current, respectively, of the two electrodes (Ni-MoN and SSM) in the electrolyzer.

5.2.6 Theoretical Calculations

Density functional theory (DFT) calculations were performed using the plane-wave technique implemented in the Vienna *ab initio* simulation package (VASP). The Perdew-Burke-Ernzerhof (PBE) formalism was employed for electron exchange and correlation. The plane wave pseudopotential with a cut-off energy of 450 eV and the Gaussian electron smearing method with an electronic temperature of $k_B T = 0.05$ eV were used in the calculation. The geometrical optimization was performed when the residual forces on the atoms were smaller than 0.05 eV \AA^{-1} and the energy difference was converged to 10^{-5} eV. The unit cell of the Ni-MoN catalyst was constructed using a Ni cluster on MoN (202). There are Ni sites on top of the Ni clusters and Mo sites near the Ni and MoN heterointerface, respective, that are exposed in Ni-MoN for DFT calculations. For comparison, models of metallic Ni (111) and Mo sites in MoN (202) were also built for the DFT calculations. All these models were constructed based on the TEM and XRD results and take into account thermodynamic stability. In the Ni-MoN catalysts, the reactant (H_2O) is first adsorbed on these active Ni and Mo sites (M) described above and then dissociates into intermediates (OH^- and M-H^*). Subsequently, the hydrogen will be desorbed *via* the Heyrovsky reaction here, in which another H_2O molecule and an extra electron will diffuse to M-H^* and form H_2 and OH^- . The adsorption energy (E_{ads}) of species X is calculated by $E_{\text{ads}} = E(X/\text{slab}) -$

$E(X) - E(\text{slab})$, where a more negative E_{ads} generally indicates stronger adsorption. To evaluate the energy barrier, the transitional state (TS) was located using the climbing image nudged elastic band method. The Gibbs free energy (G) values of the adsorbed species were calculated by $G = E_{\text{ele}} + \text{ZPE} - TS$, where E_{ele} is the electronic energy, ZPE is the zero-point energy, T is temperature (25 °C in all our calculations), and S is entropy.

5.3 Results and Discussion

5.3.1 Structural and Compositional Analysis Results

As depicted in **Figure 5.1a**, a self-supported $\text{NiMoO}_4 \cdot x\text{H}_2\text{O}$ precursor was first grown on copper foam (CF) through a water bath reaction at 90 °C for 8 h, and it was subsequently converted to Ni-MoN through a second ammonia reduction step at 400 °C for 2 h. Commercial CF was selected as a binder-free substrate for catalyst growth since it has the advantages of a three-dimensional (3D) porous structure, high conductivity, and good chemical/mechanical stability. Photographs in **Figure 5.1b-d** show that the pristine CF substrate, the $\text{NiMoO}_4 \cdot x\text{H}_2\text{O}$ precursor, and Ni-MoN are reddish, brown, and black, respectively, in color.

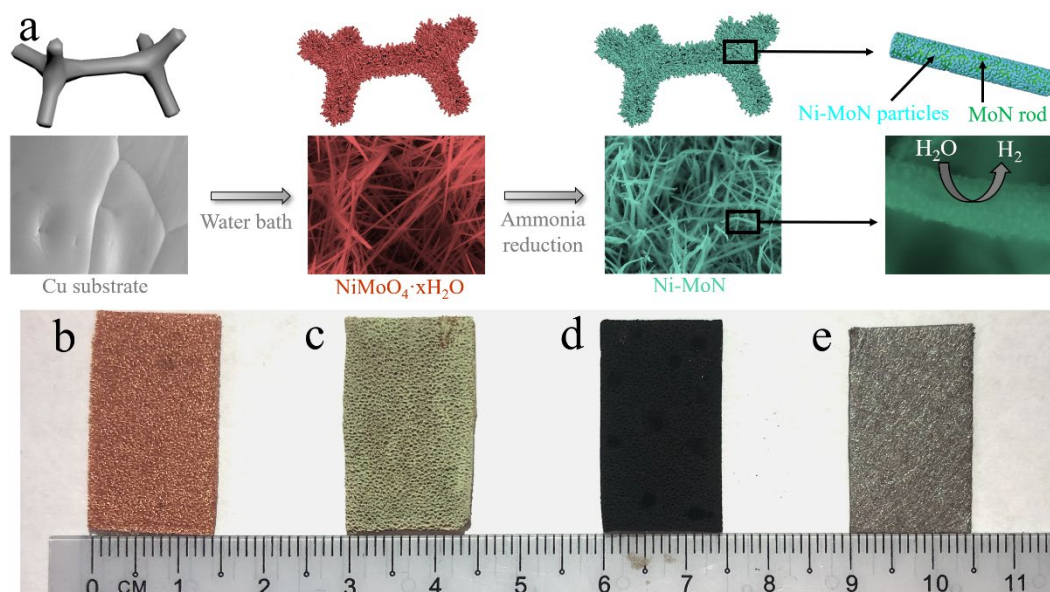


Figure 5.1. (a) Schematic illustrations of the synthesis of Ni-MoN and corresponding SEM images at different synthesis stages. Photographs of (b) CF, (c) $\text{NiMoO}_4 \cdot x\text{H}_2\text{O}$, (d) Ni-MoN, and (e) SSM.

Scanning electron microscopy (SEM, **Figure 5.2a-c**) and transmission electron microscopy (TEM, **Figure 5.2d-e**) characterizations indicate that $\text{NiMoO}_4 \cdot x\text{H}_2\text{O}$ has a smooth one-dimensional nanorod structure with diameters of between 100 and 200 nm. Such a nanorod-structured $\text{NiMoO}_4 \cdot x\text{H}_2\text{O}$ precursor is different from the widely reported microrod- or microsheet-structured precursors produced through the hydrothermal reaction, and the smaller size of its constituent components will be beneficial for reacting with the ammonia flow during the subsequent ammonia reduction step.¹⁴⁸⁻¹⁵¹ Corresponding energy dispersive spectroscopy (EDS) line scan curve (**Figure 5.2f**) and EDS mapping images (**Figure 5.2g-j**) illustrate the uniform distribution of elemental Ni, Mo, and O throughout the skeleton of the CF substrate and inside each $\text{NiMoO}_4 \cdot x\text{H}_2\text{O}$ nanorod. The X-ray diffraction (XRD) pattern in **Figure 5.2k** confirms the successful synthesis of the crystalline $\text{NiMoO}_4 \cdot x\text{H}_2\text{O}$ phase. It should be noted that urea plays an important role in the synthesis process since OH^-

from the urea can combine with metal cations to form metal hydroxides during the initial nucleation step and help to form nanorods during the water bath reaction.^{34, 61} The nanorod-structured precursor could not be obtained if urea were not added in the reactants.

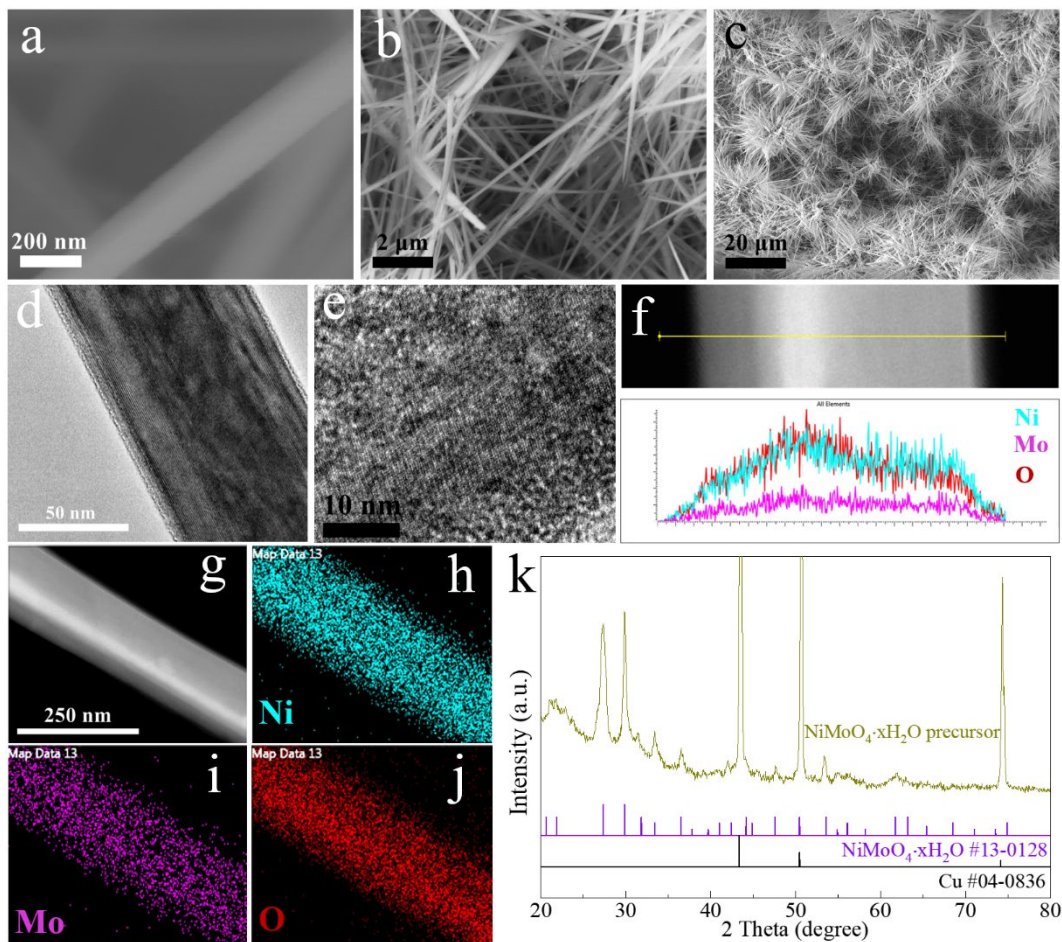


Figure 5.2. (a-c) SEM and (d-e) TEM images, (f) EDS line scan, and (k) XRD pattern of the $\text{NiMoO}_4 \cdot x\text{H}_2\text{O}$ precursor. (g) TEM image and corresponding (h) Ni, (i) Mo, and (j) O EDS mapping images of the $\text{NiMoO}_4 \cdot x\text{H}_2\text{O}$ precursor.

After annealing in mixed ammonia-argon gas, the main structure of these vertical-standing nanorods was well preserved, and newly formed nanoparticles can be found on the surfaces of these nanorods (**Figure 5.3a-c**). In addition, the Ni, Mo, and N elements can be clearly found in the EDS spectrum of Ni-MoN in **Figure 5.3d**.

Detailed TEM and aberration-corrected TEM (ACTEM) images in **Figure 5.3e-f** and **Figure 5.4a-b** show that these nanoparticles were embedded in the nanorod matrix and are several to tens of nanometers in diameter. Such a hierarchical nanorod-nanoparticle structure with a high degree of surface roughness not only exposes abundant active sites but also avoids catalyst aggregation during HER catalysis, benefiting the enhancement of both catalytic activity and durability.^{122, 152} Selected area electron diffraction (SAED), high-resolution TEM (HRTEM), and EDS characterizations were performed to identify the detailed compositions of the nanoparticles and nanorods. As shown in **Figure 5.3g**, characteristic (200) and (220) facets of metallic Ni and (202) and (220) facets of MoN can be distinguished within the SAED pattern, indicating a mixed composition of Ni and MoN in the hierarchical nanorod-nanoparticle-structured catalyst. The composition of Ni and MoN in the ammonia reduction product can further be confirmed by the EDS line scan curve in **Figure 5.3h** and the high-angle annular dark field (HAADF) EDS mapping images in **Figure 5.3i-n**, which show that elemental Ni gathers in the centers of the nanoparticles, while elemental Mo and N can both be found throughout the entire nanorod. The low-magnification HRTEM image in **Figure 5.4c** shows that the main part of the nanorod is in an amorphous state and the nanoparticles in the nanorod matrix are in a crystalline state. The phase boundaries between the amorphous nanorod matrix and the crystalline nanoparticles and between the metallic Ni and MoN phases, as well as the defects, can be clearly observed in the HRTEM image of Ni-MoN in **Figure 5.4d**. These multidimensional boundaries and defects can expose more active sites for boosting the catalytic reaction.^{28, 79} The interplanar spacings of the lattice fringes in the

center of each crystalline nanoparticle were precisely measured to be 0.176 nm (**Figure 5.4d-e**), corresponding to the (200) plane of metallic Ni. Additionally, a lattice fringe with an interplanar spacing of 0.186 nm, which is assigned to the (202) plane of MoN, can be found on the nanoparticle edges (**Figure 5.4d** and **5.4f**). Therefore, the nanorods in the hierarchical catalyst should be mainly composed of amorphous MoN, and the nanoparticles on the nanorods are mostly metallic Ni with a slight amount of MoN. It has been demonstrated that there might be a preferential reaction at the Ni sites in $\text{NiMoO}_4 \cdot x\text{H}_2\text{O}$ and that Mo-oxide reduction may only proceed *via* gas spillover from the Ni sites when being annealed in a reductive gas flow.¹⁵³⁻¹⁵⁴ Based on the characterizations above, the formation mechanism of Ni-MoN can be derived as follows: Ni sites are first reduced and gather to form metallic Ni at the centers of the nanoparticles when being annealed in ammonia flow, and Mo combines with nitrogen in the excess ammonia gas to form crystalline MoN on the edges of, or amorphous MoN between, these Ni nanoparticles. Clearly, reductive ammonia gas, serving as both the reducing agent and the nitrogen source, is the key to generate this unique nanorod-nanoparticle structure. Additionally, the loss of H_2O molecules and elemental due to the reaction with the flowing ammonia-argon gas, can create abundant atomic defects and lead to disordered atom packing in the nanorod matrix, forming amorphous regions.

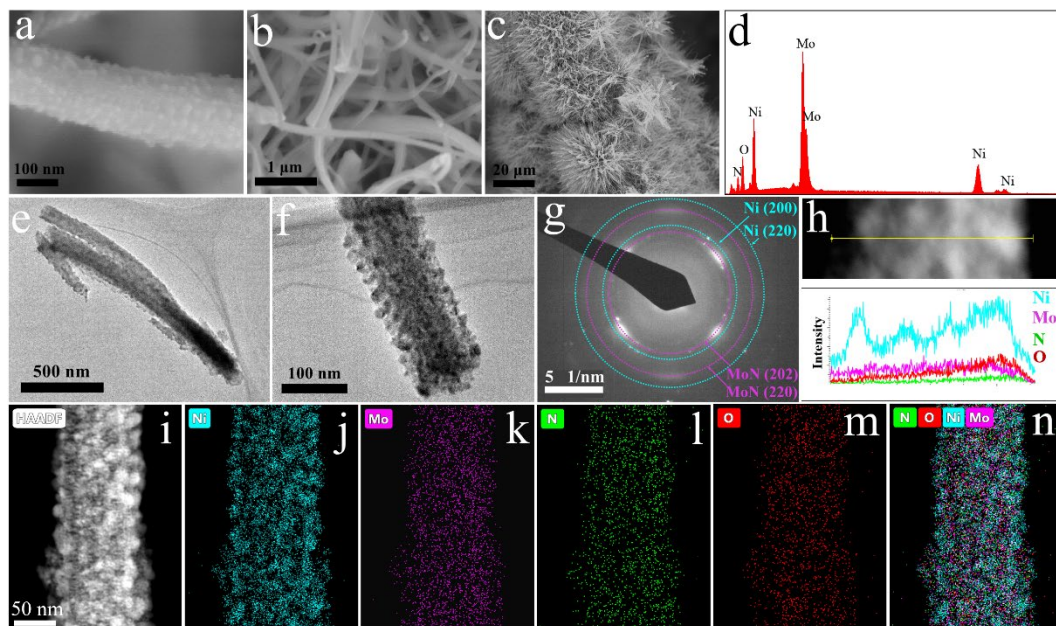


Figure 5.3. (a-c) SEM and (e-f) TEM images, (d) EDS spectrum, and (g) SAED pattern of Ni-MoN. (h) EDS line scan of a single Ni-MoN nanorod. (i) HAADF image and corresponding (j-n) EDS mapping images of Ni-MoN.

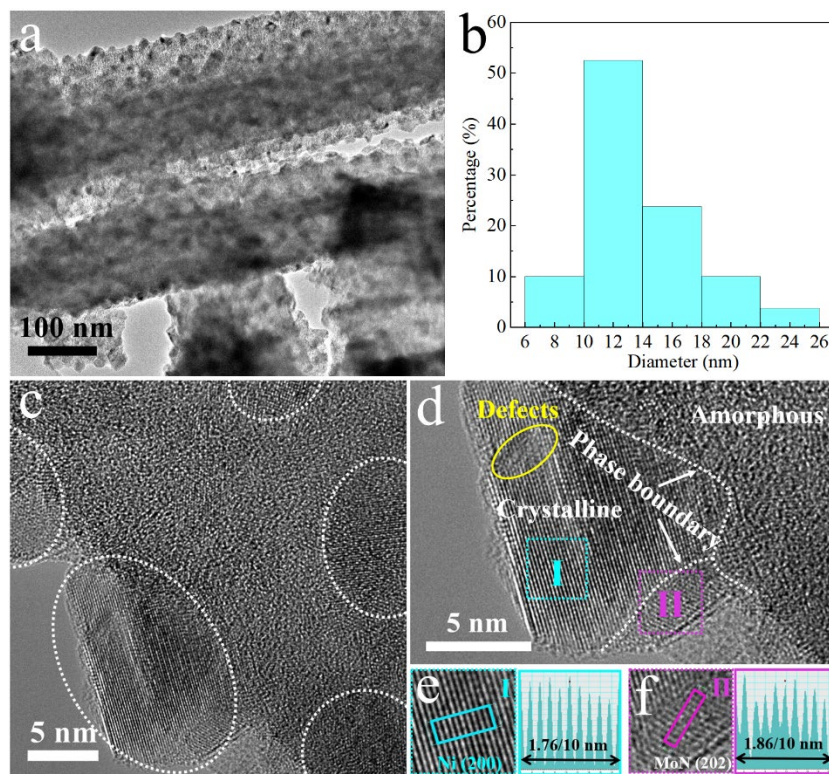


Figure 5.4. (a) TEM images of the Ni-MoN catalyst. (b) Diameter distribution of the nanoparticles. (c-d) Detailed HRTEM images of the Ni-MoN catalyst.

For a comprehensive comparison, nickel nitride and molybdenum nitride catalysts were synthesized using a similar procedure except that no Mo or Ni source was added to the initial reactants for the respective catalysts. SEM images show that nickel nitride has a nanoparticle structure (**Figure 5.5a-c**) and molybdenum nitride has an irregular film structure (**Figure 5.5g-i**). Clearly, the combination of Ni and Mo is essential for obtaining a hierarchical nanorod-nanoparticle structure. The phase composition and crystal structure of the hierarchical catalyst were further determined by XRD measurements. The XRD pattern of nickel nitride in **Figure 5.5f** shows peaks for both metallic nickel and nickel nitride (Ni_4N , JCPDS#36-1300), confirming a mixed composition of Ni and Ni_4N . There are no specific peaks in the XRD pattern of molybdenum nitride (**Figure 5.5l**) due to its poor crystallinity, so we used Mo-N to represent its composition.

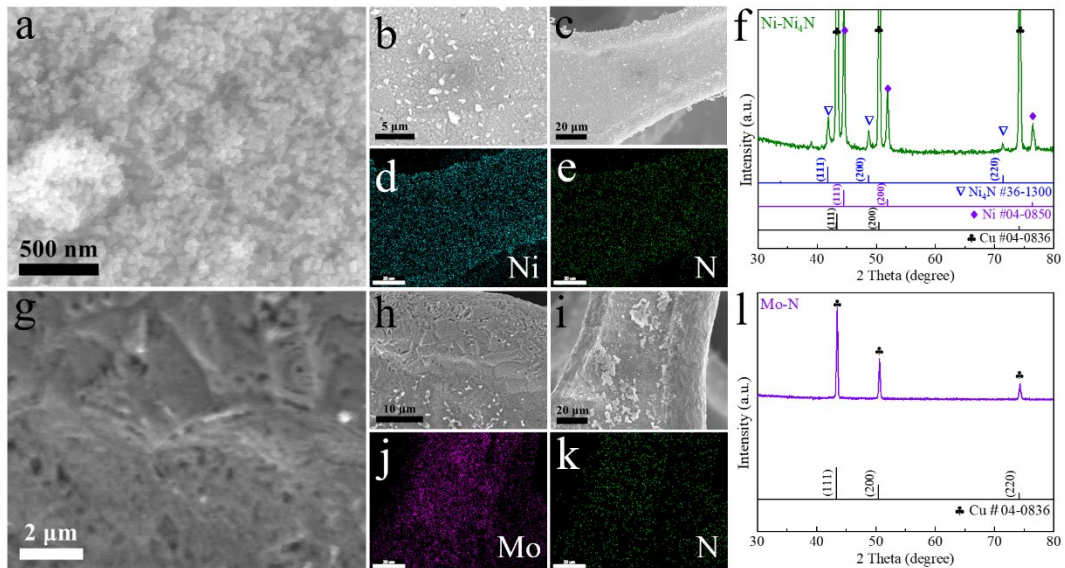


Figure 5.5. (a-c) SEM images and (f) XRD pattern of the Ni- Ni_4N . (d) Ni and (e) N EDS mapping images. (g-i) SEM images and (l) XRD pattern of the Mo-N. (j) Mo and (k) N EDS mapping images.

As shown in **Figure 5.6a**, the main peaks in the XRD pattern of Ni-MoN correspond to metallic nickel (Ni, JCPDS#04-0850) and molybdenum nitride (MoN, JCPDS#25-1367), which is consistent with the TEM results. The electron paramagnetic resonance (EPR) spectrum of Ni-MoN shows a stronger magnetic signal at around 3515 G (g factor = 2.005) than that of the NiMoO₄·xH₂O precursor (**Figure 5.6b**), indicating a higher concentration of unpaired electrons resulting from structure defects.¹⁵⁵⁻¹⁵⁶ This is in good agreement with the observation of multidimensional defects from the HRTEM images. The surface area of Ni-MoN was measured using the Brunauer-Emmett-Teller (BET) method and was found to be 27.5 m² g⁻¹ (**Figure 5.6c**), which is three times higher than that of the NiMoO₄·xH₂O precursor (7.6 m² g⁻¹), indicating that the hierarchical nanorod-nanoparticle structure efficiently enlarges the surface area. Additionally, the nitrogen adsorption-desorption isotherm of Ni-MoN shows a typical IV hysteresis loop, suggesting that it has a mesoporous structure with an average pore size of ~6.5 nm (inset, **Figure 5.6c**).¹⁵⁷⁻¹⁵⁹ A large surface area can disperse abundant active sites and a mesoporous structure can provide additional pores for electrolyte diffusion, thereby promoting effective utilization of the catalyst during water electrolysis. The surface chemical states of elemental Ni, Mo, and N for these catalysts were investigated by X-ray photoelectron spectroscopy (XPS). As shown in **Figure 5.6d**, two Ni⁰ peaks corresponding to metallic Ni can be observed at 853.4 and 870.6 eV for both Ni-MoN and Ni-Ni₄N but are absent for NiMoO₄·xH₂O, which agrees well with the metallic Ni phase observed in the XRD patterns. The remaining peaks in the XPS spectrum of Ni for Ni-MoN can be deconvoluted to Ni²⁺ 2p_{3/2} and Ni²⁺ 2p_{1/2} at 856.0 and 873.9 eV, respectively, along with a pair of satellite peaks, due

to the inevitable surface oxidation of metallic Ni in the air.^{9, 58, 145, 160} In the Mo XPS spectrum of Ni-MoN (**Figure 5.6e**), three doublets were observed: 230.0 and 233.1 eV (Mo^{3+} $3d_{5/2}$ and $3d_{3/2}$), 231.3 and 234.2 eV (Mo^{4+} $3d_{5/2}$ and $3d_{3/2}$), and 232.6 and 235.7 eV (Mo^{6+} $3d_{5/2}$ and $3d_{3/2}$).^{20, 149} Compared with the Mo XPS spectrum of $\text{NiMoO}_4 \cdot x\text{H}_2\text{O}$, the presence of Mo^{3+} in that of Ni-MoN confirms the formation of MoN and the negative shift of Mo^{4+} indicates a lower valence state caused by the reduction of Mo species under the ammonia flow.¹⁶¹⁻¹⁶² The Mo^{3+} peaks in the Mo XPS spectrum of Ni-MoN show a positive shift compared to those for Mo-N, indicating a possible electron transfer from Mo to adjacent atoms.¹⁴⁸ Additionally, the peak intensities of Ni^0 (metallic Ni) and Mo^{3+} (molybdenum nitride) are much stronger than those of Ni^{2+} (nickel oxide) and Mo^{4+} (molybdenum oxide), respectively, in the XPS spectra for Ni-MoN, confirming that elemental Ni and Mo in Ni-MoN mainly exist as metallic Ni and MoN rather than in oxide forms. Since the N 1s XPS spectrum of Ni-MoN is overlapped with that of Mo 3p (**Figure 5.6f**), three peaks were deconvolved to Mo 3p at 395.6 eV, N-Mo or N-Ni at 397.5 eV, and N-H at 399.0 eV.²⁰ In the N 1s XPS spectrum for Ni-Ni₄N, only a major peak attributed to N-Ni and a tiny peak attributed to N-H were found at 397.6 and 399.2 eV, respectively. Clearly, the N-Mo peak intensity in the XPS spectrum for Ni-MoN is much stronger than either the case of N-Ni in Ni-Ni₄N or that of N-Mo in Mo-N, indicating a tight connection between Mo and N in Ni-MoN.

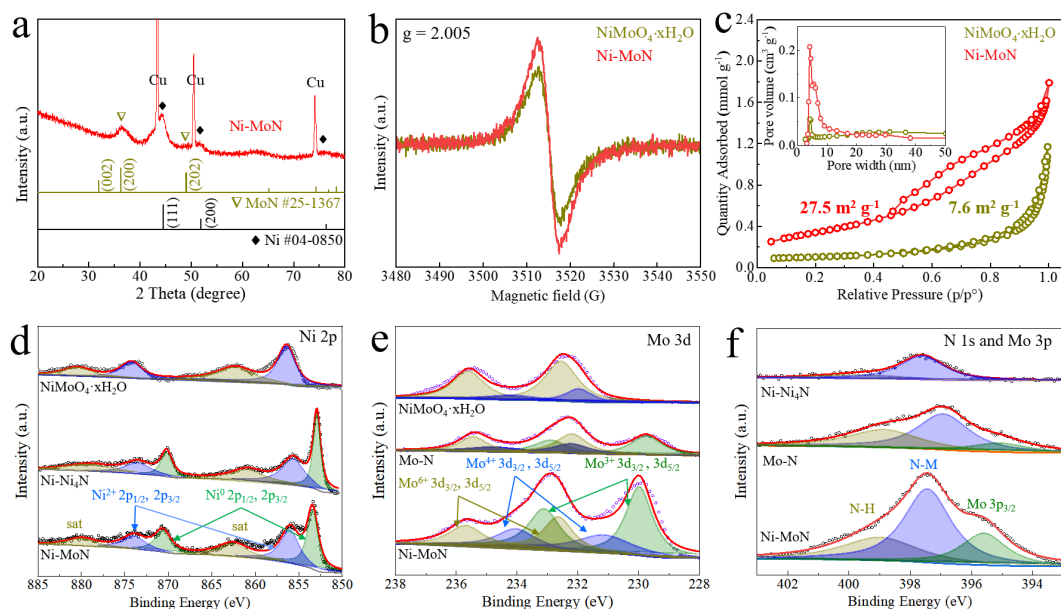


Figure 5.6. (a) XRD pattern of Ni-MoN. (b) EPR spectra and (c) nitrogen adsorption-desorption isotherms of $\text{NiMoO}_4 \cdot x\text{H}_2\text{O}$ and Ni-MoN. High-resolution XPS spectra of (d) Ni, (e) Mo, and (f) N and Mo for these catalysts.

5.3.2 HER Performance in Alkaline Freshwater

The HER catalytic performance of the as-prepared catalysts was evaluated in a typical three-electrode configuration at a scan rate of 1 mV s^{-1} . For HER activity in alkaline water (1 M KOH), the linear sweep voltammetry (LSV) curves in **Figure 5.7a** show that our Ni-MoN requires very low overpotentials (η) of 24 and 61 mV to attain current densities of 10 and 100 mA cm^{-2} , respectively, which is significantly smaller than those for the $\text{NiMoO}_4 \cdot x\text{H}_2\text{O}$ precursor (269 and 423 mV), Ni-Ni₄N (193 and 312 mV), and Mo-N (173 and 333 mV), as well as for the benchmark Pt/C (58 and 196 mV). The η_{100} of Ni-MoN (61 mV, where η_{100} is the overpotential required to attain a current density of 100 mA cm^{-2}) is even lower than that of some recently reported self-supported noble-metal-based catalysts such as Pt-IrO₂ (~70 mV),¹⁶³ Ru-MnFeP (~73 mV),¹⁶⁴ Ru-CoP (74 mV),¹⁶⁵ Pt_{SA}-NiO (85 mV),⁹⁶ and NiFeRu LDH (~110 mV).⁵² To achieve large current densities of 500 and 1000 mA cm^{-2} , which are

required for commercial applications, the Ni-MoN catalyst only requires low overpotentials of 104 and 136 mV, respectively. Tafel slope values were calculated to reveal the intrinsic catalytic kinetics of the as-prepared catalysts. As shown in **Figure 5.7b**, Ni-MoN has a small Tafel slope value of 35.5 mV dec^{-1} , which is less than one-quarter that of the $\text{NiMoO}_4 \cdot x\text{H}_2\text{O}$ precursor ($147.1 \text{ mV dec}^{-1}$), and is also much smaller than that of the comparison catalysts, including the benchmark Pt/C, indicating a higher transfer coefficient and enhanced catalytic kinetics.^{15, 34} Such efficient HER catalytic activity places this Ni-MoN catalyst among the best documented self-supported nitride and other catalysts reported to date (**Figure 5.7c**). To determine the origin of the catalytic activity of Ni-MoN, electrochemical impedance spectroscopy (EIS), electrochemically active surface area (ECSA), and turnover frequency (TOF) analyses were performed. An amorphous phase normally exhibits structure disorder and loose atom packing, which is beneficial for fast ion diffusion and electron transfer.^{93, 98} Thus, the catalyst's amorphous nanorod structure not only serves as a matrix for dispersing catalytic-active Ni-MoN nanoparticles but also acts as an expressway for electron transfer. Based on the fitted Nyquist plots and the equivalent circuit shown in **Figure 5.7d**, Ni-MoN has a much lower charge-transfer resistance (R_{ct}) of $\sim 2.7 \ \Omega$ at the electrode-electrolyte interface than that of the $\text{NiMoO}_4 \cdot x\text{H}_2\text{O}$ precursor ($\sim 161.6 \ \Omega$), suggesting a faster electron transport toward catalytic reaction. ECSA is usually calculated to evaluate the number of active sites, and it is proportional to the double-layer capacitance (C_{dl}) shown in **Figure 5.7a-e**.^{74, 166} Benefiting from the hierarchical nanorod-nanoparticle structure, abundant phase boundaries, and high concentration of defects, the ECSA of Ni-MoN ($377.5 \text{ cm}^{-2}_{\text{ECSA}}$)

is twice that of the $\text{NiMoO}_4 \cdot x\text{H}_2\text{O}$ precursor ($177.5 \text{ cm}^{-2}_{\text{ECSA}}$, **Figure 5.8f**), and much larger than that of the Ni-Ni₄N and Mo-N catalysts. When current density was normalized for ECSA (**Figure 5.7e**), Ni-MoN still exhibited the best HER performance among all the catalysts studied, confirming that it exhibits the highest intrinsic catalytic activity. Furthermore, turnover frequency (TOF) represents the number of molecules reacting per active site per unit of time and can be used to measure the instantaneous efficiency of a catalyst.¹⁶⁷ The TOF value for the Ni-MoN catalyst at the potential of -0.1 V vs. RHE is 1.79 s^{-1} (**Figure 5.7f**), which is much higher than that of the $\text{NiMoO}_4 \cdot x\text{H}_2\text{O}$ precursor (0.013 s^{-1}), indicating a high instantaneous efficiency for HER catalysis. Notably, all results from the EIS, ECSA, and TOF analyses agree well with the low overpotentials and small Tafel slope value of Ni-MoN shown in **Figure 5.7a** and **5.7b**, respectively, suggesting its ultrahigh intrinsic HER activity. For practical application of a catalyst, its durability must be taken into consideration. As shown in **Figure 5.7g** shows the results of long-term stability tests of the Ni-MoN catalyst performed at constant current densities. It can be seen that the potential fluctuation at a current density of 100 mA cm^{-2} over 200 h continuous testing in 1 M KOH is only 16 mV, which is superior to many self-supported catalysts. Furthermore, the Ni-MoN catalyst can work well at the industry-standard current density of 500 mA cm^{-2} for over 200 h despite some potential fluctuation, showing great potential for practical application.

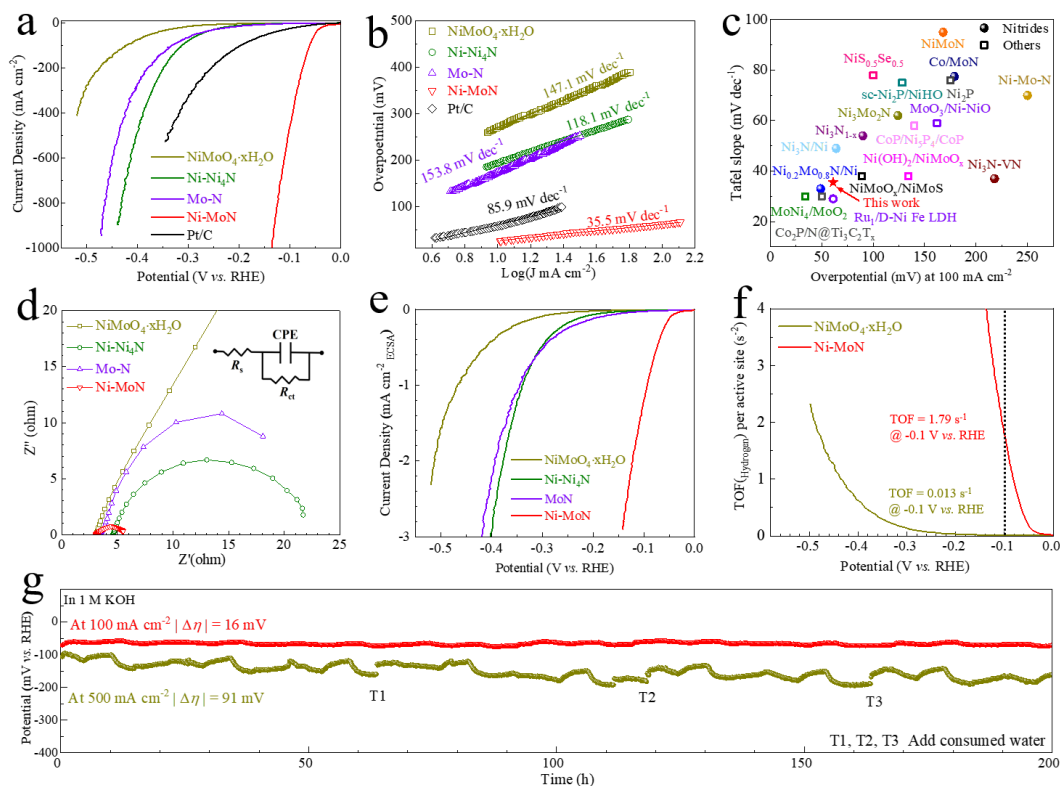


Figure 5.7. (a) HER LSV curves and (b) Tafel plots of these catalysts in 1 M KOH. (c) Comparison of HER activity. (d) Nyquist plots and (e) ECSA-normalized HER LSV curves. (f) TOF curves. (g) Stability performance of Ni-MoN.

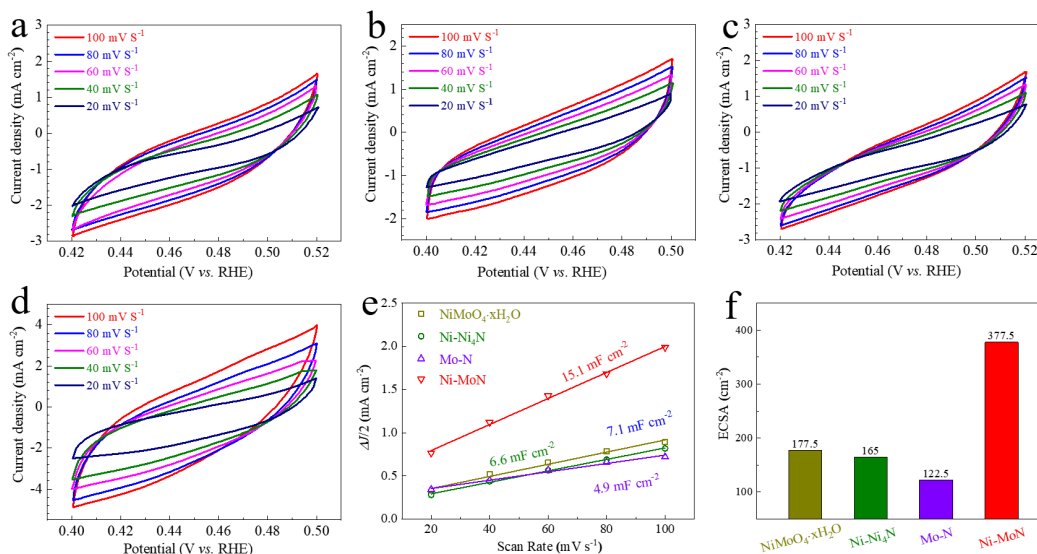


Figure 5.8. CV curves of (a) NiMoO₄·xH₂O, (b) Ni-Ni₄N, (c) Mo-N, and (d) Ni-MoN catalysts. (e) Corresponding C_{dl} values of these catalysts calculated from (a-d). (f) ECSA values of NiMoO₄·xH₂O, Ni-Ni₄N, Mo-N, and Ni-MoN.

The hierarchical nanorod-nanoparticle structure and large surface area of Ni-MoN can provide abundant active sites for water electrolysis and its hydrophilic surface helps to achieve accelerated gas-release capabilities. As a result, the hydrogen gas bubbles, when still very small in size, can be released rapidly from numerous active sites as shown in **Figure 5.9a**. A previous study confirms that a hydrophilic surface normally possesses very low adhesive force between the gas bubbles and the catalyst, which might be good for catalytic stability.¹⁵² On the other hand, the hydrogen gas bubbles will remain attached to the hydrophobic surface of CF and merge together into large-size bubbles as shown in **Figure 5.9b**. These large-size bubbles will prevent the further contact between the active sites and the electrolyte and their bursting can cause resistance/potential fluctuations.^{128, 168}

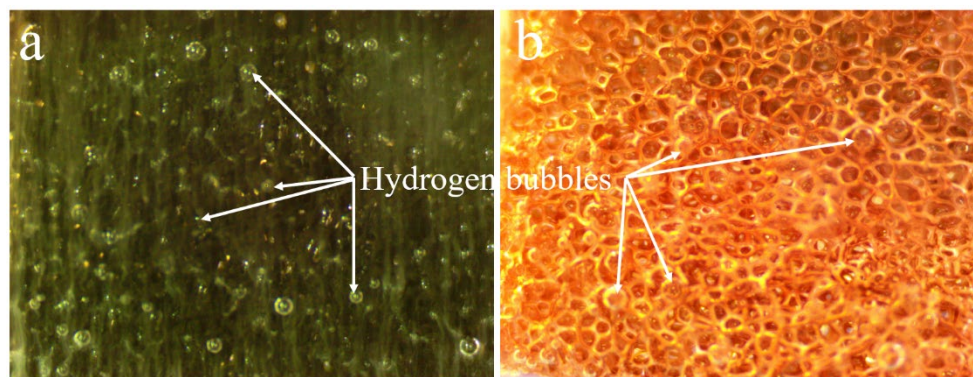


Figure 5.9. Digital images of hydrogen gas bubbles on the surfaces of (a) Ni-MoN and (b) CF at a current density of 100 mA cm^{-2} in 1 M KOH electrolyte.

The effects of the Ni:Mo ratio and ammonia reduction temperature on the final morphology and catalytic performance of Ni-MoN were investigated. Based on the SEM images of Ni-MoN catalysts produced with different Ni:Mo ratio shown in **Figure 5.10a-c**, we found that the Ni:Mo ratio in the reactants did not have a significant effect on the nanorod structure but had a huge effect on the density of the

Ni-MoN nanoparticles. Low Ni:Mo ratios of 2:7 (**Figure 5.10a**) and 4:7 (**Figure 5.10b**) resulted in sparse nanoparticles and a high Ni:Mo ratio of 12:7 (**Figure 5.10c**) resulted in dense nanoparticles. This is because these nanoparticles are mainly composed of metallic Ni and a higher Ni:Mo ratio is beneficial for forming denser Ni nanoparticles on the MoN matrix. To determine the best conditions for synthesizing the Ni-MoN catalyst, the influences of Ni:Mo ratio and ammonia-reduction temperature on its HER activity were investigated in detail. As shown in **Figure 5.10d**, all the Ni-MoN catalysts with different Ni:Mo ratios exhibit very good HER activity, and the one with a ratio of 8:7 shows the highest activity. The composition of the ammonia-treated catalysts can be tuned by varying the annealing temperature, as shown by the intensities of the diffraction peaks in the corresponding XRD patterns in **Figure 5.11**. A low annealing temperature of 300 °C results in the catalyst being mainly composed of the $\text{NiMoO}_4 \cdot x\text{H}_2\text{O}$ phase and a high temperature of 500 °C results in a mainly MoN-phase composition, which might be due to the weaker and stronger reactivity of ammonia species at low and high temperatures, respectively. So it has a significant effect on the catalytic performance as well. A low temperature of 300 °C and a high temperature of 500 °C both lead to inferior HER activity.

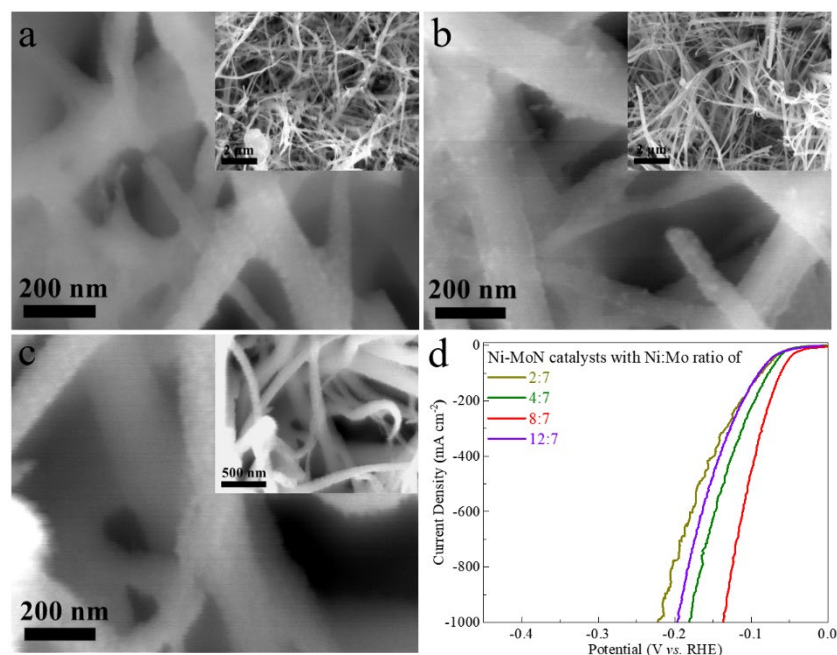


Figure 5.10. SEM images of Ni-MoN catalysts with different Ni:Mo ratios of (a) 2:7, (b) 4:7, and (c) 12:7. (d) HER LSV curves these catalysts in 1 M KOH.

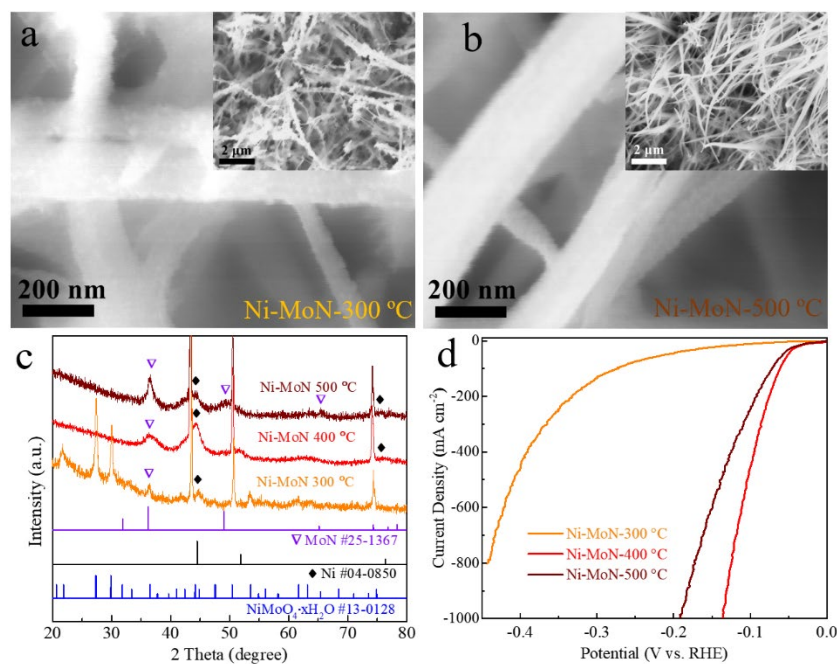


Figure 5.11. SEM images of Ni-MoN catalysts annealed at (a) 300 °C and (b) 500 °C in a mixed ammonia-argon flow. (c) XRD patterns and (d) HER LSV curves of these catalysts in 1 M KOH.

5.3.3 HER Performance in Alkaline Seawater

Seawater electrolysis is attracting increasing research interest due to the inexhaustible reserves of feedstock.^{10, 17} Considering the remarkable HER performance of Ni-MoN in alkaline water, we then measured its hydrogen-generation ability in alkaline natural seawater (1 M KOH seawater). As shown in **Figure 5.12a**, compared with their corresponding LSV curves in 1 M KOH (**Figure 5.8a**), all five as-prepared catalysts show a decline in activity in 1 M KOH seawater, which could be caused by the obstruction of active sites and the degradation in conductivity in the complicated natural seawater electrolyte. However, our Ni-MoN catalyst still exhibits very good HER activity with limited degradation in 1 M KOH seawater electrolyte. Specifically, it requires overpotentials of 29, 66, 128, and 176 mV to attain current densities of 10, 100, 500, and 1,000 mA cm⁻², respectively, in 1 M KOH seawater. The corresponding Tafel slope of Ni-MoN in 1 M KOH seawater is 36.8 mV dec⁻¹ (**Figure 5.12b**), close to that in 1 M KOH, showing good retention of catalytic activity. To verify the durability of the Ni-MoN catalyst, HER LSV curves were recorded before and after CV cycling in both 1 M KOH and 1 M KOH seawater electrolytes. As shown in **Figure 5.12c**, after 19,000 (19k) CV cycles in 1 M KOH electrolyte, the resultant LSV curve (orange) shows a slight decline compared with the initial curve (red). Even after 48,000 CV cycles in 1 M KOH seawater electrolyte (violet), the required overpotential of the Ni-MoN catalyst only increased by 1, 5, 10, and 13 mV to attain current densities of 10, 100, 500, and 1000 mA cm⁻², respectively, compared with its initial catalytic performance in 1 M KOH seawater electrolyte (brown). Even in 1 M KOH seawater electrolyte (**Figure 5.12d**), this catalyst can work stably over

100 h at a large current density of 500 mA cm^{-2} with an affordable overpotential fluctuation of 47 mV. Considering that the concentration of NaCl in seawater electrolyte will increase due to the continuous consumption of water during the process of seawater catalysis, we then measured the catalytic activity of Ni-MoN in a harsh chlorine environment to verify its robustness against corrosive chlorine. As shown in **Figure 5.12e**, the catalytic activity of Ni-MoN in 1 M KOH + 0.5 M NaCl (alkaline simulated seawater) is close to that in 1 M KOH electrolyte. After further increasing the chlorine concentration (1 M KOH + 1 M NaCl and 1 M KOH + 2 M NaCl), the HER activity exhibits slight decay, but is still better than the performance in alkaline natural seawater, demonstrating good chlorine-resistant performance. When measured at a constant current density of 100 mA cm^{-2} in harsh chlorine electrolytes, the Ni-MoN catalyst operated well for 115 h and did not show much increase in overpotential (23 mV in total, **Figure 5.12f**).

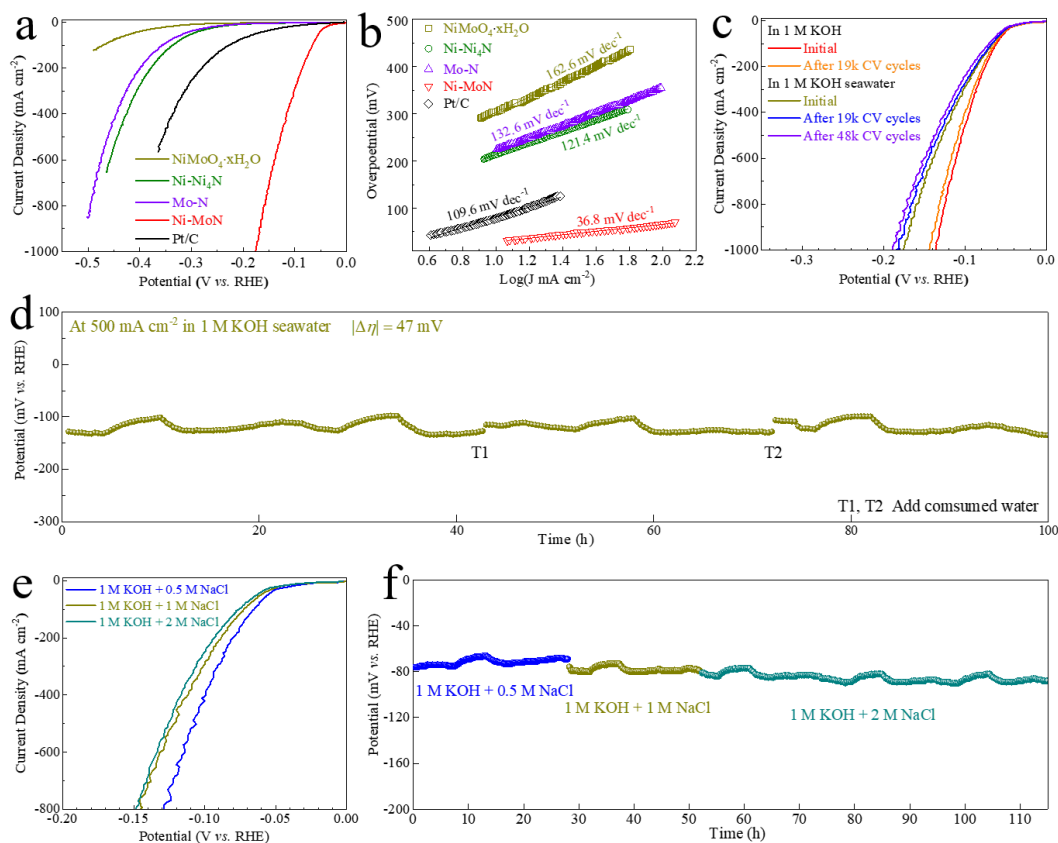


Figure 5.12. (a) HER LSV curves and (b) Tafel plots of these catalysts in 1 M KOH seawater. (c) CV cycling performance, (e) HER LSV curves, and (d) and (f) stability performance of the Ni-MoN in different electrolytes.

We further investigated changes in the morphology and composition of the Ni-MoN catalyst after long-term stability testing for HER catalysis. SEM images in **Figure 5.13a-d** show that the hierarchical nanorod-nanoparticle structure of the Ni-MoN catalyst was mostly maintained after long-term stability testing, although some of the catalyst was peeled off. The TEM image in **Figure 5.13e** shows that some nanosheets formed on the surfaces of the nanorods, the composition of which was identified as a mixture of NiOOH and NiO by SAED pattern (**Figure 5.13f**) and HRTEM image (**Figure 5.13g**) analysis. The high-resolution XPS spectrum of Ni for Ni-MoN after performing 19,000 CV cycles in 1 M KOH (**Figure 5.13h**) shows that the peaks attributed to metallic Ni disappeared and that new peaks attributed to

NiOOH emerged. The Raman spectrum (**Figure 5.13i**) of the Ni-MoN catalyst after CV cycling further confirmed the formation of the -OOH species. Similarly, the SEM images and EDS spectrum (**Figure 5.14**) of the Ni-MoN catalyst after stability testing for 115 h in alkaline saline show that the main structure of the catalyst was maintained while the intensity of the O peak was enhanced greatly in the EDS spectrum. Such results together reveal that some nanosheets formed on the surfaces of the nanorods after HER stability testing, and their composition was identified as a mixture of NiOOH and NiO, which is consistent with previous reports.^{149, 169}

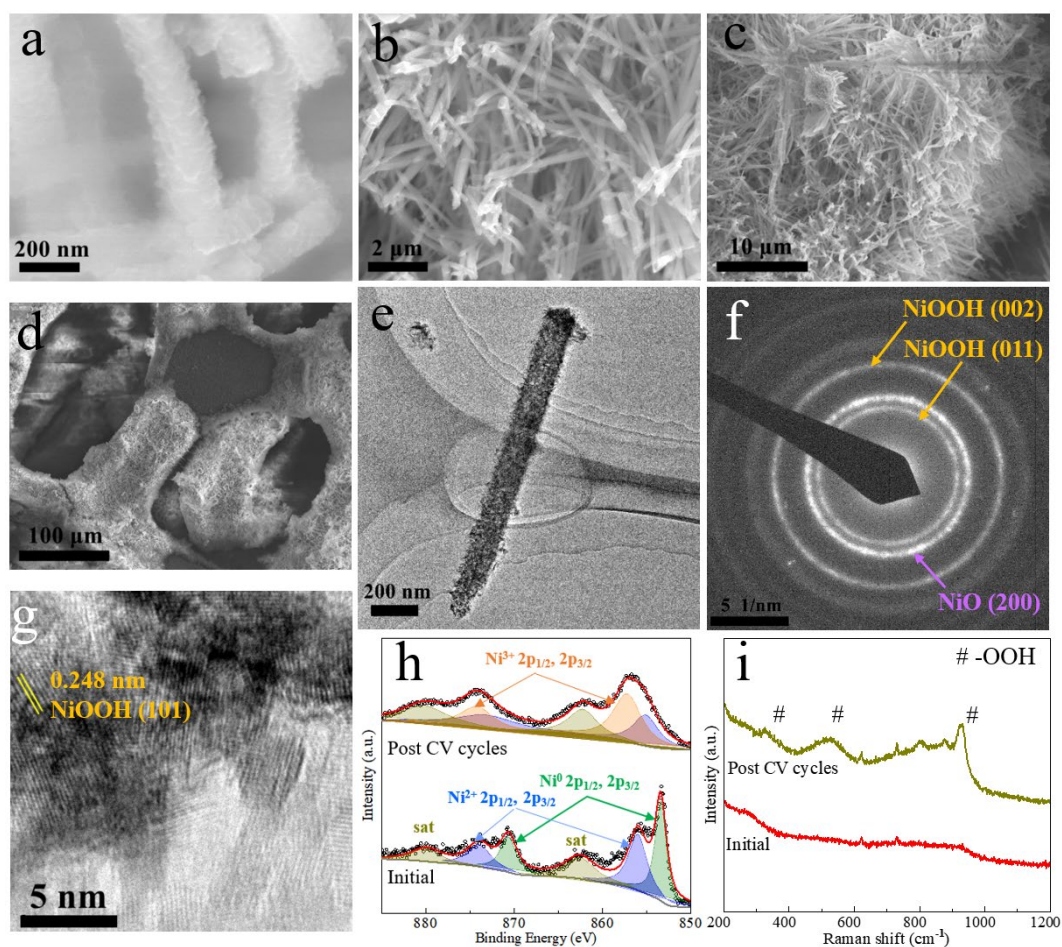


Figure 5.13. (a-d) SEM images, (e) TEM image, (f) SAED pattern, and (g) HRTEM image of the Ni-MoN after stability testing. (h) XPS and (i) Raman spectra of the Ni-MoN before and after 19,000 CV cycles in 1 M KOH.

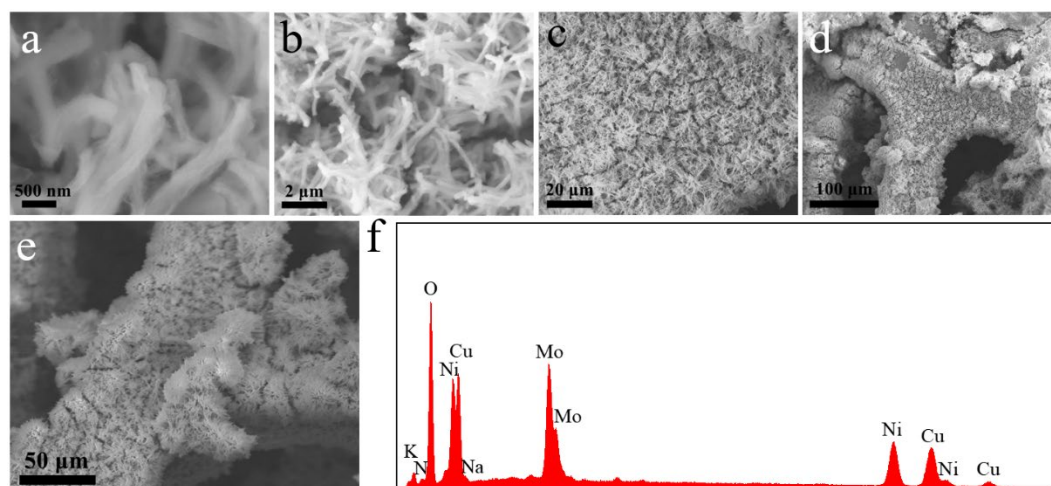


Figure 5.14. (a-e) SEM images and (f) EDS spectrum of the Ni-MoN catalyst after 115-h stability testing at a constant current density of 100 mA cm^{-2} in alkaline saline electrolytes.

5.3.4 DFT Calculation Results

To gain molecular-level insights into the high catalytic activity of Ni-MoN, density functional theory (DFT) calculations were performed. Typical models of Ni-MoN consisting of metallic Ni clusters on MoN (202), metallic Ni (111), and MoN (202) were built and are shown in **Figure 5.15a-f**. Besides the XPS data, the electronic structure tuning in Ni-MoN can also be confirmed by the charge density distributions displayed in **Figure 5.16a**, which shows that there is an accumulation of charge density on both the N and Mo sites, unlike the case of MoN (**Figure 5.16b**).¹⁷⁰⁻¹⁷¹ The charge density differences shown in **Figure 5.16c-d**, in which yellow and cyan regions represent electron accumulation and depletion, respectively, illustrate that there is electron accumulation at the heterointerface, suggesting a strong charge exchange and electronic tuning between Ni and MoN.¹⁷²⁻¹⁷³ The successive distribution of the density of states (DOS) near the Fermi level, as shown in **Figure 5.16e**, indicates that

Ni-MoN is in a metallic state, which is beneficial for achieving high electronic conductivity.^{57, 161}

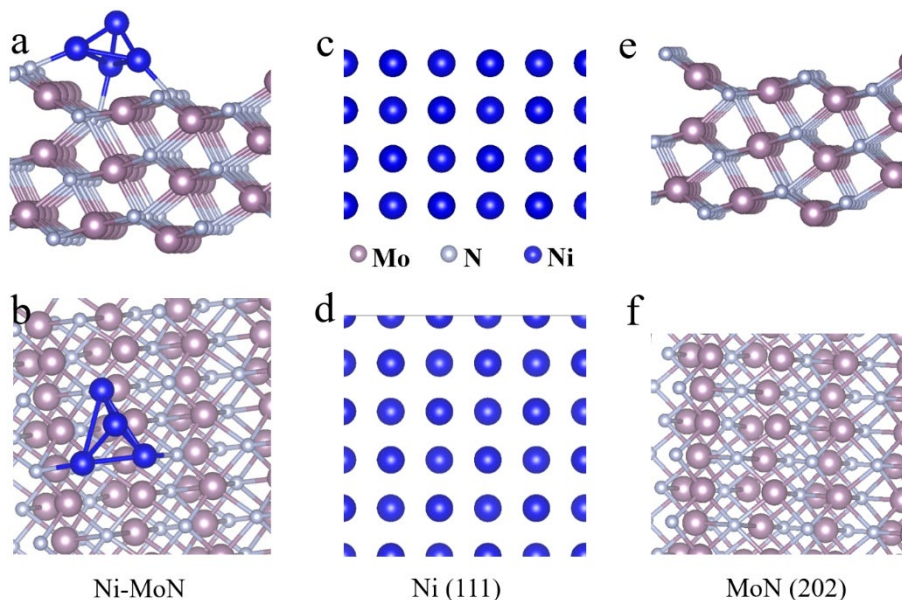


Figure 5.15. Side and top views, respectively, of the (a-b) Ni-MoN, (c-d) metallic Ni (111), and (e-f) MoN (202) models for DFT calculations.

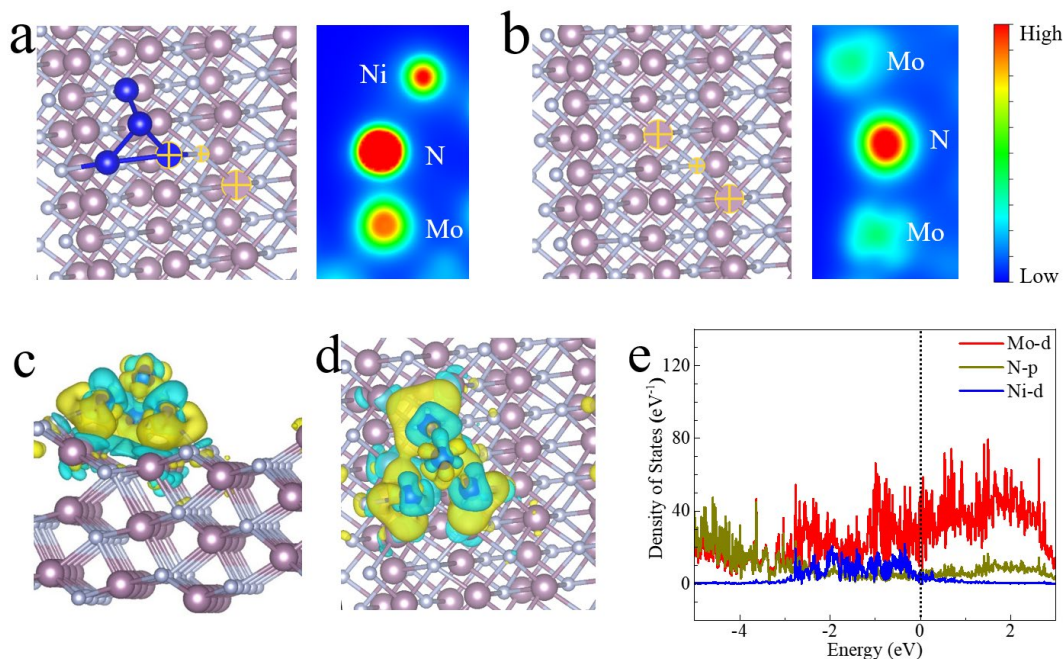


Figure 5.16. Charge density distributions of (a) MoN and (b) Ni-MoN. (c) Side and (d) top views of charge density differences in Ni-MoN. (e) DOS calculated for Mo, N, and Ni in Ni-MoN. The black dotted line indicates the Fermi level.

The Tafel slope value of Ni-MoN is 35.5 mV dec⁻¹, suggesting that the catalytic pathway of Ni-MoN follows a Volmer (H₂O dissociation, $M + H_2O + e^- \rightarrow M-H^* + OH^-$)-Heyrovsky (H adsorption/desorption, $M-H^* + H_2O + e^- \rightarrow M + OH^- + H_2$) routine.^{28, 57, 139, 174} Therefore, we further calculated the H₂O adsorption energy, the energy barrier of H₂O dissociation, and the H adsorption/desorption energy to deeply understand the Volmer-Heyrovsky pathway for the Ni-MoN catalyst. The models for DFT calculations include the (111) facet of metallic Ni, the (202) facet of pristine MoN, Ni sites on top of the Ni clusters in Ni-MoN, and Mo sites near the interface between Ni and MoN in Ni-MoN, and corresponding reaction pathways are shown in **Figure 5.17a-d**. **Figure 5.18a** shows that the Mo sites in Ni-MoN possess much lower adsorption energy for H₂O molecules (-1.082 eV) than the other three sites, indicating more favorable H₂O adsorption on the surface of Mo sites in Ni-MoN.⁹ This is important for boosting alkaline HER since absorption of H₂O molecules is the preliminary step for the subsequent H₂O dissociation process.⁵⁷ **Figure 5.18b** shows the H₂O dissociation energy results, from which it can be seen that the energy barrier of water dissociation (ΔG_{H_2O}) on metallic Ni and Mo sites in MoN are as high as 0.93 and 1.81 eV, respectively. In contrast, the ΔG_{H_2O} on Ni-MoN, especially on the Mo sites in Ni-MoN, is significantly decreased to 0.46 eV, suggesting accelerated H₂O dissociation kinetics.¹⁶³ This is crucial for alkaline HER catalysis, in which the Volmer step (H₂O dissociation) has been regarded as the rate-determining step (RDS).¹⁷⁵ The hydrogen adsorption energy (ΔG_{H^*}) on the Mo sites in Ni-MoN was calculated to be -0.487 eV (**Figure 5.18c**), the absolute value of which is smaller than that on Ni sites in Ni-MoN (-0.644 eV), from which it can be inferred that Mo sites are

more favorable for H adsorption and desorption during the Heyrovsky step.^{161, 174} It should be noted that although metallic Ni shows the lowest absolute value of ΔG_{H^*} (-0.258 eV), its sluggish H₂O dissociation and inferior H₂O absorption ability restrict its catalytic performance. Clearly, the combination of Ni and MoN lead to higher ΔG_{H_2O} on Ni sites and lower ΔG_{H_2O} on Mo sites in Ni-MoN compared with that on the pristine Ni cluster and the pristine MoN phase. Therefore, the DFT calculation results demonstrate that the introduction of Ni effectively regulates the electronic structure of MoN, which endows Mo sites in Ni-MoN with high capability towards H₂O adsorption and dissociation, thus contributing to the catalyst's outstanding HER activity in alkaline media.

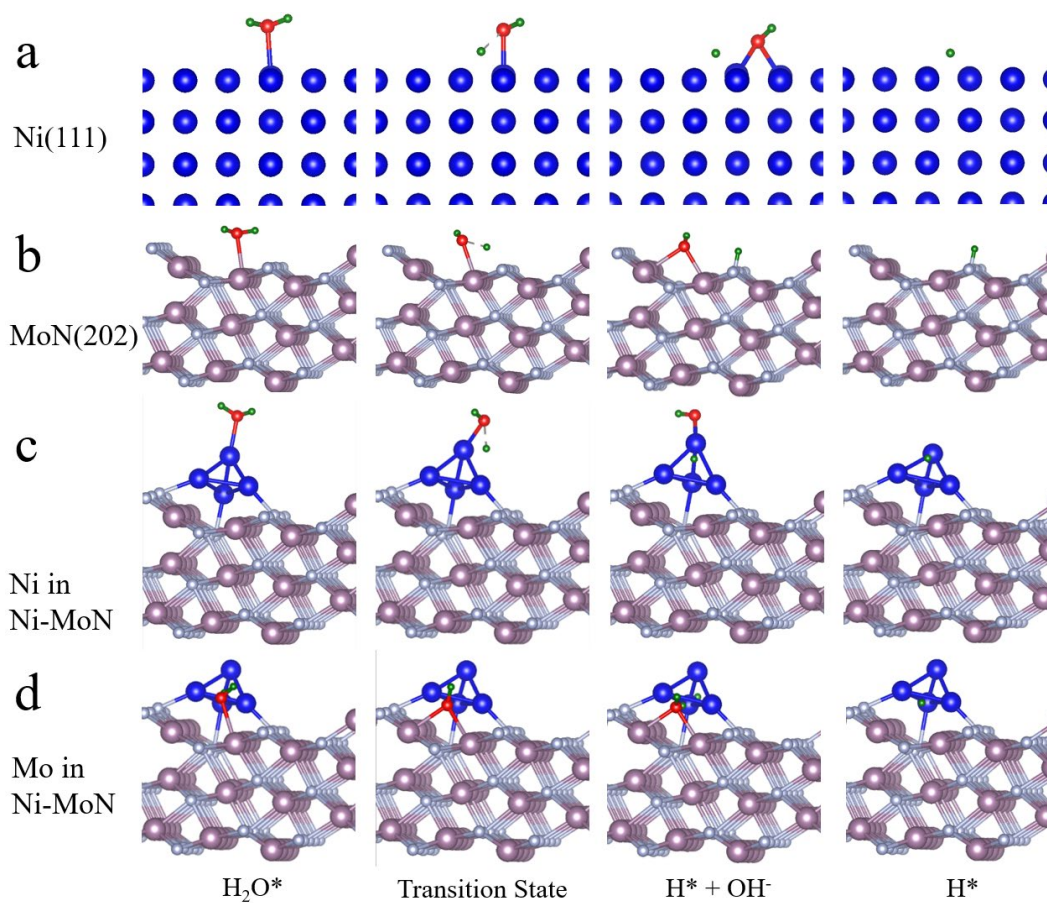


Figure 5.17. Structure models for water adsorption, transition state, water dissociation, and hydrogen adsorption over (a) Ni (111), (b) Mo (202), (c) Ni sites and (d) Mo sites in Ni-MoN. Red: O; green: H.

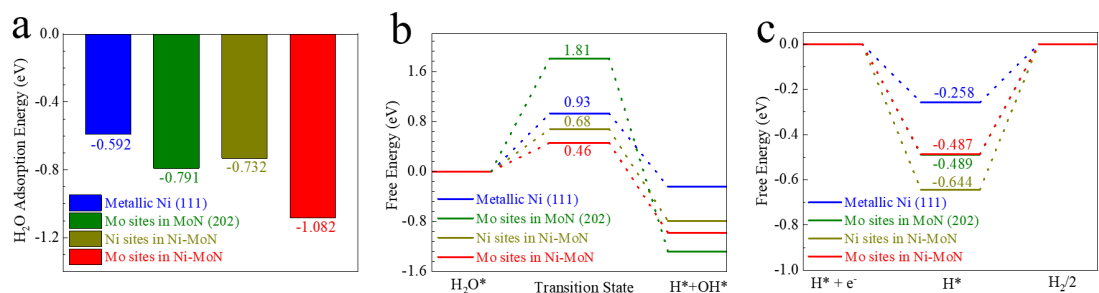


Figure 5.18. (a) Adsorption energy of H₂O, (b) energy diagram for H₂O dissociation, and (c) free energy diagram for H adsorption for metallic Ni, Mo sites in MoN, and Ni and Mo sites in Ni-MoN.

5.3.5 Overall Water/Seawater Electrolysis Performance

We then coupled our Ni-MoN catalyst with commercial stainless-steel mat (SSM) in an H-type electrolyzer with an anion exchange membrane (AEM) separator in the middle for overall water/seawater electrolysis. The silver-colored SSM electrode (**Figure 5.1e**) has a dense microrod structure with a mixed composition of Fe, Cr, Ni, and Mo.¹³³ For comparison, we grew Ni-Fe LDH, one of the most OER-active catalysts, on CF using the same water bath reaction method as for Ni-MoN and then paired it with the benchmark HER catalyst Pt/C for overall water/seawater electrolysis. Impressively, the Ni-MoN||SSM pair outperforms the benchmark Pt/C||Ni-Fe LDH pair as shown in **Figure 5.19a**. This good electrolyzer requires voltages of only 1.613 (1.635) and 1.711 (1.783) V to attain current densities of 100 and 500 mA cm⁻² in 1 M KOH (1 M KOH seawater) electrolyte, respectively (**Figure 5.19b**), which are significantly lower than those for the Pt/C||Ni-Fe LDH pair. Such low voltage requirements to drive a current density of 100 mA cm⁻² make this electrolyzer outperform many recently reported catalysts (**Figure 5.19c**) for overall water/seawater

electrolysis. For an even larger current density of $1,000 \text{ mA cm}^{-2}$, the Ni-MoN||SSM pair requires voltages of 1.779 and 1.885 V in 1 M KOH and 1 M KOH seawater electrolytes, respectively, demonstrating remarkable catalytic activity. Long-term stability of the Ni-MoN||SSM pair was assessed at constant current densities and the results are shown in **Figure 5.19d** and **5.19e**. At a constant current density of 100 mA cm^{-2} , this electrolyzer can work effectively for $\sim 100 \text{ h}$ in both 1 M KOH and 1 M KOH seawater electrolytes with only slight fluctuations of 36 and 48 mV, respectively. Although there was some voltage fluctuation under a large current density of 500 mA cm^{-2} in 1 M KOH seawater, the Ni-MoN||SSM pair still operated well for 100 h, indicating good stability for hydrogen production *via* seawater electrolysis.

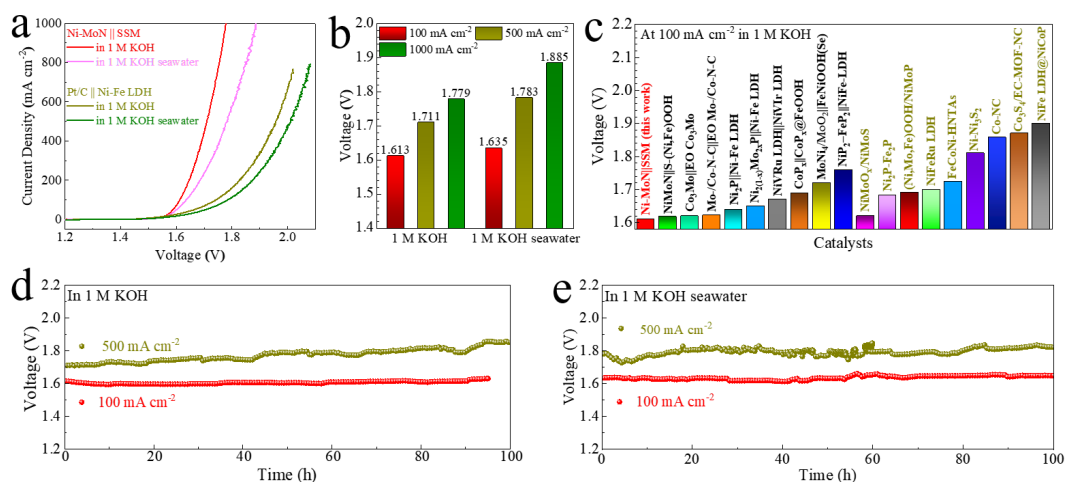


Figure 5.19. (a-b) Overall water/seawater electrolysis performance of Ni-MoN||SSM and Pt/C||Ni-Fe LDH pairs. (c) Comparison of the catalytic performance. (d-e) Stability performance of Ni-MoN||SSM pair in different electrolytes.

We also used a commercial thermoelectric (TE) module, a device that can convert thermal energy into electricity (**Figure 5.20a-b**), to drive the Ni-MoN||SSM pair in 1 M KOH electrolyte. Encouragingly, our electrolyzer can be effectively driven by a single TE module on a homemade testing platform with temperature differences of around 49, 54, and 61 °C for output current densities of 83, 129, and 190 mA cm^{-2} ,

respectively, as shown in **Figure 5.20c**. The corresponding **Figure 5.20b** recorded during testing at the temperature difference of 61 °C shows that abundant hydrogen bubbles were generated on, and immediately released from, the surface of the Ni-MoN catalyst, demonstrating that waste heat can be efficiently converted into valuable hydrogen energy through water electrolysis.

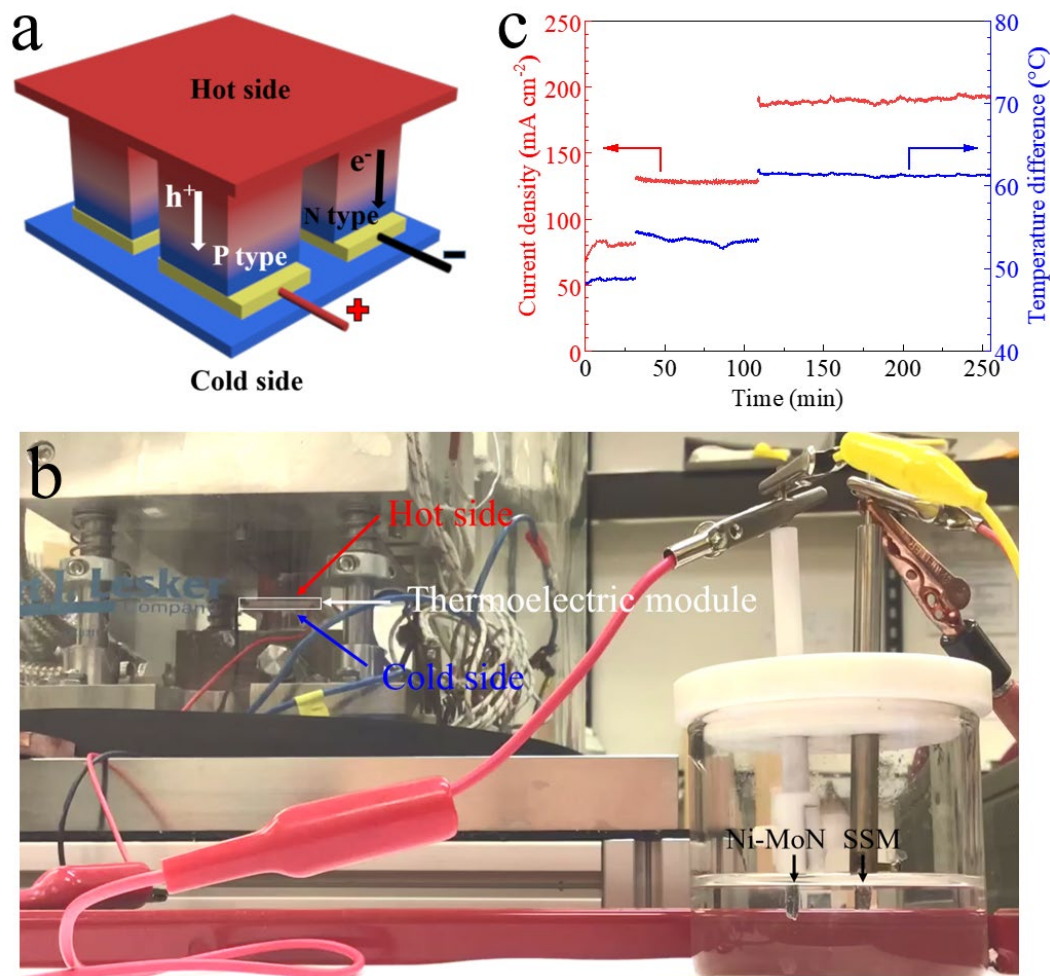


Figure 5.20. (a) Schematic illustration of a TE device. (b) Overall water electrolysis testing at the temperature difference of 61 °C. (c). Real-time dynamics of current density driven by a TE device at different temperature.

Finally, we measured the catalytic activity of Ni-MoN and the Ni-MoN||SSM pair under industrial conditions (in 6 M KOH electrolyte at 60 °C), and the results are shown in **Figure 5.21a-b**. In particular, to achieve an ultrahigh current density of 120

3,000 mA cm⁻² in 6 M KOH and 6 M KOH seawater electrolytes at 60 °C for HER, the Ni-MoN catalyst requires low overpotentials of 152 and 244 mV, respectively. For overall water and seawater electrolysis under these conditions, the Ni-MoN||SSM pair requires voltages of only 1.690 and 1.718 V, respectively, to reach the ultrahigh current density of 3000 mA cm⁻². In addition, when measured in 6 M KOH electrolyte at 60 °C, this Ni-MoN||SSM pair can work efficiently at 500 mA cm⁻² for more than 110 h (Figure 5.21c), indicating a great potential for realistic industrial freshwater electrolysis.

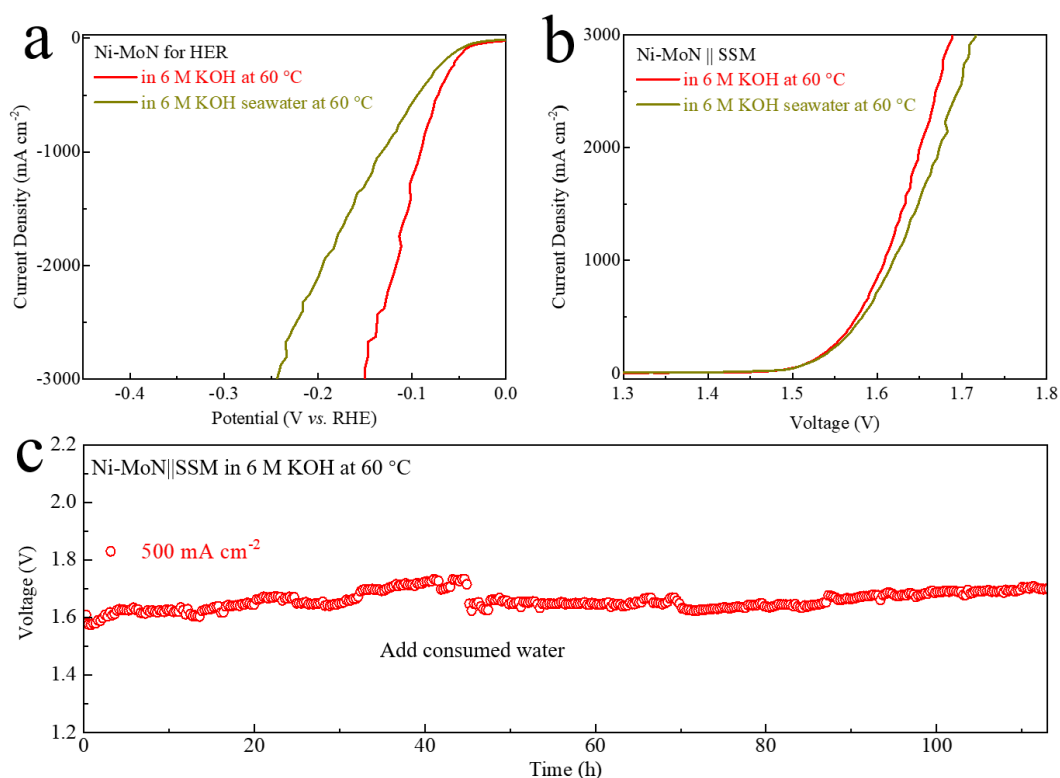


Figure 5.21. HER LSV curves of the Ni-MoN under industrial condition. (b) Overall water/seawater electrolysis curves and (c) stability performance of the Ni-MoN||SSM pair under industrial condition.

5.4 Conclusion

A heterogeneous Ni-MoN catalyst consisting of metallic Ni and MoN was synthesized and exhibits outstanding HER performance in both alkaline water and seawater electrolytes. Structure characterizations show that it has a hierarchical nanorod-nanoparticle structure with a large surface area, multidimensional boundaries/defects, and a hydrophilic surface. These characteristics allow Ni-MoN to possess abundant active sites and accelerated gas-release capabilities and to effectively avoid catalyst degradation during HER catalysis, especially at large current densities. Experimental results and DFT calculations together prove that the combination of metallic Ni and MoN can modulate the electron redistribution and enhance the sluggish water-dissociation kinetics. As a result, our Ni-MoN catalyst demonstrates remarkable HER catalytic activity and durability, outperforming the benchmark Pt/C and many other efficient alkaline HER catalysts. When Ni-MoN is coupled with SSM, an OER catalyst, the Ni-MoN||SSM pair is outstanding in overall water/seawater electrolysis, showing great promise for large-scale H₂ production.

CHAPTER 6 BIMETALLIC PHOSPHIDE $\text{Ni}_2\text{P-Fe}_2\text{P}$ AS A BIFUNCTIONAL CATALYST FOR WATER AND SEAWATER ELECTROLYSIS

Note: The material in this chapter has been published. The introduction, experimental section, and figure captions were adjusted for dissertation consistency. Reproduced with permission from Wiley.¹⁷⁶

6.1 Introduction

Among the catalysts for water electrolysis, Ir/Ru- and Pt-based compounds have been identified as state-of-the-art ones for OER and HER, respectively,^{52, 64} but the high cost and scarcity of these precious metals severely impede their large-scale application. It is thus desirable to develop cost-effective and catalytic-active non-noble-metal based catalysts to replace these expensive ones. In particular, bifunctional catalysts, which are active for both reactions, are more favorable for practical application due to the advantages of simplifying the devices and reducing the cost.¹⁷⁷ Over the past few years, transition metal phosphides (TMPs) have attracted intense attention due to their high intrinsic catalytic activity, tunable structure, and composition,¹⁸ first emerging as efficient HER catalysts in earlier research.³⁶ Very recently, there has been a focus on heterogeneous bimetallic phosphides as OER or bifunctional catalysts due to their various structural and chemical advantages.

Although significant research effort has been devoted to developing efficient TMP catalysts for water electrolysis in the freshwater condition, studies on their use in the seawater condition remain quite limited. Considering their high catalytic activity and

corrosion resistance features, bimetallic phosphides might be promising bifunctional catalysts for seawater electrolysis. Here we synthesize self-supported heterogeneous Ni₂P-Fe₂P on commercial nickel foam (denoted Ni₂P-Fe₂P/NF) *via* a novel *in situ* growth-ion exchange-phosphidation approach. This bimetallic phosphide catalyst possesses excellent bifunctional catalytic activity and long-term stability under large current density in both alkaline freshwater and seawater electrolytes. Its open, porous, and ultrathin (~7.4 nm) microsheet architecture allows for intrinsically high catalytic activity, enhanced electronic kinetics, and abundant active sites. Additionally, the Ni₂P-Fe₂P microsheet structure, along with its hydrophilic feature, can provide adequate space for diffusion of the electrolyte and accelerate the release of bubbles, leading to superior catalytic activity and stability at high current density. With optimized Fe³⁺ among its reactants, this as-prepared Ni₂P-Fe₂P/NF electrode achieves relatively low overpotential and fast current increase toward both OER and HER. Typically, it requires overpotentials of only 261 and 225 mV to drive current density of 100 mA cm⁻² for OER and HER in 1 M KOH electrolyte, respectively. As for overall water/seawater electrolysis, it requires voltages of 1.682 and 1.811 V to drive current density of 100 mA cm⁻² in 1 M KOH freshwater and 1 M KOH seawater electrolytes, respectively, which are superior to the respective voltages required by the benchmark IrO₂||Pt/C pair and which place this catalyst among best bifunctional catalysts reported thus far. Our work presents a general and economic approach toward the fabrication of heterogeneous bimetallic phosphide catalysts for highly efficient and stable hydrogen production *via* water/seawater electrolysis.

6.2 Experimental Section

6.2.1 Synthesis of Catalysts

6.2.1.1 Synthesis of Ni(OH)₂ Nanosheets

Ni(OH)₂ nanosheets were *in situ* grown on the surface of Nickel foam (NF) *via* a room-temperature etching-growth approach. Briefly, a piece of commercial NF (3 cm × 1 cm) was first cleaned by ethanol and deionized (DI) water with the assistance of ultrasonication for 15 min each. Afterward, the clean NF was immersed in hydrochloric acid (HCl, Marcon Fine Chemical, 3 M), for 1.5 h to etch the surface, followed by an immersion treatment in DI water for 24 h to grow Ni(OH)₂ nanosheets on the surface.

6.2.1.2 Synthesis of Ni₂P-Ni₅P₄ Microsheets

In a typical phosphidation procedure, 120 mg red phosphorous powder (P, Sigma-Aldrich) was placed upstream in a tube to serve as the phosphorous source. Subsequently, the as-obtained Ni(OH)₂/NF precursor was placed at the center of the tube and was phosphorized under an Ar steam at 450 °C for 1.5 h. After being cooled down, the resulting product was denoted Ni₂P-Ni₅P₄/NF.

6.2.1.3 Synthesis of Ni₂P-Fe₂P Microsheets

To synthesize Ni₂P-Fe₂P microsheets, the Ni(OH)₂/NF was first soaked in a 0.1 M aqueous iron nitrate solution [2 mmol Fe(NO₃)₃·9H₂O (Alfa Aesar) dissolved in 20 mL DI water] at room temperature for 1 h. After the ion-exchange process with Fe cations was complete, the light red (Ni,Fe)(OH)₂/NF precursor was removed from the solution and then underwent the phosphidation process as described above for synthesizing Ni₂P-Ni₅P₄/NF. Here, the resulting product was denoted Ni₂P-Fe₂P/NF.

In order to confirm the optimal iron nitrate solution concentration of 0.1 M, other Ni₂P-Fe₂P/NF-X (X = 0.025, 0.05, and 0.15) samples were prepared *via* a similar procedure except that the Ni(OH)₂/NF samples were each soaked in a different aqueous iron nitrate solution with a concentration of 0.025, 0.05, or 0.15 M, respectively.

6.2.1.4 Preparation of Pt/C and IrO₂ Electrodes

To prepare the Pt/C and IrO₂ electrodes, 80 mg active material [either platinum (Pt, nominally 20% on carbon black, Alfa Aesar) or iridium oxide (IrO₂, 99%, Alfa Aesar)] was uniformly dispersed in a mixture solution containing 90 μL Nafion solution (5%, Sigma-Aldrich), 810 μL ethanol, and 600 μL DI water with the assistance of intense ultrasonication. A clean piece of NF was then soaked in the solution for 1 h to let the active material coat the surface, followed by drying at 50 °C for 12 h in an oven. The loading masses of Ni₂P-Fe₂P, Ni₂P-Ni₅P₄, and Pt/C (IrO₂) were calculated to be around 15.0, 16.0, and 12.8 (7.7) mg cm⁻², respectively.

6.2.2 Physical and Chemical Characterization

The crystal structures and compositions of the as-prepared samples were characterized by X-ray diffraction (XRD, PANalytical X'pert PRO, Cu Kα radiation). The morphologies and X-ray energy-dispersive spectroscopy (EDS) were examined by scanning electron microscopy (SEM, LEO 1525) and transmission electron microscopy (TEM, JEOL 2010F). The X-ray photoelectron spectroscopy (XPS) was acquired using a PHI Quantera XPS scanning microprobe to determine the valence states. Atomic force microscopy (AFM) characterization was performed with a Bruker 8 atomic force microscope to measure microsheet thickness.

6.2.3 Electrochemical Characterization

Electrochemical characterizations of all samples were performed on a Gamry Reference 600 electrochemical station. The catalytic activity was determined using a three-electrode configuration in which a carbon rod and a Pt wire were used as the counter electrode for HER and OER testing, respectively; a Hg/HgO electrode was used as the reference electrode; and each as-prepared sample was used as the working electrode. The catalytic activity was evaluated in three different types of alkaline electrolytes, 1 M KOH, 1 M KOH + 0.5 M NaCl, and 1 M KOH seawater. All potentials applied were calibrated to the reversible hydrogen electrode (RHE) using the equation: $E_{RHE} = E_{Hg/HgO} + 0.098 + 0.0591 \times \text{pH}$, where the pH of all these three electrolytes is around 14. The linear sweep voltammetry (LSV) curves were recorded at a scan rate of 2 mV s^{-1} with iR (current times internal resistance) compensation. The overpotential (η) for HER was recorded as the calculated E_{RHE} and that for OER was calculated as $\eta = E_{RHE} - 1.23 \text{ V}$. The Tafel slope (b) was calculated by $\eta = a + b \log(j)$, where j is the current density. Overall alkaline water/seawater electrolysis tests were carried out in a homemade two-electrode cell using bifunctional N₂P-Fe₂P/NF as both the anode and cathode electrodes. Electrochemical impedance spectroscopy (EIS) was performed at the overpotentials of 300 mV for OER and 250 mV for HER from 0.01 Hz to 100 kHz in 1 M KOH electrolyte. For durability testing, 3,000 CV cycles were performed between 1.225 and 1.525 V vs. RHE for OER and between 0 and -0.250 V vs. RHE for HER with a scan rate of 100 mV s^{-1} , and the corresponding LSV curves were recorded before and after the CV cycles were performed. The chronopotentiometric measurements were recorded at the current densities of 100 and

500 mA cm⁻² in both 1 M KOH and 1 M KOH seawater electrolytes. Natural seawater was collected from Galveston Bay, Galveston, Texas, USA (29.303° N, 94.772° W). Before use in experiments, the natural seawater was kept in a bottle for around one week to let the sand and particles visible to the naked eye settle to the bottom, after which the supernatant was collected.

6.2.4 Calculation of TOF

The TOF value of OER/HER was estimated using the equation:^{47, 178}

$$\text{TOF} = \frac{\text{Number of total oxygen (or hydrogen) turn overs / geometrical area (cm}^2\text{)}}{\text{Number of surface active sites / geometrical area (cm}^2\text{)}}.$$

The total numbers of oxygen/hydrogen turn overs were calculated using the equations:⁴¹

$$\begin{aligned} \text{Number of O}_2 &= \left(j \frac{\text{A}}{\text{cm}^2} \right) \left(\frac{1 \text{ C s}^{-1}}{1000 \text{ mA}} \right) \left(\frac{6.02 \times 10^{23} \text{ O}_2 \text{ molecules}}{1 \text{ mol O}_2} \right) \left(\frac{1 \text{ mol e}^-}{96485.3 \text{ C}} \right) \left(\frac{1 \text{ mol O}_2}{4 \text{ mol e}^-} \right) \\ &= 1.56 \times 10^{15} \frac{\text{O}_2 \text{ s}^{-1}}{\text{cm}^2} \text{ per } \frac{\text{mA}}{\text{cm}^2}, \text{ and} \end{aligned}$$

$$\begin{aligned} \text{Number of H}_2 &= \left(j \frac{\text{A}}{\text{cm}^2} \right) \left(\frac{1 \text{ C s}^{-1}}{1000 \text{ mA}} \right) \left(\frac{6.02 \times 10^{23} \text{ H}_2 \text{ molecules}}{1 \text{ mol H}_2} \right) \left(\frac{1 \text{ mol e}^-}{96485.3 \text{ C}} \right) \left(\frac{1 \text{ mol H}_2}{2 \text{ mol e}^-} \right) \\ &= 3.12 \times 10^{15} \frac{\text{H}_2 \text{ s}^{-1}}{\text{cm}^2} \text{ per } \frac{\text{mA}}{\text{cm}^2}. \end{aligned}$$

The nature of the active sites is not yet understood, we thus estimated the number of the active sites as the total number of the surface sites from the roughness factor together with the unit cell of the catalysts, which may underestimate the real TOF. The active sites can be calculated using following equations and corresponding unit cell information shown in **Figure 6.11c-e**:

$$\text{Number of active sites} = \left(\frac{\text{Number of atoms/unit cell}}{\text{Volume/unit cell}} \right)^{2/3},$$

$$\text{Number of active sites (Ni}_2\text{P)} = \left(\frac{9 \text{ atoms/unit cell}}{100.04 \text{ \AA}^3 / \text{unit cell}} \right)^{2/3} = 2.00 \times 10^{15} \text{ atoms cm}^{-2},$$

$$\text{Number of active sites (Ni}_5\text{P}_4) = \left(\frac{36 \text{ atoms/unit cell}}{439.16 \text{ \AA}^3 / \text{unit cell}} \right)^{2/3} = 1.89 \times 10^{15} \text{ atoms cm}^{-2}, \text{ and}$$

$$\text{Number of active sites (Fe}_2\text{P)} = \left(\frac{9 \text{ atoms/unit cell}}{100.33 \text{ \AA}^3 / \text{unit cell}} \right)^{2/3} = 2.00 \times 10^{15} \text{ atoms cm}^{-2}.$$

So, the total number of the active sites of Ni₂P-Fe₂P is $2.00 \times 10^{15} \text{ atoms cm}^{-2}$ and of Ni₂P-Ni₅P₄ is around $1.95 \times 10^{15} \text{ atoms cm}^{-2}$. Then, the plots of current density can be converted into TOF plots using the following formulas:

$$\text{TOF}_{\text{OER}} = \frac{1.56 \times 10^{15} \frac{\text{O}_2 \text{ s}^{-1}}{\text{cm}^2} \text{ per } \frac{\text{mA}}{\text{cm}^2} \times j}{\text{Number of active sites} \times A_{\text{ECSA}}} \text{ and}$$

$$\text{TOF}_{\text{HER}} = \frac{3.12 \times 10^{15} \frac{\text{H}_2 \text{ s}^{-1}}{\text{cm}^2} \text{ per } \frac{\text{mA}}{\text{cm}^2} \times j}{\text{Number of active sites} \times A_{\text{ECSA}}}.$$

6.2.5 Calculation of Faradaic Efficiency

Overall seawater electrolysis for gas chromatography (GC, GOW-MAC 350 TCD) tests were performed in a gas-tight homemade two-electrode cell in 1 M KOH seawater electrolyte. Chronopotentiometry was applied with a constant current of 100 mA to maintain oxygen and hydrogen generation. For each measurement over an interval of 30 min, a 0.3 mL gas sample was extracted from the sealed cell and injected into the GC instrument using a glass syringe (Hamilton Gastight 1002).²⁰

The theoretical amount of evolved gases was calculated using the equations: $m = Q/(n \times F)$ and $Q = i \times t$, where m is the theoretical amount (mol) of gaseous products, Q is the accumulated charge (C), n is the number of electrons transferred ($n = 2$ for HER and $n = 4$ for OER), F is the Faraday constant ($96,485 \text{ C mol}^{-1}$), i is the current

(A), and t is the time (s). The faradaic efficiency (FE) of O_2 gas was calculated according to the equation: $FE = \text{measured amount of } O_2 \text{ gas} / \text{theoretical amount of } O_2 \text{ gas} \times 100\%$.

6.3 Results and Discussion

6.3.1 Structural and Compositional Analysis Results

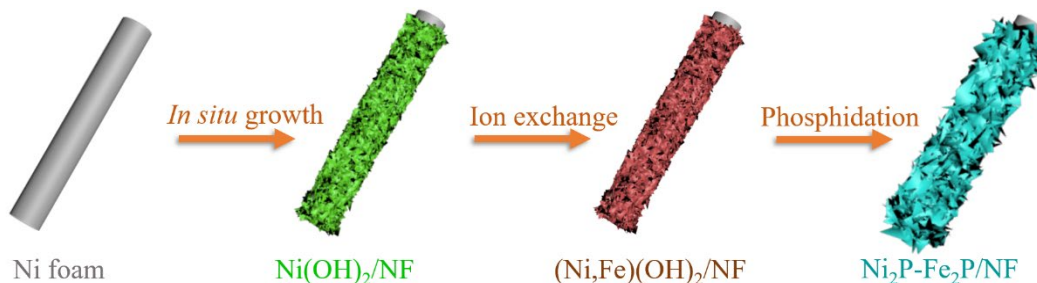


Figure 6.1. Schematic illustration of the formation of Ni₂P-Fe₂P/NF *via* a three-step *in situ* growth-ion exchange-phosphidation procedure.

As schematically illustrated in **Figure 6.1**, the Ni₂P-Fe₂P/NF catalyst was synthesized *via* a three-step *in situ* growth-ion exchange-phosphidation approach, in which commercial nickel foam (NF) was employed as both the conductive substrate and the Ni source. First, the surface of the NF (**Figure 6.2a-b**) was converted to Ni(OH)₂ nanosheets (**Figure 6.2c-d**) using a novel “etching growth” method reported here for the first time. Briefly, a piece of clean NF was etched by 3 M HCl for 1.5 h and then immersed in DI water for another 24 h at room temperature to grow uniform nanosheets. The composition of these nanosheets was determined to be Ni(OH)₂ by their X-ray diffraction (XRD) pattern (**Figure 6.2e**) and Raman curve (**Figure 6.2f**), respectively.

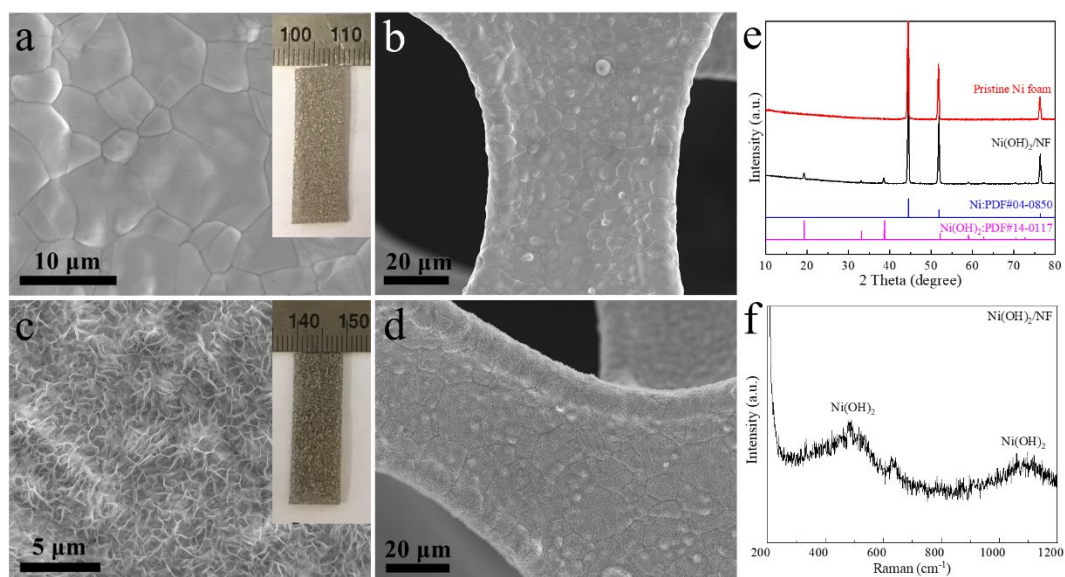


Figure 6.2. SEM images of (a, b) pristine Ni foam and (c, d) Ni(OH)₂/NF. (e) XRD patterns of pristine Ni foam and Ni(OH)₂/NF samples. (f) Raman spectrum of Ni(OH)₂/NF sample.

Following this facile conversion, the as-obtained Ni(OH)₂/NF underwent ion exchange with Fe cations by being soaked in an aqueous iron nitrate solution (**Figure 6.3**). Compared to pristine NF with a smooth surface, the nanosheet-structured Ni(OH)₂/NF with a hydrophilic feature is able to load more Fe cations to form (Ni,Fe)(OH)₂/NF, which is light red in color, as proved by the bottom photographs in **Figure 6.3**. Finally, the Ni(OH)₂/NF and (Ni,Fe)(OH)₂/NF precursors were converted to nickel phosphide and nickel iron phosphide, respectively, during the subsequent phosphidation process.

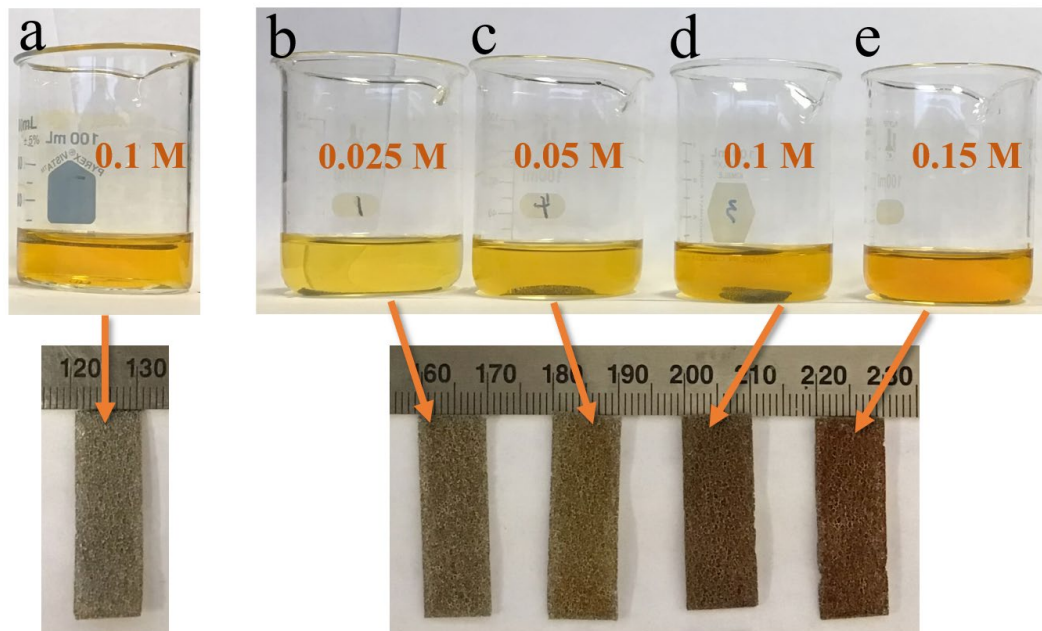


Figure 6.3. (a) Photograph of pristine NF undergoing ion exchange in 0.1 M iron nitrate solution. Photographs of $\text{Ni(OH)}_2/\text{NF}$ undergoing ion exchange in (b) 0.025 M, (c) 0.05 M, (d) 0.1 M, and (e) 0.15 M iron nitrate solutions.

The SEM images of nickel phosphide in **Figure 6.4a-c** show that numerous smooth microsheets up to 10 μm in length were grown on the NF substrate and the corresponding EDS mapping images in **Figure 6.4d-e** indicate that the P atoms were uniformly alloyed with Ni over the whole surface. XRD measurements were employed to investigate the compositions of these as-prepared phosphide-based samples. As shown in **Figure 6.4f**, the main diffraction peaks of nickel phosphide can be well indexed to Ni_2P (PDF#03-0953) and Ni_5P_4 (PDF#18-0883), indicating that the nickel phosphide sample is a Ni_2P - Ni_5P_4 hybrid. This result is similar to that from our earlier work employing a similar phosphidation approach on pristine Ni foam.⁴²

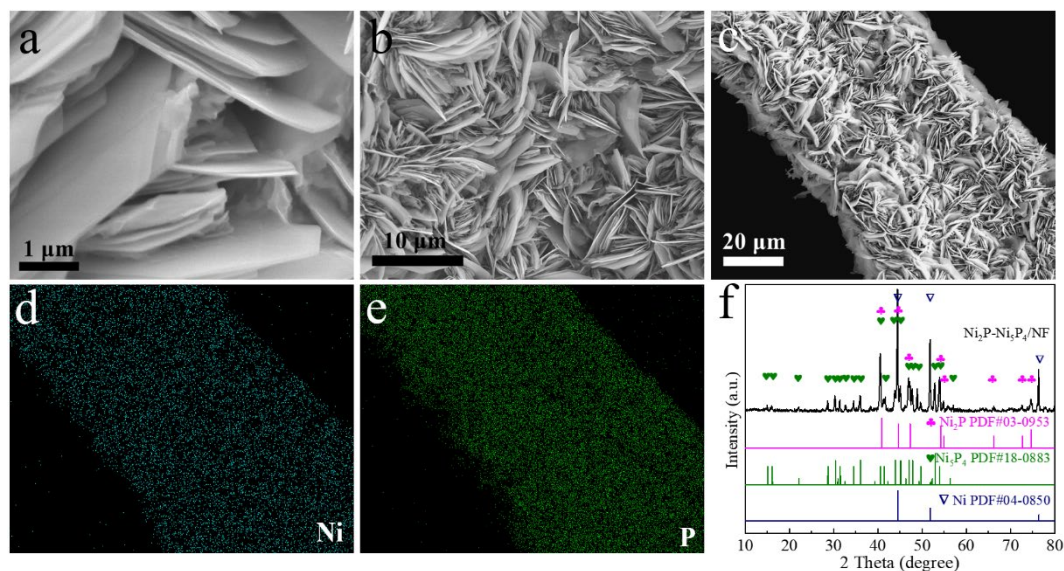


Figure 6.4. (a, b) SEM images and (c) Ni and (d) P EDS mapping images corresponding to (b) of nickel phosphide. (f) XRD pattern of a nickel phosphide sample obtained from the phosphidation of a Ni(OH)₂/NF.

Unlike for the Ni₂P-Ni₅P₄ sample, the surface morphology of the nickel iron phosphide microsheets was significantly modified by the Fe cations, resulting in a rough topography with some nanoparticles attached as shown in the SEM images (**Figure 6.5a-c**). A slice of a Ni₂P-Fe₂P microsHEET was selected for transmission electron microscopy (TEM) measurement (**Figure 6.5d**). The interplanar spacings determined by high-resolution TEM (HRTEM) and shown in **Figure 6.5e** are 0.221, 0.167, and 0.508 nm, corresponding to the (111) and (211) planes of Ni₂P and the (100) plane of Fe₂P, respectively. The heterostructure, which can produce an interfacial bonding effect and is beneficial for exposing more active sites,⁴⁹⁻⁵⁰ can be directly observed by the phase boundary between the Ni₂P and Fe₂P phases marked in **Figure 6.5e**. The ring patterns from selected area electron diffraction (SAED) shown in **Figure 6.5f** reveal the characteristic (001) and (200) facets of Fe₂P and the (111) and (210) facets of Ni₂P. The uniform distribution of elemental Ni, Fe, and P inside a

single microsheet is illustrated by the energy-dispersive X-ray spectrometry (EDX) mapping images in **Figure 6.5g-j**. This synthesis method can result in a homogeneous $\text{Ni}_2\text{P-Fe}_2\text{P}$ product in which the atomic ratio of Fe is around 3.2%. The XRD pattern of the nickel iron phosphide sample (**Figure 6.5k**) also reveals that it was transformed into a mixture of Ni_2P (PDF#03-0953) and Fe_2P (PDF#51-0943) following the introduction of Fe cations in the ion-exchange process, which matches well with the TEM characterizations above. The *in situ* growth of $\text{Ni}_2\text{P-Fe}_2\text{P}$ microsheets on the conductive NF will enhance the transportation of electrons and reduce the charge-transfer resistance between the catalyst and the electrolyte.⁵¹

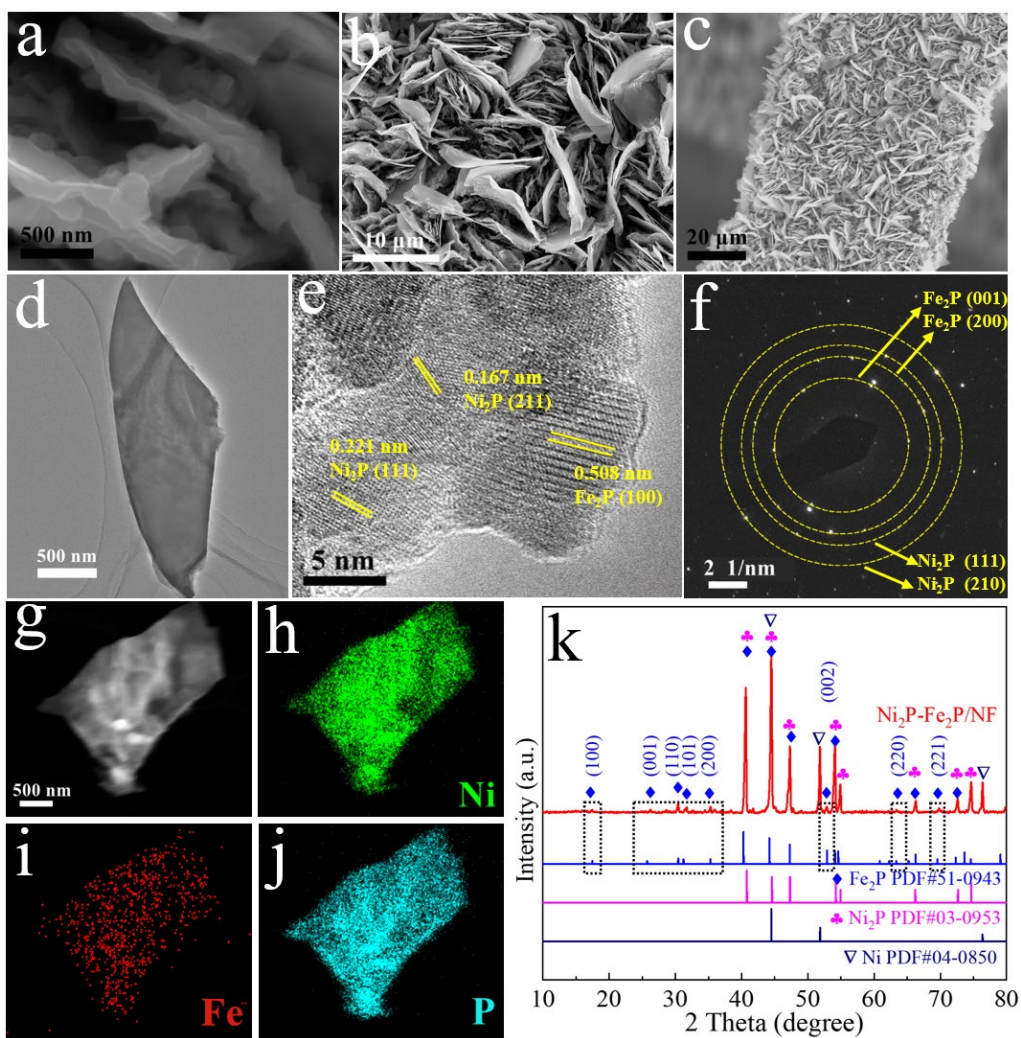


Figure 6.5. (a-c) SEM, (d) TEM, and (e) HRTEM images, and (f) SAED pattern of $\text{Ni}_2\text{P-Fe}_2\text{P}$. (g) TEM image and (h-i) corresponding EDX mapping images of a $\text{Ni}_2\text{P-Fe}_2\text{P}$ microsheet. (k) XRD pattern of nickel iron phosphide.

In addition, the thickness of a $\text{Ni}_2\text{P-Fe}_2\text{P}$ microsheet was measured to be only 7.4 nm (**Figure 6.6**), which can effectively increase the active catalytic surface area for water electrolysis. The microsheet structures of $\text{Ni}_2\text{P-Fe}_2\text{P/NF-X}$ ($X = 0.025, 0.05,$ and 0.15) samples synthesized using solutions with iron nitrate concentrations of 0.025 M, 0.05 M, and 0.15 M, respectively, show slight differences (**Figure 6.7**), in which higher Fe concentration leads to a rougher surface and larger microsheets.

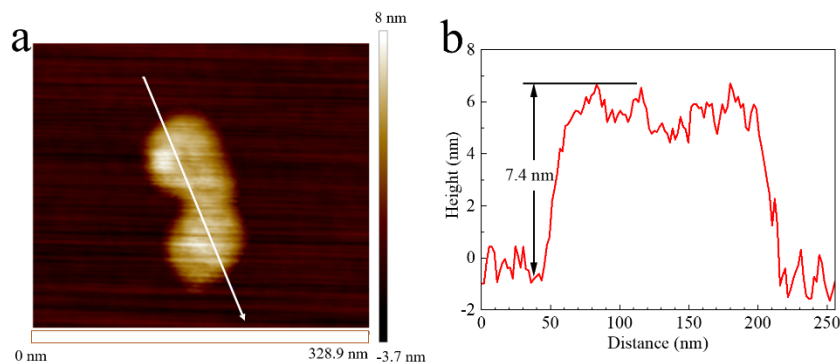


Figure 6.6. (a) AFM image and (b) corresponding height profile of a $\text{Ni}_2\text{P-Fe}_2\text{P}$ microsheet.

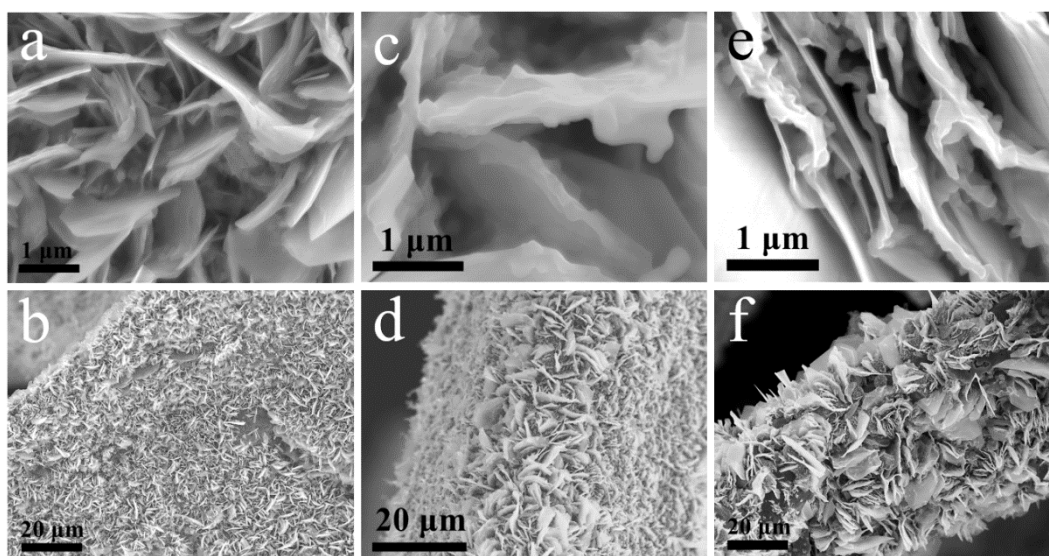


Figure 6.7. SEM images of (a-b) $\text{Ni}_2\text{P-Fe}_2\text{P/NF-0.025}$, (c-d) $\text{Ni}_2\text{P-Fe}_2\text{P/NF-0.05}$, and (e-f) $\text{Ni}_2\text{P-Fe}_2\text{P/NF-0.15}$.

To investigate the surface chemical composition and valence states of the Ni₂P-Fe₂P microsheet, X-ray photoelectron spectroscopy (XPS) depth profiling analysis was carried out. The signals of elemental Ni, P, and Fe clearly appear in the overall XPS spectra of Ni₂P-Fe₂P (red curve in **Figure 6.8a**), matching well with the sample's XRD and EDX mapping data. For elemental Ni, the high-resolution XPS spectra of Ni 2p in Ni₂P-Fe₂P (**Figure 6.8b**) can be deconvoluted to a pair of Ni²⁺ 2p_{3/2} and Ni²⁺ 2p_{1/2} peaks with binding energies at around 855.6 and 871.8 eV, respectively, in addition to two satellite peaks. The peaks of Ni for Ni₂P with binding energy at around 853.1 eV can be observed in the XPS spectra of both Ni₂P-Fe₂P and Ni₂P-Ni₅P₄. As for the high-resolution XPS spectra of P (**Figure 6.8c**), in addition to the huge oxidation peak for P-O at 134.5 eV, two peaks for P 2p at 128.6 and 129.5 eV, which are assigned to P 2p_{3/2} and P 2p_{1/2} (either Ni₂P or Fe₂P), respectively, can be found.¹⁷⁹ The intensity of the P 2p peaks in the Ni₂P-Fe₂P spectrum is relatively higher than that for Ni₂P-Ni₅P₄, suggesting the enhanced combination of P with both Ni and Fe, which leads to improved conductivity in this bimetallic phosphide composition.^{36, 45, 180} The XPS spectrum of Fe 2p in Ni₂P-Fe₂P is displayed in **Figure 6.8d**. The peaks of Fe 2p_{3/2} and Fe 2p_{1/2} located at 711.3 and 724.2 eV, respectively, are assigned to Fe²⁺.^{43, 181} The higher binding energy peaks located at around 714.8 and 725 eV, corresponding to the Fe oxide species (Fe³⁺), result from the surface oxidation of Fe₂P.¹⁸² Additionally, a peak at 707.1 eV, which is assigned to the Fe in Fe₂P, can be detected.

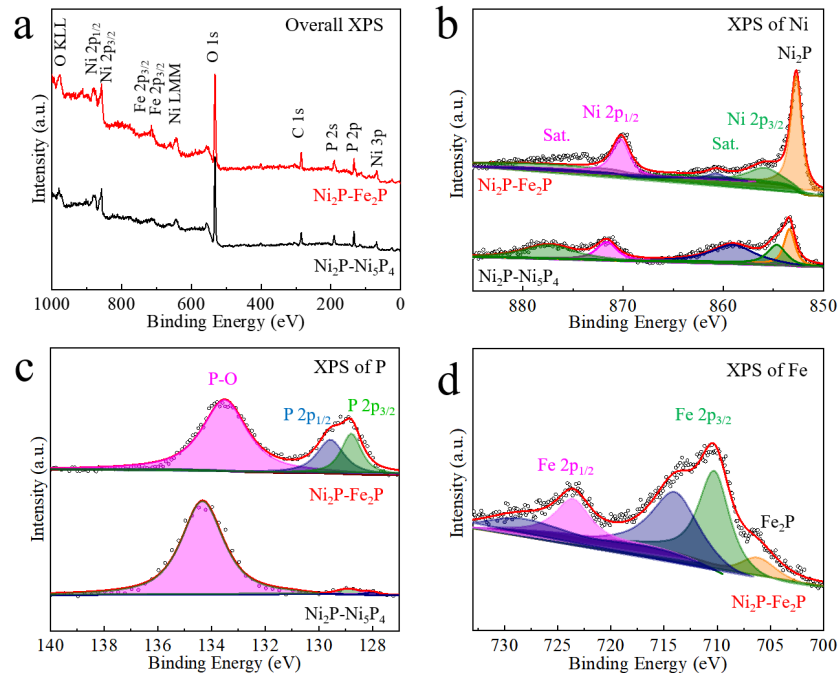


Figure 6.8. (a) Overall XPS spectra of Ni₂P-Ni₅P₄ and Ni₂P-Fe₂P. High-resolution XPS spectra of (b) Ni and (c) P in Ni₂P-Ni₅P₄ and Ni₂P-Fe₂P and of (d) Fe in Ni₂P-Fe₂P.

6.3.2 Catalytic Performance of Synthesized Catalysts

6.3.2.1 Catalytic Performance in Alkaline Freshwater

The catalytic performance of these as-prepared samples was evaluated using a three-electrode configuration with a scan rate of 2 mV s⁻¹. For comparison, IrO₂ and Pt/C catalysts loaded on NF were also examined as OER and HER references, respectively. To avoid the oxidation-peak effect and determine the overpotential of the Ni₂P-Fe₂P/NF catalyst at a small current density, CV curves were obtained using the same scan rate (**Figure 6.9a**). For OER activity in 1 M KOH electrolyte, the optimized Ni₂P-Fe₂P/NF sample, which was undergoing ion exchange in 0.1 M iron nitrate solution, needs an overpotential of only 218 mV to attain a current density of 10 mA cm⁻² (**Figure 6.9b-c**). The relevant linear sweep voltammetry (LSV) curves in **Figure 6.10a** reveal that the Ni₂P-Fe₂P/NF catalyst exhibits superior catalytic activity

compared to the others. It requires overpotentials of 261 and 337 mV to drive current densities of 100 and 1,000 mA cm⁻², respectively, which are smaller than the respective values for IrO₂ (341 and 438 mV), Ni₂P-Ni₅P₄/NF (315 and 492 mV), and Ni(OH)₂/NF (405 mV at 100 mA cm⁻²), indicating a remarkable enhancement in OER activity by synthesizing this heterogeneous bimetallic phosphide. The overpotential (218 mV) of Ni₂P-Fe₂P/NF required to achieve current density of 10 mA cm⁻² is superior to many other self-supported phosphide-based and even LDH-based catalysts reported recently, including (Co_{0.52}Fe_{0.48})₂P ribbon (270 mV),¹⁸³ NiCoP/NF (280 mV),⁴⁷ NiCoP/Cu wire (220 mV),⁴⁸ Ni-Fe-P/NF (229 mV),¹⁸⁴ N-NiCoP/Ni-Co foam (225 mV),¹⁸⁵ FeP₂/NF (240 mV),¹⁸² NiFeRu LDH/NF (225 mV),⁵² and NiFe LDH@NiCoP/NF (220 mV)⁸⁹. To further assess the intrinsic catalytic activity of these catalysts, their OER catalytic kinetics were studied using the corresponding Tafel plots calculated from **Figure 6.10a**. As shown in **Figure 6.10b**, the Tafel slope value of Ni₂P-Fe₂P/NF is as low as 58 mV dec⁻¹, which is much lower than that of Ni₂P-Ni₅P₄/NF (83 mV dec⁻¹), showing that the introduction of Fe results in a higher transfer coefficient and enhanced catalytic kinetics. Supported by conductive Ni foam, all of these catalysts exhibit a low charge-transfer resistance (R_{ct}) as revealed by the electrochemical impedance spectroscopy (EIS) analysis in **Figure 6.10c**. The R_{ct} of Ni₂P-Fe₂P/NF (~2.1 Ω) is much smaller than that of Ni₂P-Ni₅P₄/NF (~7.4 Ω), confirming that the bimetallic phosphide Ni₂P-Fe₂P/NF has enhanced conductivity.^{36,}
¹⁸⁰ Moreover, the OER turnover frequency (TOF) for Ni₂P-Fe₂P/NF at the overpotential of 300 mV is found to be 0.925 s⁻¹ (**Figure 6.11a**), and this magnitude is approximately three times as high as that of Ni₂P-Ni₅P₄/NF (0.307 s⁻¹). Notably, the

EIS and TOF analyses all agree well with the superior OER activity of Ni₂P-Fe₂P shown by the LSV curves in **Figure 6.10a**. To test the durability of the Ni₂P-Fe₂P/NF catalyst in 1 M KOH electrolyte, OER LSV curves were recorded before and after 3,000 CV scans (**Figure 6.10d**), showing negligible difference, confirming good CV cycling stability. The durability of the Ni₂P-Fe₂P/NF catalyst was also determined by a two-step chronopotentiometric measurement performed sequentially at current densities of 100 and 500 mA cm⁻² (**Figure 6.10e**). Only negligible voltage elevation can be observed even at current density of 500 mA cm⁻² for 24 h continuous testing, showing the excellent durability of Ni₂P-Fe₂P/NF under a large current density.

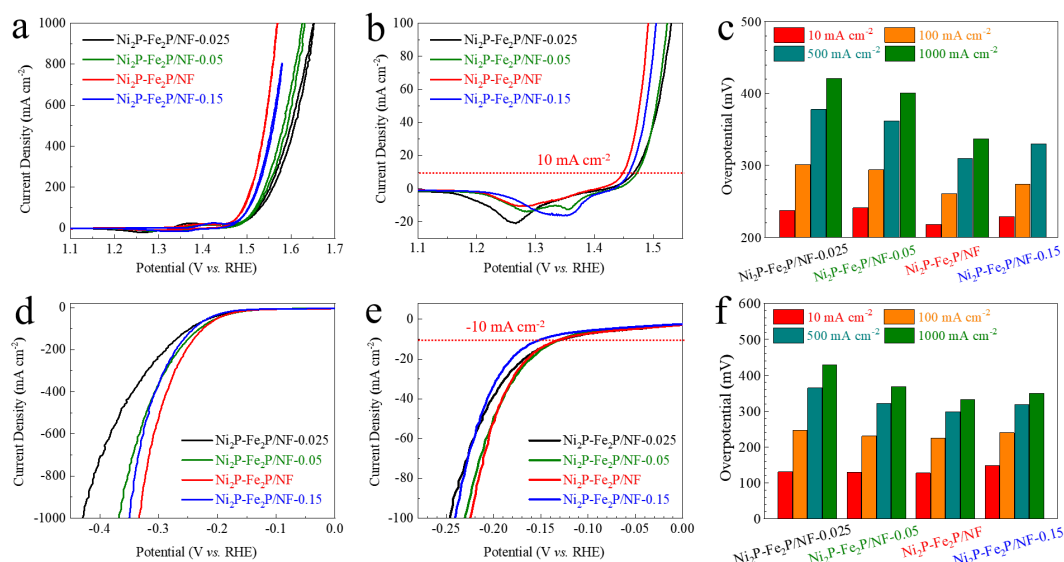


Figure 6.9. (a) OER CV and (d-e) HER LSV curves of these catalysts in 1 M KOH. (b) LSV curves collected from high to low potentials from (a). Comparison of the overpotentials of these catalysts for (c) OER and (f) HER.

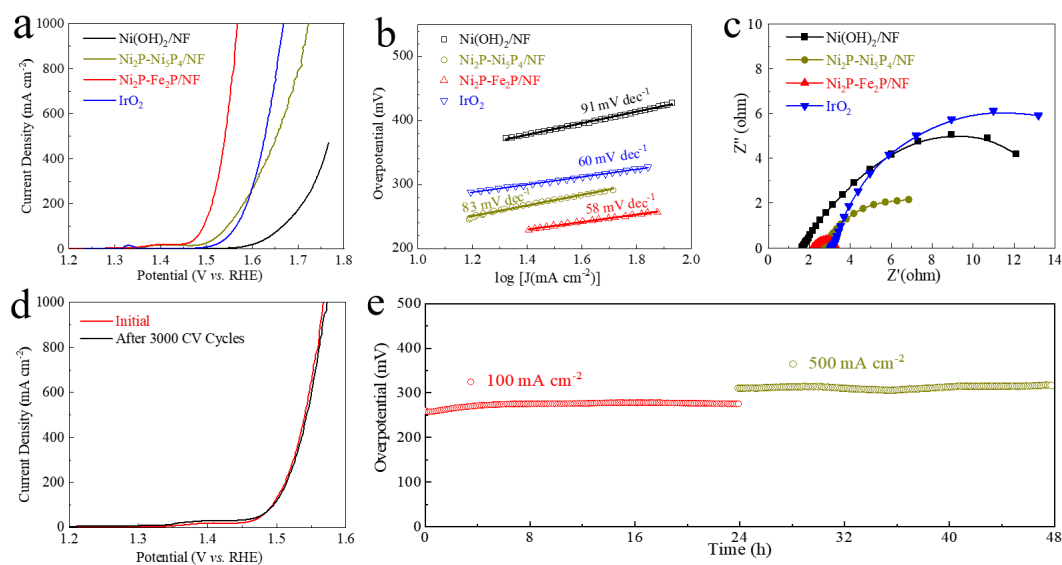


Figure 6.10. (a) OER LSV curves, (b) Tafel plots, and (c) Nyquist plots of these catalysts in 1 M KOH. (d) OER LSV curves of Ni₂P-Fe₂P/NF before and after CV cycles. (e) Stability performance of Ni₂P-Fe₂P/NF for OER.

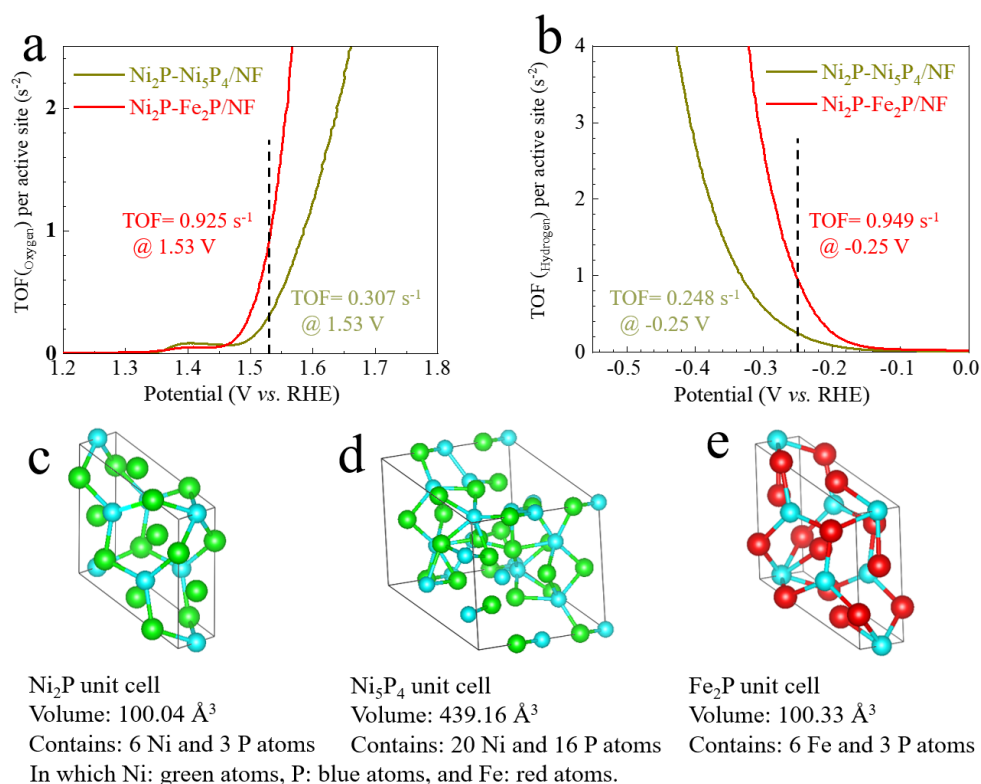


Figure 6.11. TOF curves of the corresponding of Ni₂P-Fe₂P and Ni₂P-Ni₅P₄ electrodes for (a) OER and (b) HER. Unit cells of (c) Ni₂P, (d) Ni₅P₄, and (e) Fe₂P.

The HER activity of the Ni(OH)₂/NF, Ni₂P-Ni₅P₄/NF, and Ni₂P-Fe₂P/NF samples was compared to that of Pt/C in 1 M KOH electrolyte, and the Pt/C catalyst was found to require the lowest overpotentials to drive current densities lower than 520 mA cm⁻², as shown by the HER LSV curves displayed in **Figure 6.12a**. Specifically, to drive current densities of 10 and 100 mA cm⁻², the Pt/C catalyst requires overpotentials of 41 and 107 mV, respectively, smaller than the respective values for Ni₂P-Fe₂P/NF (128 and 225 mV). Nevertheless, the *in situ* grown Ni₂P-Fe₂P/NF catalyst shows dramatically enhanced HER performance at high current density, requiring overpotentials of only 298 and 333 mV to drive current densities of 500 and 1,000 mA cm⁻², respectively. Additionally, among the four Ni₂P-Fe₂P/NF samples synthesized using solutions with different iron nitrate concentrations, the HER activity of the 0.1-M-concentration sample is the best (**Figure 6.9d-f**). The corresponding Tafel slope (86 mV dec⁻¹, **Figure 6.12b**) and R_{ct} (~0.98 Ω, **Figure 6.12c**) of Ni₂P-Fe₂P/NF are both smaller than those of Ni(OH)₂/NF (115 mV dec⁻¹ and ~7.8 Ω) and Ni₂P-Ni₅P₄/NF (125 mV dec⁻¹ and ~4.6 Ω), indicating its higher transfer coefficient and electronic conductivity. The corresponding HER TOF for Ni₂P-Fe₂P/NF at the overpotential of 250 mV is 0.949 s⁻¹ (**Figure 6.11b**), much higher than that of Ni₂P-Ni₅P₄/NF (0.248 s⁻¹). In addition, the superior stability of the Ni₂P-Fe₂P/NF catalyst for HER was confirmed by the nearly completely overlapping LSV curves before and after 3,000 CV scans (**Figure 6.12d**) and the stable long-term chronopotentiometric measurement (**Figure 6.12e**).

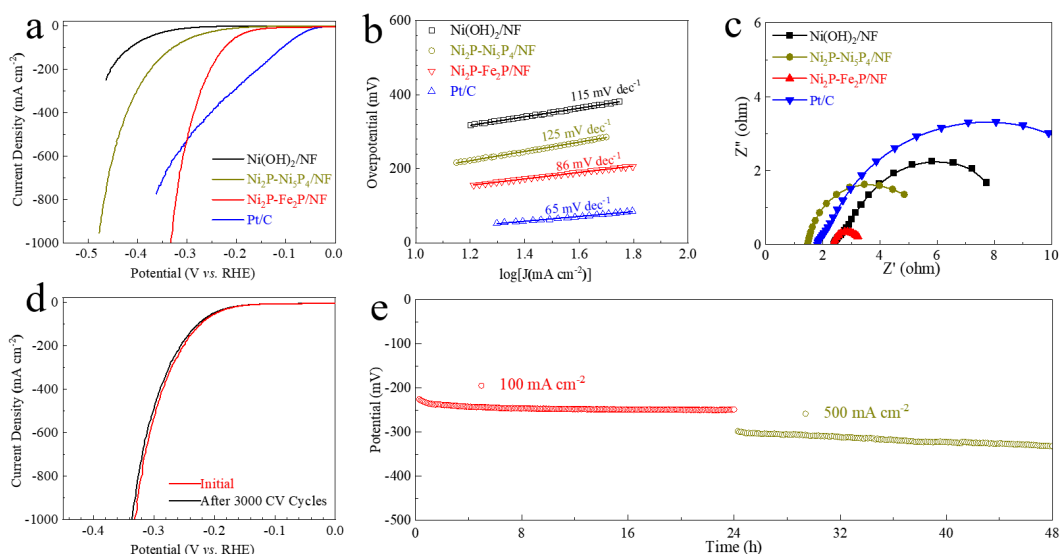


Figure 6.12. (a) HER LSV curves, (b) Tafel plots, and (c) Nyquist plots of these catalysts in 1 M KOH. (d) HER LSV curves of Ni₂P-Fe₂P/NF before and after CV cycles. (e) Stability performance of Ni₂P-Fe₂P/NF for OER.

6.3.2.2 Catalytic Performance in Alkaline Seawater

Many experimental studies and theoretical analyses have indicated that the main challenges for alkaline seawater splitting are the formation of hypochlorite on the anode side, which will compete with OER, and the problem of electrode corrosion.^{16-18, 20, 23, 186} Considering the excellent OER activity of Ni₂P-Fe₂P/NF, which requires an overpotential of only 337 mV to drive a current density of 1,000 mA cm⁻² in 1 M KOH electrolyte, well below the maximum theoretical value of ~480 mV for avoiding the formation of hypochlorite, it has a high probability of being a suitable catalyst for seawater splitting. We measured the catalytic activity of all of the as-prepared samples in alkaline seawater (1 M KOH seawater) electrolyte. As shown in **Figure 6.13a-b**, Ni₂P-Fe₂P/NF in 1 M KOH seawater exhibits worse performance for both OER and HER, respectively, than in 1 M KOH (**Figure 6.10a** and **Figure 6.12a**, respectively). The poorer catalytic activity of catalysts in seawater is mainly due to obstruction of

active sites and surface poisoning by ions or particles in the seawater.^{18, 20, 23} Specifically, Ni₂P-Fe₂P/NF needs overpotentials of 305 (252) and 431 (389) mV to drive current densities of 100 and 1,000 mA cm⁻², respectively, as an OER (HER) catalyst in 1 M KOH seawater electrolyte. The overpotentials needed for Ni₂P-Fe₂P/NF to drive current densities of 10, 100, 500, and 1,000 mA cm⁻² in 1 M KOH and 1 M KOH seawater electrolytes as an OER and a HER catalyst are summarized in **Figure 6.13c**. To verify the stability of this Ni₂P-Fe₂P/NF catalyst in seawater, we conducted both OER and HER stability tests in 1 M KOH seawater electrolyte (without any purification). As shown in **Figure 6.13d-e**, this self-supported Ni₂P-Fe₂P/NF catalyst could work continuously for 36 h at a current density of 100 mA cm⁻² and for more than 23 h at a current density of 500 mA cm⁻², exhibiting good stability.

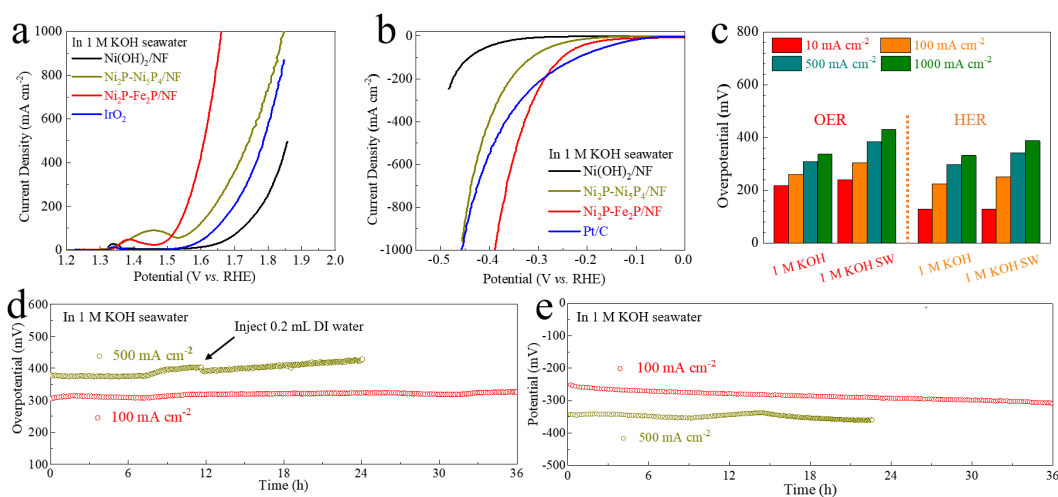


Figure 6.13. (a) OER and (b) HER LSV curves of these catalysts in 1 M KOH seawater. (c) Overpotentials required for the Ni₂P-Fe₂P/NF for OER and HER. Stability performance of Ni₂P-Fe₂P/NF for (d) OER and (e) HER.

SEM, EDS, and XPS were used to study the electrodes after OER/HER stability testing (each tested at a current density of 100 mA cm⁻² for 36 h) in 1 M KOH

seawater. As shown in **Figure 6.14a-b** and **6.14c-d**, the microsheet structure of Ni₂P-Fe₂P/NF was well maintained after either OER or HER stability testing, respectively, showing the electrode's excellent corrosion resistance and chemical stability in seawater. The corresponding EDS spectrum of the post-OER electrode (**Figure 6.14e**) shows that the peak for elemental P decreased sharply while the peak for elemental O became the highest, in comparison with the peaks in the spectrum of the initial Ni₂P-Fe₂P/NF electrode (**Figure 6.14f**), suggesting that the Ni₂P-Fe₂P surfaces were oxidized to oxides and/or hydroxides during the OER stability test.^{18, 187} For both post-OER and -HER (**Figure 6.14g**) electrodes, signals for the metals in the natural seawater (such as Ca and Mg) can be clearly detected. The valence states of elemental Ni, Fe, and P for all of these three electrodes were detected by XPS. There is no obvious change in the valence state of any of these three elements between the post-HER electrode and the initial electrode (blue and red curves, respectively, in **Figure 6.14h-j**). As for the post-OER electrode, both the Ni and Fe were oxidized to a higher oxidation state with a larger satellite peak as evidenced by the slight shifts in brown curves in **Figure 6.14h-i**, respectively, suggesting that they were oxidized to Ni-/Fe-oxides and/or -hydroxides. This can be further proved by the observations of the enhancement in P-O bonding and the decrease of P_{2p} for elemental P in the post-OER electrode (**Figure 6.14j**).^{89, 187} To further explore the catalytic activity of the Ni₂P-Fe₂P/NF electrode under real conditions,^{18, 188-189} the LSV curves for OER and HER in the three studied electrolytes without *iR* compensation were also obtained (**Figures 6.15b** and **6.15d**, respectively).

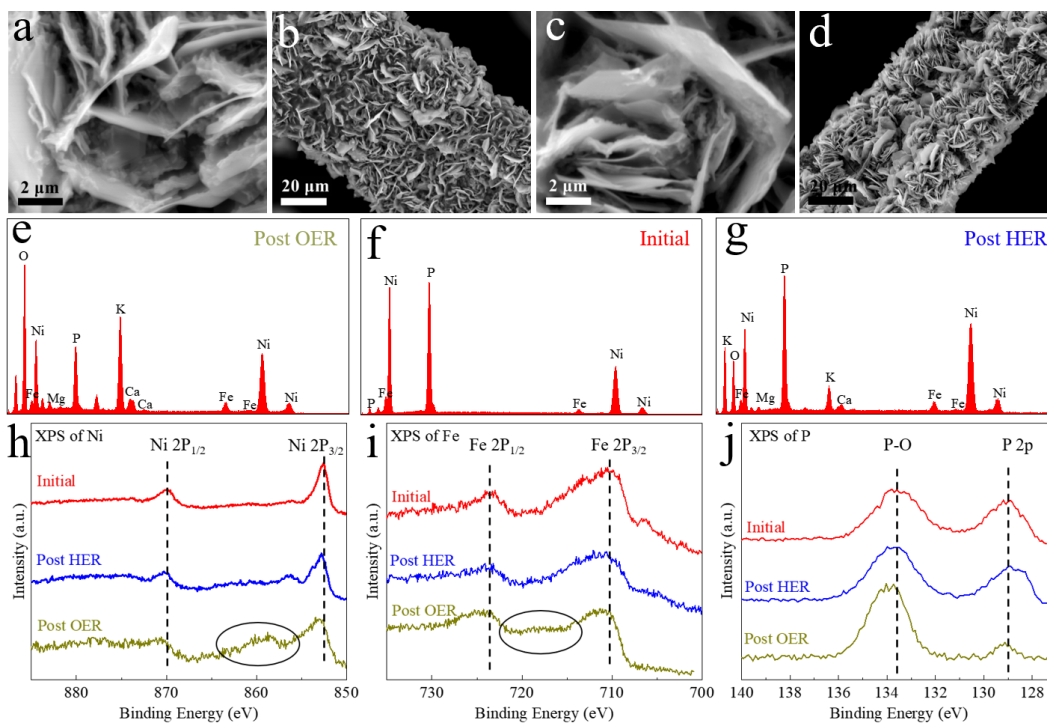


Figure 6.14. SEM images of $\text{Ni}_2\text{P-Fe}_2\text{P}$ electrodes after 36 h continuous testing for (a-b) OER and (c-d) HER catalysis. EDS spectra of (e) post-OER, (f) original, and (g) post-HER $\text{Ni}_2\text{P-Fe}_2\text{P}$. XPS spectra of (h) Ni, (i) Fe, and (j) P.

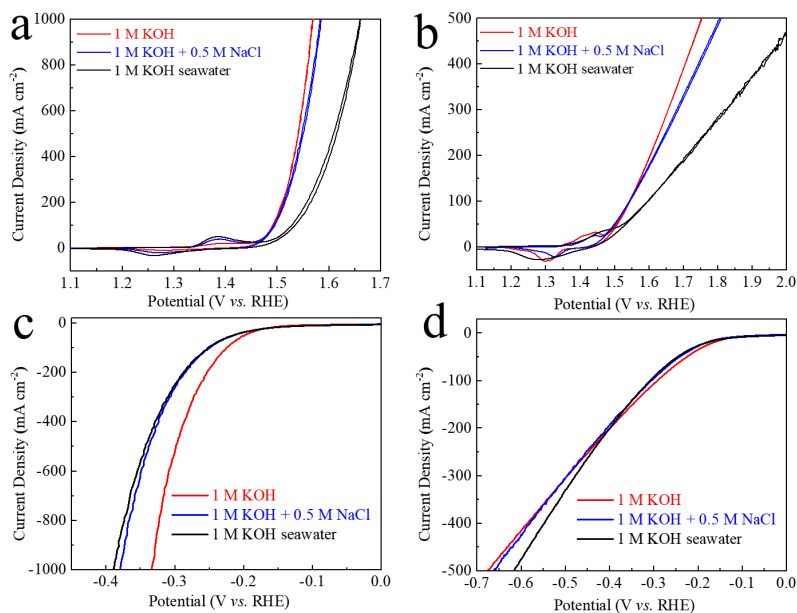


Figure 6.15. OER CV curves of $\text{Ni}_2\text{P-Fe}_2\text{P/NF}$ in different electrolytes (a) with and (b) without iR compensation. HER LSV curves of the $\text{Ni}_2\text{P-Fe}_2\text{P/NF}$ sample in different electrolytes (c) with and (d) without iR compensation.

The overall water/seawater electrolysis performance of the Ni₂P-Fe₂P/NF catalyst was investigated using a homemade two-electrode configuration in which it worked as both the anode and cathode electrodes. To drive a current density of 10 mA cm⁻² in 1 M KOH electrolyte (**Figure 6.16a**), Ni₂P-Fe₂P/NF requires voltage of 1.561 V, which is higher than that for the IrO₂||Pt/C pair (1.531V). However, this *in situ* grown Ni₂P-Fe₂P microsheet shows better catalytic performance at higher current densities, requiring voltages of 1.682 and 1.865 V to drive current densities of 100 and 500 mA cm⁻², respectively. These values are not only smaller than those for the IrO₂||Pt/C pair (1.695 and 1.954 V, respectively), but are also superior to those of many other self-supported bifunctional catalysts displayed in **Figure 6.16b**, showing the higher energy conversion efficiency of Ni₂P-Fe₂P/NF at larger current densities. For overall seawater splitting, Ni₂P-Fe₂P/NF requires voltages of 1.811 and 2.004 V to drive current densities of 100 and 500 mA cm⁻², respectively, in 1 M KOH seawater electrolyte. Additionally, the gap between the overall water and seawater splitting performance of the Ni₂P-Fe₂P/NF catalyst (red solid and dashed curves, respectively) is much narrower than that of the IrO₂||Pt/C pair (blue solid and dashed curves, respectively), confirming that its catalytic activity is well maintained even in real seawater conditions. This result matches well with the OER and HER LSV curves displayed in **Figure 6.13a-b**, respectively, which show that the performance of the respective noble-metal-based catalysts IrO₂ and Pt/C declines heavily in 1 M KOH seawater electrolyte in comparison with the results for 1 M KOH electrolyte shown in **Figure 6.10a** and **Figure 6.12a**, respectively. TMPs have also been reported to possess good corrosion resistance generated by alloying metallic cations with P,^{16, 18, 36, 190} which

can address the critical electrode corrosion problem in seawater electrolysis. This viewpoint can be confirmed by durability testing of Ni₂P-Fe₂P/NF for overall water/seawater electrolysis. As shown in **Figure 6.16c** and **6.16d**, the voltage needed by the Ni₂P-Fe₂P/NF catalyst can be well maintained with only a slight increase over 48 h of continuous operation at a current density of 100 mA cm⁻² in both alkaline water and alkaline seawater, respectively, showing excellent stability toward overall water/seawater electrolysis. Benefiting from its hydrophilic surface feature and superior corrosion resistance, this catalyst was also found to work well for more than 38 h even at a large current density of 500 mA cm⁻² in alkaline seawater despite some fluctuation. The long-term stability of the Ni₂P-Fe₂P/NF catalyst under large current densities demonstrates its promise for producing hydrogen fuels from real seawater.

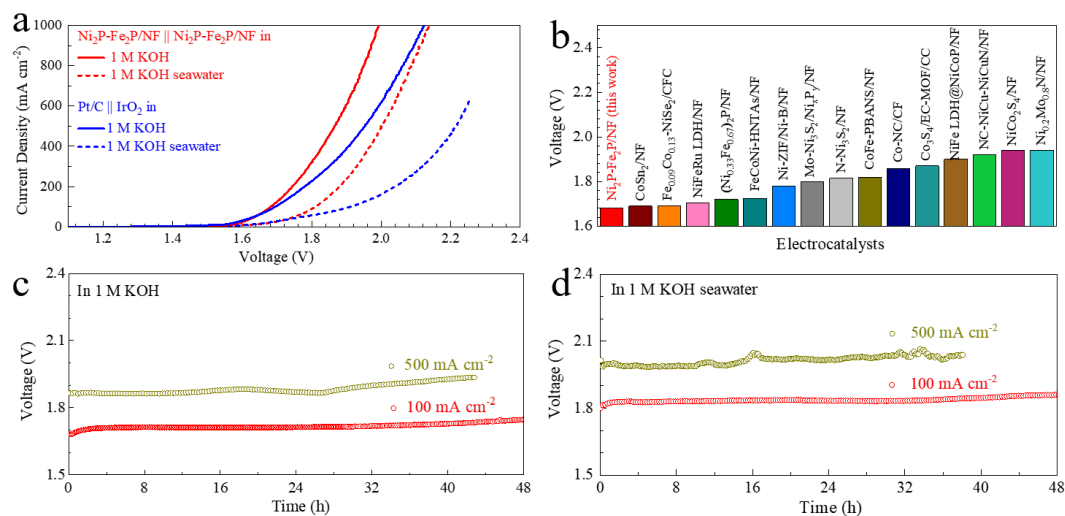


Figure 6.16. (a) Overall water/seawater electrolysis of Ni₂P-Fe₂P/NF and Pt/C||IrO₂ pairs. (b) Comparison of the catalytic performance. Stability performance of Ni₂P-Fe₂P/NF pair in (c) 1 M KOH and (d) 1 M KOH seawater.

A gas chromatography (GC) test was performed to measure the faradaic efficiency of Ni₂P-Fe₂P/NF in overall seawater electrolysis. As shown in **Figure 6.17a**, only the signals for H₂ and O₂ gas can be found in the resulting GC curves, indicating there is

no Cl_2 gas produced during the chronopotentiometry test. Meanwhile, the amount of measured H_2 and O_2 gases matches well with the theoretical gas amount, showing a nearly 100% faradaic efficiency (**Figure 6.17b**).

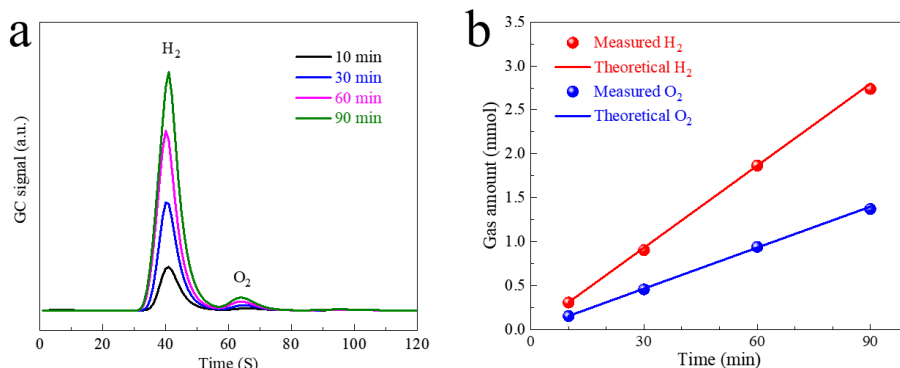


Figure 6.17. (a) GC signals of H_2 and O_2 gas during 90 min GC testing. (b) Measured (dots) and theoretical (solid line) gaseous products by the two-electrode electrolyzer at a current of 100 mA in 1 M KOH seawater.

The electrolyzer design and the pretreatment of seawater electrolytes play important roles in water electrolysis performance. Besides the homemade two-electrode configuration in **Figure 6.18a**, we also conducted all of the overall water/seawater electrolysis tests using an H-type electrolyzer with an anion-exchange membrane (Fumasep, FAA-3-PK-130) as the separator (**Figure 6.18b**) to avoid O_2/H_2 crossover, and the corresponding results are shown in **Figure 6.18c-d**. The difference in the catalytic activity of $\text{Ni}_2\text{P}-\text{Fe}_2\text{P}/\text{NF}$ tested in the different electrolyzers is less than 10 mV under the current density of 500 mA cm^{-2} . Additionally, the overall seawater electrolysis performance of the $\text{Ni}_2\text{P}-\text{Fe}_2\text{P}$ catalyst tested in the different electrolyzers with and without iR compensation is shown in **Figure 6.19a-b**. The huge difference in the performance curves for the two types of electrolyzers without iR compensation should result from the large resistance of the membrane. Overall seawater electrolysis stability test performed in the homemade two-electrode cell without iR compensation

is listed in **Figure 6.19c**. The seawater electrolyte was subsequently examined using N,N-diethyl-p-phenylenediamine (DPD) reagent to determine whether any hypochlorite was formed. As shown in **Figure 6.19d**, there is no color change in the reagent, indicating that no hypochlorite was formed during overall seawater electrolysis. This Ni₂P-Fe₂P pair can work at 500 mA cm⁻² continuously for 18 h in alkaline seawater without producing any hypochlorite.

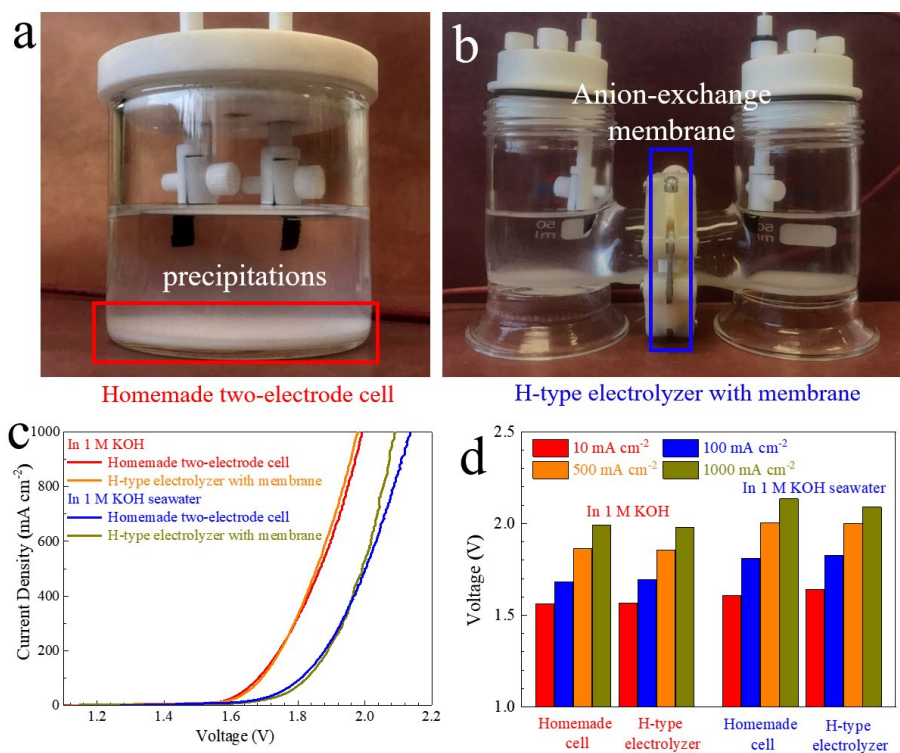


Figure 6.18. (a-b) Photographs of different electrolyzers. (c) Overall water/seawater electrolysis performance and (d) comparison of the overpotentials of Ni₂P-Fe₂P using the electrolyzers in (a) and (b), respectively.

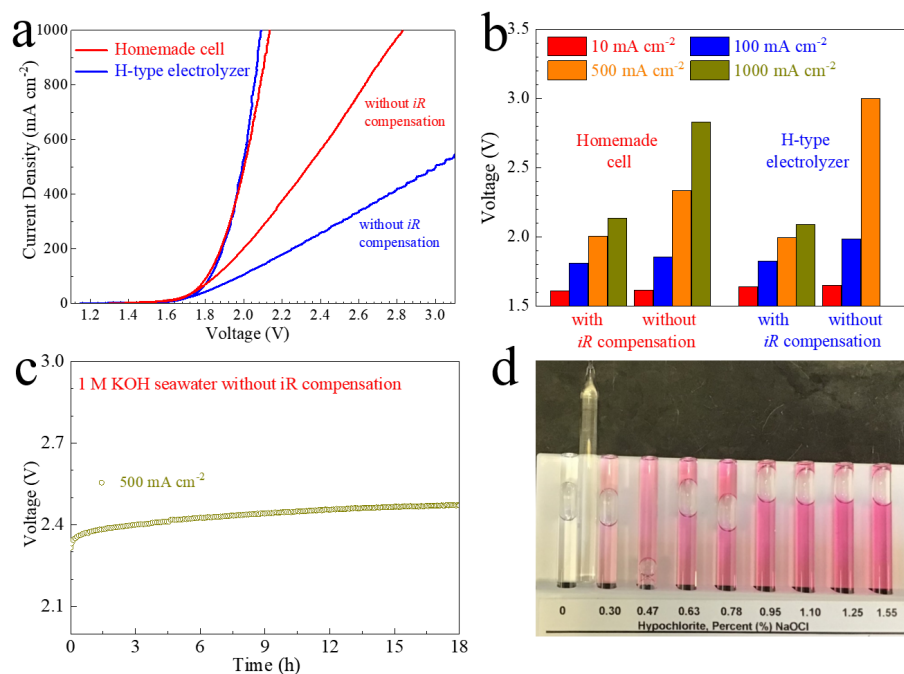


Figure 6.19. (a) Overall seawater electrolysis and (b) Voltages of Ni₂P-Fe₂P using different electrolyzers with and without *iR* compensation. (c) Stability testing of Ni₂P-Fe₂P and (d) corresponding ClO⁻ formation testing result.

6.3.3 Discussion

Based on the above characterizations and experimental results, the impressive bifunctional catalytic activity of self-supported Ni₂P-Fe₂P/NF can be attributed to the following factors. First, the *in situ* growth of ultrathin Ni₂P-Fe₂P microsheets (~7.4 nm in thickness and > 5 μm in size) on conductive Ni foam not only stabilizes the structure, but also provides a large surface area to rivet and disperse the active sites, leading to high active material loading mass and superb catalytic performance.⁵⁹ Second, the microscale Ni₂P-Fe₂P sheets with a hydrophilic surface feature ensure intimate contact between the active sites and the electrolyte media, guarantee that the active sites can always take part in the water electrolysis by providing adequate space for the diffusion of the electrolyte, and accelerate the release of vigorous bubbles at large current density. These two points could be the key factors in the large

enhancement of the catalytic performance of the Ni₂P-Fe₂P/NF catalyst at high current density. Third, the active species of this bimetallic phosphide Ni₂P-Fe₂P should be P atoms for HER and Ni-/Fe-oxides and/or -hydroxides for OER based on the post-seawater electrolysis analysis above. This heterogeneous bimetallic phosphide has a high transfer coefficient, good catalytic kinetics, and abundant catalytic active sites resulting from the introduction of Fe.^{50, 182} Especially for OER, the gradually formed Ni-/Fe- oxide/hydroxide phases on the surface, which have the optimized adsorption/desorption ability of intermediates (O*, OH*, and OOH*), and the inner Ni₂P-Fe₂P core, which has better conductivity and a high transfer coefficient, could produce synergistic effects in improving the catalytic performance.¹⁸ Finally, the enhanced stability and corrosion resistance, generated by alloying Ni and Fe with P atoms, helps the catalyst work well in seawater conditions.

Although our Ni₂P-Fe₂P catalyst exhibits HER activity that is inferior to some other reported bimetallic phosphide catalysts in base, including NiCo₂P_x ($\eta_{10} = 58$ mV and $\eta_{100} = 127$ mV, where η_{10} and η_{100} are the overpotentials required to achieve current densities of 10 and 100 mA cm⁻², respectively),⁴¹ CoP/Ni₅P₄/CoP ($\eta_{10} = 71$ mV and $\eta_{100} = 140$ mV),⁴² and Ni₂P-Cu₃P ($\eta_{10} = 78$ mV and $\eta_{100} = 190$ mV),⁴⁵ its OER and bifunctional catalytic activity in both alkaline water and seawater is very compelling. The reported preparation routines for bimetallic phosphide catalysts always require a hydrothermal reaction, electrochemical deposition, or other complex process to first obtain the precursor, and are not suitable for scaling up.¹⁷⁷ Here, our *in situ* growth-ion exchange approach, in which commercial Ni foam is directly used as both the conductive bones and the Ni source, while the Fe cations are introduced and

tuned by ion exchange with solutions of different iron nitrate concentrations at room temperature, is more facile and economic. Both the hydrochloric acid and iron nitrate solution can be recycled and used for at least one additional synthesis since the samples obtained are very similar to the original ones. In addition, some other Ni-based bimetallic phosphide Ni-M-P (M = metal) catalysts can be synthesized using the same routine except for changing the immersion solution containing M cations in the second step.

6.4 Conclusion

We have introduced a novel and economic strategy to synthesize self-supported Ni₂P-Fe₂P as an efficient bifunctional catalyst for overall water/seawater electrolysis. Its heterogeneous bimetallic phosphide microsheet structure, along with its hydrophilic feature, help it exhibit high electronic kinetics, enhanced conductivity, abundant active sites, and accelerated bubble-release ability, producing favorable synergistic effects for water electrolysis. Additionally, its enhanced stability and corrosion resistance resulting from the self-support effect and from alloying Ni and Fe with P atoms make it work well in seawater conditions. With an optimized Fe ratio (3.2% at), Ni₂P-Fe₂P/NF requires voltages of 1.682 and 1.811 V in 1 M KOH and 1 M KOH seawater to attain a current density of 100 mA cm⁻² for overall water/seawater splitting, respectively, which are superior to those for the IrO₂||Pt/C pair as well as many of the recently reported bifunctional catalysts. We believe our study opens a new avenue for the economic synthesis of bifunctional bimetallic phosphide catalysts for highly efficient and stable hydrogen production *via* water/seawater electrolysis.

CHAPTER 7 Summary and Perspective

Efficient non-noble-metal based catalysts are in demand to promote the sluggish kinetics of water and seawater electrolysis. Designing innovative catalysts with high catalytic activity and long-term durability remains a challenge. Self-supported catalysts with the merits of abundant active sites and accessible synthesis process have emerged as promising OER or HER catalysts. Here we design and investigate different LDH-, TMP-, and TMN-based catalysts for water and seawater electrolysis. High catalytic activity, long-term durability, and enhanced chemical/structural stability derived from the rational design enable these catalysts to work efficiently in both alkaline freshwater and natural seawater electrolytes. Despite the progress made thus far, more research effort might can be devoted to the following to design catalysts for practical water and seawater electrolysis.

(1) Developing novel synthesis methods and finding new substrates are reasonable ways to synthesize efficient catalysts. Different fabrication techniques result in diverse morphology and structures. Novel synthesis methods should be taken into consideration to fabricate new types of catalysts with controllable structures while retaining their chemical merits. Currently, the conductive substrates employed in lab settings are mainly nickel foam, copper foam, and carbon cloth, which are easy to use in growing specific nanostructures, while stainless steel or iron form might be more favorable in industrial applications due to their low cost and outstanding stability. It would be more reasonable to find new substrates to meet commercial needs rather than continue employing the current lab substrates for experimental studies.

(2) The weak understanding of the water and seawater electrolysis process has become an obstacle that hinders the design of catalysts. It is essential to understand the catalytic mechanisms of catalyst at the atomic level through the combination of practical experiments and theoretical analysis. For instance, operando characterization technologies such as in situ X-ray absorption spectroscopy (XAS), in situ Raman spectroscopy, and even in situ TEM would help to detect catalytic intermediates under real working conditions and lead to further insights into what is actually happening throughout the entire electrolysis process. In addition to understanding the catalytic performance of the remaining catalysts, it would be much more helpful if DFT calculation or other theoretical methods could predict potentially outstanding catalysts for experimentalists to synthesize, which could reduce much of the effort currently needed for trial and error.

(3) The practical industrial application of self-supported catalyst in water and seawater electrolysis remains a challenging task. Although the catalytic activity of self-supported catalysts has been dramatically enhanced via various kinds of techniques, the catalytic performance, either catalytic activity or long-term durability, at large current density remains far too low for practical application. Catalysts in the lab setting are mainly fabricated on the micro or nano scale. Economic expense and mechanical stability must be taken into consideration when scaling up these self-supported catalysts for industrial production. Each element used in the catalysts must be earth abundant so that the price will not be too high when large quantities are going to be used.

REFERENCES

1. Yan, Y.; Xia, B.; Xu, Z.; Wang, X., Recent Development of Molybdenum Sulfides as Advanced Electrocatalysts for Hydrogen Evolution Reaction. *ACS Catalysis* **2014**, *4* (6), 1693-1705.
2. Lyu, F.; Wang, Q.; Choi, S. M.; Yin, Y., Noble-Metal-Free Electrocatalysts for Oxygen Evolution. *Small* **2019**, *15* (1), e1804201.
3. Zhang, L.; Xiao, J.; Wang, H.; Shao, M., Carbon-Based Electrocatalysts for Hydrogen and Oxygen Evolution Reactions. *ACS Catalysis* **2017**, *7* (11), 7855-7865.
4. Wang, J.; Cui, W.; Liu, Q.; Xing, Z.; Asiri, A. M.; Sun, X., Recent Progress in Cobalt-Based Heterogeneous Catalysts for Electrochemical Water Splitting. *Advanced Materials* **2016**, *28* (2), 215-30.
5. Seh, Z. W.; Kibsgaard, J.; Dickens, C. F.; Chorkendorff, I.; Norskov, J. K.; Jaramillo, T. F., Combining theory and experiment in electrocatalysis: Insights into materials design. *Science* **2017**, *355* (6321).
6. Tang, C.; Wang, H.-F.; Zhu, X.-L.; Li, B.-Q.; Zhang, Q., Advances in Hybrid Electrocatalysts for Oxygen Evolution Reactions: Rational Integration of NiFe Layered Double Hydroxides and Nanocarbon. *Particle & Particle Systems Characterization* **2016**, *33* (8), 473-486.
7. Zhou, H.; Yu, F.; Zhu, Q.; Sun, J.; Qin, F.; Yu, L.; Bao, J.; Yu, Y.; Chen, S.; Ren, Z., Water splitting by electrolysis at high current densities under 1.6 volts. *Energy & Environmental Science* **2018**, *11* (10), 2858-2864.

8. Wang, J.; Xu, F.; Jin, H.; Chen, Y.; Wang, Y., Non-Noble Metal-based Carbon Composites in Hydrogen Evolution Reaction: Fundamentals to Applications. *Advanced Materials* **2017**, *29* (14).
9. Yu, L.; Mishra, I. K.; Xie, Y.; Zhou, H.; Sun, J.; Zhou, J.; Ni, Y.; Luo, D.; Yu, F.; Yu, Y.; Chen, S.; Ren, Z., Ternary Ni_{2(1-x)}Mo_{2x}P nanowire arrays toward efficient and stable hydrogen evolution electrocatalysis under large-current-density. *Nano Energy* **2018**, *53*, 492-500.
10. Tong, W.; Forster, M.; Dionigi, F.; Dresp, S.; Sadeghi Erami, R.; Strasser, P.; Cowan, A. J.; Farràs, P., Electrolysis of low-grade and saline surface water. *Nature Energy* **2020**, *5* (5), 367-377.
11. Vij, V.; Sultan, S.; Harzandi, A. M.; Meena, A.; Tiwari, J. N.; Lee, W.-G.; Yoon, T.; Kim, K. S., Nickel-Based Electrocatalysts for Energy-Related Applications: Oxygen Reduction, Oxygen Evolution, and Hydrogen Evolution Reactions. *ACS Catalysis* **2017**, *7* (10), 7196-7225.
12. Lv, L.; Yang, Z.; Chen, K.; Wang, C.; Xiong, Y., 2D Layered Double Hydroxides for Oxygen Evolution Reaction: From Fundamental Design to Application. *Advanced Energy Materials* **2019**, *9* (17), 1803358.
13. Gao, Q.; Zhang, W.; Shi, Z.; Yang, L.; Tang, Y., Structural Design and Electronic Modulation of Transition-Metal-Carbide Electrocatalysts toward Efficient Hydrogen Evolution. *Advanced Materials* **2019**, *31* (2), e1802880.
14. Aicher, T., Renewable Hydrogen Technologies. Production, Purification, Storage, Applications, and Safety. Edited by Luis M. Gandía, Gurutze Arzamendi, and Pedro M. Diéguez. *Energy Technology* **2015**, *3* (1), 90-91.

15. Suen, N. T.; Hung, S. F.; Quan, Q.; Zhang, N.; Xu, Y. J.; Chen, H. M., Electrocatalysis for the oxygen evolution reaction: recent development and future perspectives. *Chemical Society Reviews* **2017**, *46* (2), 337-365.
16. Tong, W.; Forster, M.; Dionigi, F.; Dresp, S.; Sadeghi Erami, R.; Strasser, P.; Cowan, A. J.; Farràs, P., Electrolysis of low-grade and saline surface water. *Nature Energy* **2020**.
17. Dresp, S.; Dionigi, F.; Klingenhof, M.; Strasser, P., Direct Electrolytic Splitting of Seawater: Opportunities and Challenges. *ACS Energy Letters* **2019**, *4* (4), 933-942.
18. Kuang, Y.; Kenney, M. J.; Meng, Y.; Hung, W.-H.; Liu, Y.; Huang, J. E.; Prasanna, R.; Li, P.; Li, Y.; Wang, L.; Lin, M.-C.; McGehee, M. D.; Sun, X.; Dai, H., Solar-driven, highly sustained splitting of seawater into hydrogen and oxygen fuels. *Proceedings of the National Academy of Sciences* **2019**, *116* (14), 6624-6629.
19. Hisatomi, T.; Domen, K., Reaction systems for solar hydrogen production via water splitting with particulate semiconductor photocatalysts. *Nature Catalysis* **2019**, *2* (5), 387-399.
20. Yu, L.; Zhu, Q.; Song, S.; McElhenny, B.; Wang, D.; Wu, C.; Qin, Z.; Bao, J.; Yu, Y.; Chen, S.; Ren, Z., Non-noble metal-nitride based electrocatalysts for high-performance alkaline seawater electrolysis. *Nature Communication* **2019**, *10* (1), 5106.
21. Hsu, S. H.; Miao, J.; Zhang, L.; Gao, J.; Wang, H.; Tao, H.; Hung, S. F.; Vasileff, A.; Qiao, S. Z.; Liu, B., An Earth-Abundant Catalyst-Based Seawater Photoelectrolysis System with 17.9% Solar-to-Hydrogen Efficiency. *Advanced Materials* **2018**, *30* (18), e1707261.

22. Yu, L.; Wu, L.; McElhenny, B.; Song, S.; Luo, D.; Zhang, F.; Yu, Y.; Chen, S.; Ren, Z., Ultrafast room-temperature synthesis of porous S-doped Ni/Fe (oxy)hydroxide electrodes for oxygen evolution catalysis in seawater splitting. *Energy & Environmental Science* **2020**.
23. Dionigi, F.; Reier, T.; Pawolek, Z.; Gliech, M.; Strasser, P., Design Criteria, Operating Conditions, and Nickel-Iron Hydroxide Catalyst Materials for Selective Seawater Electrolysis. *ChemSusChem* **2016**, *9* (9), 962-72.
24. Dresp, S.; Dionigi, F.; Loos, S.; Ferreira de Araujo, J.; Spöri, C.; Gliech, M.; Dau, H.; Strasser, P., Direct Electrolytic Splitting of Seawater: Activity, Selectivity, Degradation, and Recovery Studied from the Molecular Catalyst Structure to the Electrolyzer Cell Level. *Advanced Energy Materials* **2018**, *8* (22), 1800338.
25. Park, Y. S.; Lee, J.; Jang, M. J.; Yang, J.; Jeong, J.; Park, J.; Kim, Y.; Seo, M. H.; Chen, Z.; Choi, S. M., High-performance anion exchange membrane alkaline seawater electrolysis. *Journal of Materials Chemistry A* **2021**, *9* (15), 9586-9592.
26. Li, X.; Hao, X.; Wang, Z.; Abudula, A.; Guan, G., In-situ intercalation of NiFe LDH materials: An efficient approach to improve electrocatalytic activity and stability for water splitting. *Journal of Power Sources* **2017**, *347*, 193-200.
27. Wang, Y.; Yan, D.; El Hankari, S.; Zou, Y.; Wang, S., Recent Progress on Layered Double Hydroxides and Their Derivatives for Electrocatalytic Water Splitting. *Advanced Science (Weinh)* **2018**, *5* (8), 1800064.
28. Jiao, S.; Fu, X.; Wang, S.; Zhao, Y., Perfecting electrocatalysts via imperfections: towards the large-scale deployment of water electrolysis technology. *Energy & Environmental Science* **2021**, *14* (4), 1722-1770.

29. Chen, Y.; Rui, K.; Zhu, J.; Dou, S. X.; Sun, W., Recent Progress on Nickel-Based Oxide/(Oxy)Hydroxide Electrocatalysts for the Oxygen Evolution Reaction. *Chemistry* **2019**, *25* (3), 703-713.
30. Hou, J.; Wu, Y.; Zhang, B.; Cao, S.; Li, Z.; Sun, L., Rational Design of Nanoarray Architectures for Electrocatalytic Water Splitting. *Advanced Functional Materials* **2019**, *29* (20), 1808367.
31. Fan, G.; Li, F.; Evans, D. G.; Duan, X., Catalytic applications of layered double hydroxides: recent advances and perspectives. *Chemical Society Reviews* **2014**, *43* (20), 7040-66.
32. Li, J.; Jiang, S.; Shao, M.; Wei, M., Host-Guest Engineering of Layered Double Hydroxides towards Efficient Oxygen Evolution Reaction: Recent Advances and Perspectives. *Catalysts* **2018**, *8* (5), 214.
33. Gong, M.; Li, Y.; Wang, H.; Liang, Y.; Wu, J. Z.; Zhou, J.; Wang, J.; Regier, T.; Wei, F.; Dai, H., An advanced Ni-Fe layered double hydroxide electrocatalyst for water oxidation. *Journal of the American Chemical Society* **2013**, *135* (23), 8452-5.
34. Wu, L.; Yu, L.; Xiao, X.; Zhang, F.; Song, S.; Chen, S.; Ren, Z., Recent Advances in Self-Supported Layered Double Hydroxides for Oxygen Evolution Reaction. *Research (Wash D C)* **2020**, *2020*, 3976278.
35. Li, Y.; Dong, Z.; Jiao, L., Multifunctional Transition Metal-Based Phosphides in Energy-Related Electrocatalysis. *Advanced Energy Materials* **2019**, *10* (11), 1902104.

36. Shi, Y.; Zhang, B., Recent advances in transition metal phosphide nanomaterials: synthesis and applications in hydrogen evolution reaction. *Chemical Society Reviews* **2016**, *45* (6), 1529-41.
37. Popczun, E. J.; McKone, J. R.; Read, C. G.; Biacchi, A. J.; Wiltrout, A. M.; Lewis, N. S.; Schaak, R. E., Nanostructured nickel phosphide as an electrocatalyst for the hydrogen evolution reaction. *Journal of the American Chemical Society* **2013**, *135* (25), 9267-70.
38. Laursen, A. B.; Patraju, K. R.; Whitaker, M. J.; Retuerto, M.; Sarkar, T.; Yao, N.; Ramanujachary, K. V.; Greenblatt, M.; Dismukes, G. C., Nanocrystalline Ni₅P₄: a hydrogen evolution electrocatalyst of exceptional efficiency in both alkaline and acidic media. *Energy & Environmental Science* **2015**, *8* (3), 1027-1034.
39. Jiang, P.; Liu, Q.; Liang, Y.; Tian, J.; Asiri, A. M.; Sun, X., A cost-effective 3D hydrogen evolution cathode with high catalytic activity: FeP nanowire array as the active phase. *Angewandte Chemie International Edition* **2014**, *53* (47), 12855-9.
40. Tian, J.; Liu, Q.; Asiri, A. M.; Sun, X., Self-supported nanoporous cobalt phosphide nanowire arrays: an efficient 3D hydrogen-evolving cathode over the wide range of pH 0-14. *Journal of the American Chemical Society* **2014**, *136* (21), 7587-90.
41. Zhang, R.; Wang, X.; Yu, S.; Wen, T.; Zhu, X.; Yang, F.; Sun, X.; Wang, X.; Hu, W., Ternary NiCo₂P_x Nanowires as pH-Universal Electrocatalysts for Highly Efficient Hydrogen Evolution Reaction. *Advanced Materials* **2017**, *29* (9).
42. Mishra, I. K.; Zhou, H.; Sun, J.; Qin, F.; Dahal, K.; Bao, J.; Chen, S.; Ren, Z., Hierarchical CoP/Ni₅P₄/CoP microsheet arrays as a robust pH-universal electrocatalyst

for efficient hydrogen generation. *Energy & Environmental Science* **2018**, *11* (8), 2246-2252.

43. Li, Y.; Zhang, H.; Jiang, M.; Zhang, Q.; He, P.; Sun, X., 3D Self-Supported Fe-Doped Ni₂P Nanosheet Arrays as Bifunctional Catalysts for Overall Water Splitting. *Advanced Functional Materials* **2017**, *27* (37), 1702513.

44. Yu, F.; Zhou, H.; Huang, Y.; Sun, J.; Qin, F.; Bao, J.; Goddard, W. A., 3rd; Chen, S.; Ren, Z., High-performance bifunctional porous non-noble metal phosphide catalyst for overall water splitting. *Nature Communication* **2018**, *9* (1), 2551.

45. Yu, L.; Zhang, J.; Dang, Y.; He, J.; Tobin, Z.; Kerns, P.; Dou, Y.; Jiang, Y.; He, Y.; Suib, S. L., In Situ Growth of Ni₂P-Cu₃P Bimetallic Phosphide with Bicontinuous Structure on Self-Supported NiCuC Substrate as an Efficient Hydrogen Evolution Reaction Electrocatalyst. *ACS Catalysis* **2019**, *9* (8), 6919-6928.

46. Zhang, H.; Zhou, W.; Dong, J.; Lu, X. F.; Lou, X. W., Intramolecular electronic coupling in porous iron cobalt (oxy)phosphide nanoboxes enhances the electrocatalytic activity for oxygen evolution. *Energy & Environmental Science* **2019**, *12* (11), 3348-3355.

47. Liang, H.; Gandi, A. N.; Anjum, D. H.; Wang, X.; Schwingenschlogl, U.; Alshareef, H. N., Plasma-Assisted Synthesis of NiCoP for Efficient Overall Water Splitting. *Nano Lett* **2016**, *16* (12), 7718-7725.

48. Jothi, V. R.; Bose, R.; Rajan, H.; Jung, C.; Yi, S. C., Harvesting Electronic Waste for the Development of Highly Efficient Eco-Design Electrodes for Electrocatalytic Water Splitting. *Advanced Energy Materials* **2018**, *8* (34), 1802615.

49. Xin, Y.; Kan, X.; Gan, L. Y.; Zhang, Z., Heterogeneous Bimetallic Phosphide/Sulfide Nanocomposite for Efficient Solar-Energy-Driven Overall Water Splitting. *ACS Nano* **2017**, *11* (10), 10303-10312.
50. Zhao, G.; Rui, K.; Dou, S. X.; Sun, W., Boosting electrochemical water oxidation: the merits of heterostructured electrocatalysts. *Journal of Materials Chemistry A* **2020**, *8* (14), 6393-6405.
51. Yu, L.; Zhou, H.; Sun, J.; Qin, F.; Yu, F.; Bao, J.; Yu, Y.; Chen, S.; Ren, Z., Cu nanowires shelled with NiFe layered double hydroxide nanosheets as bifunctional electrocatalysts for overall water splitting. *Energy & Environmental Science* **2017**, *10* (8), 1820-1827.
52. Chen, G.; Wang, T.; Zhang, J.; Liu, P.; Sun, H.; Zhuang, X.; Chen, M.; Feng, X., Accelerated Hydrogen Evolution Kinetics on NiFe-Layered Double Hydroxide Electrocatalysts by Tailoring Water Dissociation Active Sites. *Advanced Materials* **2018**, *30* (10).
53. Wu, L.; Yu, L.; Zhang, F.; Wang, D.; Luo, D.; Song, S.; Yuan, C.; Karim, A.; Chen, S.; Ren, Z., Facile synthesis of nanoparticle-stacked tungsten-doped nickel iron layered double hydroxide nanosheets for boosting oxygen evolution reaction. *Journal of Materials Chemistry A* **2020**, *8* (16), 8096-8103.
54. Wang, H.; Li, J.; Li, K.; Lin, Y.; Chen, J.; Gao, L.; Nicolosi, V.; Xiao, X.; Lee, J. M., Transition metal nitrides for electrochemical energy applications. *Chemical Society Reviews* **2021**, *50* (2), 1354-1390.
55. Calais, J.-L., Band structure of transition metal compounds. *Advances in Physics* **1977**, *26* (6), 847-885.

56. Cao, B.; Veith, G. M.; Neufeind, J. C.; Adzic, R. R.; Khalifah, P. G., Mixed close-packed cobalt molybdenum nitrides as non-noble metal electrocatalysts for the hydrogen evolution reaction. *Journal of the American Chemical Society* **2013**, *135* (51), 19186-92.
57. Liu, B.; He, B.; Peng, H. Q.; Zhao, Y.; Cheng, J.; Xia, J.; Shen, J.; Ng, T. W.; Meng, X.; Lee, C. S.; Zhang, W., Unconventional Nickel Nitride Enriched with Nitrogen Vacancies as a High-Efficiency Electrocatalyst for Hydrogen Evolution. *Advanced Science (Weinh)* **2018**, *5* (8), 1800406.
58. Song, F.; Li, W.; Yang, J.; Han, G.; Liao, P.; Sun, Y., Interfacing nickel nitride and nickel boosts both electrocatalytic hydrogen evolution and oxidation reactions. *Nature Communications* **2018**, *9* (1), 4531.
59. Sun, H.; Yan, Z.; Liu, F.; Xu, W.; Cheng, F.; Chen, J., Self-Supported Transition-Metal-Based Electrocatalysts for Hydrogen and Oxygen Evolution. *Advanced Materials* **2020**, *32* (3), e1806326.
60. Anantharaj, S.; Karthick, K.; Kundu, S., Evolution of layered double hydroxides (LDH) as high performance water oxidation electrocatalysts: A review with insights on structure, activity and mechanism. *Materials Today Energy* **2017**, *6*, 1-26.
61. Yan, K.; Wu, G.; Jin, W., Recent Advances in the Synthesis of Layered, Double-Hydroxide-Based Materials and Their Applications in Hydrogen and Oxygen Evolution. *Energy Technology* **2016**, *4* (3), 354-368.

62. Wang, T.; Xu, W.; Wang, H., Ternary NiCoFe Layered Double Hydroxide Nanosheets Synthesized by Cation Exchange Reaction for Oxygen Evolution Reaction. *Electrochimica Acta* **2017**, *257*, 118-127.
63. Zou, X.; Zhang, Y., Noble metal-free hydrogen evolution catalysts for water splitting. *Chemical Society Reviews* **2015**, *44* (15), 5148-80.
64. Mishra, I. K.; Zhou, H.; Sun, J.; Dahal, K.; Ren, Z.; He, R.; Chen, S.; Ren, Z., Highly efficient hydrogen evolution by self-standing nickel phosphide-based hybrid nanosheet arrays electrocatalyst. *Materials Today Physics* **2018**, *4*, 1-6.
65. Chen, Z.; Song, Y.; Cai, J.; Zheng, X.; Han, D.; Wu, Y.; Zang, Y.; Niu, S.; Liu, Y.; Zhu, J.; Liu, X.; Wang, G., Tailoring the d-Band Centers Enables Co₄N Nanosheets To Be Highly Active for Hydrogen Evolution Catalysis. *Angewandte Chemie International Edition* **2018**, *57* (18), 5076-5080.
66. Kim, B. K.; Kim, S.-K.; Cho, S. K.; Kim, J. J., Enhanced catalytic activity of electrodeposited Ni-Cu-P toward oxygen evolution reaction. *Applied Catalysis B: Environmental* **2018**, *237*, 409-415.
67. Sun, H.; Xu, X.; Hu, Z.; Tjeng, L. H.; Zhao, J.; Zhang, Q.; Lin, H.-J.; Chen, C.-T.; Chan, T.-S.; Zhou, W.; Shao, Z., Boosting the oxygen evolution reaction activity of a perovskite through introducing multi-element synergy and building an ordered structure. *Journal of Materials Chemistry A* **2019**, *7* (16), 9924-9932.
68. Gong, M.; Dai, H., A mini review of NiFe-based materials as highly active oxygen evolution reaction electrocatalysts. *Nano Research* **2014**, *8* (1), 23-39.

69. Sun, H.; Yan, Z.; Liu, F.; Xu, W.; Cheng, F.; Chen, J., Self-Supported Transition-Metal-Based Electrocatalysts for Hydrogen and Oxygen Evolution. *Advanced Materials* **2019**, 1806326.
70. Zhang, J.; Zhang, Q.; Feng, X., Support and Interface Effects in Water-Splitting Electrocatalysts. *Advanced Materials* **2019**, e1808167.
71. Wang, A.-L.; Xu, H.; Li, G.-R., NiCoFe Layered Triple Hydroxides with Porous Structures as High-Performance Electrocatalysts for Overall Water Splitting. *ACS Energy Letters* **2016**, 1 (2), 445-453.
72. Liu, H.; Wang, Y.; Lu, X.; Hu, Y.; Zhu, G.; Chen, R.; Ma, L.; Zhu, H.; Tie, Z.; Liu, J.; Jin, Z., The effects of Al substitution and partial dissolution on ultrathin NiFeAl ternary layered double hydroxide nanosheets for oxygen evolution reaction in alkaline solution. *Nano Energy* **2017**, 35, 350-357.
73. Chen, Q. Q.; Hou, C. C.; Wang, C. J.; Yang, X.; Shi, R.; Chen, Y., Ir(4+)-Doped NiFe LDH to expedite hydrogen evolution kinetics as a Pt-like electrocatalyst for water splitting. *Chemical Communications (Camb)* **2018**, 54 (49), 6400-6403.
74. Yang, Y.; Dang, L.; Shearer, M. J.; Sheng, H.; Li, W.; Chen, J.; Xiao, P.; Zhang, Y.; Hamers, R. J.; Jin, S., Highly Active Trimetallic NiFeCr Layered Double Hydroxide Electrocatalysts for Oxygen Evolution Reaction. *Advanced Energy Materials* **2018**, 8 (15), 1703189.
75. Li, P.; Duan, X.; Kuang, Y.; Li, Y.; Zhang, G.; Liu, W.; Sun, X., Tuning Electronic Structure of NiFe Layered Double Hydroxides with Vanadium Doping toward High Efficient Electrocatalytic Water Oxidation. *Advanced Energy Materials* **2018**, 8 (15), 1703341.

76. Chen, G.; Wang, T.; Zhang, J.; Liu, P.; Sun, H.; Zhuang, X.; Chen, M.; Feng, X., Accelerated Hydrogen Evolution Kinetics on NiFe-Layered Double Hydroxide Electrocatalysts by Tailoring Water Dissociation Active Sites. *Advanced Materials* **2018**, *30* (10), 1706279.
77. Zhang, B.; Zheng, X.; Voznyy, O.; Comin, R.; Bajdich, M.; García-Melchor, M.; Han, L.; Xu, J.; Liu, M.; Zheng, L.; García de Arquer, F. P.; Dinh, C. T.; Fan, F.; Yuan, M.; Yassitepe, E.; Chen, N.; Regier, T.; Liu, P.; Li, Y.; De Luna, P.; Janmohamed, A.; Xin, H. L.; Yang, H.; Vojvodic, A.; Sargent, E. H., Homogeneously dispersed multimetal oxygen-evolving catalysts. *Science* **2016**, *352* (6283), 333-337.
78. Xu, H.; Fei, B.; Cai, G.; Ha, Y.; Liu, J.; Jia, H.; Zhang, J.; Liu, M.; Wu, R., Boronization-Induced Ultrathin 2D Nanosheets with Abundant Crystalline–Amorphous Phase Boundary Supported on Nickel Foam toward Efficient Water Splitting. *Advanced Energy Materials* **2019**, 1902714.
79. Han, H.; Choi, H.; Mhin, S.; Hong, Y.-R.; Kim, K. M.; Kwon, J.; Ali, G.; Chung, K. Y.; Je, M.; Umh, H. N.; Lim, D.-H.; Davey, K.; Qiao, S.-Z.; Paik, U.; Song, T., Advantageous crystalline–amorphous phase boundary for enhanced electrochemical water oxidation. *Energy & Environmental Science* **2019**, *12* (8), 2443-2454.
80. Danilovic, N.; Subbaraman, R.; Chang, K. C.; Chang, S. H.; Kang, Y. J.; Snyder, J.; Paulikas, A. P.; Strmcnik, D.; Kim, Y. T.; Myers, D.; Stamenkovic, V. R.; Markovic, N. M., Activity-Stability Trends for the Oxygen Evolution Reaction on Monometallic Oxides in Acidic Environments. *The Journal of Physical Chemistry Letters* **2014**, *5* (14), 2474-8.

81. Yan, N.; Detz, R. J.; Govindarajan, N.; Koelewijn, J. M.; Hua, B.; Li, P.; Meijer, E. J.; Reek, J. N. H., Selective surface functionalization generating site-isolated Ir on a MnO_x/N-doped carbon composite for robust electrocatalytic water oxidation. *Journal of Materials Chemistry A* **2019**, 7 (40), 23098-23104.
82. Yin, S.; Tu, W.; Sheng, Y.; Du, Y.; Kraft, M.; Borgna, A.; Xu, R., A Highly Efficient Oxygen Evolution Catalyst Consisting of Interconnected Nickel-Iron-Layered Double Hydroxide and Carbon Nanodomains. *Advanced Materials* **2018**, 30 (5).
83. Bo, X.; Li, Y.; Hocking, R. K.; Zhao, C., NiFeCr Hydroxide Holey Nanosheet as Advanced Electrocatalyst for Water Oxidation. *ACS Applied Materials & Interfaces* **2017**, 9 (47), 41239-41245.
84. Friebel, D.; Louie, M. W.; Bajdich, M.; Sanwald, K. E.; Cai, Y.; Wise, A. M.; Cheng, M. J.; Sokaras, D.; Weng, T. C.; Alonso-Mori, R.; Davis, R. C.; Bargar, J. R.; Norskov, J. K.; Nilsson, A.; Bell, A. T., Identification of highly active Fe sites in (Ni,Fe)OOH for electrocatalytic water splitting. *Journal of the American Chemical Society* **2015**, 137 (3), 1305-13.
85. Wu, L.; Yu, L.; Zhu, Q.; McElhenny, B.; Zhang, F.; Wu, C.; Xing, X.; Bao, J.; Chen, S.; Ren, Z., Boron-Modified Cobalt Iron Layered Double Hydroxides for High Efficiency Seawater Oxidation. *Nano Energy* **2021**, 105838.
86. Guo, M.; Zhou, L.; Li, Y.; Zheng, Q.; Xie, F.; Lin, D., Unique nanosheet–nanowire structured CoMnFe layered triple hydroxide arrays as self-supporting electrodes for a high-efficiency oxygen evolution reaction. *Journal of Materials Chemistry A* **2019**, 7 (21), 13130-13141.

87. Lu, X.; Zhao, C., Electrodeposition of hierarchically structured three-dimensional nickel-iron electrodes for efficient oxygen evolution at high current densities. *Nature Communications* **2015**, *6*, 6616.
88. Hou, Y.; Lohe, M. R.; Zhang, J.; Liu, S.; Zhuang, X.; Feng, X., Vertically oriented cobalt selenide/NiFe layered-double-hydroxide nanosheets supported on exfoliated graphene foil: an efficient 3D electrode for overall water splitting. *Energy & Environmental Science* **2016**, *9* (2), 478-483.
89. Zhang, H.; Li, X.; Hähnel, A.; Naumann, V.; Lin, C.; Azimi, S.; Schweizer, S. L.; Majenburg, A. W.; Wehrspohn, R. B., Bifunctional Heterostructure Assembly of NiFe LDH Nanosheets on NiCoP Nanowires for Highly Efficient and Stable Overall Water Splitting. *Advanced Functional Materials* **2018**, *28* (14), 1706847.
90. Yu, L.; Zhou, H.; Sun, J.; Qin, F.; Luo, D.; Xie, L.; Yu, F.; Bao, J.; Li, Y.; Yu, Y.; Chen, S.; Ren, Z., Hierarchical Cu@CoFe layered double hydroxide core-shell nanoarchitectures as bifunctional electrocatalysts for efficient overall water splitting. *Nano Energy* **2017**, *41*, 327-336.
91. Wang, D.; Li, Q.; Han, C.; Lu, Q.; Xing, Z.; Yang, X., Atomic and electronic modulation of self-supported nickel-vanadium layered double hydroxide to accelerate water splitting kinetics. *Nature Communications* **2019**, *10* (1), 3899.
92. Li, P.; Wang, M.; Duan, X.; Zheng, L.; Cheng, X.; Zhang, Y.; Kuang, Y.; Li, Y.; Ma, Q.; Feng, Z.; Liu, W.; Sun, X., Boosting oxygen evolution of single-atomic ruthenium through electronic coupling with cobalt-iron layered double hydroxides. *Nature Communications* **2019**, *10* (1), 1711.

93. Yan, S.; Abhilash, K. P.; Tang, L.; Yang, M.; Ma, Y.; Xia, Q.; Guo, Q.; Xia, H., Research Advances of Amorphous Metal Oxides in Electrochemical Energy Storage and Conversion. *Small* **2019**, *15* (4), e1804371.
94. Masa, J.; Weide, P.; Peeters, D.; Sinev, I.; Xia, W.; Sun, Z.; Somsen, C.; Muhler, M.; Schuhmann, W., Amorphous Cobalt Boride (Co₂B) as a Highly Efficient Nonprecious Catalyst for Electrochemical Water Splitting: Oxygen and Hydrogen Evolution. *Advanced Energy Materials* **2016**, *6* (6), 1502313.
95. Ren, H.; Sun, X.; Du, C.; Zhao, J.; Liu, D.; Fang, W.; Kumar, S.; Chua, R.; Meng, S.; Kidkhunthod, P.; Song, L.; Li, S.; Madhavi, S.; Yan, Q., Amorphous Fe-Ni-P-B-O Nanocages as Efficient Electrocatalysts for Oxygen Evolution Reaction. *ACS Nano* **2019**, *13* (11), 12969-12979.
96. Li, L.; Wang, B.; Zhang, G.; Yang, G.; Yang, T.; Yang, S.; Yang, S., Electrochemically Modifying the Electronic Structure of IrO₂ Nanoparticles for Overall Electrochemical Water Splitting with Extensive Adaptability. *Advanced Energy Materials* **2020**, *10* (30), 2001600.
97. Sun, S.; Zhai, T.; Liang, C.; Savilov, S. V.; Xia, H., Boosted crystalline/amorphous Fe₂O_{3-δ} core/shell heterostructure for flexible solid-state pseudocapacitors in large scale. *Nano Energy* **2018**, *45*, 390-397.
98. Fang, M.; Han, D.; Xu, W. B.; Shen, Y.; Lu, Y.; Cao, P.; Han, S.; Xu, W.; Zhu, D.; Liu, W.; Ho, J. C., Surface-Guided Formation of Amorphous Mixed-Metal Oxyhydroxides on Ultrathin MnO₂ Nanosheet Arrays for Efficient Electrocatalytic Oxygen Evolution. *Advanced Energy Materials* **2020**, *10* (27), 2001059.

99. Cai, W.; Chen, R.; Yang, H.; Tao, H. B.; Wang, H. Y.; Gao, J.; Liu, W.; Liu, S.; Hung, S. F.; Liu, B., Amorphous versus Crystalline in Water Oxidation Catalysis: A Case Study of NiFe Alloy. *Nano Lett* **2020**, *20* (6), 4278-4285.
100. Yoon, C.; Cocco, D. L., Potential of amorphous materials as catalysts. *Journal of Non-Crystalline Solids* **1986**, *79* (3), 217-245.
101. Dong, Z.; Lin, F.; Yao, Y.; Jiao, L., Crystalline Ni(OH)₂/Amorphous NiMoOx Mixed-Catalyst with Pt-Like Performance for Hydrogen Production. *Advanced Energy Materials* **2019**, *9* (46), 1902703.
102. ul Haq, T.; Mansour, S. A.; Munir, A.; Haik, Y., Gold-Supported Gadolinium Doped CoB Amorphous Sheet: A New Benchmark Electrocatalyst for Water Oxidation with High Turnover Frequency. *Advanced Functional Materials* **2020**, *30* (16), 1910309.
103. Park, H.; Lee, E.; Lei, M.; Joo, H.; Coh, S.; Fokwa, B. P. T., Canonic-Like HER Activity of Cr_{1-x}Mo_xB₂ Solid Solution: Overpowering Pt/C at High Current Density. *Advanced Materials* **2020**, *32* (28), e2000855.
104. Zhai, T.; Sun, S.; Liu, X.; Liang, C.; Wang, G.; Xia, H., Achieving Insertion-Like Capacity at Ultrahigh Rate via Tunable Surface Pseudocapacitance. *Advanced Materials* **2018**, *30* (12), e1706640.
105. Nsanzimana, J. M. V.; Peng, Y.; Xu, Y. Y.; Thia, L.; Wang, C.; Xia, B. Y.; Wang, X., An Efficient and Earth-Abundant Oxygen-Evolving Electrocatalyst Based on Amorphous Metal Borides. *Advanced Energy Materials* **2018**, *8* (1), 1701475.
106. Jiang, W. J.; Niu, S.; Tang, T.; Zhang, Q. H.; Liu, X. Z.; Zhang, Y.; Chen, Y. Y.; Li, J. H.; Gu, L.; Wan, L. J.; Hu, J. S., Crystallinity-Modulated Electrocatalytic

Activity of a Nickel(II) Borate Thin Layer on Ni₃B for Efficient Water Oxidation. *Angewandte Chemie International Edition* **2017**, *56* (23), 6572-6577.

107. Jaiswar, S.; Mandal, K. D., Evidence of Enhanced Oxygen Vacancy Defects Inducing Ferromagnetism in Multiferroic CaMn₇O₁₂ Manganite with Sintering Time. *The Journal of Physical Chemistry C* **2017**, *121* (36), 19586-19601.

108. Liu, S.; Zhu, J.; Sun, M.; Ma, Z.; Hu, K.; Nakajima, T.; Liu, X.; Schmuki, P.; Wang, L., Promoting the hydrogen evolution reaction through oxygen vacancies and phase transformation engineering on layered double hydroxide nanosheets. *Journal of Materials Chemistry A* **2020**, *8* (5), 2490-2497.

109. Wu, C.; Xue, S.; Qin, Z.; Nazari, M.; Yang, G.; Yue, S.; Tong, T.; Ghasemi, H.; Hernandez, F. C. R.; Xue, S.; Zhang, D.; Wang, H.; Wang, Z. M.; Pu, S.; Bao, J., Making g-C₃N₄ ultra-thin nanosheets active for photocatalytic overall water splitting. *Applied Catalysis B: Environmental* **2021**, *282*, 119557.

110. Louie, M. W.; Bell, A. T., An investigation of thin-film Ni-Fe oxide catalysts for the electrochemical evolution of oxygen. *Journal of the American Chemical Society* **2013**, *135* (33), 12329-37.

111. Li, J.; Chen, H.; Liu, Y.; Gao, R.; Zou, X., In situ structural evolution of a nickel boride catalyst: synergistic geometric and electronic optimization for the oxygen evolution reaction. *Journal of Materials Chemistry A* **2019**, *7* (10), 5288-5294.

112. Qiu, Z.; Tai, C.-W.; Niklasson, G. A.; Edvinsson, T., Direct observation of active catalyst surface phases and the effect of dynamic self-optimization in NiFe-layered double hydroxides for alkaline water splitting. *Energy & Environmental Science* **2019**, *12* (2), 572-581.

113. Dionigi, F.; Zeng, Z.; Sinev, I.; Merzdorf, T.; Deshpande, S.; Lopez, M. B.; Kunze, S.; Zegkinoglou, I.; Sarodnik, H.; Fan, D.; Bergmann, A.; Drnec, J.; Araujo, J. F.; Gliech, M.; Teschner, D.; Zhu, J.; Li, W. X.; Greeley, J.; Cuenya, B. R.; Strasser, P., In-situ structure and catalytic mechanism of NiFe and CoFe layered double hydroxides during oxygen evolution. *Nature Communications* **2020**, *11* (1), 2522.
114. Yu, X.; Yu, Z. Y.; Zhang, X. L.; Zheng, Y. R.; Duan, Y.; Gao, Q.; Wu, R.; Sun, B.; Gao, M. R.; Wang, G.; Yu, S. H., "Superaerophobic" Nickel Phosphide Nanoarray Catalyst for Efficient Hydrogen Evolution at Ultrahigh Current Densities. *Journal of the American Chemical Society* **2019**, *141* (18), 7537-7543.
115. Wu, L.; Yu, L.; McElhenny, B.; Xing, X.; Luo, D.; Zhang, F.; Bao, J.; Chen, S.; Ren, Z., Rational design of core-shell-structured $\text{CoP}_x@FeOOH$ for efficient seawater electrolysis. *Applied Catalysis B: Environmental* **2021**, *294*, 120256.
116. Zhong, H.; Wang, J.; Meng, F.; Zhang, X., In Situ Activating Ubiquitous Rust towards Low-Cost, Efficient, Free-Standing, and Recoverable Oxygen Evolution Electrodes. *Angewandte Chemie International Edition* **2016**, *55* (34), 9937-9941.
117. Bergmann, A.; Jones, T. E.; Martinez Moreno, E.; Teschner, D.; Chernev, P.; Gliech, M.; Reier, T.; Dau, H.; Strasser, P., Unified structural motifs of the catalytically active state of Co(oxyhydr)oxides during the electrochemical oxygen evolution reaction. *Nature Catalysis* **2018**, *1* (9), 711-719.
118. Chemelewski, W. D.; Lee, H. C.; Lin, J. F.; Bard, A. J.; Mullins, C. B., Amorphous FeOOH oxygen evolution reaction catalyst for photoelectrochemical water splitting. *Journal of the American Chemical Society* **2014**, *136* (7), 2843-50.

119. Niu, S.; Jiang, W. J.; Wei, Z.; Tang, T.; Ma, J.; Hu, J. S.; Wan, L. J., Se-Doping Activates FeOOH for Cost-Effective and Efficient Electrochemical Water Oxidation. *Journal of the American Chemical Society* **2019**, *141* (17), 7005-7013.
120. Zheng, M.; Guo, K.; Jiang, W.-J.; Tang, T.; Wang, X.; Zhou, P.; Du, J.; Zhao, Y.; Xu, C.; Hu, J.-S., When MoS₂ meets FeOOH: A “one-stone-two-birds” heterostructure as a bifunctional electrocatalyst for efficient alkaline water splitting. *Applied Catalysis B: Environmental* **2019**, *244*, 1004-1012.
121. Yu, L.; Wu, L.; McElhenny, B.; Song, S.; Luo, D.; Zhang, F.; Yu, Y.; Chen, S.; Ren, Z., Ultrafast room-temperature synthesis of porous S-doped Ni/Fe (oxy)hydroxide electrodes for oxygen evolution catalysis in seawater splitting. *Energy & Environmental Science* **2020**, *13* (10), 3439-3446.
122. Liang, C.; Zou, P.; Nairan, A.; Zhang, Y.; Liu, J.; Liu, K.; Hu, S.; Kang, F.; Fan, H. J.; Yang, C., Exceptional performance of hierarchical Ni-Fe oxyhydroxide@NiFe alloy nanowire array electrocatalysts for large current density water splitting. *Energy & Environmental Science* **2020**, *13* (1), 86-95.
123. Hong, W. T.; Risch, M.; Stoerzinger, K. A.; Grimaud, A.; Suntivich, J.; Shao-Horn, Y., Toward the rational design of non-precious transition metal oxides for oxygen electrocatalysis. *Energy & Environmental Science* **2015**, *8* (5), 1404-1427.
124. Xu, K.; Cheng, H.; Lv, H.; Wang, J.; Liu, L.; Liu, S.; Wu, X.; Chu, W.; Wu, C.; Xie, Y., Controllable Surface Reorganization Engineering on Cobalt Phosphide Nanowire Arrays for Efficient Alkaline Hydrogen Evolution Reaction. *Advanced Materials* **2018**, *30* (1).

125. Li, H.; Wen, P.; Itanze, D. S.; Kim, M. W.; Adhikari, S.; Lu, C.; Jiang, L.; Qiu, Y.; Geyer, S. M., Phosphorus-Rich Colloidal Cobalt Diphosphide (CoP₂) Nanocrystals for Electrochemical and Photoelectrochemical Hydrogen Evolution. *Advanced Materials* **2019**, *31* (24), e1900813.
126. Tang, C.; Zhang, R.; Lu, W.; He, L.; Jiang, X.; Asiri, A. M.; Sun, X., Fe-Doped CoP Nanoarray: A Monolithic Multifunctional Catalyst for Highly Efficient Hydrogen Generation. *Advanced Materials* **2017**, *29* (2), 1602441.
127. Luo, Y.; Tang, L.; Khan, U.; Yu, Q.; Cheng, H. M.; Zou, X.; Liu, B., Morphology and surface chemistry engineering toward pH-universal catalysts for hydrogen evolution at high current density. *Nature Communications* **2019**, *10* (1), 269.
128. Dastafkan, K.; Meyer, Q.; Chen, X.; Zhao, C., Efficient Oxygen Evolution and Gas Bubble Release Achieved by a Low Gas Bubble Adhesive Iron-Nickel Vanadate Electrocatalyst. *Small* **2020**, *16* (32), e2002412.
129. de Faria, D. L. A.; Venâncio Silva, S.; de Oliveira, M. T., Raman microspectroscopy of some iron oxides and oxyhydroxides. *Journal of Raman Spectroscopy* **1997**, *28* (11), 873-878.
130. Hanesch, M., Raman spectroscopy of iron oxides and (oxy)hydroxides at low laser power and possible applications in environmental magnetic studies. *Geophysical Journal International* **2009**, *177* (3), 941-948.
131. Cai, J.; Song, Y.; Zang, Y.; Niu, S.; Wu, Y.; Xie, Y.; Zheng, X.; Liu, Y.; Lin, Y.; Liu, X.; Wang, G.; Qian, Y., N-induced lattice contraction generally boosts the hydrogen evolution catalysis of P-rich metal phosphides. *Science Advances* **2020**, *6* (1), eaaw8113.

132. Yang, L.; Li, H.; Yu, Y.; Wu, Y.; Zhang, L., Assembled 3D MOF on 2D Nanosheets for Self-boosting Catalytic Synthesis of N-doped Carbon Nanotube Encapsulated Metallic Co Electrocatalysts for Overall Water Splitting. *Applied Catalysis B: Environmental* **2020**, *271*, 118939.
133. Song, S.; Yu, L.; Xiao, X.; Qin, Z.; Zhang, W.; Wang, D.; Bao, J.; Zhou, H.; Zhang, Q.; Chen, S.; Ren, Z., Outstanding oxygen evolution reaction performance of nickel iron selenide/stainless steel mat for water electrolysis. *Materials Today Physics* **2020**, *13*, 100216.
134. Otte, K.; Schmahl, W. W.; Pentcheva, R., DFT+U Study of Arsenate Adsorption on FeOOH Surfaces: Evidence for Competing Binding Mechanisms. *The Journal of Physical Chemistry C* **2013**, *117* (30), 15571-15582.
135. Chen, G.-F.; Luo, Y.; Ding, L.-X.; Wang, H., Low-Voltage Electrolytic Hydrogen Production Derived from Efficient Water and Ethanol Oxidation on Fluorine-Modified FeOOH Anode. *ACS Catalysis* **2017**, *8* (1), 526-530.
136. Millero, F. J.; Feistel, R.; Wright, D. G.; McDougall, T. J., The composition of Standard Seawater and the definition of the Reference-Composition Salinity Scale. *Deep Sea Research Part I: Oceanographic Research Papers* **2008**, *55* (1), 50-72.
137. Xiao, P.; Sk, M. A.; Thia, L.; Ge, X.; Lim, R. J.; Wang, J.-Y.; Lim, K. H.; Wang, X., Molybdenum phosphide as an efficient electrocatalyst for the hydrogen evolution reaction. *Energy & Environmental Science* **2014**, *7* (8), 2624-2629.
138. Xu, H.; Fei, B.; Cai, G.; Ha, Y.; Liu, J.; Jia, H.; Zhang, J.; Liu, M.; Wu, R., Boronization-Induced Ultrathin 2D Nanosheets with Abundant Crystalline-

Amorphous Phase Boundary Supported on Nickel Foam toward Efficient Water Splitting. *Advanced Energy Materials* **2019**, *10* (3), 1902714.

139. Wu, X.; Zhou, S.; Wang, Z.; Liu, J.; Pei, W.; Yang, P.; Zhao, J.; Qiu, J., Engineering Multifunctional Collaborative Catalytic Interface Enabling Efficient Hydrogen Evolution in All pH Range and Seawater. *Advanced Energy Materials* **2019**, *9* (34), 1901333.

140. Dresp, S.; Ngo Thanh, T.; Klingenhof, M.; Brückner, S.; Hauke, P.; Strasser, P., Efficient direct seawater electrolyzers using selective alkaline NiFe-LDH as OER catalyst in asymmetric electrolyte feeds. *Energy & Environmental Science* **2020**, *13* (6), 1725-1729.

141. Wang, Z.; Fan, J.; Cheng, B.; Yu, J.; Xu, J., Nickel-based cocatalysts for photocatalysis: Hydrogen evolution, overall water splitting and CO₂ reduction. *Materials Today Physics* **2020**, *15*, 100279.

142. Yang, L.; Liu, Z.; Zhu, S.; Feng, L.; Xing, W., Ni-based layered double hydroxide catalysts for oxygen evolution reaction. *Materials Today Physics* **2021**, *16*, 100292.

143. Bennett, J. E., Electrodes for generation of hydrogen and oxygen from seawater. *International Journal of Hydrogen Energy* **1980**, *5* (4), 401-408.

144. Ning, M.; Wu, L.; Zhang, F.; Wang, D.; Song, S.; Tong, T.; Bao, J.; Chen, S.; Yu, L.; Ren, Z., One-step spontaneous growth of NiFe layered double hydroxide at room temperature for seawater oxygen evolution. *Materials Today Physics* **2021**, *19*, 100419.

145. Zhu, C.; Wang, A. L.; Xiao, W.; Chao, D.; Zhang, X.; Tiej, N. H.; Chen, S.; Kang, J.; Wang, X.; Ding, J.; Wang, J.; Zhang, H.; Fan, H. J., In Situ Grown Epitaxial Heterojunction Exhibits High-Performance Electrocatalytic Water Splitting. *Advanced Materials* **2018**, *30* (13), e1705516.
146. Yao, N.; Li, P.; Zhou, Z.; Zhao, Y.; Cheng, G.; Chen, S.; Luo, W., Synergistically Tuning Water and Hydrogen Binding Abilities Over Co₄N by Cr Doping for Exceptional Alkaline Hydrogen Evolution Electrocatalysis. *Advanced Energy Materials* **2019**, *9* (41), 1902449.
147. Sun, J.; Xu, W.; Lv, C.; Zhang, L.; Shakouri, M.; Peng, Y.; Wang, Q.; Yang, X.; Yuan, D.; Huang, M.; Hu, Y.; Yang, D.; Zhang, L., Co/MoN hetero-interface nanoflake array with enhanced water dissociation capability achieves the Pt-like hydrogen evolution catalytic performance. *Applied Catalysis B: Environmental* **2021**, *286*, 119882.
148. Lin, F.; Dong, Z.; Yao, Y.; Yang, L.; Fang, F.; Jiao, L., Electrocatalytic Hydrogen Evolution of Ultrathin Co-Mo₅N₆ Heterojunction with Interfacial Electron Redistribution. *Advanced Energy Materials* **2020**, *10* (42), 2002176.
149. Zhang, B.; Zhang, L.; Tan, Q.; Wang, J.; Liu, J.; Wan, H.; Miao, L.; Jiang, J., Simultaneous interfacial chemistry and inner Helmholtz plane regulation for superior alkaline hydrogen evolution. *Energy & Environmental Science* **2020**, *13* (9), 3007-3013.
150. Peng, S.; Li, L.; Wu, H. B.; Madhavi, S.; Lou, X. W. D., Controlled Growth of NiMoO₄ Nanosheet and Nanorod Arrays on Various Conductive Substrates as

Advanced Electrodes for Asymmetric Supercapacitors. *Advanced Energy Materials* **2015**, *5* (2), 1401172.

151. Zhang, J.; Wang, T.; Liu, P.; Liao, Z.; Liu, S.; Zhuang, X.; Chen, M.; Zschech, E.; Feng, X., Efficient hydrogen production on MoNi₄ electrocatalysts with fast water dissociation kinetics. *Nature Communications* **2017**, *8*, 15437.

152. Li, H.; Chen, S.; Zhang, Y.; Zhang, Q.; Jia, X.; Zhang, Q.; Gu, L.; Sun, X.; Song, L.; Wang, X., Systematic design of superaerophobic nanotube-array electrode comprised of transition-metal sulfides for overall water splitting. *Nature Communications* **2018**, *9* (1), 2452.

153. Tsurov, M. A.; Afanasiev, P. V.; Lunin, V. V., Composition and catalytic properties of products from the reduction of NiMoO₄. *Applied Catalysis A: General* **1993**, *105* (2), 205-221.

154. Patil, R. B.; House, S. D.; Mantri, A.; Yang, J. C.; McKone, J. R., Direct Observation of Ni-Mo Bimetallic Catalyst Formation via Thermal Reduction of Nickel Molybdate Nanorods. *ACS Catalysis* **2020**, *10* (18), 10390-10398.

155. Dong, G.; Ho, W.; Wang, C., Selective photocatalytic N₂ fixation dependent on g-C₃N₄ induced by nitrogen vacancies. *Journal of Materials Chemistry A* **2015**, *3* (46), 23435-23441.

156. Lv, C.; Qian, Y.; Yan, C.; Ding, Y.; Liu, Y.; Chen, G.; Yu, G., Defect Engineering Metal-Free Polymeric Carbon Nitride Electrocatalyst for Effective Nitrogen Fixation under Ambient Conditions. *Angewandte Chemie International Edition* **2018**, *57* (32), 10246-10250.

157. Li, Y.; Zhang, H.; Jiang, M.; Kuang, Y.; Wang, H.; Sun, X., Amorphous Co–Mo-S ultrathin films with low-temperature sulfurization as high-performance electrocatalysts for the hydrogen evolution reaction. *Journal of Materials Chemistry A* **2016**, *4* (36), 13731-13735.
158. Ma, Y.-Y.; Wu, C.-X.; Feng, X.-J.; Tan, H.-Q.; Yan, L.-K.; Liu, Y.; Kang, Z.-H.; Wang, E.-B.; Li, Y.-G., Highly efficient hydrogen evolution from seawater by a low-cost and stable CoMoP@C electrocatalyst superior to Pt/C. *Energy & Environmental Science* **2017**, *10* (3), 788-798.
159. Li, J. S.; Wang, Y.; Liu, C. H.; Li, S. L.; Wang, Y. G.; Dong, L. Z.; Dai, Z. H.; Li, Y. F.; Lan, Y. Q., Coupled molybdenum carbide and reduced graphene oxide electrocatalysts for efficient hydrogen evolution. *Nature Communications* **2016**, *7*, 11204.
160. Wang, Q.; Huang, X.; Zhao, Z. L.; Wang, M.; Xiang, B.; Li, J.; Feng, Z.; Xu, H.; Gu, M., Ultrahigh-Loading of Ir Single Atoms on NiO Matrix to Dramatically Enhance Oxygen Evolution Reaction. *Journal of the American Chemical Society* **2020**, *142* (16), 7425-7433.
161. Yan, H.; Xie, Y.; Jiao, Y.; Wu, A.; Tian, C.; Zhang, X.; Wang, L.; Fu, H., Holey Reduced Graphene Oxide Coupled with an Mo₂N-Mo₂C Heterojunction for Efficient Hydrogen Evolution. *Advanced Materials* **2018**, *30* (2).
162. Zhang, Y.; Ouyang, B.; Xu, J.; Chen, S.; Rawat, R. S.; Fan, H. J., 3D Porous Hierarchical Nickel-Molybdenum Nitrides Synthesized by RF Plasma as Highly Active and Stable Hydrogen-Evolution-Reaction Electrocatalysts. *Advanced Energy Materials* **2016**, *6* (11), 1600221.

163. Zhou, K. L.; Wang, Z.; Han, C. B.; Ke, X.; Wang, C.; Jin, Y.; Zhang, Q.; Liu, J.; Wang, H.; Yan, H., Platinum single-atom catalyst coupled with transition metal/metal oxide heterostructure for accelerating alkaline hydrogen evolution reaction. *Nature Communications* **2021**, *12* (1), 3783.
164. Chen, D.; Pu, Z.; Lu, R.; Ji, P.; Wang, P.; Zhu, J.; Lin, C.; Li, H. W.; Zhou, X.; Hu, Z.; Xia, F.; Wu, J.; Mu, S., Ultralow Ru Loading Transition Metal Phosphides as High-Efficient Bifunctional Electrocatalyst for a Solar-to-Hydrogen Generation System. *Advanced Energy Materials* **2020**, *10* (28), 2000814.
165. Xiao, X.; Wang, X.; Li, B.; Jiang, X.; Zhang, Y.; Li, M.; Song, S.; Chen, S.; Wang, M.; Shen, Y.; Ren, Z., Regulating the electronic configuration of ruthenium nanoparticles via coupling cobalt phosphide for hydrogen evolution in alkaline media. *Materials Today Physics* **2020**, *12*, 100182.
166. Wei, C.; Sun, S.; Mandler, D.; Wang, X.; Qiao, S. Z.; Xu, Z. J., Approaches for measuring the surface areas of metal oxide electrocatalysts for determining their intrinsic electrocatalytic activity. *Chemical Society Reviews* **2019**, *48* (9), 2518-2534.
167. Kozuch, S.; Martin, J. M. L., "Turning Over" Definitions in Catalytic Cycles. *ACS Catalysis* **2012**, *2* (12), 2787-2794.
168. Fernandez, D.; Maurer, P.; Martine, M.; Coey, J. M.; Mobius, M. E., Bubble formation at a gas-evolving microelectrode. *Langmuir* **2014**, *30* (43), 13065-74.
169. Dinh, C.-T.; Jain, A.; de Arquer, F. P. G.; De Luna, P.; Li, J.; Wang, N.; Zheng, X.; Cai, J.; Gregory, B. Z.; Voznyy, O.; Zhang, B.; Liu, M.; Sinton, D.; Crumlin, E. J.; Sargent, E. H., Multi-site electrocatalysts for hydrogen evolution in neutral media by destabilization of water molecules. *Nature Energy* **2019**, *4* (2), 107-114.

170. Jiang, Y.; Song, Y.; Li, Y.; Tian, W.; Pan, Z.; Yang, P.; Li, Y.; Gu, Q.; Hu, L., Charge Transfer in Ultrafine LDH Nanosheets/Graphene Interface with Superior Capacitive Energy Storage Performance. *ACS Applied Materials & Interfaces* **2017**, *9* (43), 37645-37654.
171. Zhao, H.; Mao, Y.; Mao, X.; Shi, X.; Xu, C.; Wang, C.; Zhang, S.; Zhou, D., Band Structure and Photoelectric Characterization of GeSe Monolayers. *Advanced Functional Materials* **2017**, *28* (6), 1704855.
172. Yao, Y.; Zhu, Y.; Pan, C.; Wang, C.; Hu, S.; Xiao, W.; Chi, X.; Fang, Y.; Yang, J.; Deng, H.; Xiao, S.; Li, J.; Luo, Z.; Guo, Y., Interfacial sp C-O-Mo Hybridization Originated High-Current Density Hydrogen Evolution. *Journal of the American Chemical Society* **2021**, *143* (23), 8720-8730.
173. Li, X.; Yang, X.; Liu, L.; Zhao, H.; Li, Y.; Zhu, H.; Chen, Y.; Guo, S.; Liu, Y.; Tan, Q.; Wu, G., Chemical Vapor Deposition for N/S-Doped Single Fe Site Catalysts for the Oxygen Reduction in Direct Methanol Fuel Cells. *ACS Catalysis* **2021**, *11* (12), 7450-7459.
174. Skúlason, E.; Tripkovic, V.; Björketun, M. E.; Gudmundsdóttir, S.; Karlberg, G.; Rossmeisl, J.; Bligaard, T.; Jónsson, H.; Nørskov, J. K., Modeling the Electrochemical Hydrogen Oxidation and Evolution Reactions on the Basis of Density Functional Theory Calculations. *The Journal of Physical Chemistry C* **2010**, *114* (42), 18182-18197.
175. Subbaraman, R.; Tripkovic, D.; Strmcnik, D.; Chang, K.-C.; Uchimura, M.; Paulikas, A. P.; Stamenkovic, V.; Markovic, N. M., Enhancing Hydrogen Evolution

Activity in Water Splitting by Tailoring Li⁺-Ni(OH)₂-Pt Interfaces. *Science* **2011**, *334* (6060), 1256-1260.

176. Wu, L.; Yu, L.; Zhang, F.; McElhenny, B.; Luo, D.; Karim, A.; Chen, S.; Ren, Z., Heterogeneous Bimetallic Phosphide Ni₂P-Fe₂P as an Efficient Bifunctional Catalyst for Water/Seawater Splitting. *Advanced Functional Materials* **2021**, *31* (1), 2006484.

177. Zhao, Z.; Schipper, D. E.; Leitner, A. P.; Thirumalai, H.; Chen, J.-H.; Xie, L.; Qin, F.; Alam, M. K.; Grabow, L. C.; Chen, S.; Wang, D.; Ren, Z.; Wang, Z.; Whitmire, K. H.; Bao, J., Bifunctional metal phosphide FeMnP films from single source metal organic chemical vapor deposition for efficient overall water splitting. *Nano Energy* **2017**, *39*, 444-453.

178. Wu, Y.; Liu, X.; Han, D.; Song, X.; Shi, L.; Song, Y.; Niu, S.; Xie, Y.; Cai, J.; Wu, S.; Kang, J.; Zhou, J.; Chen, Z.; Zheng, X.; Xiao, X.; Wang, G., Electron density modulation of NiCo₂S₄ nanowires by nitrogen incorporation for highly efficient hydrogen evolution catalysis. *Nature Communications* **2018**, *9* (1), 1425.

179. Wang, M. Q.; Ye, C.; Liu, H.; Xu, M.; Bao, S. J., Nanosized Metal Phosphides Embedded in Nitrogen-Doped Porous Carbon Nanofibers for Enhanced Hydrogen Evolution at All pH Values. *Angewandte Chemie International Edition* **2018**, *57* (7), 1963-1967.

180. Blanchard, P. E. R.; Grosvenor, A. P.; Cavell, R. G.; Mar, A., X-ray Photoelectron and Absorption Spectroscopy of Metal-Rich Phosphides M₂P and M₃P (M = Cr-Ni). *Chemistry of Materials* **2008**, *20* (22), 7081-7088.

181. Liu, M.; Yang, L.; Liu, T.; Tang, Y.; Luo, S.; Liu, C.; Zeng, Y., Fe₂P/reduced graphene oxide/Fe₂P sandwich-structured nanowall arrays: a high-performance non-noble-metal electrocatalyst for hydrogen evolution. *Journal of Materials Chemistry A* **2017**, *5* (18), 8608-8615.
182. Zhang, H.; Maijenburg, A. W.; Li, X.; Schweizer, S. L.; Wehrspohn, R. B., Bifunctional Heterostructured Transition Metal Phosphides for Efficient Electrochemical Water Splitting. *Advanced Functional Materials* **2020**, 2003261.
183. Tan, Y.; Wang, H.; Liu, P.; Shen, Y.; Cheng, C.; Hirata, A.; Fujita, T.; Tang, Z.; Chen, M., Versatile nanoporous bimetallic phosphides towards electrochemical water splitting. *Energy & Environmental Science* **2016**, *9* (7), 2257-2261.
184. Wang, K.; Sun, K.; Yu, T.; Liu, X.; Wang, G.; Jiang, L.; Xie, G., Facile synthesis of nanoporous Ni-Fe-P bifunctional catalysts with high performance for overall water splitting. *Journal of Materials Chemistry A* **2019**, *7* (6), 2518-2523.
185. Zhang, R.; Huang, J.; Chen, G.; Chen, W.; Song, C.; Li, C.; Ostrikov, K., In situ engineering bi-metallic phospho-nitride bi-functional electrocatalysts for overall water splitting. *Applied Catalysis B: Environmental* **2019**, *254*, 414-423.
186. Song, H. J.; Yoon, H.; Ju, B.; Lee, D.-Y.; Kim, D.-W., Electrocatalytic Selective Oxygen Evolution of Carbon-Coated Na₂Co_{1-x}Fe_xP₂O₇ Nanoparticles for Alkaline Seawater Electrolysis. *ACS Catalysis* **2019**, *10* (1), 702-709.
187. Li, G.; Yang, Q.; Rao, J.; Fu, C.; Liou, S. C.; Auffermann, G.; Sun, Y.; Felser, C., In Situ Induction of Strain in Iron Phosphide (FeP₂) Catalyst for Enhanced Hydroxide Adsorption and Water Oxidation. *Advanced Functional Materials* **2020**, *30* (12), 1907791.

188. Yu, L.; Ren, Z., Systematic study of the influence of iR compensation on water electrolysis. *Materials Today Physics* **2020**, *14*, 100253.
189. Anantharaj, S.; Ede, S. R.; Karthick, K.; Sam Sankar, S.; Sangeetha, K.; Karthik, P. E.; Kundu, S., Precision and correctness in the evaluation of electrocatalytic water splitting: revisiting activity parameters with a critical assessment. *Energy & Environmental Science* **2018**, *11* (4), 744-771.
190. Joo, J.; Kim, T.; Lee, J.; Choi, S. I.; Lee, K., Morphology-Controlled Metal Sulfides and Phosphides for Electrochemical Water Splitting. *Advanced Materials* **2019**, *31* (14), e1806682.

LIST OF PUBLICATIONS

1. Ning, M.; Zhang, F.; Wu, L.; Xing, X.; Wang, D.; Song, S.; Zhou, Q.; Yu, L.; Bao, J.; Chen, S.; Ren, Z., Boosting Efficient Alkaline Freshwater and Seawater Electrolysis *via* Electrochemical Reconstruction. Submitted.
2. Zhang, F.; Liu, Y.; Wu, L.; Ning, M.; Song, S.; Xiao, X.; Hadjiev, V.; Fan, D.; Wang, D.; Yu, L.; Ren, Z.; Chen, S., Efficient Alkaline Seawater Oxidation by a Three-dimensional Core-shell Dendritic NiCo@NiFe Layered Double Hydroxide Electrode. Submitted.
3. Wu, L.; Zhang, F.; Song, S.; Ning, M.; Zhu, Q.; Zhou, J.; Gao, G.; Chen, Z.; Zhou, Q.; Xing, X.; Tong, T.; Yao, Y.; Bao, J.; Yu, L.; Chen, S.; Ren, Z., Efficient Alkaline Water/Seawater Hydrogen Evolution by a Nanorod-nanoparticle-structured Ni-MoN Catalyst with Fast Water-dissociation Kinetics. *Advanced Materials* DOI: 10.1002/adma.202201774.
4. Wu, L.; Yu, L.; McElhenny, B.; Xing, X.; Luo, D.; Zhang, F.; Bao, J.; Chen, S.; Ren, Z., Rational Design of Core-shell-structured CoP_x@FeOOH for Efficient Seawater Electrolysis. *Applied Catalysis B: Environmental* **2021**, 294, 120256.
5. Ning, M.; Wu, L.; Zhang, F.; Wang, D.; Song, S.; Tong, T.; Bao, J.; Chen, S.; Yu, L.; Ren, Z., One-step Spontaneous Growth of NiFe Layered Double Hydroxide at Room Temperature for Seawater Oxygen Evolution. *Materials Today Physics* **2021**, 19, 100419.
6. Wu, L.; Yu, L.; Zhu, Q.; McElhenny, B.; Zhang, F.; Wu, C.; Xing, X.; Bao, J.; Chen, S.; Ren, Z., Boron-modified Cobalt Iron Layered Double Hydroxides for High Efficiency Seawater Oxidation. *Nano Energy* **2021**, 83, 105838.

7. Zhang, F.; Yu, L.; Wu, L.; Luo, D.; Ren, Z., Rational Design of Oxygen Evolution Reaction Catalysts for Seawater Electrolysis. *Trends in Chemistry* **2021**, 3 (6), 485-498.
8. Wu, L.; Yu, L.; Zhang, F.; McElhenny, B.; Luo, D.; Karim, A.; Chen, S.; Ren, Z., Heterogeneous Bimetallic Phosphide Ni₂P-Fe₂P as an Efficient Bifunctional Catalyst for Water/Seawater Splitting. *Advanced Functional Materials* **2021**, 31 (1), 2006484.
9. Yu, L.; Wu, L.; Song, S.; McElhenny, B.; Zhang, F.; Chen, S.; Ren, Z., Hydrogen Generation from Seawater Electrolysis Over a Sandwich-like NiCoN|Ni_xP|NiCoN Microsheet Array Catalyst. *ACS Energy Letters* **2020**, 5 (8), 2681-2689.
10. Yu, L.; Wu, L.; McElhenny, B.; Song, S.; Luo, D.; Zhang, F.; Yu, Y.; Chen, S.; Ren, Z., Ultrafast Room-Temperature Synthesis of Porous S-Doped Ni/Fe (Oxy)hydroxide Electrodes for Oxygen Evolution Catalysis in Seawater Splitting. *Energy & Environmental Science* **2020**, 13 (10), 3439-3446.
11. Wu, L.; Yu, L.; Zhang, F.; Wang, D.; Luo, D.; Song, S.; Yuan, C.; Karim, A.; Chen, S.; Ren, Z., Facile Synthesis Of Nanoparticle-Stacked Tungsten-doped Nickel Iron Layered Double Hydroxide Nanosheets for Boosting Oxygen Evolution Reaction. *Journal of Materials Chemistry A* **2020**, 8 (16), 8096-8103.
12. Wu, L.; Yu, L.; Xiao, X.; Zhang, F.; Song, S.; Chen, S.; Ren, Z., Recent Advances in Self-supported Layered Double Hydroxides for Oxygen Evolution Reaction. *Research (Wash D C)* **2020**, 2020, 3976278.